
PEPTIDE BASED PLATFORMS FOR CANCER DRUG DELIVERY

Emiliana Perillo

Dottorato in Scienze Biotecnologiche XXVII ciclo
Indirizzo Biotecnologie Dottorato in azienda
Università di Napoli Federico II



Dottorato in Scienze Biotechologiche XXVII ciclo
Indirizzo Biotecnologie Dottorato in azienda
Università di Napoli Federico II



PEPTIDE BASED PLATFORMS FOR CANCER DRUG DELIVERY

Emiliana Perillo

Dottorando: Emiliana Perillo
Relatore: Dott.ssa Stefania Galdiero
Co-Relatore: Dott.ssa Patrizia Bonelli
Coordinatore: Prof. Giovanni Sannia

Where the senses fail us, reason must step in.
Galileo Galilei

A mia mamma e mio padre per il loro costante sostegno.
A Michele per essere stato sempre al mio fianco

Index

Riassunto	1
Summary	7
1. Introduction	9
1.1 Cancer	9
1.2 Obstacles to cancer treatment and the potential of nanotechnology.....	10
1.2.1 Conventional therapies for treatment of cancer	10
1.2.2 Nanomedicines and drug delivery	11
1.3 Drug delivery systems.....	12
1.3.1 Liposomes	13
1.3.2 Quantum Dots	14
1.3.3 Dendrons and dendrimers	14
1.3.4 Nanoparticles	14
1.4 Biomolecules passage across the cell membrane	15
1.4.1 Passive diffusion.....	16
1.4.2 Active transport.....	17
1.5 Nanoparticles to facilitate cellular membrane penetration.....	17
1.5.1 Cell penetrating peptides (CPPs)	17
1.5.2 Membranotropic peptides	19
1.6 Nanoparticles to facilitate targeting of tumors	21
1.6.1 Passive targeting	21
1.6.2 Active targeting.....	21
1.7 Aim of the work	22
2. Materials and methods	25
2.1 Materials and equipments	25
2.2 Solid-phase peptide synthesis	25
2.3 Conjugation of EGB targeting peptide to Cholesterol.....	26
2.4 Preparation of triflyl azide.....	26
2.5 Synthesis of Azide-AdOO-Lys(C(O)CH ₂ CH ₂ C(O)N-(C ₁₈ H ₃₇) ₂)-amide ((C ₁₈) ₂ L-N ₃).....	26
2.6 Liposomes preparation.....	27
2.7 Synthesis of SPIONs-PEG-Doxo	27

Index

2.8 Peptides conjugation to liposomes.....	29
2.9 Peptides conjugation to SPIONs.....	29
2.10 Peptides conjugation to NPs.....	29
2.11 Drugs loading into liposomes.....	30
2.12 Structural studies of conjugated peptides.....	30
2.12.1 Circular dichroism measurement.....	30
2.12.2 Zeta potential and size measurements.....	30
2.12.3 Transmission Electron Microscopy.....	31
2.12.4 Fourier Transform Infrared Spectroscopy.....	31
2.12.5 Atomic Absorption Spectroscopy.....	31
2.12.6 Analysis of the fluorescence emission of tryptophan.....	31
2.13 <i>In vitro</i> drug release from liposomes.....	31
2.14 <i>In vitro</i> studies.....	32
2.14.1 Trypan Blue assay.....	32
2.14.2 MTT viability assay.....	32
2.14.3 Alamar Blue assay.....	32
2.14.4 Cholesterol depletion.....	33
2.15 Flow cytometric analysis.....	33
2.15.1 Flow cytometric analysis of drug accumulation.....	33
2.15.2 Flow cytometric analysis of oxidative stress.....	33
2.15.3 Flow cytometric analysis of apoptosis.....	34
2.16 Confocal microscopy studies.....	34
2.16.1 Evaluation of intracellular distribution of Doxo by confocal microscopy..	34
2.16.2 <i>In vitro</i> cellular uptake and distribution by Confocal Spectral Imaging....	34
2.16.3 Atomic force microscopy.....	35
2.16.4 Colocalization with endosomes and lysosomes.....	35
2.16.5 Intracellular shooting of NPs by gene gun method.....	35
2.16.6 Multiple particle tracking.....	36
3 Results.....	37
3.1 Abstract.....	37
3.2 Peptide synthesis and characterization.....	37
3.2.1 Synthesis and characterization of gH625.....	37
3.2.2 Synthesis and characterization of EGBP.....	39

3.3 Synthesis of the lipid moiety (C ₁₈) ₂ L-N ₃	40
3.4 Liposomes preparation with and without peptides	40
3.5 Quantitative and qualitative effect of gH625 on the liposome-mediated delivery of mitoxantrone	41
3.5.1 MTX loading	41
3.5.2 Functionalization of liposomes with gH625.....	41
3.5.3 MTX fluorescence intensity and release kinetics	41
3.5.4 Liposomes Characterization	42
3.5.5 Liposomes cytotoxicity on HeLa cells	44
3.5.6 Liposomes uptake by flow cytometry	44
3.5.7 Liposomes uptake by CSI technique	45
3.6 Liposome armed with gH625 peptide to overcome resistance in lung adenocarcinoma cell lines.....	47
3.6.1 Conjugation of gH625.....	47
3.6.2 Doxo loading	48
3.6.3 Liposomes physico-chemical characterization.....	48
3.6.4 Release kinetics of Doxo	48
3.6.5 Antitumoral activity of liposomes	49
3.6.6 FACS analysis in A549 and A549 Dx cell lines: accumulation, evaluation of oxidative stress, evaluation of cell death	51
3.6.7 Intracellular distribution of Doxo in A549 and A549 Dx cells	56
3.7 Design of dual-ligand nanoliposomes using a specific ligand and gH625.....	57
3.7.1 Design of peptide conjugated to cholesterol	57
3.7.2 Preparation and characterization of peptide-targeted liposomes.....	58
3.7.3 Release kinetics of Doxo	59
3.7.4 Facs analysis: accumulation.....	60
3.8 Supermagnetic iron oxide nanoparticles coated with gH625.....	61
3.8.1 Synthesis of initial SPIONs.....	61
3.8.2 SPIONs modified with PEG and/or Doxo.....	62
3.8.3 Functionalization of SPIONs with gH625.....	64
3.8.4 Characterization of SPIONs functionalized with gH625.....	65
3.9 Surface decoration of Polystyrene NPs with gH625: method to escape endo-lysosomal compartment and reduce nanoparticles toxicity	66

Index

3.9.1 Interaction of gH625-NPs with the cell membrane.....	67
3.9.2 gH625-NP intracellular behavior.....	69
3.9.3 gH625-NP intracellular distribution	69
3.9.4 gH625-NP cytotoxicity	71
4. Discussion and conclusion	73
References	79

Riassunto

Sviluppo di nano-piattaforme a base di peptidi per il trasporto di farmaci antitumorali

Il cancro è la seconda causa di morte nel mondo. Negli Stati Uniti, la mortalità per cancro è superata solo da quella per patologie cardiache, ed è la causa di circa 1 morte su 4. Il cancro quindi costituisce un enorme onere economico per le autorità sanitarie e per la società. Inoltre, notevoli sforzi sono dedicati al miglioramento dei trattamenti clinici al fine di alleviare le sofferenze del paziente.

Le nanotecnologie offrono importanti opportunità per il trattamento e la diagnosi di numerose patologie ad elevato impatto sociale tra cui il cancro. La nanomedicina costituisce una delle più importanti applicazioni e dei più promettenti sviluppi delle nanotecnologie. Essa si propone, infatti, l'obiettivo di realizzare un monitoraggio completo e continuo dell'organismo umano e di contribuire alla tutela della salute, lavorando a livello molecolare per ottenere benefici medici e clinici mediante l'utilizzo di nanostrutture. L'utilizzo delle nanostrutture presenta, infatti, notevoli vantaggi in quanto i volumi ridotti e le aumentate superfici di contatto, permettono un miglioramento delle interazioni fra i nanomateriali e le cellule. Attualmente, le applicazioni più promettenti riguardano: l'ottimizzazione delle tecnologie già esistenti; lo sviluppo di nuovi sistemi multifunzionali per la diagnosi delle malattie e la somministrazione mirata dei farmaci; e la produzione di materiali sempre più affidabili, specializzati e riproducibili, che permettono un aumento dell'efficacia e una riduzione dei costi.

In tale contesto, l'internalizzazione di molecole attive e/o farmaci costituisce un problema importante della "teranostica". Il termine "teranostica" è stato recentemente introdotto per descrivere composti con la capacità di svolgere contemporaneamente un'azione diagnostica e terapeutica, che, quindi, possano essere applicati in medicina per entrambi gli scopi al fine di ottenere terapie personalizzate.

La membrana plasmatica rappresenta il principale ostacolo per l'internalizzazione dei farmaci, in quanto costituisce una barriera tra l'ambiente intracellulare ed extracellulare. Il successo delle nuove strategie per la teranostica si basa sullo sviluppo di nanosistemi (come liposomi, nanoparticelle e dendrimeri) in grado di migliorare l'indice terapeutico di molecole biologicamente attive favorendone l'internalizzazione.

La produzione e la caratterizzazione di nanosistemi, che possano agire da vettori efficienti per la distribuzione mirata dei farmaci, è fondamentale al fine di circoscrivere l'effetto biologico della terapia a una determinata tipologia di cellule, migliorandone l'efficacia e riducendone la tossicità sistemica.

L'obiettivo di questo progetto di tesi consiste nello sviluppo di nuove nano-piattaforme di natura peptidica, che mediano il trasporto specifico alla cellula tumorale e il rilascio intracellulare di molecole bioattive, utilizzabili sia nel settore diagnostico che terapeutico. Quest'obiettivo è stato raggiunto, modificando la superficie di diversi nanosistemi con peptidi per il trasporto e per il targeting. I peptidi per il trasporto hanno la funzione di aumentare l'internalizzazione favorendo meccanismi di internalizzazione diversi dall'endocitosi. I peptidi per il targeting hanno la funzione di direzionare il nanosistema al sito desiderato sfruttando la loro capacità di legarsi a specifici recettori espressi maggiormente sulla superficie delle

cellule tumorali.

I peptidi per il trasporto svolgono un ruolo chiave nel processo di internalizzazione perché, le membrane biologiche costituiscono un ostacolo fondamentale dal momento che questa barriera è difficilmente attraversabile da parte di molte molecole farmacologicamente attive. I *Cell Penetrating Peptides* (CPPs) sono peptidi carichi positivamente in grado di trasportare macromolecole attraverso la membrana plasmatica in modo efficiente ed il loro utilizzo si è notevolmente diffuso negli ultimi anni. Il loro principale problema è costituito dal meccanismo di traslocazione che implica essenzialmente un processo di endocitosi. Quindi, solo una piccola quantità della molecola cargo è in grado di sfuggire agli endosomi, dove avvengono le comuni reazioni di degradazione intracellulare e di raggiungere il sito di azione. È, quindi, necessario lo sviluppo di nuovi CPPs che utilizzino solo parzialmente il meccanismo endocitico, migliorando così le proprietà farmacocinetiche e farmacodinamiche, la distribuzione e localizzazione intracellulare e di conseguenza l'attività sito-specifica dei farmaci.

In tale ambito, il gruppo di ricerca che mi ha seguito nel progetto di dottorato, ha identificato un peptide di origine virale (gH625) che deriva dalla glicoproteina gH presente sull'envelope del virus *Herpes simplex* di tipo I ed è in grado di attraversare le membrane cellulari. In particolare, gH625 interagisce con le membrane biologiche ed è coinvolto nel processo di fusione con la membrana della cellula bersaglio. Il peptide è ricco in residui idrofobici quali glicine, leucine ed alanine e residui aromatici quali triptofano e tirosine, che svolgono un ruolo cruciale per l'interazione e la destabilizzazione delle membrane. Il peptide assume una struttura ad elica anfipatica dove tutti i residui idrofobici sono localizzati su una faccia e quelli idrofilici sull'altra. La faccia idrofobica della molecola svolge un ruolo attivo nel processo di interazione e fusione con le membrane. L'interazione peptide-lipide è probabilmente mediata, inizialmente, dall'arginina presente all'estremità C-terminale, infatti quando tale residuo è mutato l'attività fusogena del peptide risulta fortemente alterata. Il dominio idrofobico è coinvolto nelle fasi iniziali di perturbazione di membrana caratteristiche anche dell'infezione virale. L'internalizzazione di gH625 è probabilmente associata alla sua capacità di interagire con i fosfolipidi di membrana e di formare una struttura α -elica transiente che destabilizza temporaneamente la membrana facilitandone l'inserzione e la traslocazione. Studi di internalizzazione hanno evidenziato che il peptide gH625 attraversa la membrana cellulare utilizzando in maniera preponderante meccanismi di traslocazione passiva, mostrando solo una parziale co-localizzazione con vescicole endosomiali, risultando quindi un ottimo candidato per il trasporto intracellulare di molecole bioattive.

L'ostacolo principale all'utilizzo di nanosistemi funzionalizzati con gH625 è la mancanza di specificità. Per tale motivo in questo lavoro di tesi abbiamo associato i vantaggi dell'utilizzo di gH625 con i benefici derivanti dalla strategia di targeting attivo. Questa strategia si basa sul riconoscimento molecolare di marcatori tumorali sovra-espressi sulle cellule tumorali; in particolare, è stato scelto il recettore del fattore di crescita epidermico, sovra-espresso in diversi tipi di tumori. Abbiamo utilizzato il peptide legante il recettore del fattore di crescita epidermico (EGBP), precedentemente identificato.

Lo scopo del progetto di dottorato è stato lo sviluppo di una nuova nano-piattaforma opportunamente funzionalizzata con gH625 e il peptide EGB, che possa essere utilizzata come sistema innovativo nel campo della teranostica. In particolare, il lavoro di tesi è stato incentrato sulla coniugazione dei peptidi a nanostrutture di diversa natura, sulla loro caratterizzazione chimico-fisica (dimensioni, potenziale

zeta, efficienza di caricamento del farmaco e cinetica di rilascio) e sull'analisi dell'attività biologica (citotossicità, attività antitumorale, internalizzazione e destino intracellulare). I nanosistemi utilizzati sono: liposomi, nanoparticelle magnetiche e nanoparticelle di polistirene. La sfida di questo progetto è stata quella di unire i benefici chimici di questi nanosistemi al vantaggio associato all'utilizzo di peptidi per il *delivery* e peptidi per il *targeting*.

Nanosistema: liposomi

I liposomi sono nanostrutture vescicolari cave formate da uno o più doppi strati lipidici che delimitano all'interno un *core* idrofilico in cui possono essere disciolti/dispersi vari farmaci. Non sono tossici, né immunogenici, sono biodegradabili e di diametro compreso tra 50-500 nm. Più in dettaglio, possono trasportare diverse molecole, sia molecole idrosolubili, che si posizionano nel *core* idrofilico, sia molecole liposolubili, che si posizionano nel doppio strato fosfolipidico. I liposomi sono in grado di veicolare i farmaci all'interno delle cellule, riducendone la tossicità, modificandone la farmacocinetica e la biodistribuzione. Per questo motivo sono degli ottimi candidati per la veicolazione intracellulare di farmaci antineoplastici.

La superficie dei liposomi può essere inoltre funzionalizzata con peptidi, che possono migliorarne l'internalizzazione, il *targeting* e quindi l'efficacia antitumorale del farmaco trasportato. La strategia sintetica utilizzata per funzionalizzare la superficie di liposomi con peptidi dipende dalla natura chimico-fisica dei peptidi. Per quelli idrofobici, quali gH625, è necessario effettuare il legame del peptide al liposoma preformato. Infatti, gH625 è un peptide idrofobico con elevata tendenza a localizzarsi nella porzione lipofila; pertanto, per la preparazione dei liposomi funzionalizzati con gH625, il peptide è stato legato alla superficie dei liposomi preformati utilizzando la *click-chemistry*. L'ottenimento di liposomi bifunzionalizzati costituisce una sfida ancora maggiore, in quanto al fine di ottenere un nanosistema riproducibile, è necessario avere un preciso controllo sul rapporto molare tra i due peptidi utilizzati. A tale scopo il peptide *targeting* (EGBP) è stato derivatizzato con una componente lipidica in modo da poterlo utilizzare direttamente come componente nella preparazione dei liposomi.

La caratterizzazione *in vitro* dei nanosistemi è stata effettuata parzialmente in Francia nei laboratori del Prof. Chourpa, e parzialmente a Napoli nei laboratori della Microtech della Dott.ssa Bonelli e nei laboratori della SUN del Prof. Caraglia.

Durante la permanenza nei laboratori del Prof. Chourpa dell'Università di Tours, abbiamo preparato liposomi (costituiti da DOPG/DSPE-PEG), decorati sulla superficie con gH625 e caricati con il farmaco antitumorale mitoxantrone (MTX) al fine di analizzarne il meccanismo di internalizzazione. Abbiamo effettuato studi di citotossicità del nanosistema liposomiale e studi di uptake mediante tecniche di microscopia confocale, quali *Confocal Spectral Imaging* (CSI).

La tecnica CSI permette di evidenziare anche piccolissime variazioni di fluorescenza del farmaco (nel nostro caso l'MTX) dovuti ai diversi micro-ambienti intracellulari in cui si viene a trovare. I risultati ottenuti mostrano chiaramente che la presenza di gH625 sulla superficie dei liposomi ne favorisce l'internalizzazione in cellule HeLa. Questo si correla bene con i dati di citotossicità; infatti, entro 4 ore, il liposoma funzionalizzato con gH625 (LMTX-gH625) è più attivo rispetto a quello non funzionalizzato (LMTX). Il peptide gH625 probabilmente induce una maggiore e più rapida internalizzazione, che potrebbe contribuire alla maggiore citotossicità di

Riassunto

LMTX-gH625 rispetto al LMTX. gH625 modifica, quindi, l'internalizzazione dei liposomi e di conseguenza il trasporto del farmaco alle cellule.

Il successo dei trattamenti farmacologici è spesso ostacolato dalla comparsa della resistenza ai farmaci. La resistenza ai farmaci (MDR) rappresenta il principale meccanismo attraverso il quale molti tumori sviluppano resistenza al trattamento chemioterapico, e costituisce un notevole problema per il successo clinico. È, quindi, molto importante individuare strategie alternative per utilizzare i farmaci attualmente in commercio contro i tumori che sviluppano resistenza. A tale scopo, in collaborazione con la Microtech e con la SUN, abbiamo sviluppato liposomi con maggiori caratteristiche biomimetiche costituiti da fosfolipidi derivanti dalla soia, funzionalizzati con il PEG sulla superficie esterna e caricati con la doxorubicina (Doxo). Tali liposomi sono stati funzionalizzati con gH625 al fine di migliorarne l'efficacia antitumorale e superare i meccanismi di resistenza ai farmaci. Sono stati inizialmente effettuati studi di caratterizzazione chimico-fisica, successivamente studi di citotossicità e studi di internalizzazione mediante microscopia confocale. Gli studi di caratterizzazione chimico-fisica del nanosistema hanno rivelato un diametro di 140 nm con una distribuzione uniforme. Gli studi di inibizione della crescita sono stati effettuati sia su linee cellulari di carcinoma polmonare (A549) che sullo stesso tipo di cellule che però avevano sviluppato una doxo-resistenza (A549 Dx). Tali studi hanno evidenziato che la presenza di gH625 sulla superficie dei liposomi favorisce la loro azione su entrambe le linee cellulari con un aumento dell'inibizione della crescita cellulare specialmente nel caso delle cellule doxo-resistenti. Gli studi di internalizzazione mediante microscopia confocale dimostrano che la Doxo incapsulata nei liposomi funzionalizzati con gH625 entra nei nuclei delle cellule tumorali A549-Dx; questo risultato ci ha fatto ipotizzare che il peptide gH625 induce una maggiore e più rapida internalizzazione anche nelle cellule resistenti. Tale risultato è di fondamentale importanza perché gH625 potrebbe essere utilizzato per superare la resistenza ai farmaci.

Infine, gH625 sebbene sia molto efficace nell'aumentare l'internalizzazione di diversi cargo, non presenta specificità, quindi parte del progetto è stata dedicata alla funzionalizzazione dei liposomi anche con il peptide per il targeting. In questo studio, ci siamo spostati dall'utilizzo di liposomi non specifici funzionalizzati con gH625 a liposomi specifici diretti contro le cellule tumorali, coniugando sulla superficie dei liposomi il peptide EGB, specifico per il recettore del fattore di crescita epidermico (EGFR). Al fine di ottimizzare l'interazione del peptide EGB con il suo recettore, abbiamo utilizzato due diversi linker per coniugare il peptide al liposoma. Infatti, abbiamo sintetizzato l'EGBP con un piccolo distanziatore costituito da tre glicine e con una piccola porzione idrofilica costituita da PEG. L'EGBP è stato poi legato al colesterolo formando un componente lipidico che è stato utilizzato direttamente nella preparazione dei liposomi.

La posizione del peptide sulla superficie dei liposomi è stata determinata mediante fluorescenza. In particolare, lo spettro di fluorescenza del triptofano presente sia nel peptide gH625 che nel peptide EGBP, ci ha permesso di ipotizzare la posizione relativa dei due peptidi sul liposoma. Infatti, il confronto tra l'intensità di fluorescenza dei liposomi funzionalizzati solo con gH625 e dei liposomi doppiamente funzionalizzati ha mostrato un aumento di intensità, che potrebbe essere attribuito all'esposizione dei triptofani sia di gH625 che dell'EGBP. Il confronto tra i due liposomi doppiamente funzionalizzati ha mostrato poi un aumento di intensità per quella con il linker idrofilico, indicando che, come previsto, il triptofano è più esposto e quindi il peptide è più disponibile per l'interazione con il recettore. L'analisi

dell'accumulo della Doxo contenuta nei liposomi bifunzionalizzati in cellule KB, che sovra-esprimono il recettore EGFR, mediante citometria a flusso, ha dimostrato un aumento di accumulo della doxorubicina rispetto al nanosistema senza il peptide targeting. Sono in corso ulteriori studi sull'attività e l'internalizzazione.

In conclusione, sono stati evidenziati ulteriori dettagli sul meccanismo di internalizzazione promosso da gH625 che indicano chiaramente le potenzialità di gH625 per lo sviluppo di una nano-piattaforma da utilizzare per la terapia antitumorale, utile anche nel caso di tumori che sviluppano resistenza alla chemioterapia.

Nanosistema: nanoparticelle supermagnetiche di ossido di ferro

Un altro nanosistema di particolare interesse in campo teranostico, è costituito dalle nanoparticelle supermagnetiche di ossido di ferro (SPIONs). Le SPIONs offrono la possibilità di effettuare contemporaneamente diagnosi (agenti di contrasto nella risonanza magnetica nucleare) e terapia (se coniugate a farmaci). Dopo la somministrazione endovenosa, le SPIONs possono essere dirette in maniera specifica al sito tumorale grazie all'uso, anche combinato, dei seguenti meccanismi: I) applicazione di un campo magnetico al sito tumorale; II) sfruttamento dell'effetto di maggiore permeabilità e ritenzione (EPR), che si basa sulla maggiore permeabilità della vascolarizzazione tumorale e la mancanza di un efficace drenaggio da parte del sistema linfatico; III) internalizzazione delle nanoparticelle all'interno delle cellule tumorali. L'obiettivo di questo progetto è stato quello di sintetizzare nanoparticelle magnetiche e di funzionalizzarle con il peptide gH625 in modo da aumentarne l'internalizzazione. Ci siamo dedicati maggiormente alla messa a punto della strategia di funzionalizzazione con i CPPs, al fine di trovare il giusto compromesso tra la stabilità colloidale del nanosistema, la sua emivita nel sangue e l'efficace internalizzazione cellulare. Infatti, poco si conosce sulla densità/quantità ottimale di CPPs sulla superficie delle SPIONs necessaria per il trasporto attraverso le membrane delle cellule tumorali. Particolari difficoltà si riscontrano con sequenze peptidiche idrofobiche, come gH625, infatti un eccesso di peptide sulla superficie del nanosistema potrebbe ridurre la stabilità colloidale in mezzi acquosi e l'emivita in circolo. Per questo motivo, abbiamo posto la nostra attenzione sulla corretta concentrazione di gH625 con cui funzionalizzare il nanosistema. Abbiamo, successivamente effettuato misure di Dicroismo Circolare al fine di valutare la sua struttura secondaria quando è legato alle nanoparticelle. Dai dati si evince che la struttura elicoidale del peptide, alla concentrazione di 8×10^{-6} M, non è disturbata dal legame con le SPIONs. Un eccesso di peptide sulla superficie del nanosistema riduce la sua stabilità colloidale in mezzi acquosi e l'emivita in circolo. Così, è stato necessario ottimizzare diversi parametri importanti quali la concentrazione di gH625 sulle SPIONs. Sono ora in corso ulteriori studi di caratterizzazione chimico-fisica del nanosistema funzionalizzato con gH625 e studi per valutare la capacità di gH625 di promuovere l'internalizzazione delle nanoparticelle magnetiche.

Nanosistema: nanoparticelle di polistirene

L'utilizzo di farmaci per le patologie neurologiche attualmente in via di sperimentazione, sono limitate dall'incapacità dell'agente terapeutico di attraversare efficientemente la barriera emato-encefalica (BBB). La BBB è una barriera dinamica e selettiva che protegge il sistema nervoso dall'invasione di sostanze e organismi indesiderati; ma rappresenta anche un notevole ostacolo da un punto di vista

Riassunto

terapeutico in quanto limita l'attraversamento e il rilascio dei farmaci nel loro sito di azione. Per questo motivo è fondamentale identificare e sviluppare un sistema che permetta un migliore rilascio del farmaco nei compartimenti del sistema nervoso. La maggior parte delle strategie in fase di sperimentazione che hanno avuto un grosso impatto terapeutico, come la microiniezione diretta, risultano troppo invasive in quanto danneggiano in maniera irreversibile la BBB. Particolare interesse è stato rivolto allo studio delle nanoparticelle di polistirene (NPs), funzionalizzate, per utilizzarle come sistemi modello per il trasporto di farmaci attraverso la barriera emato-encefalica.

Sono stati condotti esperimenti di internalizzazione delle NPs, di diametro di 100 nm, opportunamente funzionalizzate con la sequenza gH625, su cellule dell'endotelio cerebrale (bEnd3). I risultati ottenuti dimostrano che la presenza, sulla superficie delle NPs di gH625 ne migliora ed in particolare ne modifica il meccanismo di internalizzazione. Infatti, le gH625-NPs sono poco presenti nei lisosomi in confronto a quelle non funzionalizzate. Inoltre, il loro movimento intracitoplasmatico risulta di tipo casuale e non direzionale, indicando una maggiore capacità di movimento perché non intrappolate nelle vescicole lisosomiali. Questi dati sono indicativi di un meccanismo passivo di internalizzazione e dimostrano che il nostro sistema, presenta delle caratteristiche ottimali, per il trasporto di molecole attraverso la barriera emato-encefalica e potrebbe essere utilizzato per la cura delle patologie del sistema nervoso centrale.

Conclusioni

In conclusione, abbiamo sviluppato una nano-piattaforma molto versatile caratterizzata dalla presenza di un nanosistema (liposoma, nanoparticelle magnetiche, nanoparticelle di polistirene), di un peptide per il *delivery*, di un peptide per il *targeting* e di un farmaco, che può essere sfruttata per ottenere specifiche terapie a seconda del peptide *targeting* e del farmaco utilizzati.

Summary

Peptide Based Platforms for Cancer Drug Delivery

Cancer remains one of main causes of death in humans, accounting for 8.2 million deaths worldwide in 2012 [1]. Chemotherapy, the most widely used cancer therapy, is the most effective and potent strategy to treat malignant tumors, but has the disadvantage of not delivering the therapeutic agents only to tumor sites. In fact, current cancer treatments kill also normal cells and cause several cytotoxic effects in healthy tissues. Nanomedicine may allow the controlled release of drugs by biodegradation and self-regulation of nanomaterials *in vitro* and *in vivo*. Nanotechnologies are potentially effective for drug encapsulation, controllable self-assembly, specificity and biocompatibility; moreover, they have the potential to overcome current chemotherapeutic barriers in cancer treatment, because of the unique nanoscale size and their distinctive bioeffects.

The goal of this PhD project was to create a delivery tool, that transports the drug to the target cells not only with high efficacy, but also with minimal toxicity against normal cells and avoiding its degradation and entrapment in endosomes. The first part of this thesis was focused on the design of the strategies for the achievement of a toolbox easily to functionalize and on its obtainment. The second phase was the physico-chemical characterization of each selected nanosystem with particular attention to the size, zeta potential and drug loading and release. The third phase was to analyze *in vitro* the subcellular fate of the vectorized drug and the effect on the cells.

Several nanosystems (liposomes, magnetic nanoparticles, polystyrene nanoparticles) were selected and functionalized with peptides both to enhance tumor targeting and facilitate intracellular uptake.

In particular, we used a novel Cell Penetrating Peptide (namely, gH625) which is able to overcome the known limits of classic CPPs. In fact, gH625 is able to efficiently traverse biological membranes, promoting lipid-membrane reorganizing processes, such as fusion or pore formation and involving temporary membrane destabilization and subsequent reorganization; it is able to circumvent the endosomal entrapment either favouring the escape from the endosome or by directly translocating the drug across the membrane.

In order to make the nanosystem cell and tissue specific, we have further functionalized the surface of the nanosystem with a targeting peptide. We exploited the EGB peptide, which recognizes the epidermal growth factor receptor (EGFR), a tyrosine kinase receptor overexpressed in several solid tumors.

The first nanoplatform is liposome based. In collaboration with Prof Igor Chourpa of Tours University, we prepared liposomes decorated with gH625 and carrying the drug mitoxantrone (MTX) to analyze the internalization mechanism. The purpose of this study was to explore the possibility of using liposomes decorated on their external surface with gH625 to change the uptake mechanism and enhance the internalization of MTX. To analyze the uptake mechanism, we used Confocal Spectral Imaging (CSI) which allows to distinguish very fine modifications of MTX intrinsic fluorescence within different intracellular microenvironments. The obtained results clearly show that the presence of gH625 on the surface of liposomes is favouring their uptake in HeLa cells.

Summary

To enhance the antitumor efficacy of liposomes encapsulating anti-cancer agents and to circumvent drug resistance, in collaboration with Dr. Bonelli of Microtech and Prof. Caraglia of SUN we used liposomes with enhanced biomimetics characteristics (phospholipids derived by soy), carrying on their external surface PEG and modified with gH625. We have evaluated the growth inhibition on either wild type (A549) or doxorubicin-resistant (A549 Dx) human lung adenocarcinoma cell lines. The presence of gH625 on the surface of liposomes is favouring their uptake in both sensitive and drug-resistant tumor cell lines allowing an increase of cell growth inhibition: in fact, a greater quantity of Doxo from functionalized liposomes is accumulated into cells. Doxo encapsulated in functionalized liposomes was able to enter in the nuclei of Doxo-resistant cancer cells indicating that the peptide gH625 was probably inducing a greater and more rapid internalization also in resistant cells, which could contribute to overcome drug resistance [2].

Moreover, we wanted to develop a nanoplatform based on dual decorated liposomes, both for the uptake and the targeting. We have also evaluated the Doxo accumulation of the dual decorated liposomes in KB cells by Fluorescence Activated Cell Sorting analysis. The conjugation of liposomes with the homing peptide increased the retention of doxorubicin into cells, overexpressing epidermal growth factor receptor. Further works is under way to characterize the uptake mechanism of dual functionalized liposomes *in vitro*.

The second nanoplatform is based on multifunctional magnetic nanoparticles (SPIONs). Our goal was to verify if we could also enhance the cellular uptake of this kind of cargo. We focused on optimization of the gH625 conjugation strategy, in order to find the best compromise between the colloidal stability of nanosystems, their half-life in blood and their efficient translocation into cells. We optimized several important parameters such as the concentration of gH625 on the polymeric surface of SPIONs and characterized the obtained nanosystem by Circular Dichroism (CD). Data confirmed that gH625 retains its helical structure when bound to the nanoparticle surface, suggesting that the secondary structure of the peptide was not disturbed by attachment to SPIONs. We are now working on the physico-chemical, characterization of the nanosystem and the eventual ability of gH625 to increase the nanoparticle uptake by cancer cells.

The third nanoplatform is based on polystyrene nanoparticles (NPs). We explored the possibility of using NPs functionalized with gH625 to deliver a drug across the Blood Brain Barrier (BBB). The uptake of NPs with gH625 by brain endothelial cells is greater than that of the NPs without the peptide. Moreover, gH625 plays a key role in controlling the uptake mechanism. In fact, most trajectories of blank NP resulted in pearls-on-a-string walk, indicative of motor protein facilitated transport, mediated by endocytic vesicles. Conversely, in presence of peptide functionalization, we observed that most trajectories showed a random walk behaviour with a very low percentage of pearls-on-a-string trajectories, suggesting a translocation across the bilayer. These studies clearly indicate that gH625 is able to change the mechanism of uptake of the cargo and it is able to cross the BBB.

In summary, these results establish that gH625 may represent a good choice for the design of promising carriers to deliver drugs for the treatment of human diseases and we have developed a nanoplatform for targeted drug delivery to be used for several pathologies.

1. Introduction

Cancer remains one of main causes of death in humans, accounting for 8.2 million deaths worldwide in 2012 [1] (Table 1).

Over the past several decades, remarkable breakthroughs have been made in advancing the understanding of how cancer originates and develops, which has in turn led to better methods for both diagnosis and treatment [3]. Chemotherapy, the most widely used type of cancer therapy, is the most effective and potent strategy to treat malignant tumors. However, the inability to delivery therapeutic agents only to tumor sites constitutes a significant impediment to successful chemotherapy. An additional obstacle is the resistance of cancer cells to the drugs. Current cancer treatments kill normal cells and cause several cytotoxic effects in healthy tissues. Therefore, it would be desirable to develop highly efficient therapeutics, that can overcome biological barriers and distinguish between malignant and benign cells, selectively targeting the cancerous tissues [4]. Nanomedicine allows the release of drugs by biodegradation and self-regulation of nanomaterials *in vitro* and *in vivo*. Nanotechnologies are potentially effective for drug encapsulation, controllable self-assembly, specificity and biocompatibility; moreover, they have the potential to overcome current chemotherapeutic barriers in cancer treatment, because of the unique nanoscale size and distinctive bioeffects of nanomaterials. Nanotechnology may thus help to solve the problems associated with traditional chemotherapy and multidrug resistance.

Estimated number (thousands)	Men		Women	
	Cases	Deaths	Cases	Deaths
World	6629	4225	6038	3345
More developed regions	2975	1528	2584	1223
Less developed regions	3653	2697	3453	2122
WHO Africa regions	253	209	318	226
WHO Americas regions	1276	611	1233	568
WHO East mediterranean regions	214	169	214	144
WHO Europe regions	1823	1044	1604	823
WHO South-East Asia regions	742	566	909	564
WHO western Pacific regions	2316	1621	1755	1016
United State of America	745	294	692	271
European Union	1332	693	1114	539

Table 1. Summary of cancer (excluding melanoma skin cancer) incidences and mortality worldwide in 2008.

1.1 Cancer

Cancer is the second leading cause of death in the world, being second only to coronary diseases. It is estimated that within the next 30 years, it will become the main reason for death. This bothersome statistic is not correlated to an increase in incidences of cancer, but to the reduction to nearly half of heart disease deaths, while the number of cancer-related deaths remains about the same. Cancer, which was once considered to be a disease of the westernized, industrialized countries, has now become a common disease also of low- and medium-resource countries

[1]. Cancer is caused by abnormalities in the genetic material of the transformed cells [5]. These abnormalities are due to mutations in the DNA of a normal cell, changing them to transformed cells or “mutants”. Mutations are mainly caused by exposure to carcinogens; such as tobacco smoke, radiation, chemicals, or infectious agents [6]. Other cancer enhancing genetic abnormalities may occur randomly due to errors in DNA replication, or are inherited [7]. The heritability of cancers is usually determined by complex interactions between carcinogens and the host genome with cancer-enhancing genetic abnormalities present in cells from birth. Although much progress has been made in cataloging the environmental causes and cellular and molecular biological basis for this dreaded disease, we still do not have a precise understanding of the differences between a cancer cell and its normal counterpart. Cancer development occurs when cells in a part of the body begin an out-of-control growth of abnormal cells, and instead of dying, they outlive normal cells and continue to form new abnormal cells. Cancer cells acquire autonomy from growth signals, evasion of growth inhibitor signals, evasion of apoptotic cell death, unlimited replication potential, angiogenesis, and invasion and metastasis, all of which are essential for carcinogenesis. Cancer cells rapidly reproduce and divide uncontrollably and their growth rate is not restricted by space, nutrients etc. Cancer cells are usually different in shapes as compared to healthy cells, which do not perform biological functions properly, and they can spread into many areas of the body.

1.2 Obstacles to cancer treatment and the potential of nanotechnology

1.2.1 Conventional therapies for treatment of cancer

The established strategies for cancer treatment, include surgery, radiation, and chemotherapy or combined strategies of these treatments. These are supplemented by some more specialized therapies such as immunotherapy or hormone therapy which can be applied only to some tumor types [8].

The oldest form of cancer treatment is surgery. It provides the greatest chance of cure, mainly for solid tumors; especially those which have not yet metastasized to other parts of the body. Radiotherapy is the second major weapon against cancer. Radiation therapy involves use of high-energy particle beams or waves (radiation), such as X-rays, gamma rays, neutrons for treating cancer [9]. Radiation is more harmful for cancerous cells than for normal cells because cancerous cells are more unstable and thus more vulnerable to the damaging radiations. Moreover, the cellular repair mechanism is also not prominently active in the highly dividing cells like cancer cells; while due to proper functionally active cellular repair mechanism normal cells can recover from the effects of radiation more easily. One of the major drawbacks of radiotherapy is selectivity, in fact it is impossible to treat only tumor cells, without affecting the surrounding healthy cells. Chemotherapy uses chemicals to treat cancer, especially suitable for those cancers that have been spread out (metastasized) and cannot be treated any longer by localized methods such as surgery and radiation. One common characteristic of most cancer cells is their rapid rate of cell division. Anticancer drugs like taxol (interferes with the depolarization of microtubules and hyperstabilized their structure), doxorubicin (is thought to intercalate in DNA) or daunorubicin (intercalates with its daunosamine residue directed toward the minor groove), all adversely affect the process of cell division; thus, they are aimed to destroy aggressive cancers. Nevertheless, chemotherapeutics have the same disadvantage as radio-therapeutics. They are

unspecific and therefore do not distinguish between healthy and cancerous cell and hence damage also healthy cells. The clinical use of most conventional chemotherapeutics is often limited due to inadequate delivery of therapeutic drug concentrations to the tumor target tissue or due to severe and harmful toxic effects on normal organs. In addition, cancer cells can be resistant to chemiotherapeutic agents in the clinic. These drug-resistant cancer cells, remaining alive after chemotherapy, are responsible for the re-appearance of tumors and the poor prognosis for patients. Multidrug resistance (MDR) is a major problem encountered in chemotherapy that negatively impacts the treatment efficacy of chemotherapeutics [10]. A number of mechanisms have been reported for MDR, including increased efflux pumping of drugs by the overexpressed ATP-binding cassette (ABC) transporters, reduced intracellular accumulation of drugs by non-ABC drug transporters, blocked apoptosis, repair of drug-induced DNA damage, metabolic modification, and detoxification by drug-metabolizing enzymes [11]. Among these mechanisms, the overexpression of plasma membrane P-glycoprotein (P-gp, or ABCB1), a member of the ABC superfamily, is one of the most common causes of MDR. A strategy suggested for overcoming MDR is association of the drug with drug delivery tools [12]. Nanotechnology has the potential to overcome current obstacles to chemotherapy, because of the unique properties of nanoparticles, in fact the encapsulation of drugs in nanometric scaled biocompatible materials is a potential strategy to improve the accumulation of the drugs in the tumor tissues.

1.2.2 Nanomedicines and drug delivery

The advent of nanotechnology brought the promise to revolutionize cancer treatment both for diagnosis and therapy. In recent years, nanotechnology has been successfully utilized to create novel drug delivery systems, which allow the reduction of unwanted side effects of systemic delivery, while increasing drug accumulation in tumours and improving the therapeutic efficacy. A delivery tool should transport the drug to the target cells not only with high efficacy, but also with minimal toxicity against healthy cells and immune response avoiding its degradation and entrapment in endosomes. The most critical issue for the design of a successful nanoplatform is quick clearance in the systemic circulation.

The nanoparticles used for drug delivery can be readily fabricated from either soft (organic and polymeric) or hard (inorganic) materials, with the sizes and compositions/structures controlled, typically in the range of 1-100 nm, and loaded with anticancer drugs [13,14]. The physico-chemical properties of the nanoparticles can also be finely controlled by adjusting their chemical compositions, sizes, shapes, structures, morphologies and properties of the surface [3,15]. Compared with traditional chemotherapeutics, the delivery of anticancer drugs through a nanoparticle-based platform presents many challenges, including: 1) improved delivery of drugs that are poorly soluble in water and delivery of a therapeutic agent into cancerous cells at a high dose; 2) better protection of a drug from harsh environments (e.g., the highly acidic environment in the stomach or the lysosomes of a cell, and the high levels of proteases or other enzymes in the blood stream) before they can reach the targets, leading to an extended plasma half-life of the drug in the systemic circulation; 3) targeted delivery of drugs in a cell or tissue in order to maximize the treatment efficacy while systemic side effects are alleviated; 4) controlled release of drugs over a manageable period of time at precise doses and

realization of on-demand release using a more sophisticated, stimuli-responsive system. [16,17,18]

1.3 Drug delivery systems

Many of the current “nano” drug delivery systems, are in the nanometer range, such as liposomes, polymeric micelles, nanoparticles and dendrimers. Liposomes were first prepared in 1960’s; nanoparticles and dendrimers in 1970’s and colloidal gold particles in nanometer sizes were first prepared by Michael Faraday more than 150 years ago, but were never referred to or associated with nanoparticles or nanotechnology until recently. Subsequently, as illustrated in Figure 1, a variety of other organic and inorganic biomaterials for drug delivery were developed. Only a few nanomedicines are approved for use in the treatment of cancer (Table 2).

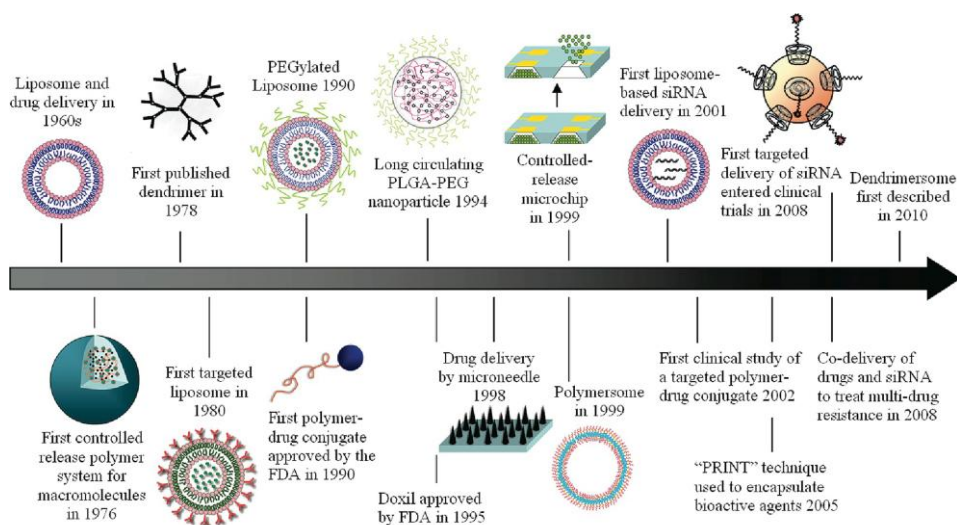


Figure 1. Biomaterials for drug delivery.

The first controlled release polymer system for delivery of macromolecules was described in 1976. More complex drug delivery systems capable of responding to changes in pH which trigger drug release, as well as the first example of cell-specific targeting of liposomes, were first described in 1980 [19,20]. The first long-circulating liposome was described in 1987, and the concept was later named “stealth liposomes” [21]. The use of polyethylene glycol (PEG) was shown to increase circulation times of liposomes [22] and polymeric nanoparticles [23] in 1990 and 1994, respectively, paving the road for the development and subsequent approval of Doxil (doxorubicin liposome) in 1995, for the treatment of AIDS-associated Kaposi’s Sarcoma.

Name	Formulation	Bioactive compound	Indication	Status
DaunoXome®	Non-PEGylated liposomes	Daunorubicin	Kaposi's sarcoma	Approved
Myocet®	Non-PEGylated liposomes	Doxorubicin	Breast cancer	Approved
Doxil®/Caelyx®	PEGylated liposomes	Doxorubicin	Breast and ovarian cancer, Kaposi's sarcoma	Approved
NL CPT	PEGylated liposomes	Irinotecan	Glioma	Phase I
Genexol-PM®	PEG-poly(lactic acid) nanoparticles	Paclitaxel	Breast cancer, lung cancer, ovarian cancer	Phase II
Opaxio™	PGA-paclitaxel	Paclitaxel	Lung cancer, ovarian cancer	Phase III
NC-6004	PEG-poly(glutamic acid)	Cisplatin	Pancreatic cancer	Phase II
Paclical®	Micellar retinoid-derived	Paclitaxel	Ovarian cancer	Phase III
Oncaspar®	PEG-L-asparaginase	Asparagine specific enzyme	Acute lymphoblastic leukemia	Approved

Table 2. Examples of nanosystems in clinic use for anticancer therapy

1.3.1 Liposomes

Liposomes are small lipid vesicles within the range of 50 to 1000 nm [24]. They are the oldest and probably most investigated drug delivery system. Their main advantage derives from the amphiphilic nature of phospholipids, allowing to encapsulate hydrophilic molecules in the liposome inner aqueous compartment, while hydrophobic molecules are spread into the bilayer [25]. They also have low toxicity and can be functionalized to improve their circulation time and to provide site-specific targeting. [26,27]. Depending upon their size and number of bilayers, liposomes can be classified into three categories: multi-lamellar vesicles (MLV); large uni-lamellar vesicles (LUV); and small uni-lamellar vesicles (SUV). The major problems associated with liposomes are their stability, their relatively fast clearance, which demonstrates a pronounced dependence on size, and their tendency to localize in the tissues of the mononuclear phagocyte system (MPS), particularly in the liver and spleen. The nanoformulation available in the market are Doxil (liposomal doxorubicin), DaunoXome (liposomal daunorubicin), and Visudyne (liposomal verteporfin) [28].

Liposomes are the simplest form of nanovector and their utility is based on the significant difference in endothelial structures defined as fenestrations between normal vasculature and tumor-associated vessels. The increase in fenestrations in tumor neovasculature allows the preferential concentration of liposome-encapsulated anti-tumor agent in close proximity to the local tumor site, a phenomenon defined as enhanced penetration and retention (EPR), which is considered to be a characteristic of passive targeting of tumors.

1.3.2 Quantum Dots

Semiconductor quantum dots (QDs) are rapidly emerging as popular luminescence probes for many biological and biomedical applications owing to their extremely small size (approximately 10 nm in diameter), high photostability, tunable optical properties, and multimodality [18,29]. Such inorganic–organic composite nanomaterials have shown extreme efficiency in cancer diagnosis *in vivo*, with their small size which facilitates unimpeded systemic circulation and attached targeting molecules [30,31]. Similar to other nanoparticles, QDs can be modified via conjugation of various surface molecules for targeted delivery [32,33] and also provide sufficient surface area to attach therapeutic agents for simultaneous drug delivery and *in vivo* imaging [34].

In a recent study, Bagalkot et al. [35] used QD–aptamer (Apt) doxorubicin (Doxo) conjugate for targeted cancer therapy, imaging, and sensing. It was shown that this multifunctional nanoparticle system can deliver doxorubicin to the targeted prostate cancer cells and sense the delivery of doxorubicin by activating the fluorescence of QDs, while allowing for simultaneous imaging of cancer cells. QDs also found application in the near infrared (NIR) imaging (700–1000 nm) [36]. The use of NIR-QDs can maximize the depth of tissue penetration, allowing for more accurate and sensitive detection of photons *in vivo*, which is limited by absorption and light scattering in conventional imaging. NIR-QDs have tremendous potential for *in vivo* imaging, and have already been used in various *in vivo* studies, including lymphatic mapping in animal models [37].

1.3.3 Dendrons and dendrimers

Dendrons and dendrimers are highly branched macromolecules that can incorporate either synthetic polymeric building blocks or natural components [38]. Their hierarchical factorial structure presents numerous conjugation sites for cargoes or targeting moieties. Although spherical in shape, dendrons and dendrimers possess a large cavity that can be utilized for passive entrapment and eventual release of drugs or other cargoes. The physico-chemical nature of the cavity determines the entrapment efficiency and release profile of the cargo. The ability to selectively tune the cavity's properties is considered a significant advantage of dendrons and dendrimers. They have the benefit of a highly controlled synthesis as well as yielding a single monodisperse compound, giving perfect control over the size, weight, and terminal functionalities of the resulting structure.

1.3.4 Nanoparticles

Nanoparticle drug delivery systems are nanometric carriers used to deliver drugs or biomolecules. Generally, nanometric carriers also comprise sub-micron particles with size below 1000 nm and with various morphologies [39]. Nanoparticles have outstanding advantages: 1) they can pass through the smallest capillary vessels because of their ultra-tiny volume and avoid rapid clearance by phagocytes so that their duration in blood stream is greatly prolonged; 2) they could show controlled release properties due to the biodegradability, pH, ion and/or temperature sensibility of materials; 4) they can improve the utility of drugs and reduce toxic side effects. As drug delivery system, nanoparticles can entrap drugs or biomolecules into their interior structures and/or absorb drugs or biomolecules onto their exterior surfaces. Presently, nanoparticles have been widely used to deliver drugs, polypeptides, proteins, vaccines, nucleic acids, genes and so on. Over the years, nanoparticles

have shown huge potential in biological, medical and pharmaceutical applications [18,40].

1.4 Biomolecules passage across the cell membrane

When a drug delivery tool is administered by any route, it must be absorbed into the bloodstream from the site of administration. Many of these macromolecular drugs exploit specific cellular processes, which require internalization of the molecules and their delivery to appropriate cellular compartments. The barely permeable cell membrane remains a formidable barrier to exert their efficacy. Indeed, an important function of a biological membrane is to serve as a barrier against the outside world. However, membranes are not impenetrable walls; obviously, nutrients must enter the cell and waste products have to leave in order for the cell to survive; for example, the movement of ions across membranes is important in regulating vital cell features such as cellular pH and osmotic pressure.

The phospholipids, that compose the biological membrane, are amphipathic molecules, consisting of two hydrophobic fatty acid chains linked to a phosphate-containing hydrophilic head group, arranged with the hydrophilic heads on both sides, in contact with water and the lipophilic chains facing the interior of the membrane. This gives a sandwich effect, with two hydrophilic layers surrounding the central hydrophobic one. Spanning this bilayer or attached to the outer or inner leaflets are proteins, which may act as ion channels, receptors, intermediate messengers (G-proteins) or enzymes. The efficacy of a biomolecule, which should be used as a therapeutic and/or diagnostic agent in biomedical research and in the pharmaceutical industry, is subject to its pharmacodistribution properties. Thus, cell compartmentalization and impermeability of membranes represent the major obstacle for delivery of therapeutic molecules; in fact, many bioactive molecules are incapable of overcoming the membrane permeability barrier and this represents the major impediment for gene and drug targeting in theranostics. Although a wide variety of biomolecules, including peptides and proteins, are now produced on a commercial scale, one challenging task for pharmaceutical researchers is to devise ways to deliver these drugs effectively and safely via non-invasive, patient-friendly routes.

In particular, many pharmaceutical agents should be delivered intracellularly to exert their therapeutic action inside the cytoplasm or onto individual organelles, such as nuclei (target for gene and antisense therapy), lysosomes (target for the delivery of deficient lysosomal enzymes), and mitochondria (target for pro-apoptotic anticancer drugs). Thus, intracellular delivery of therapeutic molecules is one of the key problems in drug delivery [41].

The intracellular bioavailability depends on several parameters relative to biomolecules and membrane physicochemical properties in particular: molecular size, concentration gradient, ionization, lipid solubility.

Molecular size.

The rate of passive diffusion is inversely proportional to the square root of molecular size (Graham's law). In general, small molecules will diffuse much more readily than large ones.

Concentration gradient.

Fick's law states that the rate of transfer across a membrane is proportional to the concentration gradient across the membrane. Thus, increasing the plasma concentration of the unbound fraction of drug will increase its rate of transfer across

Introduction

the membrane and will accelerate the onset of its pharmacological effect.

Ionization.

The lipophilic nature of the cell membrane only permits the passage of the uncharged fraction of any drug. The degree to which a drug is ionized in a solution depends on the molecular structure of the drug and the pH of the solution in which it is dissolved and is given by the Henderson–Hasselbalch equation.

Lipid solubility.

The lipid solubility of a drug reflects its ability to pass through the cell membrane; this property is independent of the pKa of the drug. However, high lipid solubility alone does not necessarily result in a rapid onset of action.

Several basic cellular mechanisms can be exploited for the intracellular delivery of biomolecules across the plasma membrane (Figure 2). There are active mechanisms, such as endocytosis, and passive mechanisms, such as translocation across the lipid bilayer; alternatively, there are highly invasive procedures, such as microinjection and/or electroporation, which could cause transient damage to membranes. The internalization processes are mainly classified in two types and a brief description is reported below.

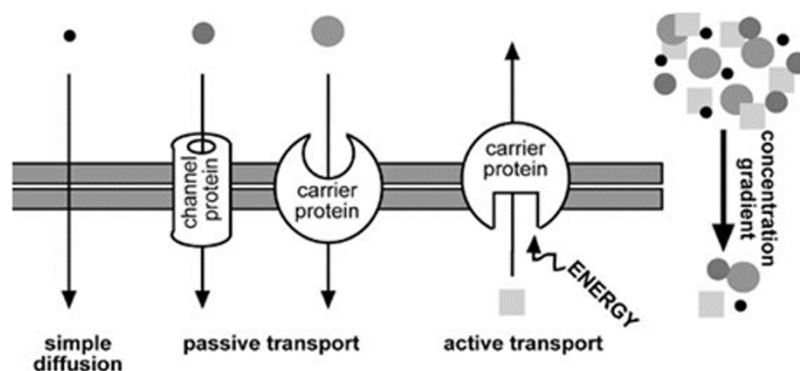


Figure 2. Mechanism of intracellular delivery.

1.4.1 Passive diffusion

Passive transport is a movement of biochemicals and other atomic or molecular substances across cell membranes. Unlike active transport, it does not require an input of chemical energy, being driven by the growth of entropy of the system. The rate of passive transport depends on the permeability of the cell membrane, which, in turn, depends on the organization and characteristics of the membrane lipids and proteins. The four main kinds of passive transport are facilitated diffusion, filtration and osmosis.

Facilitated diffusion

Facilitated diffusion, also called carrier-mediated diffusion, is the movement of molecules across the cell membrane via special transport proteins that are embedded within the cellular membrane. Facilitated diffusion is a passive process: the solutes move down the concentration gradient and do not use extra cellular energy to move. The rate of diffusion of the molecule protein complex is still down a concentration gradient but is faster than would be expected by diffusion alone. Examples of this process include the absorption of steroids and amino acids from the gut lumen. The absorption of glucose, a very polar molecule, would be relatively

slow if it occurred by diffusion alone and requires facilitated diffusion to cross membranes (including the blood brain barrier) rapidly.

Filtration

Filtration is movement of water and solute molecules across the cell membrane due to hydrostatic pressure generated by the cardiovascular system. Depending on the size of the membrane pores, only solutes of a certain size may pass through it. For example, the membrane pores of the Bowman's capsule in the kidneys are very small, and only albumins, the smallest of the proteins, have chances of being filtered through. On the other hand, the membrane pores of liver cells are extremely large, to allow a variety of solutes to pass through and be metabolized.

Osmosis

Osmosis is the diffusion of water molecules across a selectively permeable membrane. The net movement of water molecules through a partially permeable membrane from a solution of high water potential to an area of low water potential. A cell with a less negative water potential will draw in water but this depends on other factors such as solute potential (pressure in the cell e.g. solute molecules) and pressure potential (external pressure e.g. cell wall).

1.4.2 Active transport

Active transport is the movement of molecules across a cell membrane in the direction against their concentration gradient, i.e. moving from an area of lower concentration to an area of higher concentration. Active transport is usually associated with accumulating high concentrations of molecules that the cell needs, such as ions, glucose and amino acids. Energy can be supplied either directly to the ion pump, or indirectly by coupling pump-action to an ionic gradient that is actively maintained.

Among the means of active transport the endocytosis is an energy-using process by which cells absorb molecules (such as proteins) by overfilling them. It is the process by which cells take in materials. The cellular membrane folds around the desired materials outside the cell. The ingested particle becomes trapped within a pouch, vacuole or inside the cytoplasm. Often enzymes from lysosomes are then used to digest the molecules absorbed by this process.

There are essentially two main types of endocytosis: pinocytosis and phagocytosis. In pinocytosis, cells overfill liquid particles (in humans this process occurs in the small intestine, cells there overfill fat droplets). In phagocytosis, cells overfill solid particles.

1.5 Nanoparticles to facilitate cellular membrane penetration

One of the most important features of nanosystems is the possibility to functionalize them with delivery ligands, in order to overcome barriers that reduce access of agents used for treatment of tumors and for imaging of tumors. Delivery ligands are sequences able to cross the membrane bilayer, such as cell penetrating peptides (CPPs) and membranotropic peptides.

1.5.1 Cell penetrating peptides (CPPs)

CPPs are a group of peptides, usually containing a cluster of basic residues that have been recognized as promising drug delivery vectors over the last decade. It was found that the coupling of CPPs to different cargoes (e.g., small molecules, peptides

Introduction

or proteins, genes, or nanoparticles) enabled efficient internalization of these cargoes into cells [42,43]. The exact mechanism of CPP entry into cells still remains unknown and probably each peptide uses more than one mechanism (Figure 3). Their properties determine which mechanism is predominant, in particular concentration, length, charge, hydrophobicity and other chemical and physical features.

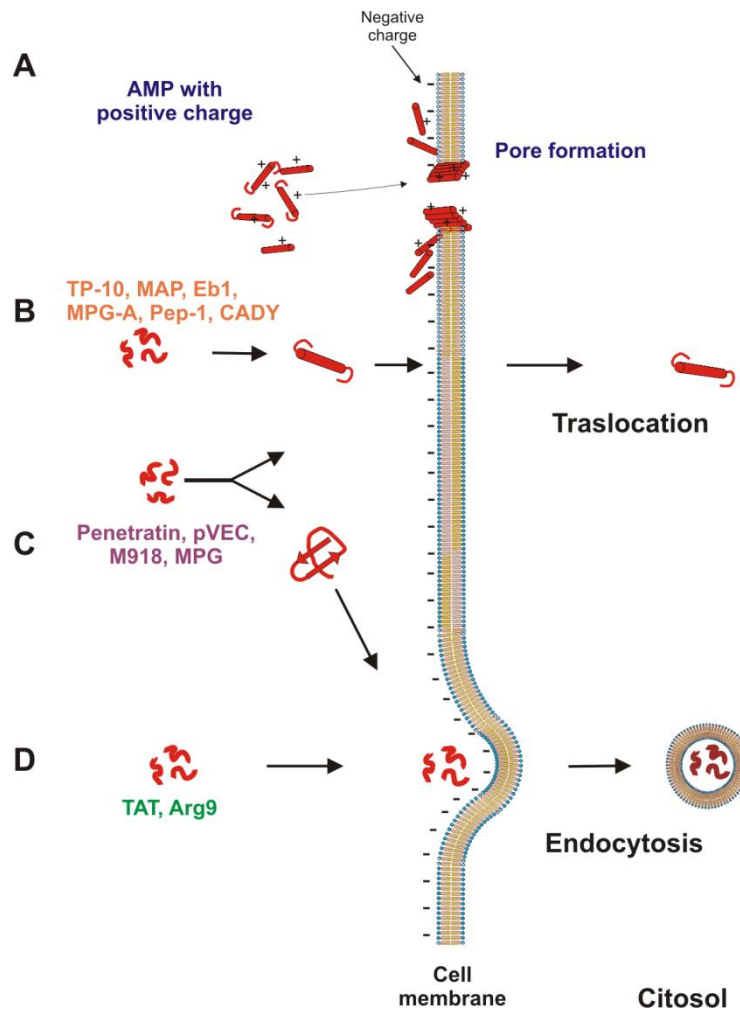


Figure 3. Proposed mechanisms of cellular internalization pathways of different CPPs. For simplicity; the pathways described have been indicated for specific peptides; but none of the pathways proposed is mutually exclusive.

Historically, two hypotheses were put forward to explain how these peptides could cross the plasmatic membrane and possibly deliver various kinds of molecules into the cell. [44] It was first proposed that CPPs, especially Tat and Antennapedia, but also others such as poly-Arg [45], Transportan [46], MPG [47] or Pep-1 [48], could pass through the plasma membrane via an energy-independent pathway. This hypothesis of a direct translocation through the plasma membrane became less popular when the entry mechanism for the Tat and the poly-arginine CPPs had to be re-evaluated following evidences of fixation artifacts during the preparation of samples for microscopic observation [49]. Indeed, fixation has been described to interfere with the sub-cellular localization of constructs with a high content of cationic residues, such as histones and the VP22 protein [50].

As a consequence, the majority of the new microscopic studies on CPPs localization have been conducted on living cells and the conclusions drawn from these very elegant works indicated that CPPs mainly follow a cellular endocytosis-mediated uptake [51,52,53].

According to this mechanism, CPPs, particularly those with a high content in cationic residues, are first simply adsorbed at the cell surface bearing numerous anionic moieties, such as heparan sulfate, sialic or phospholipidic acid [54,55,56]; then CPP-mediated transport proceeds through different endocytosis routes [49]: caveolae [57], macropinocytosis [58,59], clathrin-dependent pathway [60], cholesterol-dependent clathrin-mediated pathways [61] or the trans-Golgi network [62].

Since the endosomal pathway is mainly involved in the cellular delivery of CPPs and CPPs-conjugated molecules independent from initial route, a strong enzymatic degradation within this compartment and consequently a poor cytoplasmic release of intact molecules are expected, leading to a global weak drug transfer into the cytoplasm. In conclusion, the endosomal entrapment may limit the utility of CPPs.

1.5.2 Membrantropic peptides

Although the uptake mechanism of CPPs is largely debated it seems to involve mainly the endocytic pathway, trapping the conjugated cargo (eventually transported) in endosomes and lastly ending in lysosomes where common enzymatic degradation processes take place decreasing its intracellular bioavailability.

Therefore, it is particularly challenging the possibility of exploiting alternative mechanisms of internalization which may avoid completely or partially the endocytic pathways in order to optimize the uptake kinetic/rate and the intracytoplasmatic distribution improving thus their target-specific bioactivity. A novel intriguing hypothesis is that hydrophobic peptides that partition into membranes may also be able to cross cell membranes and enter cells. Therefore, these peptides may also cross endothelial layers *in vivo*, including the blood–brain barrier [63,64]. The hydrophobic peptides characterized by a propensity for membrane binding and a high interfacial hydrophobicity or amphipathicity, such as those derived from enveloped virus glycoproteins, represent a novel alternative to CPPs. These peptides can interfere with enveloped virus entry by direct physical interaction with the hydrophobic surfaces present on membranes and/or fusion proteins and are, thus, critical for both fusion and entry.

Fusion peptides are typically 20-30 residues long and potentially fold into amphipathic helices and are rich in glycines and alanines, providing them a high degree of conformational flexibility. There are numerous studies demonstrating that a delicate balance between α and β structures, is essential for membrane fusion and is influenced by environmental conditions such as pH, ionic strength, peptide sequence, presence or absence of divalent cations, cholesterol content and also by the lipid/peptide ratio.

Aromatic residues are generally present in fusion peptides and may help in overcoming the energy cost of peptide bond partitioning into membranes. The interactions with phospholipid moieties located at the membrane interfaces may also help in stabilizing the insertion into just one leaflet of the bilayer. The initial interaction with the external leaflet is thought to generate elastic stresses which drive to bilayer fusion, helping to overcome the hydration repulsion forces between approaching bilayers by orienting the poorly solvated face toward the external

Introduction

medium [65]. The asymmetric insertion into one membrane monolayer may promote expansion of the polar head region and determine a curvature stress onto the overall lipid bilayer; the created bulges that protrude from the membrane can facilitate the formation of lipid contacts between fusing bilayers [66]. Hydrophobic peptides traverse efficiently biological membranes, promote lipid-membrane reorganizing processes, such as fusion or pore formation [67,68] may be able to circumvent the endosomal entrapment either favouring the escape from the endosome or by translocating a cargo through the plasma membrane directly into the cytosol.

The twenty residue peptide gH625 (from aa 625 to aa 644) is a membrane-perturbing domain, derived from glycoprotein H of *Herpes simplex virus* type I, that interacts with biological membranes and is implicated in the merging of the viral envelope and the cellular membrane [69,70].

It contains particular residues that are crucial for the capacity of the peptide to interact and destabilize target lipid membranes. It is rich in hydrophobic residues including glycines, leucines, alanines, and aromatic residues such as tryptophan and tyrosines, which are known to be located preferentially at the membrane interface (Figure 4). An amphipathic α -helix is believed to be an important feature of fusion peptides playing a crucial role in mediating lipid-protein interactions during the binding of proteins to membranes and once bound, the hydrophobic face of the amphipathic peptide would then allow the peptide to enter.

The membrane interior, thereby triggering local fusion of the membrane leaflets, pore formation, cracks and membrane fusion. gH625 has been shown to strongly interact and to spontaneously penetrate the lipid-phase and insert into membranes [71]. The peptide-lipid interactions are initiated by the arginine residue located at the C-terminus, in fact, when the arginine is mutated the fusogenic activity of the peptide is strongly impaired. The hydrophobic domain is also crucial for insertion of the peptide into the membrane and corroborates the notion that hydrophobic interactions between fusion proteins and cell-membrane phospholipids initiate membrane perturbation in the early stages of viral fusion. gH625 cellular uptake is thus associated with its ability to interact with membrane lipids and to form a transient helical structure that temporarily affects membrane organization, thereby facilitating insertion into the membrane and translocation [41].

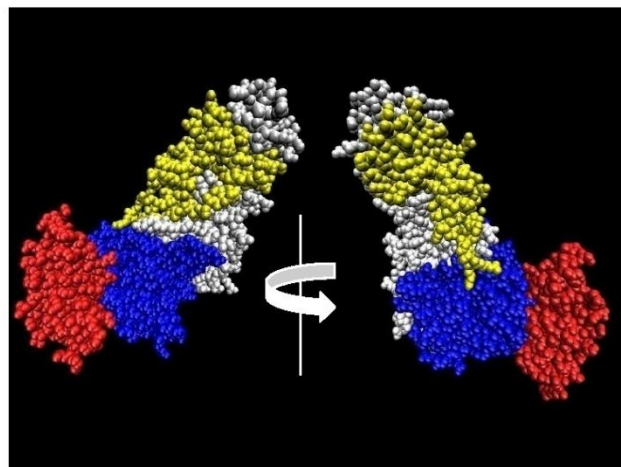


Figure 4. Crystal structure of gH-gL complex. White: H1 Domain; Blue: H2 Domain and Red: H3 Domain of gH. Yellow: gL interacting with H1 of gH.

1.6 Nanoparticles to facilitate targeting of tumors

Advancement in nanomaterials and nanotechnology have provided a promising strategy for cancer targeted drug delivery. The accumulation of nanocarriers in tumor tissue might be realized by either passive or active targeting mechanisms (Figure 5). Passive targeting exploits accumulation phenomena that are based on the pathophysiological peculiarities of the target tissue. Active targeting, on the other hand, recruits targeting vectors that specifically recognize biomarkers which are mutated or overexpressed solely in the target tissue [72,73].

1.6.1 Passive targeting

Passive targeting relies on the preferential accumulation of the nanoparticles at the target site based on their inherent bio-physico-chemical properties (such as size, shape, charge, modulus (flexibility), etc.) [72,74]. It can be applied if the target tissue manifests a distinct pathophysiology as compared to the neighbouring healthy tissue. The nanoparticles after opsonisation could be rapidly cleared from the bloodstream through phagocytosis by mononuclear phagocyte system (MPS) in the liver and by spleen filtration [75]. An approach that was first used with liposome nanovectors that has found utility with other types of nanovectors is “PEGylation,” a modification of surface characteristics using poly(ethylene glycol) (PEG), resulting in what has been defined as sterically stabilized nanoparticle platforms. This PEG modification provides protection against uptake by resident macrophages within the RES, thus increasing the circulation time of tool delivery of antitumor agent, resulting in significantly increased tumor accumulation and therapeutic efficacy [76].

In tumor tissue, there is an uncontrolled angiogenesis and abnormal vasculature, [77] so the tumor blood vessels are heavily branched and present large gaps between the endothelial cells. These vascular fenestrations facilitate the leakage of nanomaterials from the blood vessels into the tumor interstitium. In addition, the absence in tumor tissue of lymphatic vessels, allows nanomaterials to enter and not be efficiently removed and thus accumulate in the tumor over time. This phenomenon of leaky vasculature and lack of sufficient lymphatic drainage is collectively known as the enhanced permeability and retention (EPR) effect and is considered the gold standard for cancer targeting [78,79,80]. Passive targeting of nanoprobe via the EPR effect is largely dependent on their molecular size and circulation time. These two factors are closely related as the kidneys have a filtration threshold of 7 nm (or 40 kDa) and particles that exceed this threshold can evade renal clearance [78,81].

1.6.2 Active targeting

While passive targeting relies solely on the physico-chemical properties of the nanoparticles, active targeting recruits one or several targeting vectors that are conjugated to the functionalized nanoprobe surface. These targeting vectors are moieties that have a high affinity and specificity to biomarkers that are excessively or exclusively expressed on the membrane surface of target tissue cells. The targeting vectors thereby direct the nanoprobe to its target tissue and retain it there. A big benefit of actively targeted nanoprobe is that they generally improve internalization in target cells [72]; it is particularly useful in theranostic for the delivery of therapeutic and diagnostic agents to intracellular targets [48,82].

Commonly used targeting vectors can be divided into several categories:

1) monoclonal antibodies (mAbs, e.g., trastuzumab, anti-mesothelin mAbMB),

2) antibody-fragments, Fab (fragment, antigen binding), 3) proteins (e.g., transferrin), 4) peptides (e.g., bombesin, Arg-Gly-Asp (RGD) sequence), 5) carbohydrates (e.g., glucose, mannose, galactose), (6) aptamers (e.g., ssDNA), and 7) small molecules (e.g., folate, biotin) [82]. The most common targeted biomarkers are transmembrane proteins expressed on the outer membrane of the tumor cells. Most targeting vectors are covalently attached to the nanoprobe surface via conjugation chemistries; some are attached via electrostatic, coordinative, or hydrophobic interactions, avoiding to lose their targeting activity because chemical modification does not interfere with the binding region [83].

Peptides represent a viable targeting moiety with several advantageous characteristics, including low molecular weight (ca. 1 kDa), tissue penetration capability, lack of immunogenicity, ease of production, and relative flexibility in chemical conjugation processes [48]. Various peptides that can recognize cancer-specific epitopes overexpressed on tumor cells and vasculature have been used as targeting moieties for drugs and drug carriers. For examples, the epidermal growth factor receptor binding peptide (EGFP) showed a high binding affinity to the epidermal growth factor receptor (EGFR). EGFR is a transmembrane protein in the tyrosine kinase receptor family and is overexpressed in several solid tumors.

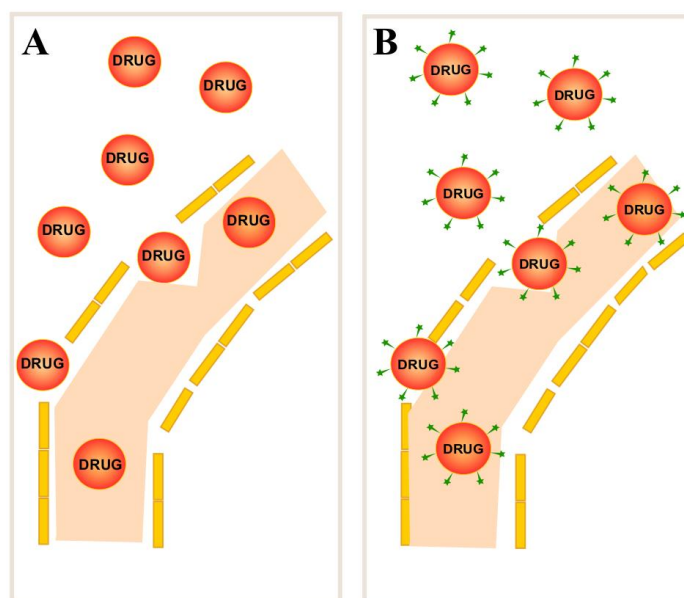


Figure 5. A Passive drug targeting. Circulating nanoparticles passively extravasate in solid tumor tissue via the enhanced permeability of blood vessels (EPR effect). **B Active drug delivery.** Once nanoparticles passively extravasate and concentrate in the target tissue via the EPR effect, the presence of ligands grafted onto the nanoparticle surface enable active targeting of the nanoparticles to receptors that are overexpressed on tumor cells.

1.7 Aim of the work

The aim of this project is to develop and design new nanotechnological systems for theranostic. A fundamental limitation of current diagnostics and therapeutics is the poor water solubility of most anticancer drugs, lack of targeting capability, non specific distribution, systemic toxicity, and low therapeutic index. Actual treatments of cancer disease remain an elusive alternative, offering limited efficacy with extensive secondary effects as a result of severe cytotoxic effects in healthy tissues.

Over the past years, my research team has worked extensively on peptides derived from *Herpes simplex virus* type 1 (HSV-1) glycoprotein H. They have identified the membranotropic sequence, gH625 (Figure 6), as a potential intracellular transporter, that interacts and spontaneously penetrates the lipid-phase and inserts into membranes [71]. The peptide-lipid interactions are initiated by the arginine residue located at the C-terminus; the hydrophobic domain is crucial for insertion of the peptide into the membrane. gH625 cellular uptake is associated with its ability to interact with membrane lipids and to form a transient helical structure that temporarily affects membrane organization, thereby facilitating insertion into the membrane and translocation.

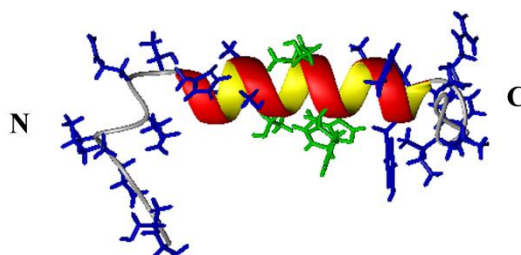


Figure 6. *Three dimensional NMR structure of gH625-644*

Compared to the commonly used CPPs, such as Tat (RKKRRQRRR, derived from HIV-1), which mainly exploits the endocytic pathway, the viral membranotropic peptide gH625 crosses membrane bilayers mainly through a translocation mechanism and is non-toxic to cells up to a concentration of 400 μM .

The specific goal of this project was to combine the benefits of the drug delivery tool with a peptide that can overcome the cell membrane mainly via a non-active translocation mechanism and a peptide that can selectively target cancer cells. In particular, several nanosystems with different composition, shape and size, were decorated on their surface with gH625 and with the targeting sequence EGBP. EGBP is a targeting sequence with a high binding affinity to the epidermal growth factor receptor, overexpressed in several solid tumors. The nanosystem functionalization can significantly increase the amount of drug to target cells.

Two different drugs were selected for the development of our drug delivery tool: doxorubicin (Doxo) and mitoxantrone (MTX). Doxo is an anthracycline closely related to the natural product daunomycin. MTX is a synthetic anthracenedione antineoplastic agent derived from the anthraquinone dye ametantrone [84]. It is structurally similar to the anthracycline agent Doxo. Both drugs having a planar aromatic ring structure which enables them to interact with DNA by intercalation between base pairs and can inhibit the activity of nuclear enzyme DNA topoisomerase (II). Their main side effect is cardiotoxicity; although also neutropenia, bone marrow suppression and secondary acute myelogenous leukemia have been reported in patients treated with MTX [85].

Liposomes and nanoparticles were selected as nanosystems.

Liposomes provide substantial advantages over many other nanoparticulate drug delivery systems because they meet clinical manufacturing requirements, such as low batch-to-batch variability, ease of synthesis, scalability, and biocompatibility.

Introduction

Benefits associated with liposomal drugs are: i) protection of encapsulated drugs from chemical and biological degradation into the blood stream; ii) controlled release and reduced toxicity through decreased exposure of healthy tissues to anti-cancer drugs; iii) increased anti-tumor activity resulting from a relatively long systemic circulation time (especially in the case of PEGylated liposomes) [24,86,87]; iv) subsequent extended exposure and accumulation in growing tumor sites. Moreover, liposomes, can be easily surface functionalized with targeting ligands to enhance the selective targeting of tumors [79,88]. The grafting of targeting ligands to the liposome surface can further enhance tumor targeting and facilitate intracellular uptake.

Nanoparticles (NPs) are colloidal systems that range in size from 1 to 100 nm. They can be fabricated by a variety of substances such as polymers, lipids, dendrimers, ceramics, and carbon nanotubes; and can be structurally adapted to deliver a wide variety of drugs, enhance delivery efficiency, and reduce side effects by targeted delivery [89,90]. Polystyrene (PS) NPs are widely used as a model to study interactions between NPs and cells due to various practical reasons including their commercial availability, high quality and wide variety of size and surface chemistry.

Superparamagnetic iron oxide nanoparticles (SPIONs) are extensively studied as platforms for numerous clinical applications, such as cancer diagnostics by magnetic resonance imaging (MRI) [91] and cancer treatment by hyperthermia [91,92] and/or magnetically targeted drug delivery [93]. Multifunctional SPIONs simultaneously modified with biocompatible polymers, anticancer agents, and fluorescence labels are especially interesting, because they combine the possibility of targeted drug delivery and *in vivo* imaging of treated tumors. Proper modification of the SPIONs surfaces should provide stability against aggregation at physiological pH and ionic strength, reduce capture by the body's immune system, and provide reactive sites suitable for further binding of drugs and biological ligands.

The nanosystems obtained were characterized in terms of physico-chemical properties (size, zeta potential, loading and release of the drug) and biological activity (cytotoxicity, antitumoral activity, cellular uptake and subcellular fate).

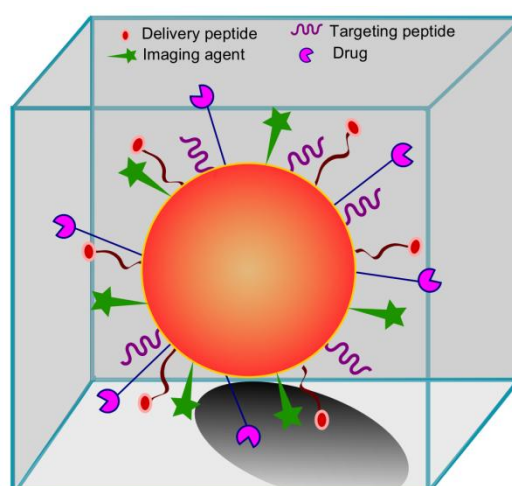


Figure 7. Schematic representation of nanosystem obtained.

2. Materials and methods

2.1 Materials and equipments

Peptides were synthesized by standard solid-phase techniques on a Syro I MultiSynThec GmbH automatic synthesizer. Protected Fmoc-amino acid derivatives, coupling reagents and Rink amide *p*-methylbenzhydrylamine (MBHA) resin were purchased from Calbiochem-Novabiochem (Laufelfingen, Switzerland), Wang resin was purchased from Fluka. The Fmoc-8-amino-3,6-dioxaoctanoic acid (Fmoc-AdOO-OH) and Fmoc-L-propargylglycine (Fmoc-Pra-OH) were purchased from Polypeptide (Strasbourg, France). All phospholipids were purchased from Avanti Polar Lipids (Alabaster, AL). Doxorubicin hydrochloride, and the other chemicals were purchased from Sigma–Aldrich, Fluka (Buchs, Switzerland), or LabScan (Stillorgan, Ireland) and were used as received, unless otherwise stated. Dialysis membranes (SpectraPor 6) were purchased from Spectrum Labs and used after rinsing the membrane in water for 30 min.

Peptide purification was performed on LC8 Shimadzu HPLC with a Phenomenex C₁₈ column (300 Å, 250x21.20 mm, 5 μ) and a UV lambda-Max model 481 detector. Peptide purity was analyzed by a Finnigan Surveyor MSQ single quadrupole ESI LC-MS with a Phenomenex C₁₈ column eluted with an H₂O/0.1% TFA (A) and CH₃CN/0.1% TFA (B). Size-exclusion chromatography was performed using a 1x18 cm Sephadex G-50 column. Cell media (Phosphate buffered saline [PBS, pH 7.4], Fetal bovine serum [FBS], 0.25% trypsin in EDTA, Eagle's minimum essential medium [EMEM], and penicillin/streptomycin solution) were purchased from Invitrogen. Cell microscopy was done by a Nikon Eclipse Ti inverted microscope equipped with a FITC filter set for fluorescence imaging. Dynamic light scattering (DLS) was performed at 25°C on a Zetasizer Nano ZS, Malven, UK in aqueous solution.

2.2 Solid-phase peptide synthesis

Peptides (Table 3) were synthesized using standard solid-phase-9-fluorenylmethoxycarbonyl (Fmoc) procedures using a Syro I MultiSynThec GmbH (Wullener, Germany) automatic synthesizer. The Rink-amide MBHA resin (substitution 0.51 mmol/g) was used as the solid-phase support, and syntheses were performed on a scale of 50 μmol. Fmoc-amino acids, 4 equivalents relative to resin loading, were coupled according to the PyBop/HOBt/DIPEA (benzotriazol-1-yl-oxytris(pyrrolidino)phosphonium/N-hydroxybenzotriazole/Di-iso-ropylethylamine) method: 1 equivalent of Fmoc-amino acid, 1 equivalent of PyBOP, 1 equivalent of HOBt (0.5 M HOBt in DMF) and 2 equivalents of DIPEA (2 M DIPEA in DMF). The Fmoc protecting group was removed with 30% piperidine in DMF (v/v). All couplings were performed twice for 35 minutes.

When necessary Fmoc-Pra-OH and Fmoc-8-amino-3,6-dioxaoctanoic acid (PEG₂) were coupled once for 45 min with 2 equivalents of PyBop/HOBt and 4 equivalents of DIPEA. Fully-synthesized peptides were deprotected from the resin with trifluoroacetic acid (TFA) with 2.5% (v/v) water, 2.0% (v/v) anisole, 2.0% (v/v) thioanisole as scavengers, at room temperature, and then precipitated in ice-cold ethyl ether, filtered, dissolved in water and lyophilized. The crude peptides were purified by RP-HPLC on a LC8 Shimadzu HPLC system (Shimadzu Corporation, Kyoto, Japan) equipped with a UV lambda-Max Model 481 detector using a Phenomenex (Torrance, CA) C₁₈ (300 Å, 250x21.20 mm, 5 μ) column eluted with an

H₂O/0.1% TFA (A) and CH₃CN/0.1% TFA (B) from 20% to 80% over 20 minutes at 20 mL/min flow rate. Purity and identity were assessed by analytical LC–MS analysis by using Finnigan Surveyor MSQ single quadrupole electrospray ionization (Finnigan/Thermo Electron Corporation San Jose, CA), column: C₁₈-Phenomenex eluted with H₂O/0.1% TFA (A) and CH₃CN/0.1% TFA (B) from 20% to 80% over 10 minutes at 0.8 mL/min flow rate. The final yields of purified peptides ranged between 20 and 40%.

PEPTIDES	SEQUENCES	M.W
Ac-gH625	Ac-NH ₂ -HGLASTLTRWAHYNALIRAF-COOH	2339.6
gH625-Pra	NH ₂ -HGLASTLTRWAHYNALIRAF-Pra-CONH ₂	2391.3
Ac- gH625-GGG	Ac-NH ₂ -HGLASTLTRWAHYNALIRAFGGG-COOH	2510.8
GGG-EGBP (TP1)	NH ₂ -GGGFPMFNHWEQWPPG-CONH ₂	1844.1
PEG ₂ -EGBP (TP2)	NH ₂ -PEG ₂ -FPMFNHWEQWPPG-CONH ₂	1817.1
Chol-GGG-EGBP (Chol-TP1)	Chol- GGGFPMFNHWEQWPPG-CONH ₂	2257.2
Chol-PEG ₂ -EGBP (Chol-TP2)	Chol-PEG ₂ -FPMFNHWEQWPPG-CONH ₂	2231.2

2.3 Conjugation of EGB targeting peptide to Cholesterol

Chol-GGG-EGBP (Chol-TP1) and Chol-PEG₂-EGBP (Chol-TP2) were prepared conjugating NH₂-GGGEGBP-CONH₂ (TP1) or NH₂-PEG₂EGBP-CONH₂ (TP2) with the cholesteryl chloroformate. In particular, 20 mg of purified TP1 and TP2 were dissolved in 2.5 mL of DMSO, and 6 mg of cholesteryl chloroformate (1.2 eq), dissolved in 420 μL of THF were added. 15 μL (1% v/v) of DIPEA was added to the mixture, which was moderately stirred at room temperature overnight. The conjugation efficiency was determined by LC-MS ((Finnigan/Thermo Electron Corporation San Jose, CA) with a column Kinetex PFP Phenomenex (100 Å 150 x 4.6 mm 5 u) using as eluents (A) 0.1% trifluoroacetic acid in water and (B) 0.1% trifluoroacetic acid in acetonitrile, and the following linear gradient: 20–95% (B) in 15 min, flow rate 0.8 mL min⁻¹. The resulting cholesteroylated peptides were precipitated in water to remove the organic solvent. The purified peptides were characterized by LC/MS on a Finnigan Surveyor MSQ single quadrupole electrospray ionization.

2.4 Preparation of triflyl azide

Sodium azide (650 mg, 10 mmol) was dissolved in distilled water (1.5 mL) and then dichloromethane (DCM, 2.4 mL) was added. The mixture was cooled on ice bath for 20 min. Triflyl anhydride (336 μL, 2 mmol) was added slowly over 5 min and the mixture was stirred for 2 h. The mixture was extracted with DCM two times. The organic portions, containing the triflyl azide, were pooled, washed once with saturated Na₂CO₃, and evaporated to dryness.

2.5 Synthesis of Azide-AdOO-Lys(C(O)CH₂CH₂C(O)N-(C₁₈H₃₇)₂)-amide ((C₁₈)₂L-N₃)

(C₁₈)₂L-N₃ monomer was synthesized in solid phase under standard conditions using Fmoc/tBu strategy. Rink-amide MBHA resin (0.51 mmol/g, 0.1 mmol scale, 0.196 g) was used as polymeric support. The Fmoc protecting group on the resin was removed by a DMF/Piperidine (70/30) mixture. Fmoc-Lys(Mtt)-OH residue (0.125 g,

0.2 mmol) was activated by 1 equiv of PyBop and HOBt and 2 equiv of DIPEA in DMF and coupled on the resin stirring the suspension for 1 h. The N^α amine function of the lysine residue was deprotected from Fmoc group, and two equivalents of Fmoc-AdOO-OH were coupled under standard condition in DMF for 1 h. After Fmoc removal from linker, peptidyl-resin was washed three times with DMF and three times with MeOH, and treated by 1 mL of solution containing K₂CO₃ (0.04 mmol) CuSO₄·5H₂O (0.01 mol) and TFN₃ (2 mmol). The resin was stirred at room temperature overnight. The solution was filtered and the resin was washed 4 times with DCM; the Mtt-protecting group on the N^ε amino function of lysine was removed by treatment with the DCM/TIS/TFA (94:5:1) mixture. The peptide resin was stirred with 5.0 mL of this solution for 2 min. This procedure was repeated several times until the solution became colorless. The resin was washed 3 times by DCM and 3 times by DMF. Then, N,N-dioctadecylsuccinamic acid (0.249 g, 0.4 mmol) was coupled twice for 1 h in the NMP (N-methylpyrrolidone)/DCM (1/1) mixture. N,N-dioctadecylsuccinamic acid was synthesized according to published procedure. The lipophilic moiety was activated in situ by the standard HOBt/PyBop/DIPEA procedure. The coupling was monitored by the qualitative Kaiser test [94]. The resin was washed 3 times by DMF, 3 times by DCM, and 3 times by ethyl ether. (C18)2L-N3 was removed from the resin by treatment with TFA containing TIS (2.5%) dithiothreitol (DTT, 2.5%) and water (2.5%) under vortexing for 2 hours. The crude product was slowly precipitated at 0 °C by adding water drop-wise, washed several time with small portions of water, and lyophilized in order to remove the solvent. The white solid was recrystallized from MeOH/H₂O and recovered with high yields (>85%). The product was identified by MS (ESI+) and NMR spectra. ¹H NMR and ¹³C-NMR spectra were recorded on a Varian 400 MHz spectrometer (Palo Alto, CA).

2.6 Liposomes preparation

Liposomes were prepared by the thin lipid film hydration procedure. Two different liposomes compositions were prepared: DOPG/DSPE-PEG/(C₁₈)₂ (85:5:10 molar ratio) and soy-lipids/Chol/DSPE-PEG/(C₁₈)₂ (57:28:5:10 molar ratio). They were prepared by dissolving the lipids in a small amount of chloroform, and subsequently evaporating the solvent by slowly rotating the tube containing the solution under a stream of nitrogen and lyophilized overnight. In this way a thin film of amphiphiles was obtained. The dry lipid film was suspended in HEPES-NaCl buffer (5 mM-100mM) at pH 7.4 by vortexing for 1 h; then the lipid suspension was freeze–thawed ten times and extruded ten times through a polycarbonate membrane with 100 nm pore size using a thermobarrel extruder (Northern Lipids).

2.7 Synthesis of SPIONs-PEG-Doxo

Unfunctionalized SPIONs were prepared by the coprecipitation method as previously described [95]. Magnetite nanoparticles were precipitated by adding ammonia solution (30 mL, 35%) to an aqueous mixture of Fe³⁺ (0.032 mol, 350 mL) and Fe²⁺ (0.016 mol, 20 mL, HCl 1.5 M) salts. The black precipitate was isolated from the solution by magnetic decantation and washed three times with water. Nanoparticles were treated with nitric acid (30 mL, 2 M) prior to the oxidation of the outer shell by iron(III) nitrate (60 mL, 0.33 M) at 100°C and peptized again with nitric acid (30 mL, 2 M). Finally, nanoparticles were washed three times with acetone and redispersed in water at pH 3. The prepared nanoparticles were characterized by TEM, dynamic light scattering (DLS), zeta potential measurements, and FTIR spectroscopy.

Materials and Methods

Functionalized SPIONs were prepared according to a one-pot synthesis protocol similar to that previously published [96]. 100 μL aqueous suspension of SPIONs at an iron concentration of 20 g/L was suspended in 5 mL of DMSO, and water was removed by evaporation. The suspension of SPIONs in DMSO was sonicated for 30 min prior to functionalization. $\text{NH}_2\text{-PEG-OCH}_3$, $\text{NH}_2\text{-PEG-NH}_2$, and Doxo were freeze-dried. An approximately 4:1 molar mixture of $\text{NH}_2\text{-PEG-OCH}_3$ (250 mg, 0.05 mmol) and $\text{NH}_2\text{-PEG-NH}_2$ (35 mg, 0.058 mmol) dissolved in 10 mL of anhydrous DMSO was allowed to react with GOPTS (12 μL , 0.054 mmol), dissolved in 1 mL of anhydrous DMSO, for 4 h at 65°C (Figure 8, step I). Doxo (1.2 mg, 2 μmol), dissolved in 1 mL of anhydrous DMSO, was added to the reaction mixture and left to react with GOPTS for 1 h (Figure 8, step II).

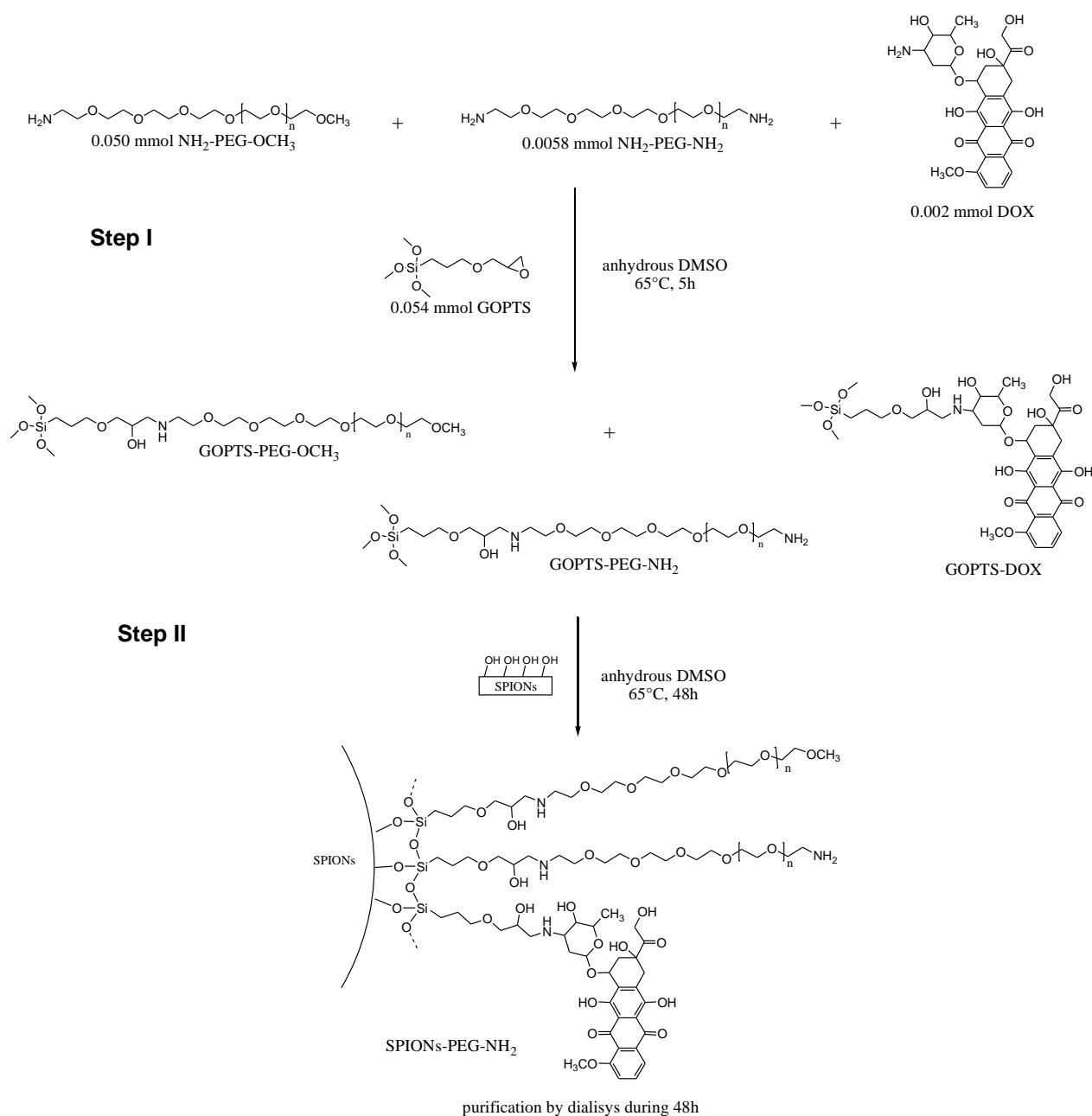


Figure 8. Schematic representation of surface functionalization of superparamagnetic iron oxide nanoparticles (SPIONs) with Doxo and PEG.

Then, SPIONs in DMSO were added, and the reaction was kept under stirring for 48 h at 65°C in the dark under nitrogen (Figure 8, step II). The suspension was dispersed in 10 mL of ultrapure water and purified by dialysis against deionized water on MWCO 25000 Da. Dialysis was carried out for 48 h, while water in the acceptor volume was changed every 2 h for the first 12 h and then every 12 h. The donor/acceptor volume ratio was 10 mL/5 L. This purification eliminates molecules not bonded to the SPION surface (NH₂-PEG-OCH₃, NH₂-PEG-NH₂, and Doxo). A small amount of non functionalized nanoparticles was removed by magnetic decantation at pH 7. The resulting nanoparticles were characterized by TEM, DLS, zeta potential measurements, FTIR.

2.8 Peptides conjugation to liposomes

The click reaction was carried out on liposomes adding CuSO₄•5H₂O (4.4 equiv), ascorbic acid (6.7 equiv), and the peptide derivative (1 equiv) with respect to the azido moiety. In particular, solutions containing CuSO₄•5H₂O (60.5 mM, solution A), ascorbic acid (81.4 mM, solution B), and the alkyn-modified peptide (1 mM, solution C) were freshly prepared in water.

Solution A, solution B, and solution C were added to a suspension of azido-functionalized preformed liposomes in HEPES-NaCl buffer. The concentration of solution C was determined measuring the tryptophan absorbance at 280 nm on a UV/Vis Jasco V-5505 spectrophotometer.

The reaction mixture was stirred at 40°C for 30 min and then left overnight at room temperature. After the conjugation step the liposomes were purified by exclusion chromatography on a 1×18 cm Sephadex G-50 (Amersham Biosciences) column pre-equilibrated with HEPES buffer.

The peptide EGBP, conjugated to cholesterol, was included directly during the preparation of lipids film.

2.9 Peptides conjugation to SPIONs

A solution of the peptide, EDC (1-ethyl-3(3-dimethylamino-propyl)-carbodiimide, hydrochloride) and NHS (N-Hydroxysuccinimide) in molar ratio of 4:4:1 was prepared in PBS buffer at pH 7.4, at room temperature under stirring for 30 min. SPIONs were conjugated with preactivated-peptide in DMSO at room temperature for 36 h in presence of Tween 20. The peptide-SPIONs were purified from unconjugated SPIONs by dialysis against deionized water on MWCO 25000 Da. Dialysis was carried out for 48 h, while water in the acceptor volume was changed every 2 h for the first 12 h and then every 12 h. The donor/acceptor volume ratio was 10 mL/5 L. This purification eliminates peptides not bonded to the SPION surface. Peptide-NPs were prepared with a ratio molar of 1:0.3 respect to NH₂-PEG-NH₂.

2.10 Peptides conjugation to NPs

A solution of the peptide, EDC (1-ethyl-3(3-dimethylamino-propyl)-carbodiimide, hydrochloride) and NHS (N-Hydroxysuccinimide) in molar ratio of 4:4:1 was prepared in PBS buffer at pH 7.4, at room temperature under stirring for 30 min. NPs were conjugated with the preactivated-peptide, in MES 0.1 M buffer at pH 5.5 over night at room temperature in presence of Tween 20 (0.2%v/v) and the yield of the reaction was higher than 90%. The peptide-NPs were purified from the unconjugated-NPs by exclusion chromatography on a 1×18 cm Sephadex G-50 (Amersham Biosciences) column pre-equilibrated in PBS buffer at pH7.4. The

fluorescence spectra of peptide-NPs and un-conjugated NPs were measured in a Cary Eclipse Varian fluorescence spectrophotometer in the same condition. Peptide-NPs were prepared with 35% degrees of functionalization

2.11 Drugs loading into liposomes

Doxorubicin (Doxo) and Mitoxantrone (MTX) were remote-loaded in liposomes via an ammonium sulfate gradient method and the free drugs were removed by gel filtration. Briefly, a liposomal solution was prepared as reported above in an ammonium sulphate solution (250 mM) at pH 5.5. Next, the external buffer was removed by ultracentrifugation at 151332 g, at 4°C for 3 h, and the liposomes were resuspended in HEPES-NaCl buffer (5-100 mM) at pH 7.4. A drug solution in water was added to the liposomal solution, to achieve a final lipid to drug weight ratio of 10:1. This suspension was stirred for 30 min at 60°C. Unloaded drug was removed with a Sephadex G50 column for determination of entrapment efficiency. The drug concentration was determined by UV spectroscopy measuring the drug absorbance. The Drug Loading Content (DLC, defined as the weight ratio of encapsulated drug vs. the amphiphilic moieties) was quantified by subtracting the amount of drug removed from the total amount loaded. Finally, the drug pre-loaded liposomes were modified with gH625 by using the click-chemistry reaction procedure, as reported above.

2.12 Structural studies of conjugated peptides

2.12.1 Circular dichroism measurement

CD spectra were recorded from 260 to 195 nm on a Jasco J-810 spectropolarimeter using a 1.0, 0.1 cm quartz cell at 25°C. For the measurements, the DOPG/DSPE-PEG liposomes decorated with gH625 were diluted 10 times in a H₂O and placed in a 0.1 cm quartz cell stabilized at 25°C. The SPIONs conjugated with gH625 were diluted 10 times in H₂O and in presence of trifluoroethanol (TFE) and placed in a 1.0 cm quartz cell at 25°C. Other experimental settings were: scan speed of 10 nm min⁻¹, sensitivity of 50 mdeg, time constant of 16 s, bandwidth of 1 nm. Each spectrum was obtained through averaging three scans, subtracting the contributions from other species present in solution, and converting the signal to mean molar ellipticity. CD spectra were recorded using a Jasco J-715 spectropolarimeter in a 1.0 or 0.1 cm quartz cell at room temperature. The spectra are an average of 3 consecutive scans from 260 to 195 nm, recorded with a band width of 3 nm, a time constant of 16 s, and a scan rate of 10 nm/min. Spectra were recorded and corrected for the blank sample.

2.12.2 Zeta potential and size measurements

For Dynamic light scattering characterizations of self-assembled liposomes in HEPES-NaCl solution were prepared at the final concentration of 1x10⁻³ M. The SPIONs and polystyrene nanoparticles measurements were conducted at 25°C at and with a pH varying from 3 to 10. The measurements were performed with a Malvern Nanosizer Nano ZS (Malvern Instruments, Worcestershire, UK), a He-Ne laser 4mW source operating at 633 nm with the scattering angle fixed at 173°. All the measurements were performed at (25.00± 0.05)°C. For zeta potential analysis of liposome preparations and SPIONs was used a Zetasizer Nano-ZS (Malvern Instruments, Worcestershire, UK). The measurements were conducted at 25°C at pH from 3 to 10. All measurements were performed in triplicate for each sample.

2.12.3 Transmission Electron Microscopy

The morphology and size of SPIONs were examined by transmission electron microscopy using a JEOL JEM-1230 microscope with 0.2 nm resolution, operating at 120 kV. Samples were diluted with ultrapure H₂O to an iron concentration of 20 mg/L before being deposited on a carbon-coated copper grid and left to air-dry.

2.12.4 Fourier Transform Infrared Spectroscopy

The chemical composition of nanoparticles was studied by FTIR on a Bruker Vector 22 FTIR spectrometer. All dried samples were prepared as KBr pellets. FTIR spectra were recorded from 400 to 4000 cm⁻¹ with a resolution of 4 cm⁻¹, using a pure KBr pellet as zero absorbance reference.

2.12.5 Atomic Absorption Spectroscopy

The total iron concentration of SPIONs was determined by atomic absorption spectrophotometry at 248 nm. The measurements were performed on an atomic absorption spectrometer (AAS) iCE 3000 Series Thermo Scientific. Prior to AAS measurements, samples were digested by concentrated hydrochloric acid (37%) and then diluted with hydrochloric acid (1%). The calibration procedure for the iron absorbance at 248 nm was performed with a series of Fe solutions at concentrations of 0.5, 1, 1.5, 2, 2.5, and 3 mg/L (prepared from a 1 g/L Fe standard solution).

2.12.6 Analysis of the fluorescence emission of tryptophan

The fluorescence emission spectra were recorded using a Jasco Model FP-750 spectrofluorimeter (Easton, MD) equipped with a Peltier temperature controller in 1.0 cm path length quartz cell at 25°C. Emission spectra of liposomes dual decorated with gH625 and EGBP were obtained in the range 310 to 400 nm exciting at 295 nm at a peptide concentration of 1×10⁻⁵ M. Equal excitation and emission bandwidths were used throughout the experiments, with a recording speed of 125 nm min⁻¹ and automatic selection of the time constant.

2.13 In vitro drug release from liposomes

The *in vitro* release of Doxo from biomimetic liposomes functionalized with gH625 and biomimetic liposomes functionalized with gH625 and EGBP was determined using a dialysis method. Briefly, free Doxo and Doxo-loaded liposomes (with free Doxo removed) were placed in a dialysis bag (MW cut off of 1000 Da) and dialyzed against HEPES-NaCl and HEPES-NaCl with 50% fetal bovine serum under continuous stirring at 37°C. At predetermined time intervals, aliquots were withdrawn and replaced with an equal volume of fresh medium. The Doxo concentrations were calculated based on the fluorescence absorbance intensity of Doxo excited at 485 nm using a previously established calibration curve. The cumulative amount of Doxo released over the 72 h was quantified, and results were plotted against time.

The *in vitro* release kinetics of MTX from liposomes was determined using UV-visible spectrophotometry. LMTX and LMTX-gH625 at equivalent MTX concentration were placed into 2 mL of HEPES-NaCl buffer and into under continuous stirring at 37°C. The release studies were carried out in triplicate. At predetermined time intervals, 200 µL aliquots were withdrawn and replaced with equal volume of fresh medium. The free drug was collected by a Sephadex G50 column and MTX was quantitated based on the UV-Vis absorbance at 655 nm using a previously established calibration curve. The cumulative amount of MTX released over 24 h was quantified,

and results were plotted against incubation time.

2.14 *In vitro* studies

2.14.1 *Trypan Blue assay*

The estimation of cell viability for MTX loaded liposomes, composed of DOPG/DSPE-PEG was performed by staining with Trypan Blue (TB) (Invitrogen). This marker, added to a cell suspension, is able to cross cell membranes that have been changed significantly. The TB penetrates only into damaged cells giving them a blue colour observable under an optical microscope. The viable cells, which are not permeable to the marker, remain colourless. This assay was performed on HeLa, cervical cancer cell of an African-American woman (ATCC, Rockville, MD, USA, CCL-2) grown as monolayers in Dulbecco's Minimal Essential Medium (Gibco BRL, Invitrogen Corporation, Carlsbad, CA, USA), supplemented with 10% fetal bovine serum (FBS-Euroclone, Milan, Italy), 100mg/ml sodium pyruvate, 100g/ml of nonessential amino acids, 100g/ml penicillin/streptomycin and 100U/ml glutamine (Invitrogen - Life technologies, Italy). These cells were cultured at 37°C, in a humidified incubator in presence of 5% CO₂, using sterile flasks. After reaching the confluence of the flask, the medium was removed and the cells were washed with phosphate buffer saline (PBS). Subsequently, the cells were incubated with a solution of trypsin (0.05% trypsin, 0.0022% EDTA) and PBS at 37°C in the presence of 5% CO₂ for 3 minutes. Finally, cells detached from the flask were transferred into a sterile tube (Falcon) and centrifuged at 325 g for 10 minutes. The cell pellet obtained was resuspended in fresh culture medium and the cells were seeded in 12 well plates (Falcon) in complete medium at a concentration of 350.000-400.000 cells/well. The following day, the cells were treated with different concentrations of LMTX and LMTX-gH625; controls were used as untreated cells (negative control) and cells treated with H₂O₂ (positive control). At the end of the treatments of 1, 4, 6, 12, 24, 48 and 72 hours, cells were washed three times with PBS to remove the liposomes in excess, and then trypsinized. The cells completely detached were transferred in falcon tubes and 25 µl of the cell suspension were mixed with 475 µl of TB. The cells were counted using the appliance Countess[®] Cell Counter (Invitrogen). The results were expressed as percentage of control.

2.14.2 *MTT viability assay*

The evaluation of cell proliferation for Doxo loaded liposomes composed of soy/CHOL/DSPE-PEG was performed on human lung adenocarcinoma cell line wild type and doxorubicin resistant in the presence of increasing concentrations of samples in a range of 5-0.04 µM or free Doxo in a range of 3-0.02 µM. A549 and A549 Dx cells were seeded in 96-well plates in a number of 25x10² per well. The growth inhibition was assessed by MTT viability assay after 72 h of treatment as previously described [97]. Then the concentrations inhibiting 50% of cell growth (IC₅₀) were obtained and these values were used for subsequent experiments. MTT assay was carried out by triplicate determination on at least three separate experiments. All data are expressed as mean ± SD.

2.14.3 *Alamar Blue assay*

The cytotoxicity of polystyrene NPs was quantified on bEnd.3 by Alamar Blue assay and compared to non-treated cells, which were used as a control. Briefly, 3x10⁴ cells were seeded on a 35 mm cell culture dish and incubated 24 h with NP suspensions to allow endocytosis. Conversely, for NP shooting, cells were shot with NPs by gene

gun, washed roughly with PBS and, then, allowed to recover for 24 h at 37°C. After recovery, cells were trypsinized, counted and seeded on fresh 35 mm cell culture dishes. Alamar Blue Assay was performed according to the manufacturer's procedure at 1 day after NP exposure. Absorbance of Alamar Blue reagent solution was read at 570 nm and 600 nm by a plate reader (Perkinelmer). Data were reported as percentage of viable cells normalized to non-treated cells.

2.14.4 Cholesterol depletion

To extract cholesterol from cell membrane, cells were incubated with 10 mM M β CD for 30 minutes at 37°C as previously described [98,99]. After M β CD treatment, NPs were added to cell culture medium and incubated with cells for 15 minutes at 37°C. Then, cells were rinsed twice with PBS to remove non-internalized NPs and fixed with 4% paraformaldehyde for 20 min. Finally, cell nuclei and membranes were stained with DAPI and red fluorescent wheat germ agglutinin (WGA), respectively. All samples were then observed at confocal microscope (SP5 Leica) with a 63 \times oil immersion objective. Confocal images were analyzed with ImageJ analysis software to quantify NP uptake. At least 20 cells of each three independent experiments were analyzed. Data were shown as mean \pm standard deviation.

2.15 Flow cytometric analysis

2.15.1 Flow cytometric analysis of drug accumulation

The cellular uptake of MTX-loaded liposomes was analyzed by flow cytometry. HeLa cells, cultured in Dulbecco's Minimal Essential Medium supplemented with 10% fetal bovine serum, were seeded into six-well at a density of 3×10^5 cells per mL at 37 °C for 48 h. Then, cells were treated with a final concentration of 5 μ M of LMTX and LMTX-gH625 in PBS medium for 1 and 4 hours in a volume of 1 mL. Thereafter, cells were washed three time, trypsinized, harvested and then resuspended in 0.5 mL of PBS. The MTX fluorescence associated to the cells was measured by FACs analysis (BD Accuri), using FL4 channel 675/25 nm. The events collected were ten thousand and BD Accuri C6 software was used to calculate mean fluorescence intensity (MFIs) for each sample. MFIs values were reported as histogram. The accumulation of Doxo was analyzed by FACS Aria™ (BD Biosciences) after treating A549 and A549 Dx cells with a fixed concentration (10 μ M) of Lipo, LipoDoxo, LipoDoxo-gH625 and Doxo. Briefly, A549 and A549 Dx cells were seeded in 6-well plates in a number of 2×10^5 cells per well and were treated 24 h later with each formulation and free Doxo. After 3, 6, 12 and 24 h of treatment cells were trypsinized, washed twice with PBS 1X and pellets were resuspended in 500 μ L of PBS 1X. Doxo fluorescence associated to the cells was measured using FL2 channel and calculated as mean fluorescence intensity (MFIs) for each sample. For each sample, 2×10^4 events were acquired. Analysis was carried out by triplicate determination on at least three separate experiments.

2.15.2 Flow cytometric analysis of oxidative stress

The evaluation of ROS accumulation was detected using dihydroethidium (DHE), a specific marker for the determination of reactive oxygen species, in detail superoxide anion. Once oxidized within the cell, DHE is converted into ethidium (HE) and emits at the wavelength of 605 nm. Briefly, A549 and A549 Dx cells were seeded in 6-well plates in a number of 2×10^5 cells per well and were treated 24 h later with concentration inhibiting 50% of cell growth of each formulation and Doxo. A549 and

Materials and Methods

A549 DX cells were also treated with 500 μM of H_2O_2 , which is able to induce superoxide anion formation, 200 μM of N-acetylcysteine (NAC) as antioxidant agent, and H_2O_2 in combination with NAC. At the end of treatments, A549 and A549 Dx cells were incubated for 1 h with 20 ng/mL DHE stock solution (2.5 mg/mL). At the time of processing, cells were trypsinized, washed twice with PBS 1X and the pellet was resuspended in 500 μl of PBS 1X. The dye accumulation was analyzed by BD FACSAria™ (BD Biosciences). For each sample, 2×10^4 events were acquired. Analysis was carried out by triplicate determination on at least three separate experiments.

2.15.3 Flow cytometric analysis of apoptosis

Apoptotic cell death was analyzed by Annexin-V–FITC staining and by propidium iodide (PI) detection systems (eBiosciences, Vienna, Austria). Briefly, A549 and A549 Dx cells were seeded in 6-well plates in a number of 2×10^5 cells per well and were treated 24 h later with concentration inhibiting 50% of cell growth of LipoDoxo, LipoDoxo-gH625, Doxo and 5 μM of Lipo (concentration proved to be not toxic). After 3-6-12-24 h of treatment cells were trypsinized, washed twice with PBS 1X and pellets were resuspended in 200 μL Binding Buffer 1X. Then, 5 μL Annexin V-FITC were added to 195 μL cell suspension, mixed and incubated for 10 min at room temperature. Cells were washed with 200 μL Binding Buffer 1X, resuspended in 190 μL Binding buffer 1X and 10 μL Propidium Iodide (20 $\mu\text{g}/\text{mL}$) was added. The detection of viable cells, early apoptosis cells, late apoptosis cells and necrotic cells were performed by FACSAria™ (BD Biosciences). For each sample, 2×10^4 events were acquired. Analysis was carried out by triplicate determination on at least three separate experiments.

2.16 Confocal microscopy studies

2.16.1 Evaluation of intracellular distribution of Doxo by confocal microscopy

After 6 and 24 h of incubation of A549 and A549 Dx cells with fluorescent Lipo, cells were fixed for 20 minutes with a 3% (w/v) paraformaldehyde (PFA) solution and permeabilized for 10 minutes with 0.1% (w/v) Triton X-100 in phosphate-buffered saline (PBS) at room temperature. To prevent nonspecific interactions of antibodies, cells were treated for 2 h in 5% bovine albumin serum (BSA) in PBS, then cells were incubated with a specific mouse monoclonal Ab raised against vimentin (1:1,000 in blocking solution, 3% (w/w) BSA in TBS-Tween 0.1%, Sigma) for 2 h at 37 °C. After several washes, cells were incubated with a secondary IgG goat anti-mouse antibody (Alexa Fluor 488, Life Technologies, Carlsbad, CA) diluted 1:1,000 in blocking solution for 1 h at room temperature. The slides were mounted on microscope by Mowiol. The analyzes were performed with a Zeiss LSM 510 microscope equipped with a plan-apochromat objective X 63 (NA 1.4) in oil immersion. The fluorescences of the Doxo and Alexa Fluor 488 were collected in multi-track mode using BP550-625 and LP650 as emission filters, respectively.

2.16.2 In vitro cellular uptake and distribution by Confocal Spectral Imaging

HeLa cells were plated at a density of 4×10^4 cells/well in 24-well plates onto cover glasses for 48 h in DMEM media supplemented with 10% serum. HeLa cells were then incubated with either LMTX or LMTX-gH625 at drug concentration of 1 μM for 1 and 4 h at 37 °C in DMEM media without serum. After the incubation with the liposomes, the medium was removed and the cells were washed three times with fresh HBSS (Hank's Balanced Salt Solution, Fisher Bioblock Scientific, Illkirch,

France). Washed cells were placed between slide and slip cover. Fluorescence measurements were carried out using a LabRam confocal microspectrometer (Horiba, Villeneuve d'Ascq, France). The MTX fluorescence was excited with a 632.8 nm line of an internal, air-cooled, helium-neon laser. The power on the samples was ~30 μ W, the acquisition time was 0.02 or 0.05 s/spectrum. After the acquisition, all the spectra were normalized to an intensity corresponding to the same acquisition duration. Treatment of spectral maps was made using LabSpec 4.18 software (Horiba Villeneuve d'Ascq, France).

2.16.3 Atomic force microscopy

For atomic force microscopy (AFM), cells were incubated 10 minutes with blank and gH625-NPs, washed twice to remove non internalized NPs and fixed with 4% paraformaldehyde for 20 min. Cells not incubated with NPs were used as a control. AFM (NanoWizard II, JPK, GMBH) analysis was performed in contact mode by using triangular tip with a nominal spring constant of 0.03 N/m (MLCT, Brukerprobes). $30 \times 10 \mu\text{m}^2$ images were taken at different size applying a force of 1.5 nN with a scan rate of 1 Hz and a resolution of 512×171 . At least 10 images were used to calculate the mean roughness (RMS) and processed by JPK analysis software mapping the different regions of the whole cell surface.

2.16.4 Colocalization with endosomes and lysosomes

For co-localization experiments, after 100 nm PS NPs incubation, cells were firstly rinsed twice with PBS to remove non-internalized nanoparticles and fixed. For endosome staining, cells were fixed with 4% paraformaldehyde for 10 min at room temperature (RT). Then, cells were permeabilized with 0.01% saponin-PBS for 8 min and blocked with FBS-PBS 10% for 20 min at RT. Endosomes were localized with rabbit anti-Rab 5 polyclonal (Abcam) primary antibodies and with AlexaFluor 633 goat anti-rabbit secondary antibodies (Molecular Probes, Invitrogen). For lysosomes staining, cells were fixed with 4% paraformaldehyde for 20 min at RT. Then, cells were permeabilized with 0.05% saponin-PBS for 20 min and blocked with FBS-PBS 10% for 20 min at RT. Lysosomes were localized with rabbit anti-LAMP 2 polyclonal (Abcam) primary antibodies and with AlexaFluor 633 goat anti-rabbit secondary antibodies (Molecular Probes, Invitrogen). All samples were then observed at confocal microscope (SP5 Leica) with a 63 \times oil immersion objective and dual-channel images were acquired. The co-localization analyzes were performed by LAS AF (Leica) and ImageJ analysis softwares. Data were expressed as co-localization percentage. Moreover, Pearson's coefficient was also calculated by JACoP plugin [100] to have an estimation of the correlation among the pixels in the dual-channels images.

2.16.5 Intracellular shooting of NPs by gene gun method

To have free NPs in the cytoplasm, a ballistic system (gene gun, BioRad) was used as described elsewhere.[101] Briefly, 100 nm amine-modified polystyrene NPs were suspended in 30 μ l of distilled water at the final concentration of 4.5×10^{12} NPs/ml, respectively, deposited and left to dry on a rupture disk under a sterile hood. After solvent drying, a 900 psi pressure was used to shoot NPs within cells. After shooting, cells were roughly rinsed with PBS to remove non-internalized NPs and, the day after, the cells were recovered and 3×10^4 cells were seeded in each fresh 35 mm culture dish.

2.16.6 Multiple particle tracking

Images of shot and endo 100 nm NPs in bEnd3 cells were collected in time-lapse for 100 s with a sampling time of 1 second by using a wide field fluorescence microscope (Olympus Cell-R, 60x oil immersion objective, NA = 1.35). Tracking algorithm has been described in details elsewhere.[102] NP trajectories were built and then the mean square displacement (MSD) was calculated and correlated with the NP diffusion by the equation: $MSD = 4Dt^\alpha$, where D is the diffusion coefficient and α represents the time dependence. The MSD curve of each tracked NP was fitted by using equation (1), in order to gain information about the nature of particle motion into the cells. Briefly, we indicate as Brownian or sub-diffusive, NPs exhibiting MSD curve that undergoes a power law with exponent $\alpha = 1$ and $\alpha < 1$, respectively, and super-diffusive, particles presenting MSD, whose dependence on time was described by the power law with $\alpha > 1$. NPs presenting a MSD curves with a time exponent $\alpha \leq 1$ at low Δt and $\alpha \approx 0$ were classified as entrapped (random caged) in confined endo-lysosomal regions and not computed. The percentages of randomly moving NPs ($\alpha \leq 1$) and transported NPs ($1 < \alpha < 2$) were evaluated and compared for shooting and endocytosis as a function of NP surface functionalization with gH625 peptides. For each experiment, at least, 5 cells were analyzed.

3 Results

3.1 Abstract

The work was aimed at exploring the possible applications of a drug delivery nanoplatform for cancer diagnostic and therapy. Cancer is the second leading cause of death in the world. Nanomedicine has opened up a new world of opportunities for the development of efficient medical diagnostic methods and of selective cancer therapy. In this project three different nanosystems were investigated, in order to exploit the benefits of each one. Moreover, peptides were used to overcome the cellular barriers.

1. The first nanoplatform is liposome based. We focused on:
 - The analysis of quantitative and qualitative effects of gH625-liposomes on the delivery of the anticancer drug mitoxantrone in HeLa cells.
 - The analysis of the eventual ability of gH625-liposomes to deliver the anticancer drug doxorubicin and to overcome resistance in lung adenocarcinoma cells.
 - The analysis of the eventual ability of gH625-liposomes also decorated with the EGB peptide to actively target the epidermal growth factor receptor (EGFR) and thus determine the selectivity of the nanoplatforms.
2. The second nanoplatform is based on multifunctional magnetic nanoparticles (SPIONs). We focused on the preparation of SPIONs carrying the doxorubicin and functionalized with gH625 in order to obtain a novel theranostic system with enhanced uptake.
3. The third nanoplatform is based on polystyrene nanoparticles. We focused on the possibility to functionalize the NPs with gH625 and enhance the crossing of the blood brain barrier.

3.2 Peptide synthesis and characterization

3.2.1 Synthesis and characterization of gH625

The peptide gH625 (Table 4) was synthesized using standard solid-phase-Fmoc method. We synthesized it with different functionalizations which allowed use to couple it on the selected nanosystems with different strategies. The peptide was synthesized with an acetyl protecting group at the N terminus and a carboxyl group at the C-terminus in order to couple it to SPIONs and polystyrene NPs and with a propargylglycine moiety (Pra) at C-terminus to couple it to liposomes. After the synthesis, the final products were cleaved from the resin and purified by RP-HPLC. The purified peptides were characterized using LC-MS. Figure 9 reports the TIC profile, HPLC spectrum (panel A) and mass spectrum (panel B) of gH625 Pra, as an example.

Table 4. Peptide sequences and their molecular weight		
PEPTIDES	SEQUENCES	M.W
Ac-gH625	Ac-NH ₂ -HGLASTLTRWAHYNALIRAF-COOH	2339.6
gH625-Pra	NH ₂ -HGLASTLTRWAHYNALIRAF-Pra-CONH ₂	2391.3
Ac-gH625-GGG	Ac-NH ₂ -HGLASTLTRWAHYNALIRAFGGG-COOH	2510.8
GGG-EGBP (TP1)	NH ₂ -GGGFPMFNHWEQWPPG-CONH ₂	1844.1
PEG ₂ -EGBP (TP2)	NH ₂ -PEG ₂ -FPMFNHWEQWPPG-CONH ₂	1817.1
Chol-GGG-EGBP (Chol-TP1)	Chol- GGGFPMFNHWEQWPPG-CONH ₂	2257.2
Chol-PEG ₂ -EGBP (Chol-TP2)	Chol-PEG ₂ -FPMFNHWEQWPPG-CONH ₂	2231.2

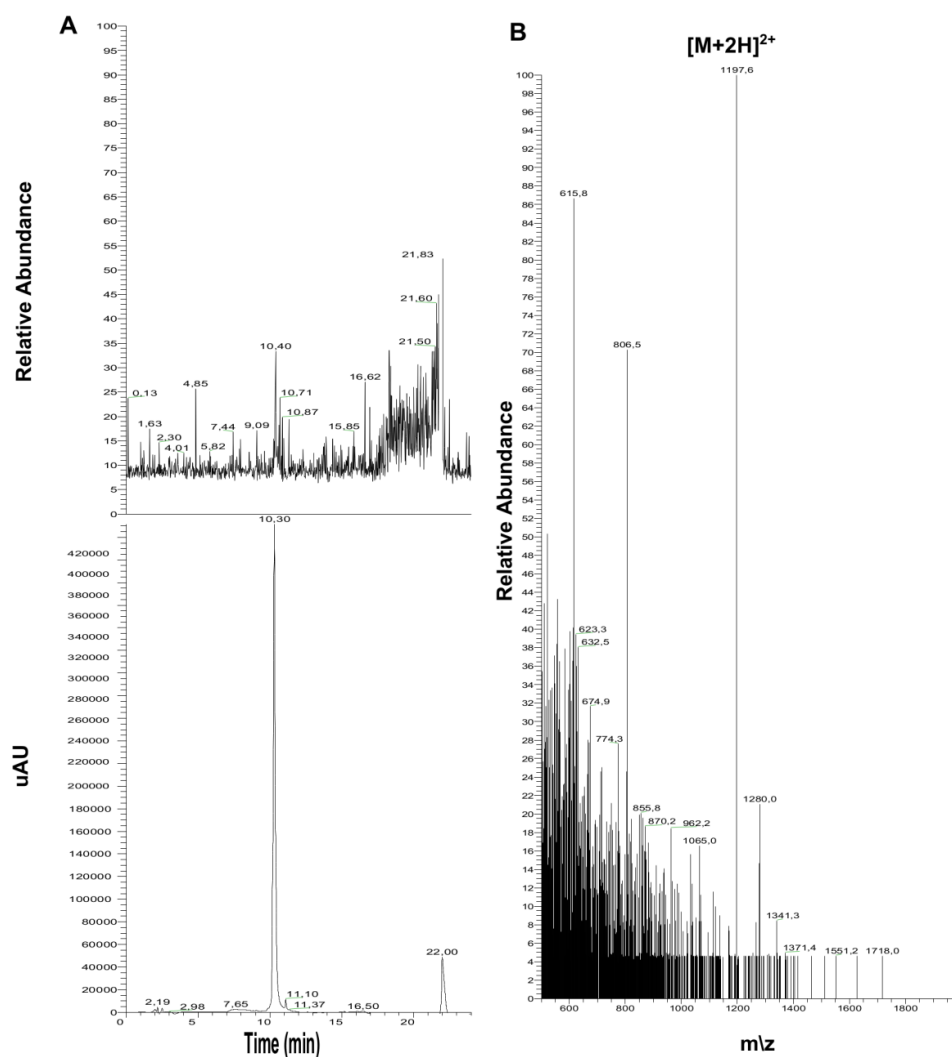


Figure 9. gH625-Pra: TIC profile and HPLC spectrum (A); mass spectrum (B)

3.2.2 Synthesis and characterization of EGBP

The EGBP peptide (Table 4) was synthesized using standard solid-phase-Fmoc method. We synthesized it with a spacer of three glycines and with a hydrophilic PEG based linker at N-terminus. The linker is necessary to expose the targeting peptide and enhance its interaction with the receptor. The glycine linker increases the space between the peptide and the nanosystem and increases the flexibility of the peptides. The PEG linker, not only increases the flexibility but thanks to its hydrophilic nature, exposes more the targeting peptide on the liposome surface. The synthesis of the GGG-EGBP (TP1) and PEG₂-EGBP (TP2) were carried out entirely on a solid phase using standard Fmoc/tBu (tBu=tert-butyl) chemistries. The final products were cleaved from the resin and purified by RP-HPLC and analyzed by mass spectrometry.

The N-terminus of both EGBP peptides were conjugated to cholesterol in solution as reported in "Materials and Methods" in order to use them directly in the liposome preparation. The conjugates obtained were analyzed by LC-MS. Figure 10 reports the TIC profile, HPLC spectrum (panel A) and mass spectrum (panel B) of Chol-TP2, as an example.

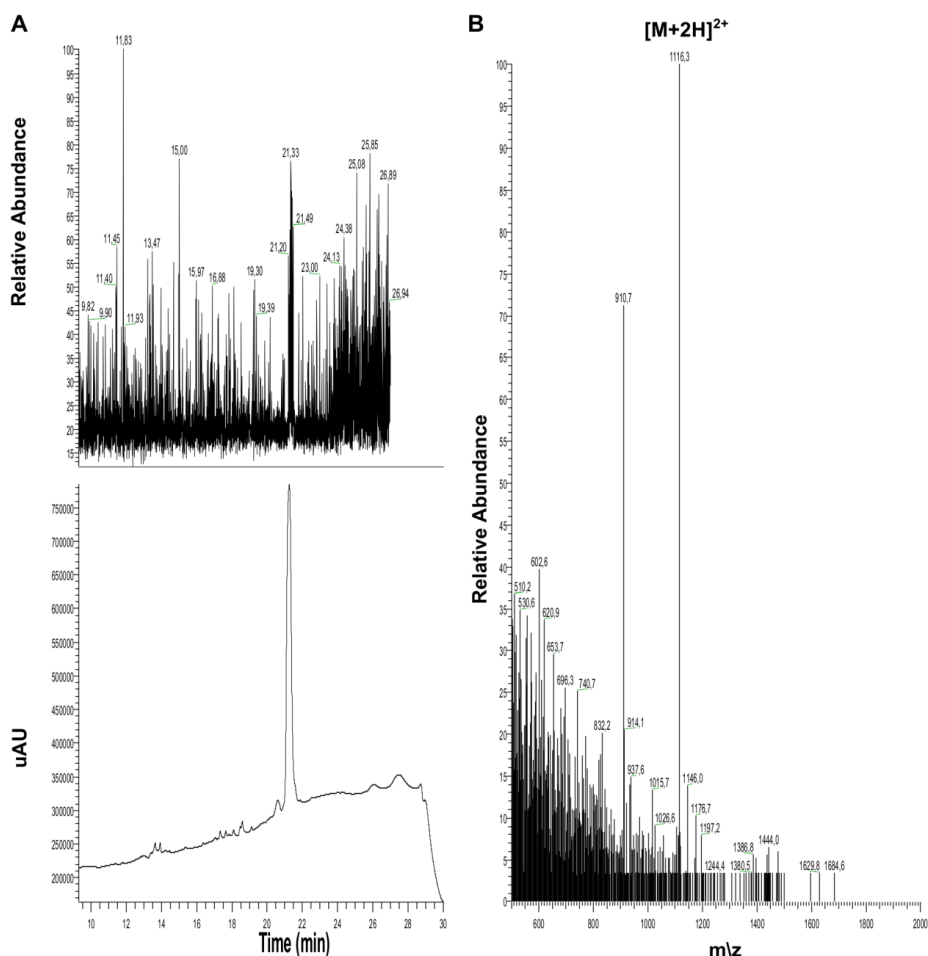


Figure 10. Chol-TP2: TIC profile and HPLC spectrum (A); mass spectrum (B)

3.3 Synthesis of the lipid moiety (C₁₈)₂L-N₃

The lipid moiety (C₁₈)₂L-N₃ was synthesized on solid phase following a modified protocol of the classical Fmoc/tBu strategy (Figure 11). The Fmoc-Lys(Mtt)-OH was anchored on the Rink amide resin. The Fmoc protecting group was removed and an ethoxylic linker was introduced. Its NH₂ function was converted into azide by diazo transfer using a sulfonyl azide, as previously reported in literature [94]. After removal of the Mtt group from the Nε of the lysine, the lipid chain was added. As expected, no reductive side reaction of azide functionalized derivative was observed during the cleavage step of the lysine derivative from the resin (data not shown) [103]. The obtained compound was analyzed by ¹H and ¹³C-NMR to confirm compound identity.

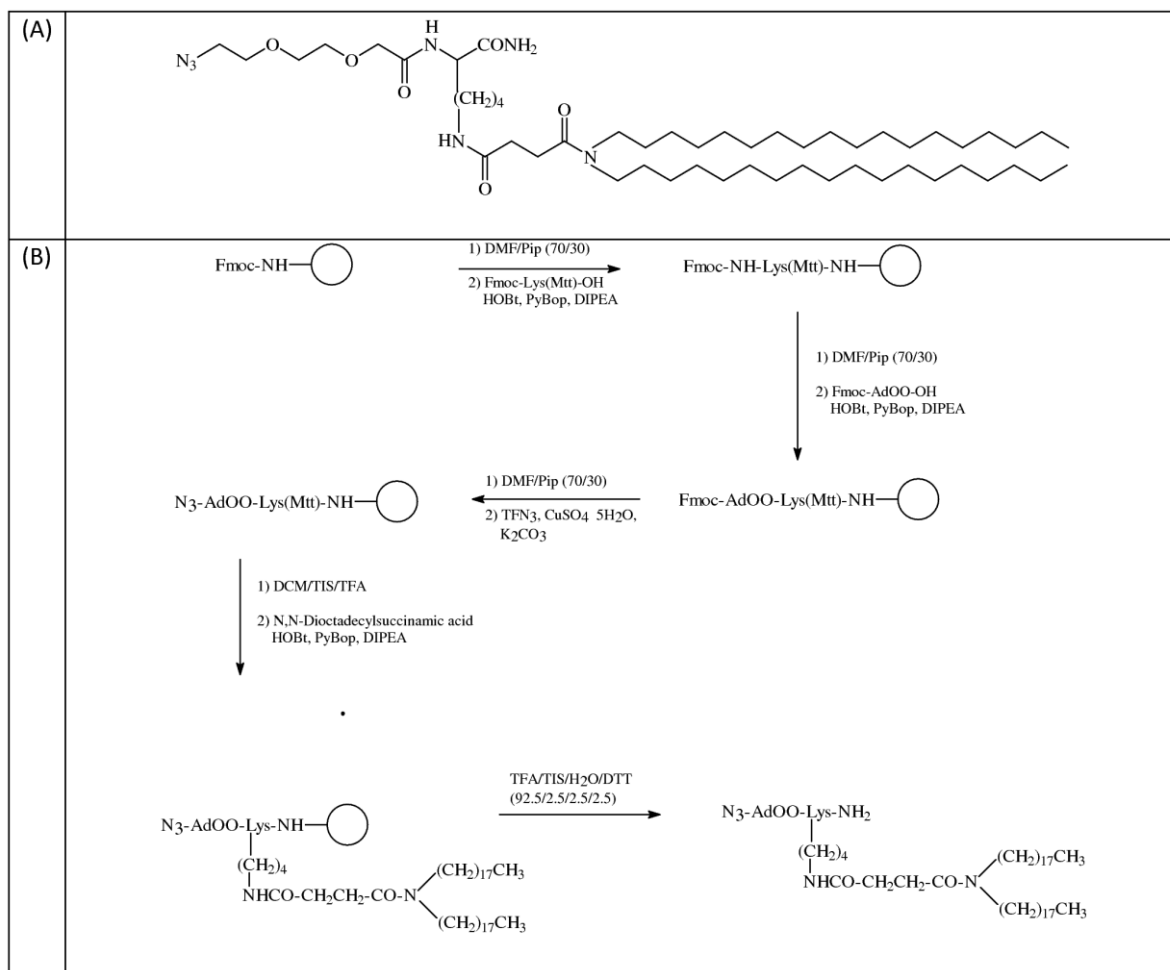


Figure 11. (A) Schematic representation of (C₁₈)₂L-N₃ synthetic monomer; (B) Scheme for the solid-phase synthesis of the (C₁₈)₂L-N₃ monomer. Rink-amide Resin is schematically represented as an empty circle

3.4 Liposomes preparation with and without peptides

Liposomes were generated by the thin-film hydration method [104]. Briefly, the lipid mixture was prepared by dissolving the lipids and when necessary Chol-GGG-EGBP (Chol-TP1) or Chol-PEG₂-EGBP (Chol-TP2) in a small amount of organic solvent, and subsequently evaporating the solvent. The lipid film was then dissolved in aqueous media and extruded to ensure the desired size, thought a polycarbonate

membrane with 100 nm pore size using a thermobarrel extruder (Northern Lipids). The composition of the liposomes is reported in each paragraph.

3.5 Quantitative and qualitative effect of gH625 on the liposome-mediated delivery of mitoxantrone

The *in vitro* delivery of the anticancer drug mitoxantrone (MTX) to HeLa cancer cells by liposomes, composed of DOPG and DSPE-PEG functionalized with the cell penetrating peptide gH625 was investigated. In order to get a better insight into the role of gH625 on the mechanism of liposome-mediated drug delivery, we treated HeLa cells with liposomes functionalized and not with gH625 and loaded with MTX. The subcellular drug distribution was analyzed by fluorescence-based techniques, such as fluorescence-activated cell sorting (FACS) and confocal spectral imaging (CSI).

3.5.1 MTX loading

MTX was loaded into DOPG/DSPE-PEG/(C₁₈)₂L-N₃ (85/5/10 molar ratio) liposomes using the well-assessed procedure based on the ammonium sulphate gradient [105]; in particular, a solution containing MTX was incubated under stirring for 30 min at 60°C. Subsequently, unloaded MTX was removed using a Sephadex G50 column pre-equilibrated with HEPES-NaCl buffer (5mM-100mM) at pH 7.4. The drug/lipid weight ratio chosen for the loading experiments was 0.1. The drug loading efficiency calculated from the unloaded MTX absorbance at $\lambda=655$ nm was higher than 97% of the total amount incubated.

3.5.2 Functionalization of liposomes with gH625

The resulting liposomes loaded with MTX (LMTX) further modified with the gH625-Pra (to become LMTX-gH625) via click-chemistry reaction performed in aqueous medium. The coupling of the Pra moiety of the gH625 to the liposome surface was obtained due to a copper^(I)-catalyzed Huisgen 1,3-dipolar cycloaddition reaction of azides and alkynes [106]. Cu^I catalyser was generated *in situ* by reduction of CuSO₄ with ascorbic acid [107]. The LMTX-gH625 was obtained with a yield higher than 90% after 12 h at room temperature. The unreactive nature of both azides and alkynes towards any other functional group present in the biomolecules, as well as the thermal and hydrolytical stability of their cycloaddition product make this reaction particularly appealing for liposome functionalization with peptides. After the conjugation step, liposomes were purified by exclusion chromatography on a 1x18 cm Sephadex G-50 (Amersham Biosciences) column pre-equilibrated with HEPES buffer.

3.5.3 MTX fluorescence intensity and release kinetics

In spite of the same concentration inside the liposomes, the MTX fluorescence intensity from LMTX in aqueous suspension was about 5.7 times higher than in LMTX-gH625. The MTX fluorescence in gH625 is partially quenched by Cu ions used to catalyze the peptide coupling to the liposomes. This result was obtained by the experiment described below. Both LMTX and LMTX-gH625 were dissolved with 0.2% of Triton X-100 and incubated for 1 h with EDTA (10 mM) at 37°C. This treatment brought to a full restoration of the absorbance intensity of the MTX released from LMTX-gH625, while for LMTX, which did not contain copper, the absorbance intensity of the released drug was not affected (Figure 12). Therefore,

Results

copper ions are able to penetrate LMTX-gH625 and to quench the loaded MTX fluorescence and absorbance.

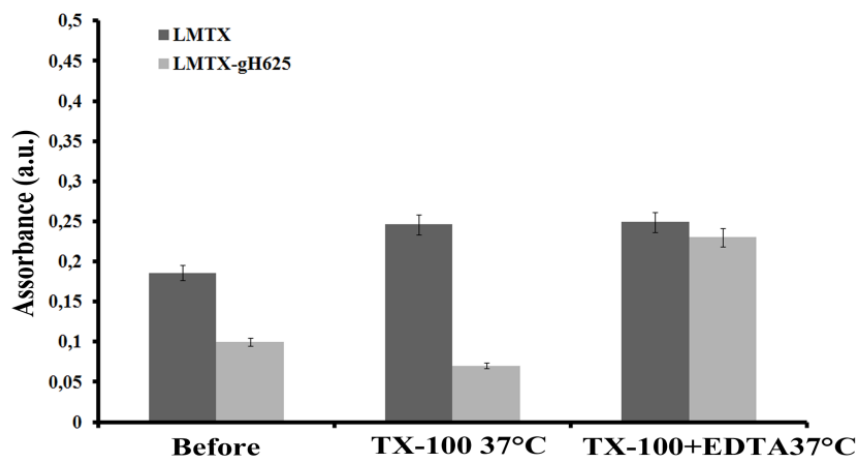


Figure 12. Effect of combination of Triton and EDTA on LMTX and LMTX-gH625. Both liposomes were treated by Triton X-100 (TX-100) and 10 mM of EDTA at 37°C. The presence of EDTA brought full restoration of MTX absorbance intensity in LMTX-gH625, while on LMTX had not effect.

There were no pronounced differences between LMTX and LMTX-gH625 from the point of view of the drug release kinetics *in vitro*, in HEPES-NaCl buffer (Figure 13). Less than 30% of loaded MTX was released within 24 h, indicating the good stability of liposomes.

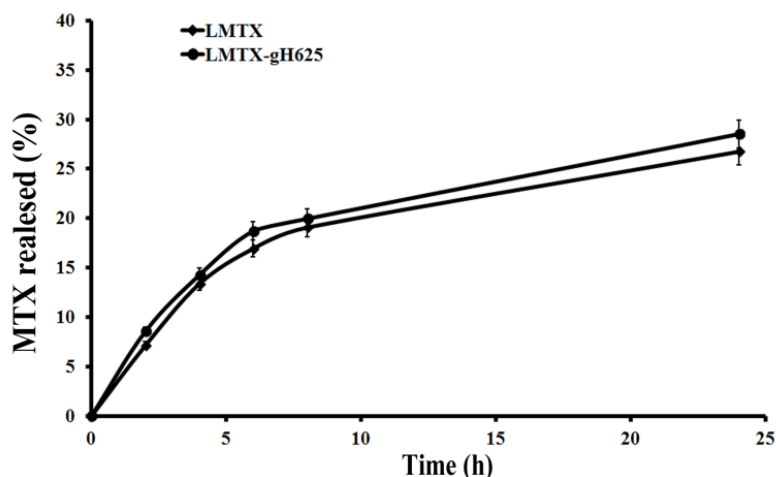


Figure 13. Kinetics of *in vitro* release of MTX from LMTX and LMTX-gH625.

3.5.4 Liposomes Characterization

Physico-chemical characterization of liposomes alone and functionalized with gH625 was performed by Circular Dichroism (CD) and Dynamic light scattering (DLS). CD

spectra showed that gH625 when conjugated to liposomes at a concentration of 1.25×10^{-6} M adopts an α helical conformation (Figure 14), while the peptide alone in buffer adopts a random coil structure; suggesting that the coupling on the surface of the liposomes was sufficient to induce the secondary structure which is probably playing a key role in translocation across the membrane bilayer.

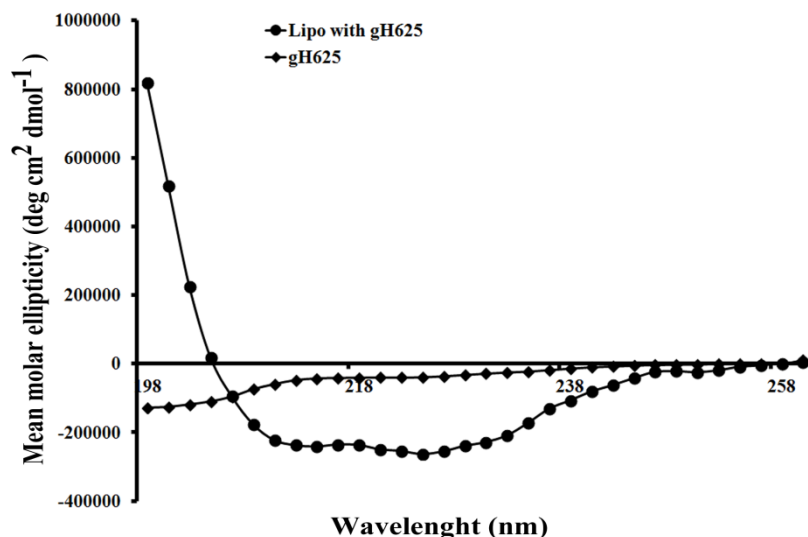


Figure 14. Circular dichroism spectrum of gH625 conjugated to liposomes and of gH625 alone

DLS data on LMTX and on LMTX-gH625 dispersed in aqueous medium at pH 7 (Table 5) showed that the liposome functionalization with gH625 only slightly increased their average hydrodynamic diameter, from ca. 111.80 to 122.05 nm. The polydispersity index changed from ca. 0.09 to ca. 0.19, indicating that the distribution of the liposome size remained rather narrow and there are no signs of aggregation. These parameters should favour both the effective extravasation of liposomes and their longer retention in tumor tissues. The surface charge of the liposomes, as determined by measurement of their zeta potential, was also slightly reduced on going from LMTX to LMTX-gH625, from ca. -26.30 to -21.30 mV (Table 5). It is widely accepted that at high values of zeta potential (over 20 mV, positive or negative) the electrostatic repulsions between particles are strong enough to ensure their colloidal stability. The aqueous suspensions of both LMTX to LMTX-gH625 were stable colloids.

Table 5. Colloidal characteristics of LMTX and LMTX-gH625

Liposome type	Average size (nm)	PDI	Zeta potential (mV)
LMTX	111.80±1.42	0.09±0.02	-26.30±1.00
LMTX-gH625	122.05±1.05	0.19±0.07	-21.30±1.10

Data obtained for three independently prepared batches of each liposome type, with at least 13 runs per batch.

3.5.5 Liposomes cytotoxicity on HeLa cells

The cytotoxicity of liposomes was evaluated staining Triptan Blue on HeLa cells. Within 4 and 6 h treatment duration, a higher cytotoxicity was observed for LMTX-gH625 than LMTX (Figure 15 a). At 48 and 72 h, no significant differences were noticed between the two types of liposomes; indicating that at high incubation times both are significantly toxic to the cells.

3.5.6 Liposomes uptake by flow cytometry

The uptake of LMTX and LMTX-gH625 in HeLa cells was determined using flow cytometry analysis.

Flow cytometry allowed to compare quantitatively the MTX uptake by HeLa cells treated with LMTX-gH625 or with LMTX (Figure 15 b). An increased uptake of MTX from liposomes was clearly observed in presence gH625.

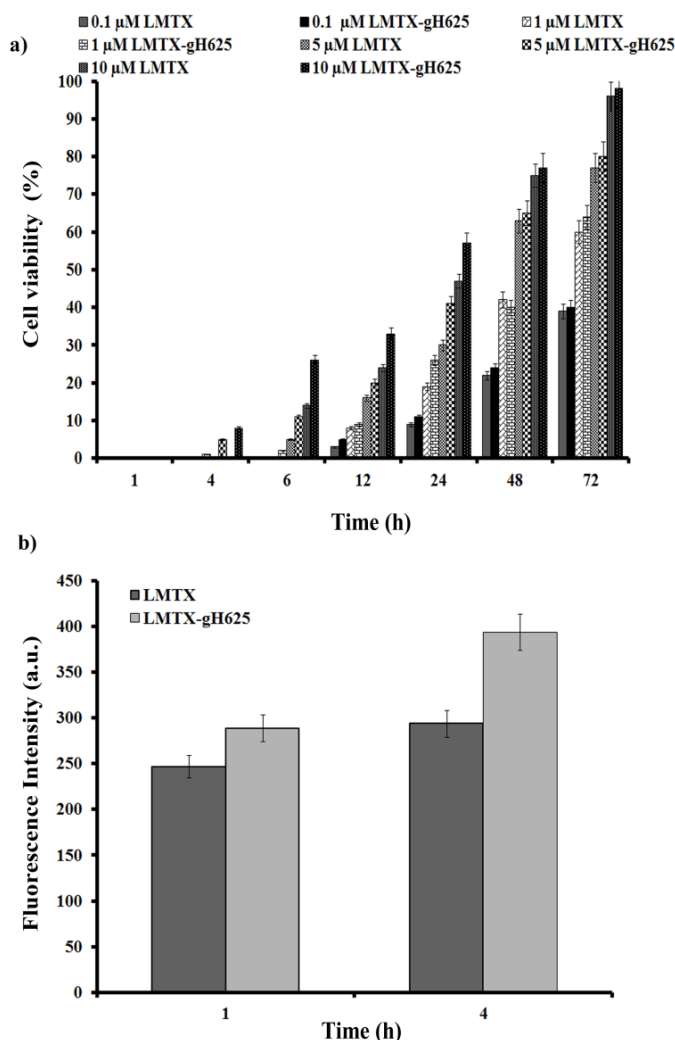


Figure 15. Cytotoxicity of liposomes on HeLa cells at several times of incubation (**panel a**). Flow cytometry data on the MTX uptake by HeLa cells (**panel b**).

3.5.7 Liposomes uptake by CSI technique

For better understanding of the observed cytotoxicity and uptake, the subcellular distribution and interaction of the delivered MTX in live HeLa cancer cells was determined by confocal spectral imaging (CSI) technique. As described above, the CSI approach consists in recording the complete fluorescence at each scanned point of the cell and therefore exploiting both the spectral shape and intensity. Full fluorescence spectra (in the 640-920 nm range) were then recorded via point-by-point scanning of the equatorial optical section of the treated cells (see the Experimental section). From these spectra, the parametric maps were generated using either total fluorescence intensity (area of the whole spectrum) or coefficients determined from fitting each experimental spectrum with spectra characteristic of 3 intracellular molecular interactions of the drug: I) MTX at lipophilic environment, where the spectrum is very close in shape to that of the drug in LMTX suspension (blue zones and spectra in Figure 16); II) MTX in nucleus, where a significant bathochromic shift of the spectrum is observed due to the drug intercalation between DNA base pairs (green zones and spectra in Figure 16); and III) an oxidative metabolite of the drug stained in the low polarity environment, with the blue-shifted spectrum (red zones and spectra in Figure 16). These characteristic spectra are consistent with those previously reported by Prof. Chourpa group for the MTX incubated as aqueous solution with MDA-MB-231 and MCF-7 cancer cell lines [108]. In the present study, the fact that not only the blue spectra but also the shifted ones were observed indicates that the drug was released, at least in part, from the liposomes and was able to reach the nucleus. Interestingly, the blue and red spectra were highly co-localized in some perinuclear regions, indicating that the lipophilic locations favour the drug oxidative metabolism. In previous studies, [108] it was found that the metabolite co-localized with the fluorescent label of endoplasmic reticulum and its presence was correlated with higher sensitivity of cancer cells to chemotherapeutic drug MTX. From the point of view of the fluorescence intensity, it is difficult to establish the exact quantum yields in these three subcellular situations. Nevertheless, it is commonly believed that the lower polarity environment of fluorophore favours higher quantum yields while the DNA intercalation leads to a partial quenching of the drug fluorescence. For this reason, the intensities used in Figure 16 allow only a comparative discussion, but could be calibrated to concentrations once the quantum yields are established (it was not a subject of the present study).

The results shown in Figure 16 allow to analyze two effects, incubation duration (1 h versus 4 h) and liposomes functionalization with gH625. The spectral maps show that the increase of the incubation duration from 1 h to 4 h, determines a significant increase in the total intracellular drug fluorescence (2 to 5 fold, see the statistical summary in Figure 16). Similar total fluorescence intensity was reached with both types of nanosystems. In contrast, for the LMTX and not for the LMTX-gH625, 4 h versus 1 h incubation resulted in a different subcellular redistribution of the MTX fluorescence: the relative fractions of lipophilic vs nuclear locations were inverted. The analysis of this inversion together with the nearly 2-fold increase of total intensity in LMTX between 1 h and 4 h, lead to the supposition that the total drug in the nucleus is probably not decreased while the drug presence in the perinuclear locations is more pronounced. For the LMTX-gH625, the drug fluorescence from the hydrophobic perinuclear regions was dominant even after only 1h of incubation and the subcellular distribution remained nearly constant between 1 h and 4 h of

Results

incubation. The latter means that the 5-fold increase of the intracellular fluorescence intensity for the gH625-modified liposomes is related to the increased uptake of the liposomes and not to the quantum yields changes.

The subcellular distribution of MTX delivered with liposomes was different from that of MTX in solution: while the drug solution was mainly and rapidly stained in nucleus of cancers cells [108], liposomes mainly directed the drug to the perinuclear zones where the metabolite production/staining by the cells was also more significant than with solutions. This could be the effect of the liposomal delivery of MTX. The above described results lead to the following conclusions about the effect of the liposomes functionalization with gH625: I) it makes the MTX uptake to the hydrophobic perinuclear staining zones even more efficient; II) it favours even more the presence of an oxidative metabolite of the drug in the same perinuclear regions.

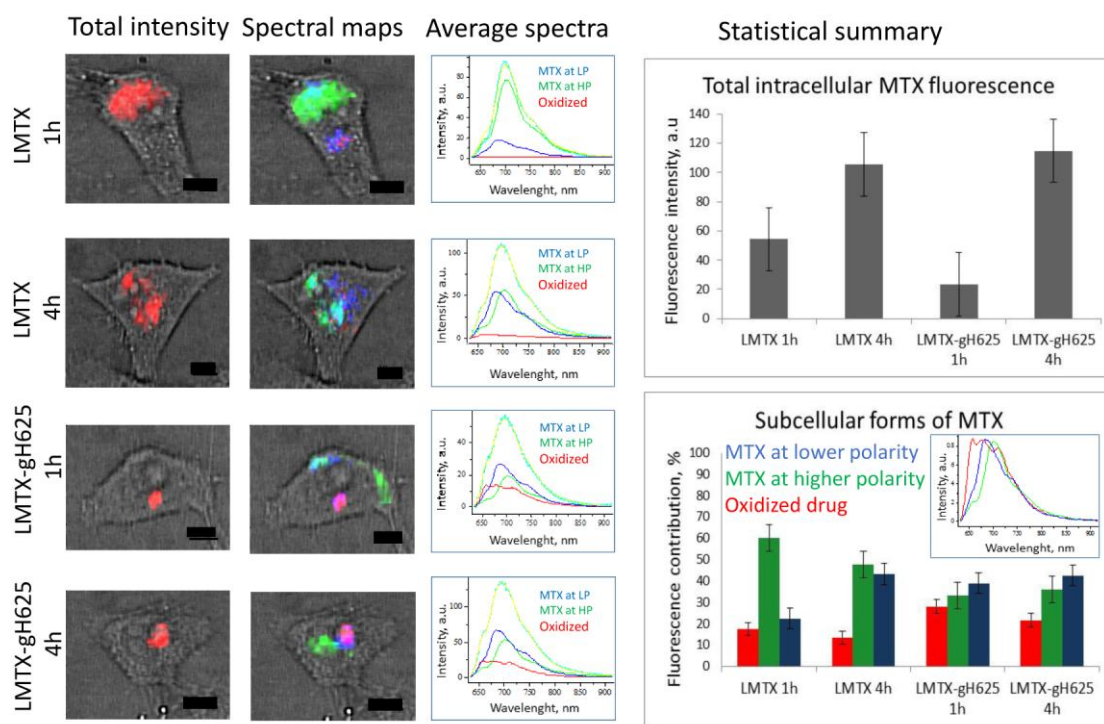


Figure 16. *In vitro* study of subcellular interaction and distribution of MTX delivered from LMTX and LMTX-gH625 to live HeLa cancer cells. Left panel: representative images of individual cells, i.e. merge of the white light images with the fluorescence spectral maps showing either total spectral intensity (yellow zones) or merged spectral maps characteristic of 3 intracellular molecular interactions of the drug: MTX at lipophilic environment (blue zones and spectra), MTX-DNA complex in nucleus (green zones and spectra) and presence of an oxidative metabolite of the drug (red zones and spectra). Average spectra of the respective cells are shown in the middle column. Right panel: statistical summary of the data over a population of at least 6 cells.

3.6 Liposome armed with gH625 peptide to overcome resistance in lung adenocarcinoma cell lines

Liposomes with enhanced biomimetics characteristics (phospholipids derived by soy) and functionalized on their external surface with PEG were used for this study. The success of pharmacological treatments is often hampered by the onset of the drug resistance. MDR is due to the selection of cancer cell clones expressing molecules that protect tumor cells from anti-cancer agents [109,110]. New delivery systems including liposomes have been developed to circumvent drug resistance; they have attracted great attention since they are ideal for loading and delivery of different molecules, therefore, offering novel opportunities for cancer treatment [64,82,111]. Here, the anti-cancer activity of Doxo-encapsulating liposomes was investigated *in vitro*. The liposomes were constituted by soy phospholipids, cholesterol and 1,2-distearoyl-sn-glycero-3-phosphoethanolamine-N-[amino(polyethylene glycol)-2000] (DSPE-PEG), in order to improve biocompatibility and lead to a prolonged presence in the systemic circulation.

3.6.1 Conjugation of gH625

The coupling of gH625 on the surface of preformed liposomes, composed of soy phospholipid mixture/cholesterol/DSPE-PEG/(C₁₈)₂L-N₃ (57:28:5:10 molar ratio) was performed by click chemistry (Figure 17). This procedure involves a copper^(I)-catalyzed Huisgen 1,3-dipolar cycloaddition reaction of azides and alkynes yielding 1,4-disubstituted 1,2,3-triazole-linked conjugates [106]. The click reaction was performed in an aqueous solution and was catalyzed by Cu^I generated, *in situ*, by reduction of CuSO₄ with ascorbic acid [107]. An equimolar mixture of NH₂-gH625-Pra and azido functions on the liposome surface were used and the expected gH625-functionalized liposomes were obtained with a yield higher than 90% after 12 h at room temperature. In the absence of the copper catalyst no reaction was observed.

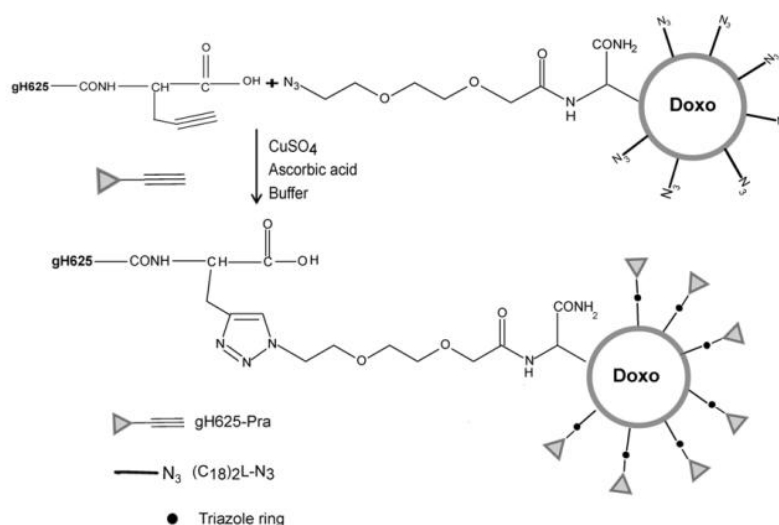


Figure 17. Scheme of the functionalization reaction of gH625 to LipoDoxo

3.6.2 Doxo loading

Doxo was loaded into soy phospholipid mixture/cholesterol/DSPE-PEG/(C₁₈)₂L-N₃ liposomes using the well-assessed procedure based on the ammonium sulphate gradient [105]; in particular, a solution containing Doxo was incubated under stirring for 30 min at 60°C. Subsequently, unloaded Doxo was removed using a Sephadex G50 column pre-equilibrated with HEPES-NaCl buffer (5mM-100mM) at pH 7.4. The drug/lipid weight ratio chosen for the loading experiments was 0.1. The drug loading content (DLC) was above 90% of the total. The drug loaded liposomes (LipoDoxo) were then efficiently modified with the gH625-Pra peptide (LipoDoxo-gH625) according to the click-chemistry procedure used in the case of empty liposomes.

3.6.3 Liposomes physico-chemical characterization

Dynamic light scattering (DLS) measurements were performed on liposomes alone and on gH625 functionalized liposomes. All liposome solutions (Table 6) present a monomodal distribution with a polydispersity index (PDI) < 0.2, indicating a narrow and homogenous size distribution, optimal not only for the more effective extravasation of liposomes, but also for their longer retention in tumor tissues. The analysis of the zeta potential shows a change between Lipo and LipoDoxo compared to LipoDoxo-gH625, which indicates a change in the surface of the liposomes upon functionalization with the peptide.

Table 6. Zeta potential, size, expressed as z-average, as measured by DSL and polydispersity index (PDI). Data are expressed as means±standard deviation (SD) of three separate experiments for each of two batch formulations, with at least 13 measurements for each.

Liposomes	Average Size (nm)	PDI	Zeta potential (mV)
<i>Lipo</i>	104.95±1.63	0.17±0.01	-7.40±1.50
<i>LipoDoxo</i>	129.85±1.82	0.15±0.03	-7.43±1.84
<i>LipoDoxo-gH625</i>	143.90±0.64	0.14±0.02	9.43±1.61

3.6.4 Release kinetics of Doxo

The release of Doxo was carried out in HEPES-NaCl buffer or HEPES-NaCl buffer with 50% FBS and the results are presented in Figure 18. Free Doxo was used as control and its release rate was nearly 100% in 2 h, which means that the release of Doxo from dialysis membrane to buffer solution is not a restricting factor and the release of Doxo from the liposomes is the only rate limiting step. There were no pronounced differences in Doxo release (Figure 18) from LipoDoxo and LipoDoxo-gH625 at each time point, indicating that the decoration of the surface of the liposomes with gH625 did not substantially change the release kinetics of liposomes. The Doxo release from liposomes decorated and not with gH625 is less than 30% within 72 h, indicating their good stability.

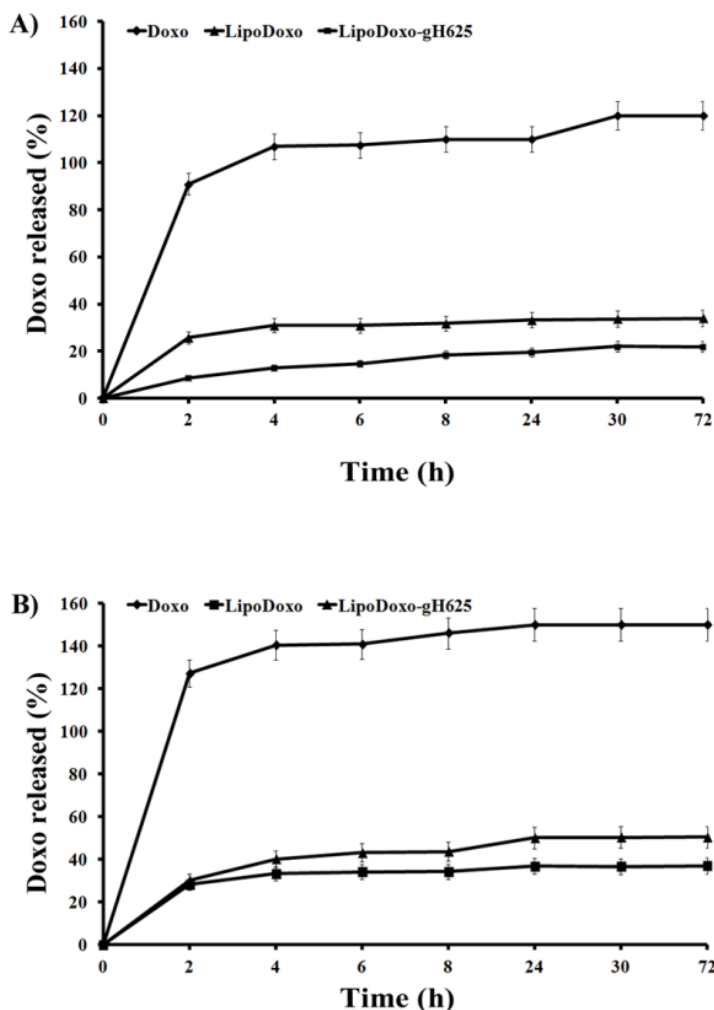


Figure 18. Release profile of doxorubicin from liposomes at 37 °C in HEPES-NaCl buffer (A) and in HEPES-NaCl buffer with 50% FBS (B).

3.6.5 Antitumoral activity of liposomes

The effects of Doxo, empty liposomes and liposomes encapsulating Doxo conjugated or not with gH625 were evaluated on the proliferation of either parental A549 or Doxo-resistant cells (A549 Dx) by MTT assay. Doxo, LipoDoxo and LipoDoxo-gH625 induced a dose-dependent growth inhibition in both cell lines after 72 h, while treatment with Lipo produced no significant cytotoxic effects in both cell lines (Figure 19 A e B). In Table 6, the results are reported as concentrations inhibiting 50% of cell growth (IC_{50}) after 72 h of treatment. The IC_{50} was reached with 0.06 μ M and 0.2 μ M of Doxo (Figure 19 C, Table 7), with 2.5 μ M and 5 μ M of LipoDoxo (Figure 19 A e B, Table 7), with 0.5 μ M and 2.7 μ M of LipoDoxo-gH625 (Figure 19 A e B, Table 7) in A549 and A549 Dx cells, respectively. These data suggested that A549 cells were more sensitive to the treatment with Doxo compared to A549 DX, confirming the drug-resistant phenotype of this cell line. Both cell lines were more responsive to LipoDoxo-gH625 compared to LipoDoxo. These data

Results

suggested that the conjugation of liposomes with gH625 probably facilitated the entry and retention of doxorubicin in both sensitive and drug-resistant tumor cell lines allowing an increase of cell growth inhibition.

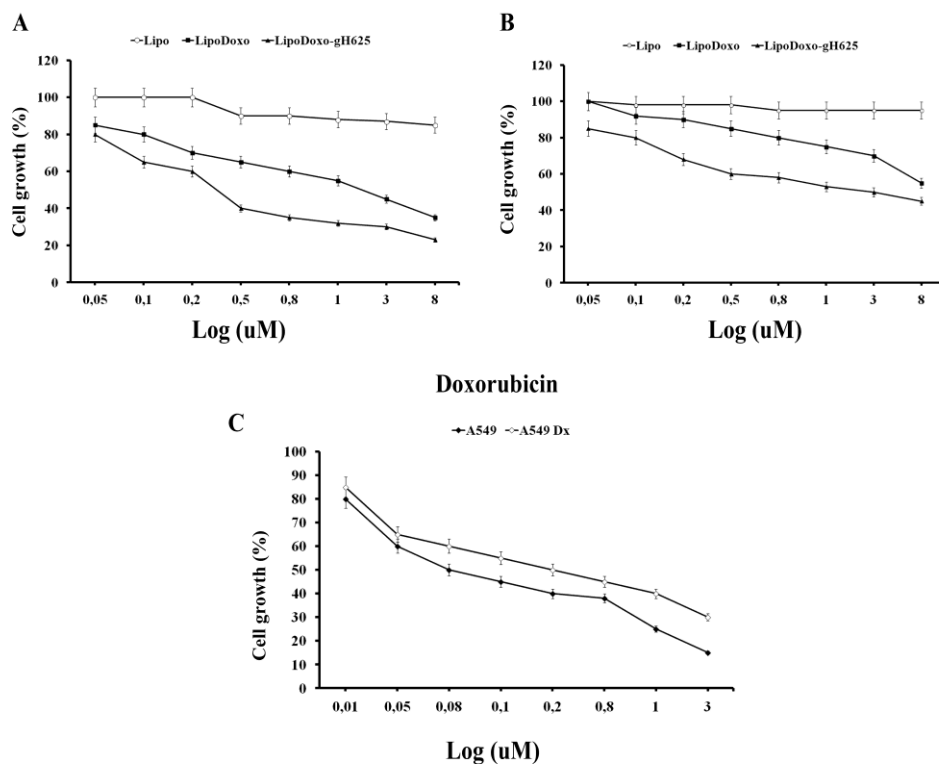


Figure 19. Evaluation of cell growth in lung adenocarcinoma cell line sensitive (A549) and resistant (A549 Dx) to doxorubicin after 72 h of treatment with Lipo, LipoDoxo, LipoDoxo-gH625 (A- B) and doxorubicin (Doxo) (C).

Table 7. IC₅₀ values of the different formulations Concentration inhibiting 50% of cell growth (IC₅₀) reached after 72 h of treatment with Lipo, LipoDoxo, LipoDoxo-gH625, Doxo in A549 and A549 Dx cells. Data are shown as mean ± SD.

Compounds	IC ₅₀ ± SD A549	IC ₅₀ ± SD A549 DX
Lipo	>5.00 μM ± 0.02	>5.00 μM ± 0.02
LipoDoxo	2.50 μM ± 0.02	5.00 μM ± 0.02
LipoDoxo-gH625	0.50 μM ± 0.02	2.70 μM ± 0.04
Doxo	0.06 μM ± 0.03	0.20 μM ± 0.02

3.6.6 FACS analysis in A549 and A549 Dx cell lines: accumulation, evaluation of oxidative stress, evaluation of cell death

The accumulation of doxorubicin, free or encapsulated in liposomes conjugated or not with gH625, was investigated by flow cytometry analysis. A time-dependent accumulation of free and encapsulated Doxo was observed in A549 and A549 Dx cells and the maximal levels were reached after 24 h (Figure 20 and 21). Moreover, LipoDoxo-gH625 induced in both cell lines a greater doxorubicin accumulation than LipoDoxo (Figure 20 and 21). In particular, A549 Dx cells showed an early accumulation of doxorubicin after 3 h of treatment with both liposomal formulations and the accumulation was higher if compared to the one observed in parental A549 cells (Figure 20 and 21). This effect was more evident in resistant cells treated with LipoDoxo-gH625 that induced an increase of about 86.9% of MFI against an increase of about 64.3% of MFI induced in parental cells (Figure 20 and 21, respectively). Moreover, after 24 h we observed a two-fold increase of percentage of MFI in A549 Dx cells treated with LipoDoxo-gH625 if compared to those exposed to LipoDoxo (Figure 20). Similar data were also obtained in parental cells but to a lesser extent (Figure 21). Therefore, these data suggested that the conjugation of liposomes with the viral peptide increased the retention of doxorubicin into the cells supporting the data obtained on the growth inhibition.

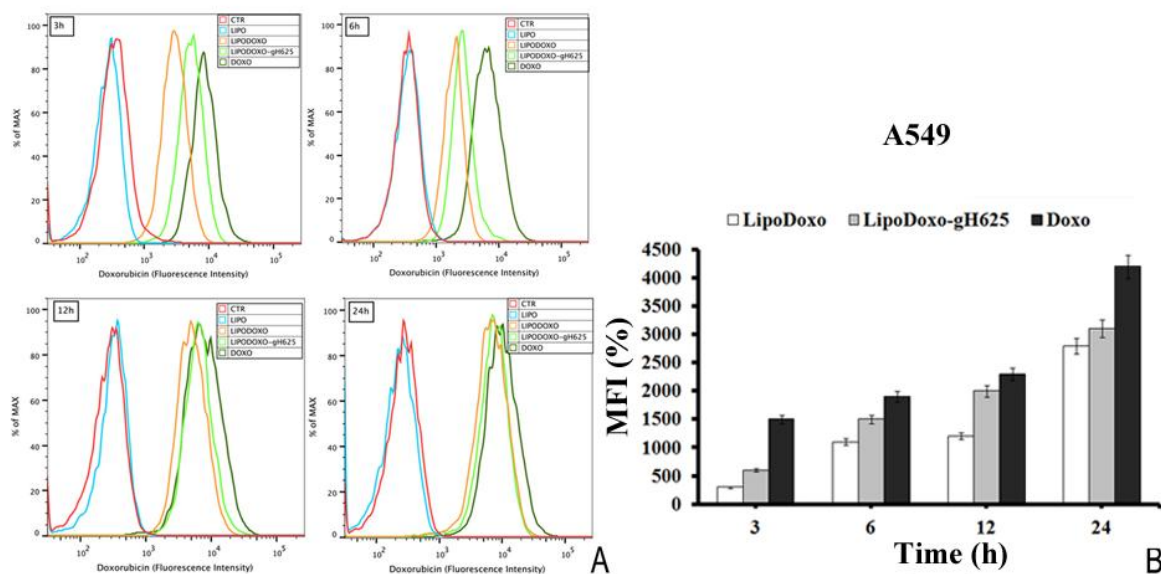


Figure 20. Doxorubicin accumulation in A549 cells after 3, 6, 12 and 24 h of treatment with LipoDoxo, LipoDoxo-gH625 and Doxo. (A) Flow cytometry overlay of Doxo fluorescence intensity. (B) Histogram of Doxo mean fluorescence intensity (% of control). The bars represent means \pm SD of three independent experiments. Asterisks indicate significant difference between LipoDoxo vs LipoDoxo-gH625 (** $P < 0.01$) (* $P < 0.05$)

Results

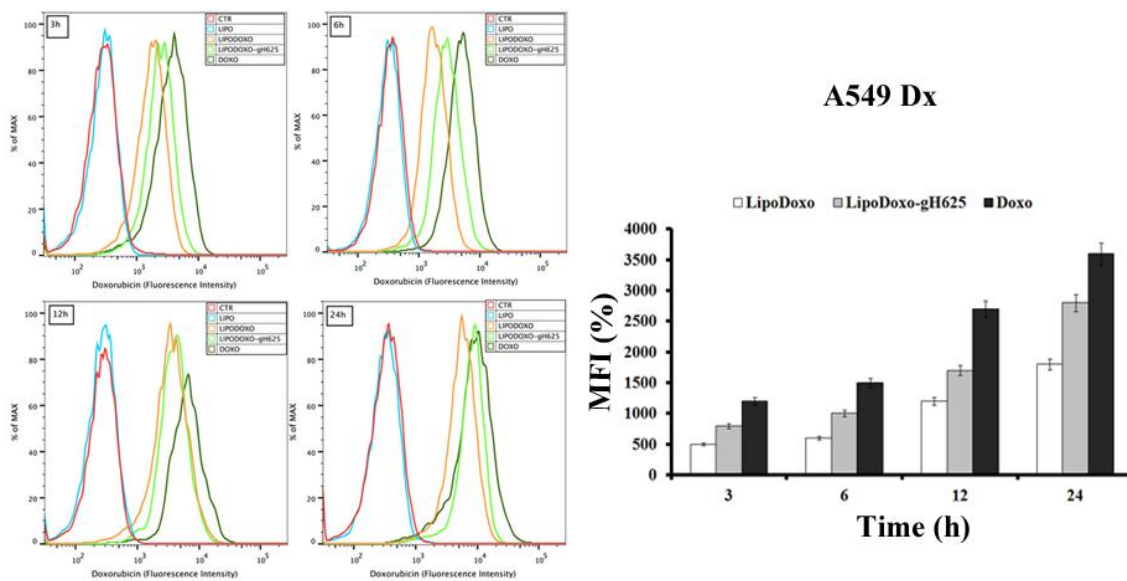


Figure 21. Doxorubicin accumulation in A549 Dx cells after 3, 6, 12 and 24 h of treatment with LipoDoxo, LipoDoxo-gH625 and Doxo. (A) Flow cytometry overlay of Doxo fluorescence intensity. (B) Histogram of Doxo mean fluorescence intensity (% of control). The bars represent means \pm SD of three independent experiments. Asterisks indicate significant difference between LipoDoxo vs LipoDoxo-gH625 (** $P < 0.01$) (* $P < 0.05$).

The accumulation of superoxide anions ($O_2^{\cdot -}$) in A549 e A549 Dx was also studied. In both cell lines free doxorubicin induced a time-dependent accumulation of superoxide anions (Figure 22 and 23) significantly lower compared to that induced by both liposomal formulations. In details, the maximal $O_2^{\cdot -}$ level increase in A549 cell line was detectable after 48 h of treatment with LipoDoxo. LipoDoxo-gH625 induced an accumulation of $O_2^{\cdot -}$ lower than LipoDoxo but this effect was maintained up to the end of treatment (72 h) differently from LipoDoxo (Figures 22). On the other hand, both formulations induced similar effects on A549 Dx cells after 24 h of treatment, but a significant increase of oxidative stress was observed after 72 h of treatment with LipoDoxo-gH625 if compared to the one induced by LipoDoxo (Figure 23). In both cell lines NAC had no effect on the increase of $O_2^{\cdot -}$ levels in contrast to H_2O_2 and acted as a scavenger in combination with H_2O_2 (Figures 22 and 23) decreasing the accumulation of superoxide anions.

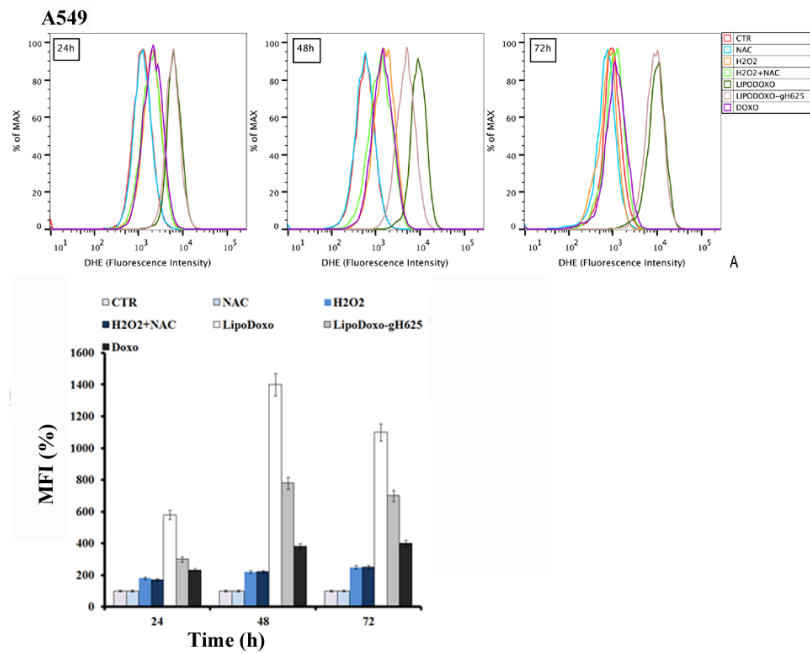


Figure 22. Evaluation of oxidative stress in A549 cells after 24, 48 and 72 h of treatment with LipoDoxo, LipoDoxo-gH625 and Doxo. (A) Flow cytometry overlay of dihydroethidium (DHE) fluorescence intensity. (B) Histogram of DHE mean fluorescence intensity (% of control). The bars represent means \pm SD of three independent experiments. Asterisks indicate significant difference between LipoDoxo vs Doxo and LipoDoxo-gH625 vs Doxo (** $P < 0.01$) (* $P < 0.05$).

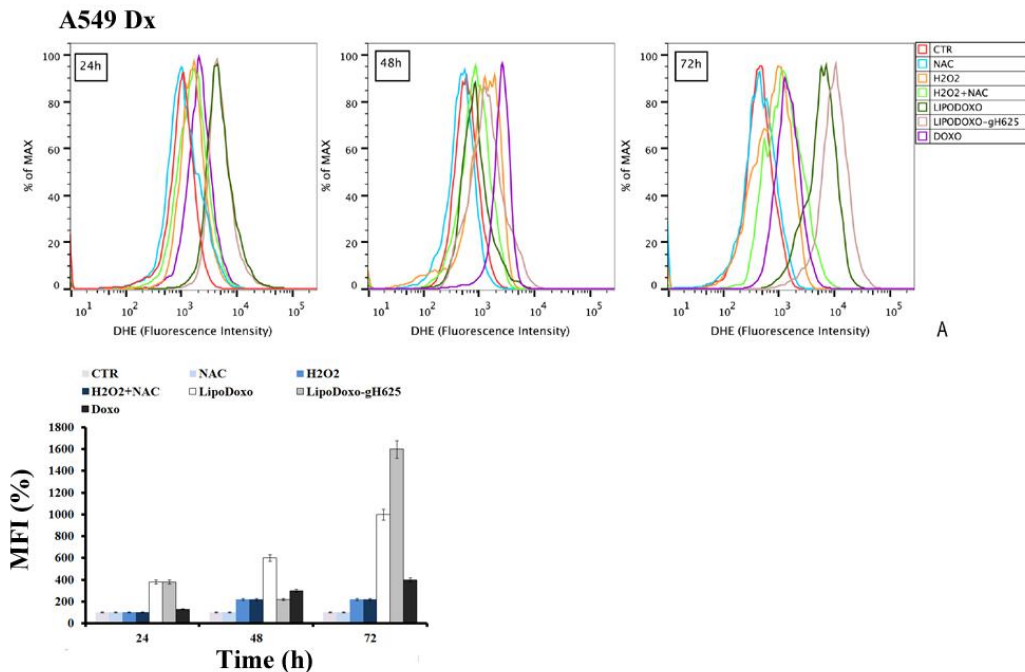


Figure 23. Evaluation of oxidative stress in A549dx cells after 24, 48 and 72 h of treatment with LipoDoxo, LipoDoxo-gH625 and Doxo. (A) Flow cytometry overlay of dihydroethidium (DHE) fluorescence intensity. (B) Histogram of DHE mean fluorescence intensity (% of control). The bars represent means \pm SD of three independent experiments. Asterisks indicate significant difference between LipoDoxo vs Doxo and LipoDoxo-gH625 vs Doxo (** $P < 0.01$).

Results

A further experiment was performed to evaluate the effects of Doxo and liposomal preparation on inducing apoptosis or necrosis. In agreement with the data obtained from the MTT assay, empty liposomes did not induce any significant toxic effects on both cell lines at any time-point tested (Figure 24 and 25).

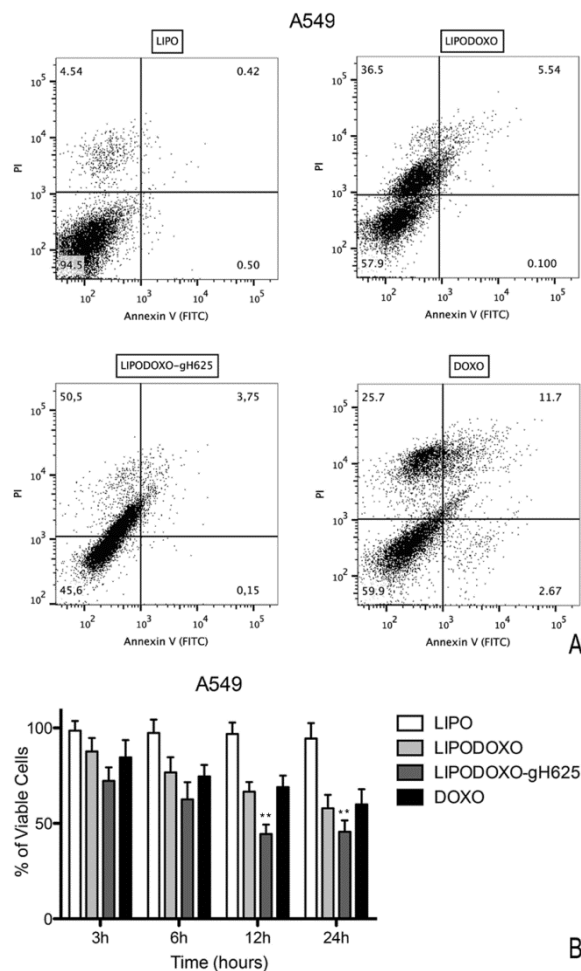


Figure 24. Evaluation of apoptosis in A549 cells by Annexin V/PI assay (flow cytometry) after 48 h of treatment with LipoDoxo, LipoDoxo-gH625 and Doxo. (A) Flow cytometry dot plots. (B) Histogram of data expressed as percentage of viable cells, early/late apoptotic cells and necrotic cells after 3, 6, 12 and 24 h. The bars represent means \pm SD of three independent experiments. Asterisks indicate significant difference between LipoDoxo-gH625 vs Doxo (** $P < 0.01$).

In contrast, LipoDoxo caused an accumulation of about 27.7% necrotic cells in parental A549 and about 21.1% of late apoptotic cells were recorded after 24 h. This effect was more marked when using LipoDoxo-gH625 with about 41.8% of necrotic cells and about 23.3% of apoptotic cells (Figure 24).

On the other hand, LipoDoxo induced late apoptosis in about 5.5% of A549 Dx cells while necrosis was recorded in about 36.5% of A549 Dx cells after 24h of treatment (Figure 25). This effect was potentiated also in doxorubicin-resistant cells by LipoDoxo-gH625 that caused about 3.8% of late apoptosis and about 50.5% of necrosis (Figure 25). Free doxorubicin induced more significant effects on A549 cells than on A549 Dx cells but to a lesser extent. In fact, it caused an accumulation of

about 25.7% and 16.4% of necrotic cells in A549 and A549 Dx cells, respectively (Figure 24 and 25, respectively).

On the basis of these results, it can be suggested that LipoDoxo-gH625 induced more significant effects on cell death in both cell lines, but with different mechanisms. In fact, we have found that the main mechanism by which LipoDoxo caused cell death in parental A549 was necrosis while it caused apoptosis in doxorubicin-resistant counterpart. These effects were potentiated by LipoDoxo-gH625 in both experimental cell models (Figure 24 and 25).

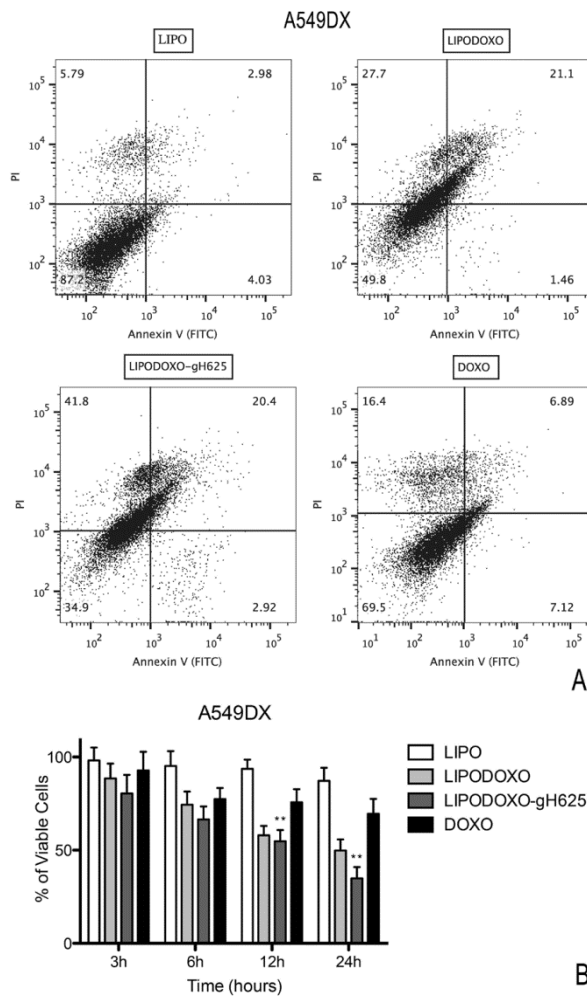


Figure 25. Evaluation of apoptosis in A549dx cells by Annexin V/PI assay (flow cytometry) after 48 h of treatment with LipoDoxo, LipoDoxo-gH625 and Doxo. (A) Flow cytometry dot plots. (B) Histogram of data expressed as percentage of viable cells, early/late apoptotic cells and necrotic cells 3, 6, 12 and 24 h. The bars represent means \pm SD of three independent experiments. Asterisks indicate significant difference between LipoDoxo-gH625 vs Doxo (** $P < 0.01$).

3.6.7 Intracellular distribution of Doxo in A549 and A549 Dx cells

In order to investigate the intracellular distribution of the different formulations, the Doxo fluorescence associated to the cells was evaluated by confocal laser scanning microscopy (CLSM). A549 and A549 Dx were incubated with IC_{50} of free Doxo, LipoDoxo and LipoDoxo-gH625 for 6 and 24 h. After 6 h, free Doxo and LipoDoxo-gH625 entered A549 cells and translocated into the nucleus as indicated by the red fluorescence in the center of the cell body (Figure 26) while LipoDoxo accumulate in the cytoplasm, without entering into the nucleus (Figure 26). In fact, cell nuclei are dark and only few red fluorescent spots, distributed in the cytoplasm, are visible. No fluorescence was observed in A549 treated with empty liposome as expected. On the other hand, in A549 Dx free Doxo was not able to enter into the nucleus accumulating in perinuclear region while CLSM results showed a widespread and intense fluorescence, with intranuclear red spots for cells incubated with LipoDoxo-gH625 (Figure 26). Cells treated with LipoDoxo evidenced a significant lower fluorescence intensity, with visible red spots into the cytoplasm. We observed a time-dependent accumulation of free and encapsulated Doxo and the maximal levels were reached after 24 h in both cell lines (Figure 27). Therefore, the intracellular uptake of liposomes armed with gH625 could contribute to overcome resistance in lung adenocarcinoma cell lines

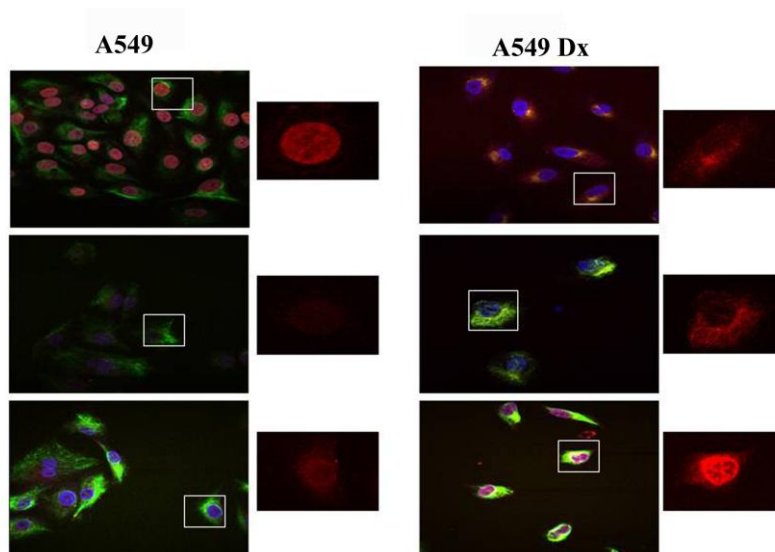


Figure 26. Confocal microscopy images of A549 and A549 Dx cells after 6 h incubation with free Doxo, LipoDoxo, or LipoDoxo-gH625. On the left, merged image (green vimentin; red doxo; blue dapi). On the right, Doxo distribution.

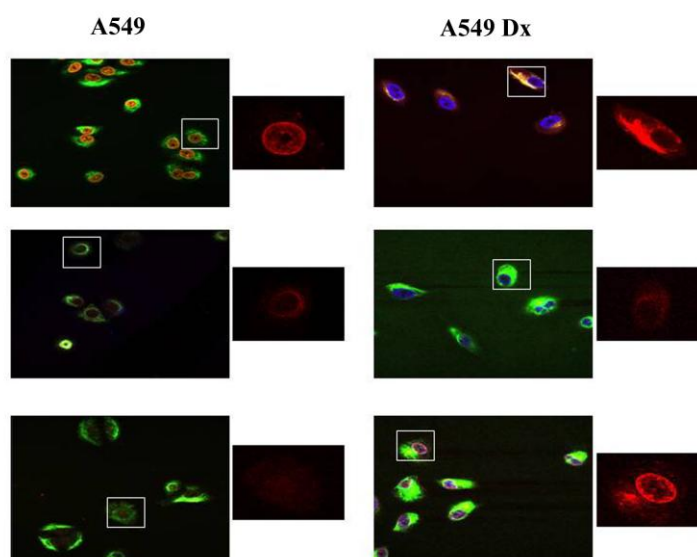


Figure 27. Confocal microscopy images of A549 (A) and A549 Dx (B) cells after 24 h incubation with free Doxo, LipoDoxo, or LipoDoxo-gH625. On the left, merged image (green vimentin; red doxo; blue dapi). On the right, Doxo distribution.

3.7 Design of dual-ligand nanoliposomes using a specific ligand and gH625

Liposomes conjugated to gH625 are promising because the internalization is highly efficient; however, the major obstacle for their use in therapy is the lack of specificity. Thus, in order to develop a novel dual-ligand modified liposomal nanocarrier to overcome the nonselectivity of gH625 liposomes, multifunctional liposomes decorated on their surface with gH625 and the EGBP peptide specifically targeting EGFR, which is overexpressed in several type of cancer cells, were designed. The addition on the liposome surface of targeting ligands to selectively target tumor cells that overexpress a particular cell surface receptor can significantly increase the amount of drug delivery to the target cell relative to free drug or passively targeted liposomes.

3.7.1 Design of peptide conjugated to cholesterol

The design of peptide-targeted liposomes is crucial. The strategy, followed in this study, was to synthesize the targeting peptide conjugated to cholesterol which could be used directly in the preparation of liposomes and then to further decorate the surface of preformed liposomes with gH625. In particular, in our design, the targeting conjugates consist of: 1) a receptor specific peptide (EGBP), 2) a spacer, 3) a lipid molecule to enable insertion into the lipid bilayer of the liposomes. The linker used to conjugate the targeting ligand to cholesterol is fundamental for effective activity. EGBP was conjugated to cholesterol both with a glycine spacer or with a hydrophilic PEG linker. The linker aids in presenting the targeting peptide on the liposomes surface and in facilitating binding to the target receptor.

3.7.2 Preparation and characterization of peptide-targeted liposomes

Liposomes were prepared using: soy-lipids, cholesterol, DSPE-PEG and (C₁₈)₂L-N₃ (57:28:5:10 molar ratio), when necessary Chol-TP1 or Chol-TP2. The components were mixed at specific stoichiometries to achieve precise control over the number of functional ligands on each particle and thus allowing reproducibility in liposome preparation. The liposomes were sized through the extrusion method.

Cytotoxic Doxo was loaded into liposomes using the well-assessed procedures based on an ammonium sulphate gradient [105]. Unloaded Doxo was removed on a Sephadex G50 column. The drug/lipid weight ratio chosen for the loading experiments was 0.1. The drug loading content (DLC) was calculated by UV/Vis measurements at $\lambda=480$ nm and was above 90% of the total.

The resulting drug loaded liposomes were then efficiently modified with the gH625-Pra peptide. In particular, the coupling of gH625 on the surface of liposomes was performed by click chemistry and the expected gH625-functionalized liposomes were obtained with a yield higher than 90% after 12 h at room temperature.

Dynamic light scattering (DLS) data on liposomes preparations (Table 8) showed that the liposome functionalization with gH625 had an average hydrodynamic diameter of 143.90 nm and the presence of EGBP does not influence the size of the liposomes: 148.62 nm for LipoDoxo-gH625-TP1 and 144.52 nm for LipoDoxo-gH625-TP2. The polydispersity index remains stable in all the preparations (Table 8). The values are below 0.2, indicating that the distribution of the liposome size remained rather narrow and there are no signs of aggregation. These parameters should favour both the effective extravasation of liposomes and their longer retention in tumour tissues.

The analysis of the zeta potential shows a change between LipoDoxo-gH625 compared to LipoDoxo-gH625-TP1/TP2, which indicates a change in the surface of the liposomes upon functionalization with the peptide.

Table 8. Zeta potential, size, expressed as z-average, as measured by DSL and polydispersity index (PDI). Data are expressed as means \pm standard deviation (SD) of three separate experiments for each of two batch formulations, with at least 13 measurements for each.

Liposomes	Average Size (nm)	PDI	Zeta potential (mV)
LipoDoxo-gH625	143.90 \pm 0.64	0.14 \pm 0.02	9.43 \pm 1.60
LipoDoxo-gH625-TP1	148.62 \pm 2.12	0.15 \pm 0.03	4.41 \pm 0.63
LipoDoxo-gH625-TP2	144.52 \pm 1.60	0.11 \pm 0.05	3.82 \pm 0.54

Moreover, the analysis of the tryptophan fluorescence spectra recorded on the liposomal suspension on Lipo-gH625, Lipo-gH625-TP1 and Lipo-gH625-TP2 showed an increase in fluorescence emission in the last two preparation, due to the presence of tryptophan also in the sequence of EGBP. In particular the emission is greater for LipoDoxo-gH625-TP1, indicating that the peptide is more exposed on the surface (Figure 28).

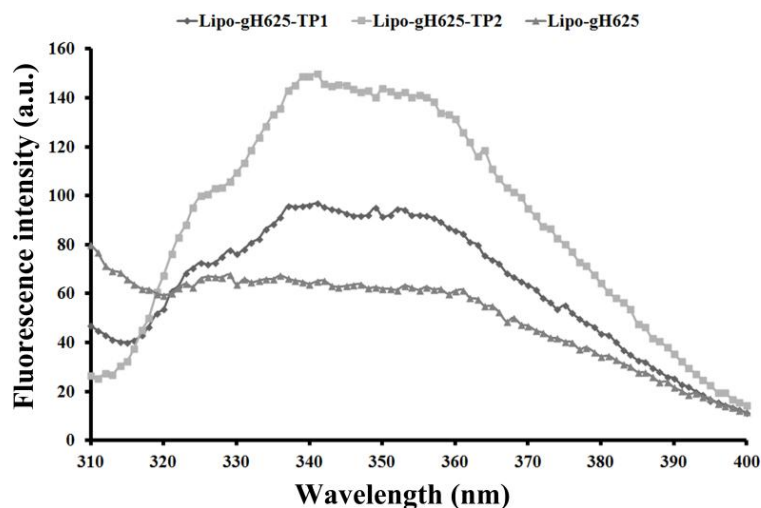


Figure 28. Fluorescence spectra of tryptophan residue at 25°C and 1×10^{-5} M peptide concentrations. The spectrum was excited at 280 nm and recorded between 310 and 400 nm.

3.7.3 Release kinetics of Doxo

The release of Doxo was carried out in HEPES-NaCl buffer or HEPES-NaCl buffer with 50% FBS and the results are presented in Figure 29. Free Doxo was used as control and its release rate was nearly 100% in 2 h, which means that the release of Doxo from dialysis membrane to buffer solution is not a restricting factor and the release of Doxo from the liposomes is the only rate limiting step. There were no pronounced differences in Doxo release (Figure 29) from LipoDoxo-gH625, LipoDoxo-gH625-TP1 and LipoDoxo-gH625-TP2 at each time point, indicating that the decoration of the surface of the liposomes with both peptides did not substantially change the release kinetics of liposomes. The Doxo release from liposomes is less than 30% within 72 h, indicating their good stability.

Results

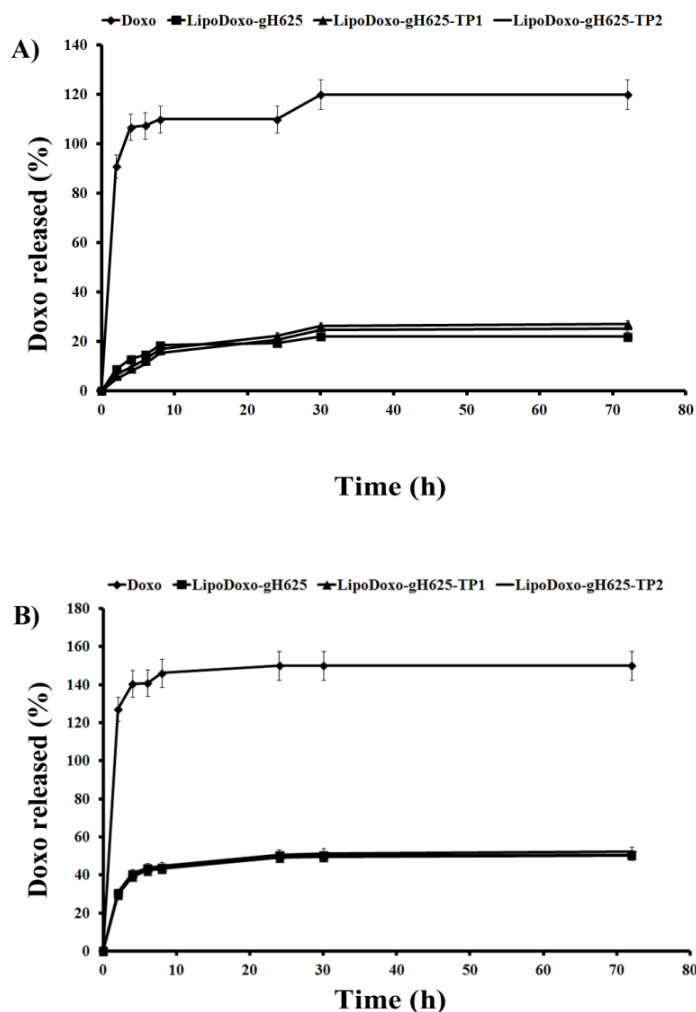


Figure 29. Release profile of doxorubicin from liposomes at 37 °C in HEPES-NaCl buffer (A) and in HEPES-NaCl buffer with 50% FBS (B).

3.7.4 Facs analysis: accumulation

The accumulation of doxorubicin, free or encapsulated in liposomes conjugated with gH625 or in liposomes conjugated with gH625 and EGBP, was investigated by flow cytometry analysis. A time-dependent accumulation of free and encapsulated Doxo was observed in KB cells. We used two types of KB cells, which overexpress the EGFR: one type with 35000 EGFR/cell and another with 300000 EGFR/cell. In particular, we observed a greater accumulation of doxorubicin when using LipoDoxo-gH625-TP2 compared to the other two preparations (Figure 30). Therefore, these data suggested that the conjugation of liposomes with the homing peptide increased the retention of doxorubicin into the cells, that overexpress EGF receptor. Further *in vitro* studies are now being carried out to better unravel mechanism of the activity of these liposomal preparation.

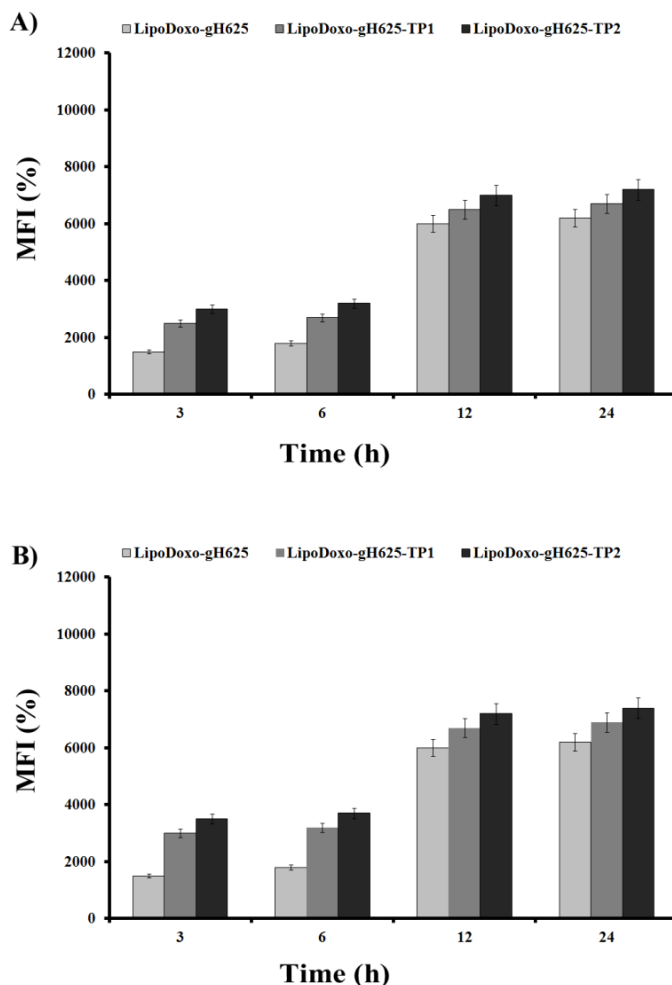


Figure 30. Doxorubicin accumulation in KB cells with 35000 EGFR/cell (A) and with 30000 EGFR/cell (B), after 3, 6, 12 and 24 h of treatment with LipoDoxo-gH625 LipoDoxo-gH625-TP1 and LipoDoxo-gH625-TP2.

3.8 Supermagnetic iron oxide nanoparticles coated with gH625

Superparamagnetic iron oxide nanoparticles (SPIONs) are extensively studied as platforms for numerous biomedical applications including cancer therapy and diagnosis. They can be coated with a biocompatible polymer to enhance stability and stealthiness properties; but in order to achieve high intracellular drug concentrations, nanoparticles have to release their drug load inside tumor cells. In this study SPIONs were functionalized with gH625 to improve drug delivery into cancer cells.

3.8.1 Synthesis of initial SPIONs

The initial suspension of SPIONs was prepared as described previously [95]. The nanoparticles were precipitated from a basic medium containing iron(II) and iron(III) salts. The material obtained is known to consist of two iron oxide phases, namely, magnetite (Fe_3O_4) (particle core) and maghemite ($\gamma\text{-Fe}_2\text{O}_3$) (superficial layers) [112].

Results

The treatment of nanoparticles with iron nitrate and nitric acid ensures the enrichment of the superficial maghemite layer and prevents further uncontrollable oxidation. To confirm the chemical composition of the initial material, we performed FTIR analysis. The FTIR spectrum of the freeze-dried initial SPIONs (Figure 31 A) confirms the presence of the two iron oxide phases maghemite and magnetite [113]. In agreement with literature, the band at 630 cm^{-1} is assigned to maghemite, while the band at 590 cm^{-1} corresponds to both magnetite and maghemite vibrations [114]. The strong narrow band at 1380 cm^{-1} is due to traces of NO_3^- anions on the surface of SPIONs. There is also a wide band at 3400 cm^{-1} attributed to surface OH groups of SPIONs. These data were in agreement with Raman microspectroscopy analysis described previously [112] that also indicated that magnetite and maghemite were the two major oxide species, at a relative fraction of ca. 60 and 40%, respectively. The morphology and size of initial SPIONs were analyzed by means of transmission electron microscopy (Figure 31 C) and DLS. The nanoparticles appear to have a uniform roughly spherical morphology, with an average size of ca. 10.02 nm. This value and the DLS data for the aqueous suspension of SPIONs (average diameter $70.02 \pm 1.05\text{ nm}$) are similar to those reported in the literature [115].

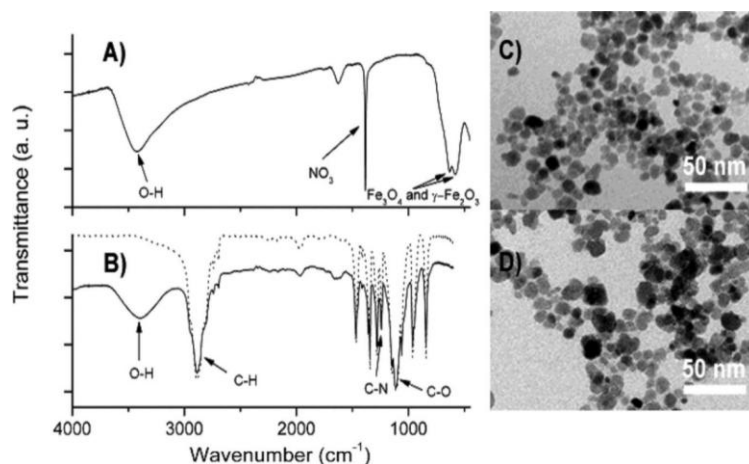
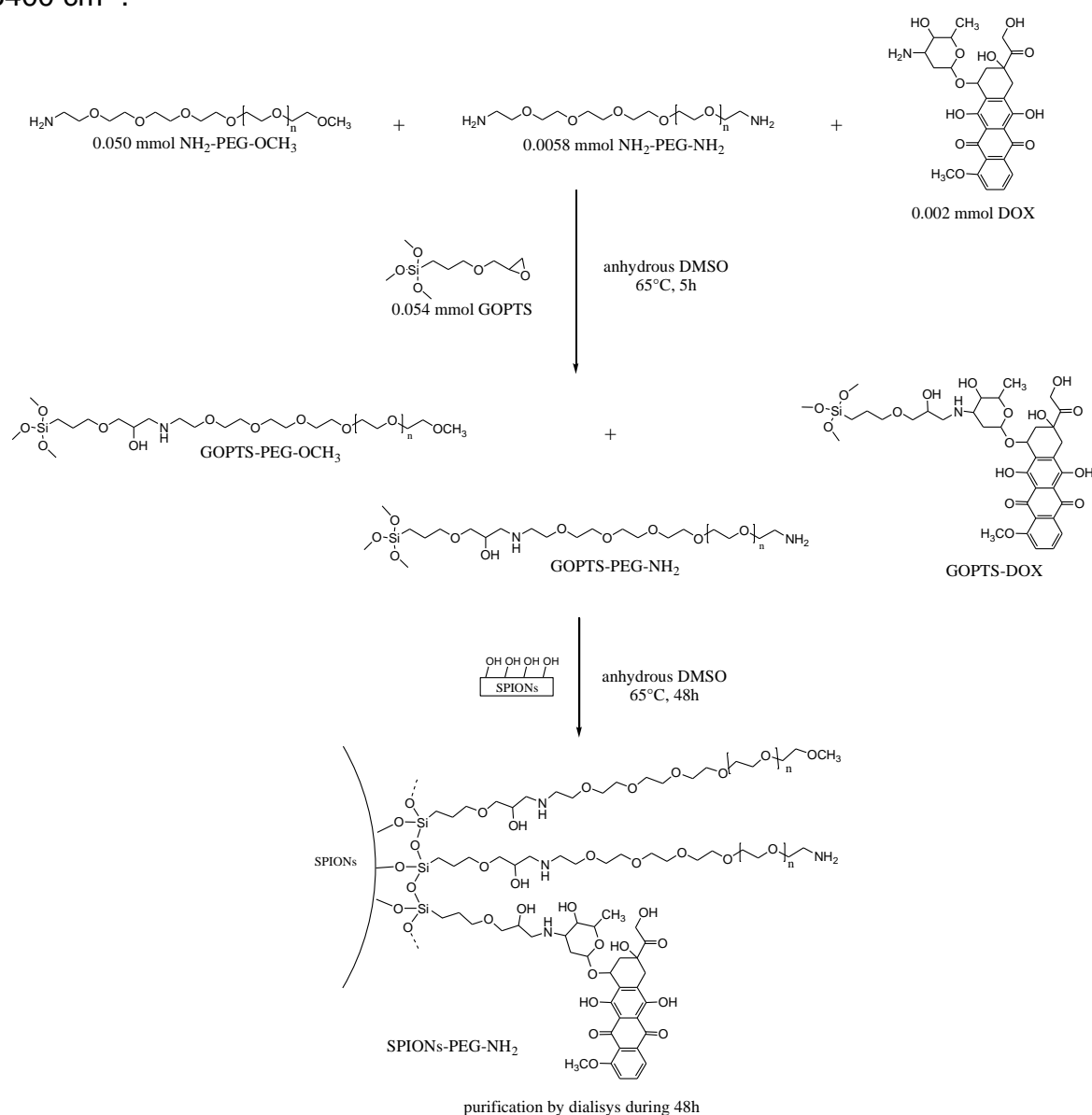


Figure 31. Typical FTIR spectra of freeze-dried samples of initial SPIONs (A) and SPIONs-DOX-PEG (B) (the dashed line is a spectrum of initial methoxy poly(ethylene glycol) amine). TEM images of initial SPIONs (C) and SPIONs-DOX-PEG (D).

3.8.2 SPIONs modified with PEG and/or Doxo

The surface modification of nanoparticles was performed according to a protocol developed in the Prof. Chourpa's laboratory involving the reaction between amine and epoxide functional groups. The use of this type of chemistry offers sufficient reactivity at room temperature. In addition, compared to adsorption, the covalent linkage of the drug to the carrier is more stable and will require a specific release mechanism for drug delivery, for instance, enzymatic cleavage. The synthesis procedure we used to generate SPIONs modified with both Doxo and PEG (SPIONs-Doxo-PEG) comprises three stages (Figure 32): Doxo, $\text{NH}_2\text{-PEG-OCH}_3$, and $\text{NH}_2\text{-PEG-NH}_2$ were coupled to epoxysilane to form silylated conjugates (step I e II). The reaction consists in the opening of the epoxide ring by the amino group to form an amine linkage. These silylated conjugates were bonded to the SPIONs surface by reaction of the silanol groups with the hydroxyl groups of iron oxide reaction between epoxy silane and doxorubicin, and condensation of the silanized polymer and drug on

the surface of SPIONs. To avoid a lengthy separation process and purification of the intermediates, all synthetic stages were combined into a one pot synthesis procedure. This method allows easy and efficient preparation of PEG- and Doxo-modified SPIONs. Several experiments were performed to set up the best ratio between $\text{NH}_2\text{-PEG-OCH}_3$ and $\text{NH}_2\text{-PEG-NH}_2$; eventually a ratio of 1:4 was chosen. Freeze-dried samples of SPIONs-Doxo-PEG contained ca. 60 mg/L (w/w) of iron as determined by atomic adsorption spectroscopy. Since the concentration of iron in the sample is lower than the typical sensitivity threshold in IR spectroscopy ($\sim 5\%$ (w/w)), the iron oxide bands were no more detectable in the FTIR spectra of modified nanoparticles (Figure 31 B). These IR spectra showed the major bands characteristic of PEG at 1113 (C-O), 1242 (C-N), and 2888 (CH) cm^{-1} , as well as a band of OH at 3400 cm^{-1} .



Step I e II

Figure 32. Schematic representation of surface functionalization of superparamagnetic iron oxide nanoparticles (SPIONs) with Doxo and PEG.

Results

To further investigate the effect of the organic coating on the nanoparticles, we performed DLS measurements. After functionalization, the hydrodynamic size of SPION-Doxo-PEG dispersed in aqueous medium at pH 7 was 65.05 nm (Figure 33). These values are close to those reported in literature for PEG-modified SPIONs [95,116]. The colloidal stability of functionalized SPIONs was studied by means of zeta potential and hydrodynamic diameter (D_H) measurements versus pH. For the initial SPIONs, the colloidal stability is strongly pH dependent because it is mainly due to electrostatic repulsion between particles. It is widely admitted that at high values of zeta potential (over 30 mV, positive or negative) the electrostatic interactions between particles are strong enough for electrostatic stability, while at lower values of zeta potential, particles can flocculate, resulting in increased D_H . Initial iron oxide nanoparticles typically tend to flocculate near their isoelectric point, [95] i.e., between $5 < \text{pH} < 9$. Figure 33 shows plots of both zeta potential (left axis) and mean hydrodynamic diameter (right axis) of SPION-Doxo-PEG in aqueous dispersion at different pH between 3 and 11. Unlike for unfunctionalized SPIONs, the D_H of the functionalized particles remained nearly constant over the entire pH range, with no sign of aggregation in spite of the low values of the zeta potential. Such a behavior is typical of particles coated with the neutral polymer PEG, and it highlights that their stabilization is via steric hindrance rather than electrostatic repulsion.

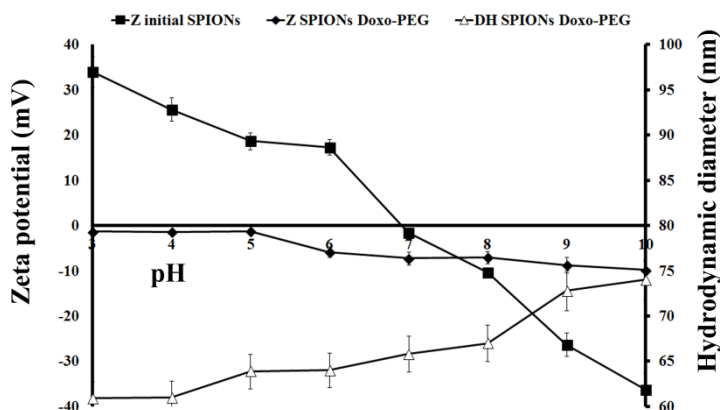


Figure 33. Variation of zeta potential and hydrodynamic diameter versus pH of SPIONs and functionalized SPIONs.

3.8.3 Functionalization of SPIONs with gH625

The carboxy terminal end of the peptide gH625 was activated by EDC and NHS, as described in Materials and Methods. Functionalization of SPIONs was performed in DMSO (Figure 34) in presence of Tween and the obtained peptide-SPIONs were purified from the un-conjugated NPs by dialysis.

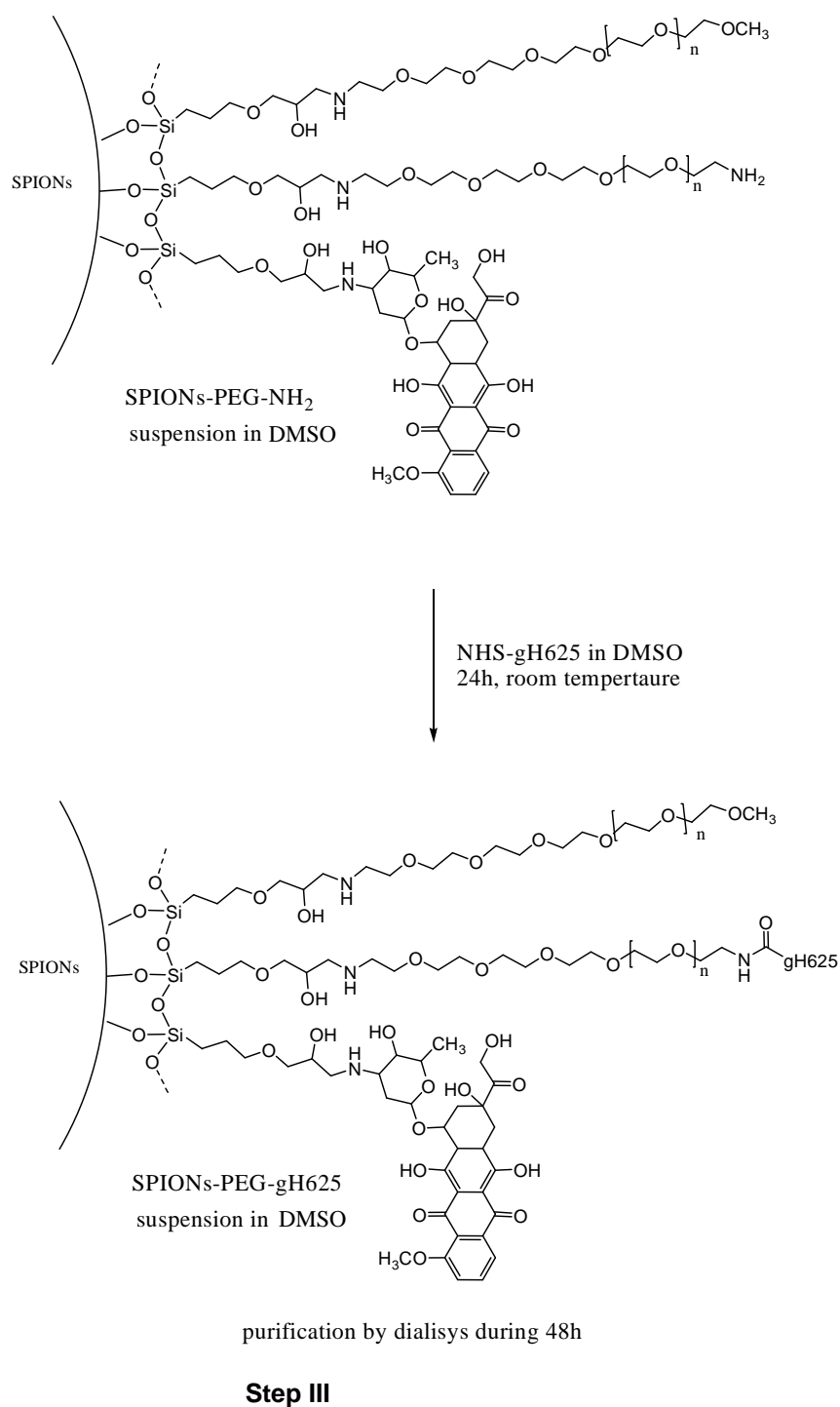


Figure 34. Schematic representation of functionalization of SPIONs with gH625

3.8.4 Characterization of SPIONs functionalized with gH625

As previously reported [117], gH625 adopts a random coil conformation in aqueous media, but forms a helix in membrane-mimetic environments. To verify the secondary structure of the peptide bound to the SPIONs circular dichroism (CD)

Results

experiments were performed. CD spectra in several percentages of trifluoroethanol (TFE, allowing the solution to mimic the environment of the membrane) show that gH625 at a concentration of 8 μM adopts an α helix (Figure 35). This result confirmed that gH625 retains its helical structure when bound to the nanoparticle surface, suggesting that the secondary structure of the peptide was not disturbed by coupling to SPIONs.

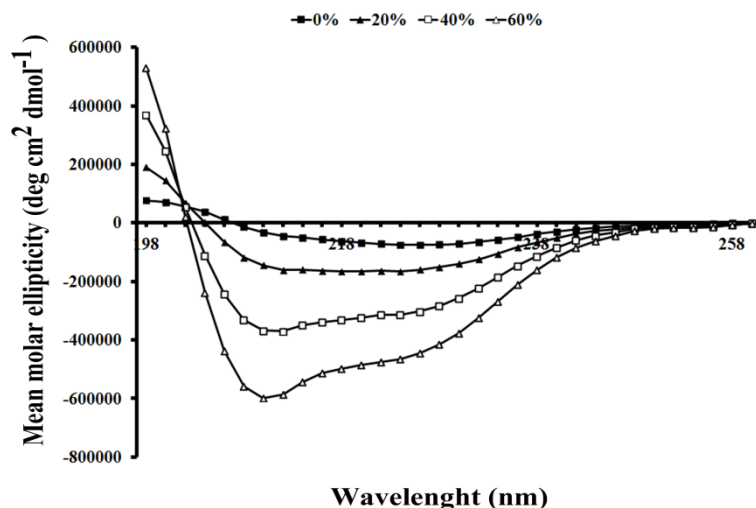


Figure 35. Circular dichroism of SPIONs functionalized with gH625

3.9 Surface decoration of Polystyrene NPs with gH625: method to escape endo-lysosomal compartment and reduce nanoparticles toxicity

Many therapeutic drugs are excluded from entering the brain, due to their lack of transport through the blood-brain-barrier (BBB) [118]. The BBB is formed by the endothelial cells of brain capillaries, and restricts the exchange of most endogenous molecules between the blood and the brain; the very tight regulation of brain homeostasis imposed by the BBB prohibits many therapeutic compounds from entering brain tissues [119]. The development of new strategies for enhancing drug delivery to the brain is of great importance in diagnostics and therapeutics of central nervous diseases. To overcome this problem, it was hypothesized that brain delivery of polystyrene nanoparticles conjugated with gH625 should be efficiently enhanced. gH625 was coupled to the surface of fluorescent aminated polystyrene nanoparticles (NPs) via a covalent binding procedure and NP uptake mechanism and permeation across an *in vitro* BBB model were studied.

Clear understanding of the detailed uptake mechanism of gH625-functionalized polystyrene nanoparticles in mouse brain endothelial cells, from their interaction with the cell membrane to their intracellular final destination was the principal aim of this part of the thesis in order to elucidate how gH625 affects the behavior of the nanoparticles and their cytotoxic effect on an *in vitro* model of the BBB. This novel theranostic platform may be broadly applicable for the development of new therapeutics with increased brain penetration.

3.9.1 Interaction of gH625-NPs with the cell membrane

gH625 was synthesized with an acetyl protecting group at the N terminus and with 3 glycines at the C-terminus for this study. 35% of the functional group present on the nanoparticles were functionalized with gH625; this percentage of functionalization was previously shown to be sufficient for enhanced internalization. gH625 enhances nanoparticle cellular uptake at early incubation times. In fact, we observed a 2-fold increment of NP internalization within endothelial cells in presence of gH625 compared to blank NPs already after 10 minute incubation [120]. Moreover, accordingly to cellular uptake kinetics, scanning electron microscopy (SEM) analyzes indicated a better and more rapid adsorption of gH625-NPs on cell membrane, compared to blank-NPs after 10 min incubation, probably due to the membrane tropism of the peptide and, thus, an enhancement of gH625-NPs internalization [120]. To better elucidate the interaction of gH625-NPs with the cell membrane, coupling of confocal laser scanning microscopy (CLSM) images with atomic force microscopy (AFM) was carried out. This analysis is very instructive on assessing the status of the NPs at the cell membrane [121]. Indeed, by matching topographical features of cell membrane with fluorescence signal, we observed that, after 10 minute incubation, there was a partial co-localization between NP fluorescence and cell membrane humps, suggesting that gH625-NPs are both on cell membrane and inside the cytoplasm (Figure 36 B). Moreover, NP deposition on the cell membrane was examined at different time points upon incubation with NPs. As shown by the chart in Figure 36 E, an overall increment of cell membrane roughness is observed upon 10 minute incubation with gH625-NPs compared to control cells (non-treated with NPs) and cells incubated with blank NPs. Conversely, no differences in cell membrane roughness are present among all samples after 24 h incubation, likely due to NP cellular uptake. These observations further confirm the higher interaction of gH625-NPs with the cell membrane compared to blank NPs, in agreement with previously reported results [120]. gH625 assumes in membrane mimetic environments a helical conformation that makes it particularly affine for lipids [122]. Indeed, we previously demonstrated its capability to hemi-fuse liposomes and its tropism for cholesterol enriched membranes *in vitro* [122]. Therefore, we hypothesized that a similar mechanism could be used by gH625-NPs to bind the cell membrane and, thus, for their translocation within the cell. To address this issue, cells were treated with methyl beta cyclodextrin (M β CD) in order to deplete cholesterol from the cell membrane and investigate the effect of this treatment on nanoparticle cellular uptake. Results, reported in Figure 37 A-B, show no effects on intracellular distribution of blank NPs after 30 minute treatment with 10 mM M β CD. On the other hand, gH625-NP uptake is inhibited by cholesterol depletion (Figure 37 C and D). In particular, we observed a reduction of about 40% in cellular uptake for gH625-NPs after 30 minute of M β CD treatment compared to non-treated cells (Figure 37 E). Taken altogether these data suggest that the interaction with the cell membrane lipids plays a pivotal role in controlling the mechanism of gH625-NPs uptake.

Results

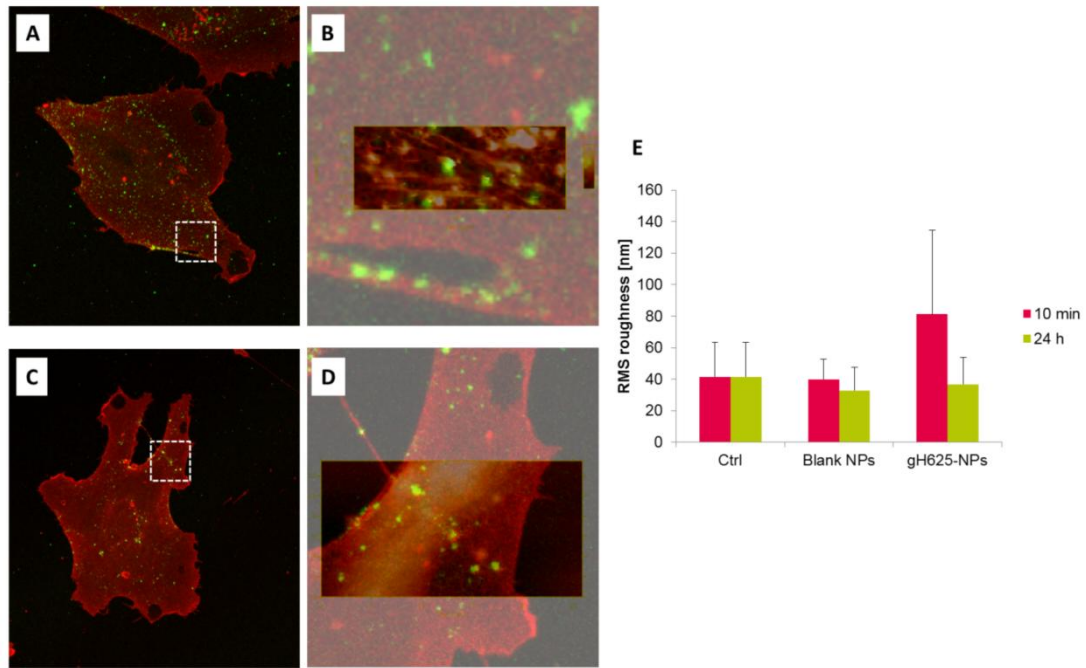


Figure 36. AFM/CLSM coupling analysis. CLSM z-sectioning maximum projection of bEnd.3 cells incubated for 10 min at 37°C with gH625-NPs (a) and blank NPs (c). Red fluorescence: cell membrane staining with WGA; green fluorescence: NPs; the dashed squares indicate the zoomed areas in b (scan area is about $3 \times 8 \mu\text{m}$) and d (scan area is about $14 \times 25 \mu\text{m}$). Transparency image merge of CLSM image and AFM scanning of cell membrane (b and d).

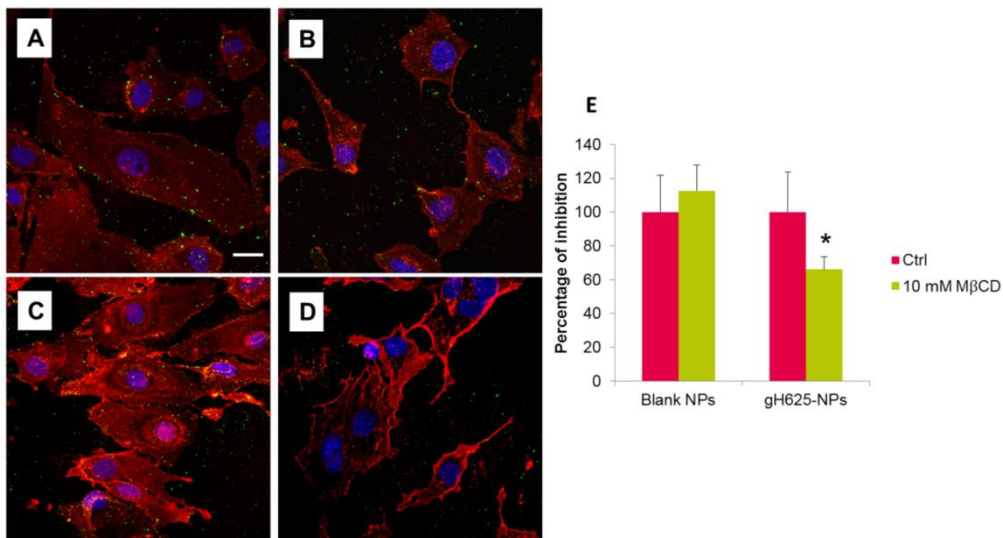


Figure 37. Blank and gH625-NP cellular uptake upon cholesterol depletion treatment. Confocal microscope images of bEnd.3 cells incubated with blank (a and b) and gH625- (c and d) NPs; b and d represent cells treated with 10 mM MβCD. Cell membranes are stained with red fluorescent WGA, cell nuclei are stained with DAPI and green spots are fluorescent NPs. Scale bar 20 μm . Quantification of NP uptake inhibition (e). Data are reported as mean \pm standard deviation. $p < 0.05$ is considered statistically significant (*).

3.9.2 gH625-NP intracellular behavior

In order to confirm that the presence of gH625 affects the intracellular behavior of NPs by-passing the endo-lysosomal pathway, cell membrane was forced crossing by shooting NPs with gene gun method [101].

As previously reported, [101,120] once internalized by cells, blank NPs show prevalently a pearl-on-a-string behavior, with a little percentage of random walk trajectories (Figure 38 A). On the contrary, if forced to enter cell by using gene gun method, shot blank NPs show almost exclusively random walk trajectories, suggesting very low NP confinement inside endo-lysosomal compartments (Figure 38 B) [101]. In the case of gH625-NPs, no significant changes in intracellular trajectories were observed upon delivery of NPs using gene gun method (Figure 38 B). These data strongly suggest that gH625 allows NPs to by-pass/escape the endo-lysosomal pathway.

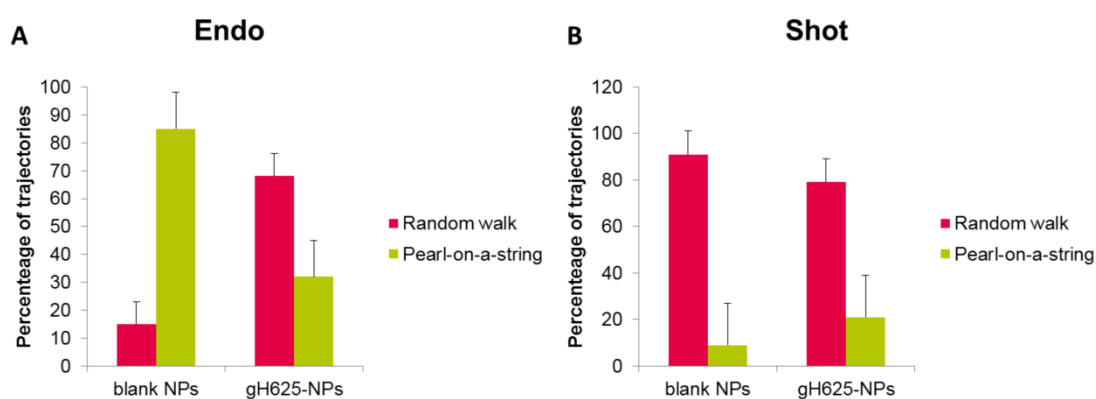


Figure 38. Intracellular trajectories of endocytosed (endo) (a) and shot (b) NPs analyzed by MPT technique. The number of analyzed trajectories was 226 for endo blank NPs, 216 for shot blank NPs, 38 for endo gH625-NPs and 101 for shot gH625-NPs.

3.9.3 gH625-NP intracellular distribution

To further investigate the fate of gH625-NPs, nanoparticles intracellular distribution was followed by co-localization experiments within endocytic compartments, namely endosomes and lysosomes. After 10 minute incubation, both NPs were able to enter cells and partially co-localize with Rab5 protein, a marker of early endosomes, thus indicating that both NPs use vesicular structures to enter cells (Figure 39).

In particular, at earlier incubation time, no significant differences of co-localization percentages were observed between blank and gH625-NPs. By increasing the incubation time, the percentage of co-localization for blank NPs increased up to 30 min and then decreased becoming about 4% at 2 h. Conversely, for gH625-NPs the percentage of co-localization with Rab5 protein remained almost constant with time.

Results

Already after 2 h incubation, both blank and gH625-NPs partially co-localize with lysosomes (Figure 40). However, the percentage of co-localization of blank NPs increased over time, reaching almost 80%. On the other hand, for gH625-NPs, the percentage of co-localization was lower than blank NPs and increased up to 6 h remaining almost constant after 24 h incubation. These observations suggested a partial lysosomal escape of gH625-NPs.

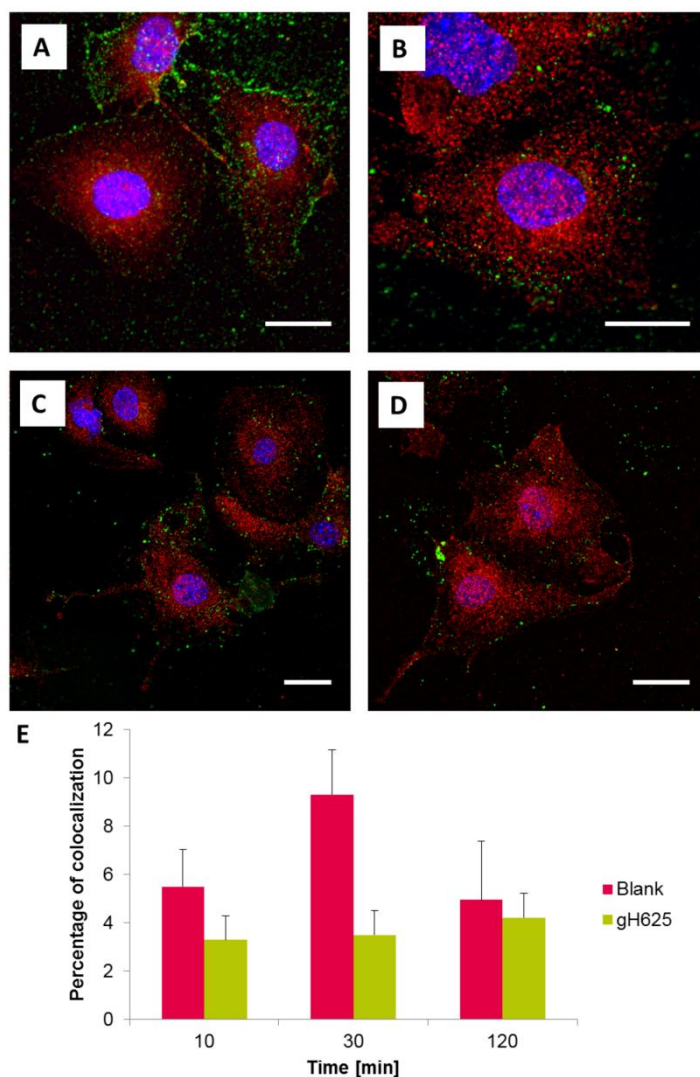


Figure 39. Co-localization of blank and gH625-NPs with endosomes over time. Confocal images of blank (a and c) and gH625-NPs (b and d) upon 10 min (a and c) and 1 h (b and d) of incubation. Scale bar 20 μ m. Quantification of colocalization by ImageJ analysis software (e).

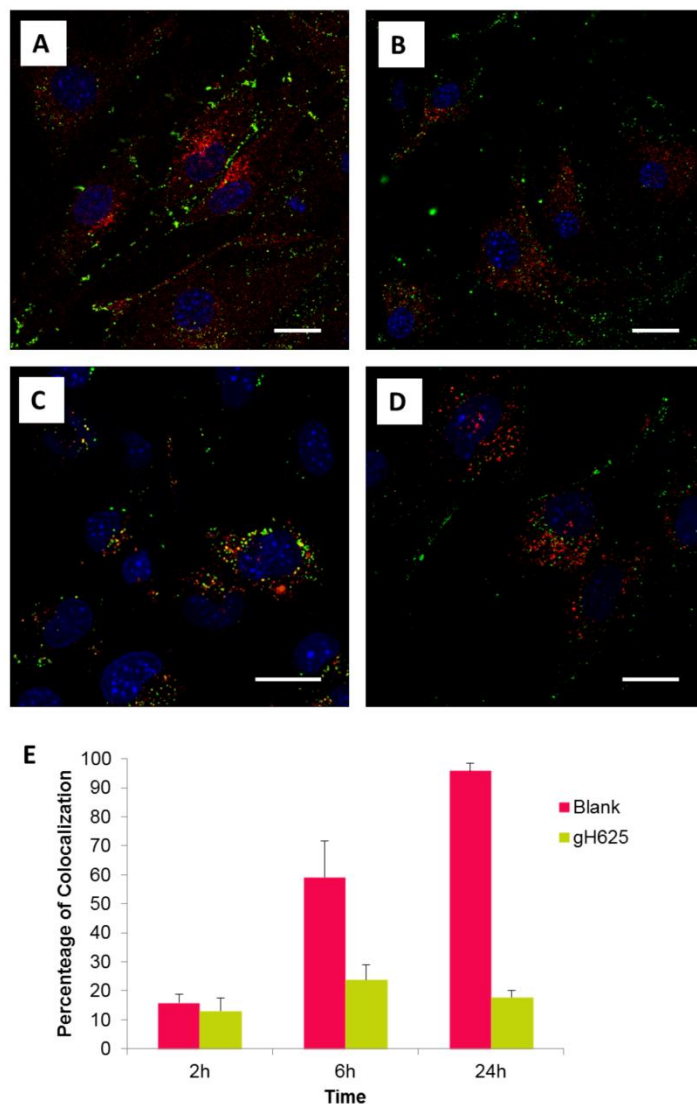


Figure 40. Co-localization of blank and gH625-NPs with lysosomes over time. Confocal images of blank (a and c) and gH625-NPs (b and d) upon 2 h (a and c) and 24 h (b and d) of incubation. Scale bar 20 μ m. Quantification of colocalization by ImageJ analysis software (e).

3.9.4 gH625-NP cytotoxicity

The capability to by-pass the lysosomal compartment can offer great advantages in terms of efficacy of nanocarriers to overcome biological barriers [120] and of reduced nanotoxicity [101]. Recent works reported on the cytotoxic effects of positively charged polystyrene NPs as a consequence of their localization in lysosomes and interaction with lysosomal components [123,124]. Therefore, we tested the effect of gH625 on cytotoxicity of positively charged polystyrene nanoparticles and compared results to cells treated with blank NPs delivered by “classical” endocytosis and gene gun method, as positive and negative controls, respectively. The used particle concentration of 50 μ g/ml, reported in literature as cytotoxic [123] and corresponding to 6×10^4 NPs/cell for 100 nm NPs.

Results

Data indicated a reduction of viability of cells treated with positively charged NPs, as expected (Figure 41). On the other hand, after NP shooting, no cytotoxic effect was observed, clearly indicating that the cytotoxicity was strongly dependent on NP intracellular localization. More interestingly, after incubation with gH625-NPs, a recovery of cell viability was observed, compared to endocytosed blank NPs. However, the reduction in cytotoxicity of gH625-NPs was less evident than shot blank NPs likely due to their partial co-localization with lysosomes as shown above.

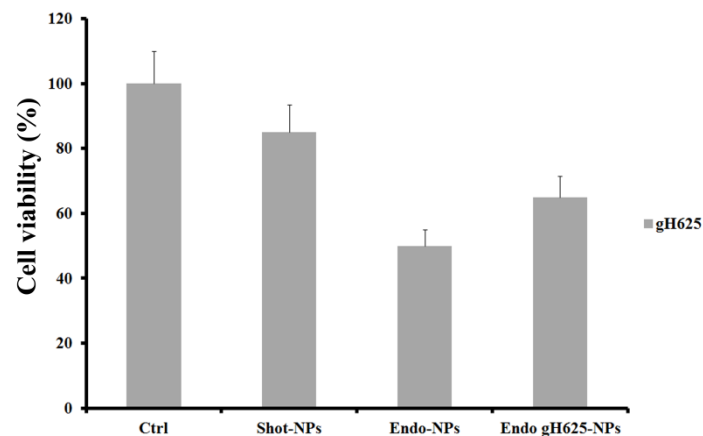


Figure 40. Cytotoxicity of gH625-NPs compared to non-treated control cells (*ctrl*) and cells incubated for 24 h with blank NPs delivered by “classical” endocytosis (*endo-NPs*) and by gene gun method (*shot-NPs*).

4. Discussion and conclusion

The goal of this PhD project was to design a toolbox to easily functionalize with different delivery, targeting and drug moieties which could be adapted to several cancer pathologies. The delivery tool should transport the drug to the target cells not only with high efficacy, but also with minimal toxicity against normal cells and immune response avoiding its degradation and entrapment in endosomes. In fact, one of the major challenges in cancer therapy, is the selective delivery of the chemotherapeutic agents to specific tumor cells and tissues.

The first part of this thesis was focused on the design of the strategies for the achievement of a toolbox easily to functionalize and on its obtainment. The second phase was the physico-chemical characterization of each selected nanosystem with particular attention to the size, zeta potential and drug loading and release. The third phase was to analyze *in vitro* the subcellular fate of the vectorized drug and the effect on the cells.

Several nanosystems (liposomes, magnetic nanoparticles, polystyrene nanoparticles) were selected and functionalized with peptides both to enhance tumor targeting and facilitate intracellular uptake. Peptides or peptidomimetics are emerging as favoured targeting and uptake enhancers owing to their ease of preparation, lower cost, lower antigenicity, decreased opsonization, increased resistance to enzymatic degradation, high affinity and selectivity [125]. In particular, development of a delivery carrier which successfully combines specific targeting and enhancement of uptake using high affinity and selectivity of peptides, may potentially lead to decreased administered doses and therefore to lower toxicity of the chemotherapeutics. Notwithstanding the use of peptides, following intravenous injection, many drug delivery tools are easily recognized by the reticulo-endothelial system (RES) resulting in rapid clearance and nonlinear pharmacokinetics. To reduce this effect we used polyethylene glycol (PEG) coupled on the surface of our nanosystem, which is a milestone breakthrough in the field of drug delivery, known as stealth technology [76].

In order to facilitate the interaction between the nanosystem and cells, we have decorated their surface with cell penetrating peptides (CPPs), which were shown to be able to enhance drug delivery into target cells. In particular, we used a novel CPP (namely, gH625) which is able to overcome the known limits of classic CPPs. In fact, classic CPPs uptake mechanism seems to involve mainly the endocytic pathway, trapping the conjugated drug in endosomes eventually ending in lysosomes where common enzymatic degradation mechanisms take place, therefore leading to a limited delivery of therapeutic agents to the intracellular target. On the contrary, gH625 is able to efficiently traverse biological membranes, promoting lipid-membrane reorganizing processes, such as fusion or pore formation and involving temporary membrane destabilization and subsequent reorganization; gH625 was thus shown to be able to circumvent the endosomal entrapment either favouring the escape from the endosome or by directly translocating the drug across the membrane.

In order to make the nanosystem cell and tissue specific, we have further functionalized the surface of the nanosystem with a targeting peptide. Active targeting allows to target the nanosystem to tumor cells that overexpress a particular cell surface receptor. We exploited the EGB peptide, which recognizes the

Discussion and Conclusion

epidermal growth factor receptor (EGFR), a tyrosine kinase receptor overexpressed in several solid tumors.

Liposomes platform

The first nanosystem was based on liposomes. The coupling of a bioactive ligand on the surface of liposomes can be obtained according to several synthetic approaches. The choice of the strategy depends on whether it is necessary to perform the coupling before or after the liposome assembly. gH625 is a hydrophobic peptide with high tendency to locate in the hydrophobic portion of liposomes; thus, for the preparation of liposomes carrying on their surface gH625 we used a post-aggregation pathway based on the click chemistry technology. In order to obtain the dual functionalized liposomes with a precise control on the molar ratio between the two peptides, we decided to prepare a lipid derivative of the EGB peptide to use directly in the assembly of liposomes, a strategy usually preferred for amphiphilic peptides; then, gH625 was attached on pre-formed liposomes with the previously described strategy.

In collaboration with Prof Igor Chourpa of Tours University, we prepared liposomes (made of DOPG/DSPE-PEG = 85/5 molar ratio) functionalized with gH625 and carrying the drug MTX to analyze the internalization mechanism. The purpose of this study was to explore the possibility of using nanoliposomes decorated on their external surface with gH625 to change the uptake mechanism and enhance the internalization of mitoxantrone (MTX). The clarification of the mechanism of internalization is useful to improve the design of anticancer delivery tools that may determine an increase of internalization and may also help in overcoming resistance problems. Liposomes decorated with gH625 and carrying the drug (LMTX-gH625) were prepared and characterized. The drug loading was very high and resulted to be around 97%; moreover, less than 30% of loaded MTX was released after 24 h, which further supports the stability data obtained by the analysis of the zeta potential. To analyze the uptake mechanism, we used Confocal Spectral Imaging (CSI) which allows to distinguish very fine modifications of MTX intrinsic fluorescence within different intracellular microenvironments. The obtained results clearly show that the presence of gH625 on the surface of liposomes is favouring their uptake in HeLa cells. This correlates well with toxicity data; within 4 h, the LMTX-gH625 was more active than LMTX. The gH625 peptide probably induced a greater and more rapid internalization, which could contribute to the earlier cytotoxicity of LMTX-gH625 compared to LMTX. It has also been reported in literature that a fast cytoplasmic delivery of the drug can be related to a better chance to overcome drug resistance [2]. Nevertheless, at high incubation times there were no significant differences. From the CSI spectra, we detected three intracellular molecular situations for the drug: MTX at lipophilic environment, MTX in nucleus and an oxidative metabolite of the drug stained in the low polarity environment. The spectra observed indicate that the drug was partially released from the liposomes and was able to reach the nucleus; moreover, the effect of gH625 consists also in an increased presence of an oxidative metabolite of the drug which Prof. Chourpa previously demonstrated to be correlated with sensitivity of cancer cells to chemotherapy by MTX [108]. Our results support the view that, in addition to the nuclear one, several mechanisms may be involved in the cytotoxicity of LMTX-gH625 internalization. To summarize, gH625 modifies the internalization of liposomes and therefore the drug transport to the cells. Although the liposome-mediated drug delivery to the nucleus is delayed compared to the drug solution, it

could be compensated by complementary mechanisms of cytotoxicity taking place into the cytosol, namely those involving the oxidative metabolism of the drug. These mechanisms are of particular interest for the anticancer activity evaluation of the nanosystem for drug delivery.

The success of pharmacological treatments is often hampered by the onset of the drug resistance. The multidrug resistance (MDR) represents the principal mechanism by which many cancers develop resistance to chemotherapy, and poses the major obstacle to the successful clinical treatments of cancers. Due to these problems, it is highly important to explore alternative strategies for utilizing currently available drugs against MDR cancer cells. In collaboration with Dr. Bonelli of Microtech and Prof. Caraglia of SUN we used liposomes with enhanced biomimetics characteristics (phospholipids derived by soy), carrying on their external surface PEG. These liposomes were armed with gH625 to enhance the antitumor efficacy of liposomes encapsulating anti-cancer agents and to circumvent drug resistance. Physico-chemical characterization of the liposome system revealed a diameter of 140 nm with uniform distribution and high doxorubicin encapsulation efficiency. We have evaluated the growth inhibition on either wild type (A549) or doxorubicin-resistant (A549 Dx) human lung adenocarcinoma cell lines treated with increasing concentrations of liposomes encapsulating Doxo (LipoDoxo), liposomes encapsulating Doxo conjugated to gH625 (LipoDoxo-gH625), empty liposomes (Lipo) or free Doxo for 72 h. The presence of gH625 on the surface of liposomes is favouring their uptake in both sensitive and drug-resistant tumor cell lines allowing an increase of cell growth inhibition: in fact, a greater quantity of Doxo from functionalized liposomes is accumulated into cells. A higher oxidative stress is obtained after treatment with functionalized liposomes for 72 h indicating that probably also other mechanisms contribute to the activity in presence of gH625. Doxo encapsulated in functionalized liposomes was able to enter in the nuclei of Doxo-resistant cancer cells indicating that the peptide gH625 was probably inducing a greater and more rapid internalization also in resistant cells, which could contribute to overcome drug resistance [2]. In conclusion, further details have been shed on the mechanism of internalization promoted by gH625 which clearly indicates that this translocating peptide hold promise for the development of a platform for cancer therapy, which could be useful also for cancers developing resistance to chemotherapy.

Moreover, we worked to develop a nanoplatform based on dual decorated liposomes, both for the uptake and the targeting. gH625 is widely used for its highly efficient but nonspecific translocation into many cell types. Although these features enable gH625 to deliver therapeutic agents into cells efficiently, they also make very difficult to achieve target-specific delivery. In this study, we converted the non specific gH625 liposomes into an EGFR targeting delivery carrier by conjugating the EGBP moiety on the surface of the gH625-liposomes. In order to find the best way to enhance the interaction of the EGBP peptide with its receptor, we used two different linkers for conjugating the peptide to the liposome. Thus, the EGBP was synthesized with a small spacer of three glycines and with a small hydrophilic PEG based linker. In order to evaluate the position of the peptide on the liposome surface, we recorded tryptophan fluorescence spectra on Lipo-gH625 and Lipo-gH625-EGBP with both types of linkers. The comparison between the fluorescence intensity of Lipo-gH625 and the dual-functionalized liposomes showed an increase which could be attributed to the exposure of both tryptophans that of gH625 and EGBP. The comparison

Discussion and Conclusion

between the two dual-functionalized liposomes showed a higher intensity for the one with the PEG linker indicating that in this case thanks to the longer linker the tryptophan is more exposed as expected. We have also evaluated the Doxo accumulation of the dual decorated liposomes in KB cells by FACS analysis. The conjugation of liposomes with the homing peptide increased the retention of doxorubicin into cells, overexpressing EGF receptor. Further works is under way to characterize the uptake mechanism of dual functionalized liposomes *in vitro*.

Magnetic nanoparticles platform

The second nanosystem which was selected to be developed for the obtainment of the nanoplatform was magnetic nanoparticles. Our goal was to verify if we could enhance the cellular uptake also of this kind of cargo. We focused on optimization of the peptide conjugation strategy, in order to find the best compromise between the colloidal stability of nanosystems, their half-life in blood and their efficient translocation into cells. Indeed, a little is known about the optimal density/quantity of CPPs on a nanosystem which is required for its efficient transport through membranes of a given cancer cell line. In addition, depending on the peptide sequence, we add a certain hydrophobicity; thus an excess of peptide on the nanosystem surface reduces its colloidal stability in aqueous media and may reduce its half-life in blood circulation. We optimized several important parameters such as the concentration of gH625 on the polymeric surface of SPIONs. Moreover, we found that Circular Dichroism (CD) data confirmed that gH625 retains its helical structure when bound to the nanoparticle surface, suggesting that the secondary structure of the peptide was not disturbed by attachment to SPIONs. We are now working on the physico-chemical, characterization of the nanosystem and the eventual ability of gH625 to increase the nanoparticle uptake by cancer cells.

Polystyrene nanoparticles platform

The last system selected in this thesis was polystyrene nanoparticles (NPs). We explored the possibility of using NPs functionalized with gH625 to deliver a drug across the Blood Brain Barrier (BBB). The BBB is formed by the endothelial cells of brain capillaries, and restricts the exchange of most endogenous molecules between the blood and the brain; the very tight regulation of brain homeostasis imposed by the BBB prohibits many therapeutic compounds from entering brain tissues [119]. The development of new strategies for enhancing drug delivery to the brain is of great importance in diagnostics and therapeutics of central nervous diseases. The uptake and subcellular localization of the NPs were investigated by exposing an *in vitro* BBB model to 100 nm polystyrene NPs functionalized and not with gH625. The functionalized nanoparticles were thoroughly characterized using a variety of complementary techniques to gain a better understanding of their properties. In particular, gH625 only slightly modified the particle sizes with a zeta potential indicative of colloidal stability at pH 7. gH625-NPs translocated efficiently across the *in vitro* model of the BBB and their mechanism of uptake does not seem to exclusively involve classical endocytosis mechanisms. In fact, conjugation with gH625 facilitated the delivery of nanoparticles across the BBB, leading to significant higher cell uptake and crossing. It is clear from our results that the majority of blank NPs end up in intracellular organelles, mostly in lysosomes, similarly to several other NP systems [92,93]. A significant number of blank NPs are observed associated with lysosomes and after 24 h the degree of lysosomal accumulation was around 80%. Interestingly, gH625-NPs only slightly co-localize with lysosomes and their degree of

lysosomal accumulation did not increase with time. The endothelial brain cells are rich in cholesterol. To verify if gH625-NPs were still able to cross the membrane depleted of cholesterol, we have studied the interaction with an *in vitro* model of the BBB depleted of cholesterol. Our results showed that the depletion of cholesterol did not have any effect on the intracellular distribution of blank NPs but significantly reduced the uptake of gH625-NPs. We also demonstrated by the gene gun experiments, that gH625-NP interaction with the cell membrane plays a key role in controlling the uptake mechanism. In fact, most trajectories of blank NP resulted in pearls-on-a-string walk, indicative of motor protein facilitated transport, mediated by endocytic vesicles. Conversely, in presence of peptide functionalization, we observed that most trajectories showed a random walk behaviour with just a lower percentage of pearls-on-a-string trajectories, suggesting a translocation across the bilayer. Furthermore, we also observed a significant reduction of cytotoxicity compared to blank NPs. These studies clearly indicate that gH625 is able to change the mechanism of uptake of the cargo and it is able to cross the BBB in a fashion that can be distinguished from other cell-penetrating peptides such as TAT and penetratin [91].

Conclusion

In conclusion we have developed a nanoplatform based on different nanosystems (liposomes, magnetic nanoparticles, polystyrene nanoparticles) which could be decorated on their surface with gH625 and a targeting peptide; these nanoplatforms could be exploited for obtaining target-specific therapeutics. In fact, replacing the EGBP moiety with a different molecule targeting another tumor surface marker, along with the relevant therapeutic agent, we might be able to obtain a theranostic system specific for each pathology.

References

1. Ferlay J, Soerjomataram I, Ervik M, Dikshit R, Eser S, et al. (2014) GLOBOCAN 2012 v1. 0, Cancer Incidence and Mortality Worldwide: IARC CancerBase No. 11. Lyon, France: International Agency for Research on Cancer; 2013. Visit: <http://globocan.iarc.fr>.
2. Shen Y, Tang H, Zhan Y, Van Kirk EA, Murdoch WJ (2009) Degradable poly(beta-amino ester) nanoparticles for cancer cytoplasmic drug delivery. *Nanomedicine* 5: 192-201.
3. Steichen SD, Caldorera-Moore M, Peppas NA (2013) A review of current nanoparticle and targeting moieties for the delivery of cancer therapeutics. *Eur J Pharm Sci* 48: 416-427.
4. Stiuso P, Caraglia M, De Rosa G, Giordano A (2013) Bioactive peptides in cancer: therapeutic use and delivery strategies. *J Amino Acids* 2013: 568953.
5. Bunz F, Hwang PM, Torrance C, Waldman T, Zhang Y, et al. (1999) Disruption of p53 in human cancer cells alters the responses to therapeutic agents. *J Clin Invest* 104: 263-269.
6. Raub CB, Orwin EJ, Haskell R (2004) Immunogold labeling to enhance contrast in optical coherence microscopy of tissue engineered corneal constructs. *Conf Proc IEEE Eng Med Biol Soc* 2: 1210-1213.
7. Lengauer C, Kinzler KW, Vogelstein B (1998) Genetic instabilities in human cancers. *Nature* 396: 643-649.
8. Miller AB, Hoogstraten B, Staquet M, Winkler A Reporting results of cancer treatment.
9. Rosch PJ.
10. Krishna R, Mayer LD.
11. Saraswathy M, Gong S.
12. Kubiak C, Couvreur P, Manil L, Clausse B.
13. Lobatto ME, Fuster V, Fayad ZA, Mulder WJM (2011) Perspectives and opportunities for nanomedicine in the management of atherosclerosis. *Nat Rev Drug Discov* 10: 963-963.
14. Hong H, Gao T, Cai W (2009) Molecular Imaging with Single-Walled Carbon Nanotubes. *Nano Today* 4: 252-261.
15. LaVan DA, McGuire T, Langer R (2003) Small-scale systems for in vivo drug delivery. *Nat Biotechnol* 21: 1184-1191.
16. Farokhzad OC, Langer R (2009) Impact of nanotechnology on drug delivery. *ACS Nano* 3: 16-20.
17. Matsumura Y, Maeda H (1986) A new concept for macromolecular therapeutics in cancer chemotherapy: mechanism of tumorotropic accumulation of proteins and the antitumor agent smancs. *Cancer Res* 46: 6387-6392.
18. Bao G, Mitragotri S, Tong S (2013) Multifunctional nanoparticles for drug delivery and molecular imaging. *Annu Rev Biomed Eng* 15: 253-282.
19. Leserman LD, Barbet J, Kourilsky F, Weinstein JN (1980) Targeting to cells of fluorescent liposomes covalently coupled with monoclonal antibody or protein A. *Nature* 288: 602-604.
20. Heath TD, Fraley RT, Papahdjopoulos D (1980) Antibody targeting of liposomes: cell specificity obtained by conjugation of F(ab')₂ to vesicle surface. *Science* 210: 539-541.
21. Allen TM, Chonn A (1987) Large unilamellar liposomes with low uptake into the reticuloendothelial system. *FEBS Lett* 223: 42-46.

References

22. Klibanov AL, Maruyama K, Torchilin VP, Huang L (1990) Amphipathic polyethyleneglycols effectively prolong the circulation time of liposomes. *FEBS Lett* 268: 235-237.
23. Gref R, Minamitake Y, Peracchia MT, Trubetskoy V, Torchilin V, et al. (1994) Biodegradable long-circulating polymeric nanospheres. *Science* 263: 1600-1603.
24. Allen TM, Cullis PR (2013) Liposomal drug delivery systems: from concept to clinical applications. *Adv Drug Deliv Rev* 65: 36-48.
25. Moghimi SM, Hunter AC, Murray JC (2005) Nanomedicine: current status and future prospects. *FASEB J* 19: 311-330.
26. Sahoo SK, Parveen S, Panda JJ (2007) The present and future of nanotechnology in human health care. *Nanomedicine* 3: 20-31.
27. Beija M, Salvayre R, Lauth-de Viguerie N, Marty JD (2012) Colloidal systems for drug delivery: from design to therapy. *Trends Biotechnol* 30: 485-496.
28. Madni A, Sarfraz M, Rehman M, Ahmad M, Akhtar N, et al. (2014) Liposomal drug delivery: a versatile platform for challenging clinical applications. *J Pharm Pharm Sci* 17: 401-426.
29. Cinteza LO (2010) Quantum dots in biochemical applications: advances and challenges. *J Nanophoton* 4.
30. Medintz IL, Pons T, Delehanty JB, Susumu K, Brunel FM, et al. (2008) Intracellular delivery of quantum dot-protein cargos mediated by cell penetrating peptides. *Bioconjug Chem* 19: 1785-1795.
31. Mahajan SD, Law WC, Aalinkeel R, Reynolds J, Nair BB, et al. (2012) Nanoparticle-mediated targeted delivery of antiretrovirals to the brain. *Methods Enzymol* 509: 41-60.
32. Xu G, Mahajan S, Roy I, Yong KT (2013) Theranostic quantum dots for crossing blood-brain barrier and providing therapy of HIV-associated encephalopathy. *Front Pharmacol* 4: 140.
33. Yang H (2010) Nanoparticle-mediated brain-specific drug delivery, imaging, and diagnosis. *Pharm Res* 27: 1759-1771.
34. Ye L, Yong KT, Liu L, Roy I, Hu R, et al. (2012) A pilot study in non-human primates shows no adverse response to intravenous injection of quantum dots. *Nat Nanotechnol* 7: 453-458.
35. Bagalkot V, Zhang L, Levy-Nissenbaum E, Jon S, Kantoff PW, et al. (2007) Quantum dot-aptamer conjugates for synchronous cancer imaging, therapy, and sensing of drug delivery based on bi-fluorescence resonance energy transfer. *Nano letters* 7: 3065-3070.
36. Chan WC, Maxwell DJ, Gao X, Bailey RE, Han M, et al. (2002) Luminescent quantum dots for multiplexed biological detection and imaging. *Current opinion in biotechnology* 13: 40-46.
37. Hama Y, Koyama Y, Urano Y, Choyke PL, Kobayashi H (2007) Simultaneous two-color spectral fluorescence lymphangiography with near infrared quantum dots to map two lymphatic flows from the breast and the upper extremity. *Breast cancer research and treatment* 103: 23-28.
38. Gillies ER, Frechet JM (2005) Dendrimers and dendritic polymers in drug delivery. *Drug Discov Today* 10: 35-43.
39. Davis ME, Chen ZG, Shin DM (2008) Nanoparticle therapeutics: an emerging treatment modality for cancer. *Nat Rev Drug Discov* 7: 771-782.
40. Azarmi S, Roa WH, Lobenberg R (2008) Targeted delivery of nanoparticles for the treatment of lung diseases. *Adv Drug Deliv Rev* 60: 863-875.

41. Falanga A, Vitiello MT, Cantisani M, Tarallo R, Guarnieri D, et al. (2011) A peptide derived from herpes simplex virus type 1 glycoprotein H: membrane translocation and applications to the delivery of quantum dots. *Nanomedicine* 7: 925-934.
42. Arrighi RB, Ebikeme C, Jiang Y, Ranford-Cartwright L, Barrett MP, et al. (2008) Cell-penetrating peptide TP10 shows broad-spectrum activity against both *Plasmodium falciparum* and *Trypanosoma brucei brucei*. *Antimicrob Agents Chemother* 52: 3414-3417.
43. El Andaloussi S, Said Hassane F, Boisguerin P, Sillard R, Langel U, et al. (2011) Cell-penetrating peptides-based strategies for the delivery of splice redirecting antisense oligonucleotides. *Methods Mol Biol* 764: 75-89.
44. Dietz GP, Bahr M (2004) Delivery of bioactive molecules into the cell: the Trojan horse approach. *Mol Cell Neurosci* 27: 85-131.
45. Futaki S (2002) Arginine-rich peptides: potential for intracellular delivery of macromolecules and the mystery of the translocation mechanisms. *Int J Pharm* 245: 1-7.
46. Pooga M, Soomets U, Hallbrink M, Valkna A, Saar K, et al. (1998) Cell penetrating PNA constructs regulate galanin receptor levels and modify pain transmission in vivo. *Nat Biotechnol* 16: 857-861.
47. Morris MC, Vidal P, Chaloin L, Heitz F, Divita G (1997) A new peptide vector for efficient delivery of oligonucleotides into mammalian cells. *Nucleic Acids Res* 25: 2730-2736.
48. Morris MC, Depollier J, Mery J, Heitz F, Divita G (2001) A peptide carrier for the delivery of biologically active proteins into mammalian cells. *Nat Biotechnol* 19: 1173-1176.
49. Richard JP, Melikov K, Vives E, Ramos C, Verbeure B, et al. (2003) Cell-penetrating peptides. A reevaluation of the mechanism of cellular uptake. *J Biol Chem* 278: 585-590.
50. Lundberg M, Johansson M (2002) Positively charged DNA-binding proteins cause apparent cell membrane translocation. *Biochem Biophys Res Commun* 291: 367-371.
51. Futaki S (2005) Membrane-permeable arginine-rich peptides and the translocation mechanisms. *Adv Drug Deliv Rev* 57: 547-558.
52. Jones SW, Christison R, Bundell K, Voyce CJ, Brockbank SM, et al. (2005) Characterisation of cell-penetrating peptide-mediated peptide delivery. *Br J Pharmacol* 145: 1093-1102.
53. Duchardt F, Fotin-Mleczek M, Schwarz H, Fischer R, Brock R (2007) A comprehensive model for the cellular uptake of cationic cell-penetrating peptides. *Traffic* 8: 848-866.
54. Vives E, Richard JP, Rispal C, Lebleu B (2003) TAT Peptide Internalization: Seeking the Mechanism of Entry. *Curr Protein Pept Sci* 4: 125-132.
55. Brooks H, Lebleu B, Vives E (2005) Tat peptide-mediated cellular delivery: back to basics. *Adv Drug Deliv Rev* 57: 559-577.
56. Nakase I, Tadokoro A, Kawabata N, Takeuchi T, Katoh H, et al. (2007) Interaction of arginine-rich peptides with membrane-associated proteoglycans is crucial for induction of actin organization and macropinocytosis. *Biochemistry* 46: 492-501.
57. Fittipaldi A, Ferrari A, Zoppe M, Arcangeli C, Pellegrini V, et al. (2003) Cell membrane lipid rafts mediate caveolar endocytosis of HIV-1 tat fusion proteins. *J Biol Chem*: 34141 - 34149.
58. Kaplan IM, Wadia JS, Dowdy SF (2005) Cationic TAT peptide transduction domain enters cells by macropinocytosis. *J Control Release* 102: 247-253.

References

59. Nakase I, Niwa M, Takeuchi T, Sonomura K, Kawabata N, et al. (2004) Cellular uptake of arginine-rich peptides: roles for macropinocytosis and actin rearrangement. *Mol Ther* 10: 1011-1022.
60. Richard JP, Melikov K, Brooks H, Prevot P, Lebleu B, et al. (2005) Cellular uptake of unconjugated TAT peptide involves clathrin-dependent endocytosis and heparan sulfate receptors. *J Biol Chem* 280: 15300-15306.
61. Vandenbroucke RE, De Smedt SC, Demeester J, Sanders NN (2007) Cellular entry pathway and gene transfer capacity of TAT-modified lipoplexes. *Biochim Biophys Acta* 1768: 571-579.
62. Fischer R, Kohler K, Fotin-Mleczek M, Brock R (2004) A Stepwise Dissection of the Intracellular Fate of Cationic Cell-penetrating Peptides. *J Biol Chem* 279: 12625-12635.
63. Guarnieri D, Falanga A, Muscetti O, Tarallo R, Fusco S, et al. (2013) Drug Delivery: Shuttle-Mediated Nanoparticle Delivery to the Blood–Brain Barrier (*Small* 6/2013). *Small* 9: 806-806.
64. Galdiero S, Falanga A, Vitiello M, Grieco P, Caraglia M, et al. (2014) Exploitation of viral properties for intracellular delivery. *J Pept Sci* 20: 468-478.
65. Larsson P, Kasson PM (2013) Lipid tail protrusion in simulations predicts fusogenic activity of influenza fusion peptide mutants and conformational models. *PLoS computational biology* 9: e1002950.
66. Kozlov MM, McMahon HT, Chernomordik LV (2010) Protein-driven membrane stresses in fusion and fission. *Trends in biochemical sciences* 35: 699-706.
67. Falanga A, Cantisani M, Pedone C, Galdiero S (2009) Membrane fusion and fission: enveloped viruses. *Protein Pept Lett* 16: 751-759.
68. Galdiero S, Vitiello M, Falanga A, Cantisani M, Incoronato N, et al. (2012) Intracellular delivery: exploiting viral membranotropic peptides. *Curr Drug Metab* 13: 93-104.
69. Galdiero S, Vitiello M, D'Isanto M, Falanga A, Cantisani M, et al. (2008) The identification and characterization of fusogenic domains in herpes virus glycoprotein B molecules. *Chembiochem* 9: 758-767.
70. Galdiero S, Falanga A, Vitiello M, Raiola L, Russo L, et al. (2010) The presence of a single N-terminal histidine residue enhances the fusogenic properties of a Membranotropic peptide derived from herpes simplex virus type 1 glycoprotein H. *J Biol Chem* 285: 17123-17136.
71. Galdiero S, Falanga A, Vitiello G, Vitiello M, Pedone C, et al. (2010) Role of membranotropic sequences from herpes simplex virus type I glycoproteins B and H in the fusion process. *Biochim Biophys Acta* 1798: 579-591.
72. Kamaly N, Xiao Z, Valencia PM, Radovic-Moreno AF, Farokhzad OC (2012) Targeted polymeric therapeutic nanoparticles: design, development and clinical translation. *Chem Soc Rev* 41: 2971-3010.
73. Ramogida CF, Orvig C (2013) Tumour targeting with radiometals for diagnosis and therapy. *Chem Commun (Camb)* 49: 4720-4739.
74. Wang J, Byrne JD, Napier ME, DeSimone JM (2011) More Effective Nanomedicines through Particle Design. *Small (Weinheim an Der Bergstrasse, Germany)* 7: 1919-1931.
75. Alexis F, Pridgen E, Molnar LK, Farokhzad OC (2008) Factors affecting the clearance and biodistribution of polymeric nanoparticles. *Molecular pharmaceuticals* 5: 505-515.
76. Immordino ML, Dosio F, Cattel L (2006) Stealth liposomes: review of the basic science, rationale, and clinical applications, existing and potential. *International journal of nanomedicine* 1: 297.

77. Arvizo RR, Miranda OR, Moyano DF, Walden CA, Giri K, et al. (2011) Modulating pharmacokinetics, tumor uptake and biodistribution by engineered nanoparticles. *PLoS One* 6: e24374.
78. Maeda H, Wu J, Sawa T, Matsumura Y, Hori K (2000) Tumor vascular permeability and the EPR effect in macromolecular therapeutics: a review. *J Control Release* 65: 271-284.
79. Caraglia M, Marra M, Misso G, Lamberti M, Salzano G, et al. (2012) Tumour-specific uptake of anti-cancer drugs: the future is here. *Curr Drug Metab* 13: 4-21.
80. Maruyama K (2011) Intracellular targeting delivery of liposomal drugs to solid tumors based on EPR effects. *Adv Drug Deliv Rev* 63: 161-169.
81. Fox ME, Szoka FC, Frechet JM (2009) Soluble polymer carriers for the treatment of cancer: the importance of molecular architecture. *Acc Chem Res* 42: 1141-1151.
82. Chaudhury A, Das S (2015) Folate Receptor Targeted Liposomes Encapsulating Anti-Cancer Drugs. *Curr Pharm Biotechnol*.
83. Gunaseelan S, Gunaseelan K, Deshmukh M, Zhang X, Sinko PJ (2010) Surface modifications of nanocarriers for effective intracellular delivery of anti-HIV drugs. *Adv Drug Deliv Rev* 62: 518-531.
84. Dunn CJ, Goa KL (1996) Mitoxantrone: a review of its pharmacological properties and use in acute nonlymphoblastic leukaemia. *Drugs Aging* 9: 122-147.
85. Kroger N, Damon L, Zander AR, Wandt H, Derigs G, et al. (2003) Secondary acute leukemia following mitoxantrone-based high-dose chemotherapy for primary breast cancer patients. *Bone Marrow Transplant* 32: 1153-1157.
86. Allen C, Dos Santos N, Gallagher R, Chiu GN, Shu Y, et al. (2002) Controlling the physical behavior and biological performance of liposome formulations through use of surface grafted poly(ethylene glycol). *Biosci Rep* 22: 225-250.
87. Nag OK, Awasthi V (2013) Surface engineering of liposomes for stealth behavior. *Pharmaceutics* 5: 542-569.
88. Tosi G, Costantino L, Rivasi F, Ruozi B, Leo E, et al. (2007) Targeting the central nervous system: in vivo experiments with peptide-derivatized nanoparticles loaded with Loperamide and Rhodamine-123. *J Control Release* 122: 1-9.
89. Yang H (2010) Nanoparticle-Mediated Brain-Specific Drug Delivery, Imaging, and Diagnosis. *Pharmaceutical Research* 27: 1759-1771.
90. Paolino D, Cosco D, Molinaro R, Celia C, Fresta M (2011) Supramolecular devices to improve the treatment of brain diseases. *Drug discovery today* 16: 311-324.
91. Hervé F, Ghinea N, Scherrmann J-M (2008) CNS delivery via adsorptive transcytosis. *The AAPS journal* 10: 455-472.
92. Ye D, Ragnnaill MN, Bramini M, Mahon E, Åberg C, et al. (2013) Nanoparticle accumulation and transcytosis in brain endothelial cell layers. *Nanoscale* 5: 11153-11165.
93. Ragnnaill MN, Brown M, Ye D, Bramini M, Callanan S, et al. (2011) Internal benchmarking of a human blood-brain barrier cell model for screening of nanoparticle uptake and transcytosis. *European Journal of Pharmaceutics and Biopharmaceutics* 77: 360-367.
94. Liu Y, Zhang L, Wan J, Li Y, Xu Y, et al. (2008) Design and synthesis of cyclo [-Arg-Gly-Asp-Ψ (triazole)-Gly-Xaa-] peptide analogues by click chemistry. *Tetrahedron* 64: 10728-10734.
95. Herve K, Douziech-Eyrolles L, Munnier E, Cohen-Jonathan S, Souce M, et al. (2008) The development of stable aqueous suspensions of PEGylated SPIONs for biomedical applications. *Nanotechnology* 19: 465608.

References

96. Vereda F, Vicente J, Hidalgo-Alvarez R (2007) Influence of a magnetic field on the formation of magnetite particles via two precipitation methods. *Langmuir* 23: 3581-3589.
97. Caraglia M, Passeggio A, Beninati S, Leardi A, Nicolini L, et al. (1997) Interferon alpha2 recombinant and epidermal growth factor modulate proliferation and hypusine synthesis in human epidermoid cancer KB cells. *Biochem J* 324 (Pt 3): 737-741.
98. Rodal SK, Skretting G, Garred O, Vilhardt F, van Deurs B, et al. (1999) Extraction of cholesterol with methyl-beta-cyclodextrin perturbs formation of clathrin-coated endocytic vesicles. *Mol Biol Cell* 10: 961-974.
99. Karnik R, Ludlow MJ, Abuarab N, Smith AJ, Hardy ME, et al. (2013) Endocytosis of hERG Is Clathrin-Independent and Involves Arf6. *PloS one* 8: e85630.
100. Bolte S, Cordelières FP (2006) A guided tour into subcellular colocalization analysis in light microscopy. *Journal of microscopy* 224: 213-232.
101. Guarnieri D, Sabella S, Muscetti O, Belli V, Malvindi MA, et al. (2014) Transport across the cell-membrane dictates nanoparticle fate and toxicity: a new paradigm in nanotoxicology. *Nanoscale* 6: 10264-10273.
102. Guarnieri D, Guaccio A, Fusco S, Netti PA (2011) Effect of serum proteins on polystyrene nanoparticle uptake and intracellular trafficking in endothelial cells. *Journal of Nanoparticle Research* 13: 4295-4309.
103. McIntyre JC, Sleight RG (1991) Fluorescence assay for phospholipid membrane asymmetry. *Biochemistry* 30: 11819-11827.
104. Hope MJ, Bally MB, Webb G, Cullis PR (1985) Production of large unilamellar vesicles by a rapid extrusion procedure: characterization of size distribution, trapped volume and ability to maintain a membrane potential. *Biochim Biophys Acta* 812: 55-65.
105. Tardi PG, Boman NL, Cullis PR (1996) Liposomal doxorubicin. *J Drug Target* 4: 129-140.
106. Said Hassane F, Frisch B, Schuber F (2006) Targeted liposomes: convenient coupling of ligands to preformed vesicles using "click chemistry". *Bioconjug Chem* 17: 849-854.
107. Sharma A, Sharma US (1997) Liposomes in drug delivery: Progress and limitations. *International Journal of Pharmaceutics* 154: 123-140.
108. Vibet S, Maheo K, Gore J, Dubois P, Bougnoux P, et al. (2007) Differential subcellular distribution of mitoxantrone in relation to chemosensitization in two human breast cancer cell lines. *Drug Metab Dispos* 35: 822-828.
109. Kibria G, Hatakeyama H, Harashima H (2014) Cancer multidrug resistance: mechanisms involved and strategies for circumvention using a drug delivery system. *Arch Pharm Res* 37: 4-15.
110. Liang XJ, Chen C, Zhao Y, Wang PC (2010) Circumventing tumor resistance to chemotherapy by nanotechnology. *Methods Mol Biol* 596: 467-488.
111. Estanqueiro M, Amaral MH, Conceicao J, Sousa Lobo JM (2015) Nanotechnological carriers for cancer chemotherapy: The state of the art. *Colloids Surf B Biointerfaces*.
112. Chourpa I, Douziech-Eyrolles L, Ngaboni-Okassa L, Fouquenot J-F, Cohen-Jonathan S, et al. (2005) Molecular composition of iron oxide nanoparticles, precursors for magnetic drug targeting, as characterized by confocal Raman microspectroscopy. *Analyst* 130: 1395-1403.
113. Tang J, Myers M, Bosnick KA, Brus LE (2003) Magnetite Fe₃O₄ nanocrystals: spectroscopic observation of aqueous oxidation kinetics. *The Journal of Physical Chemistry B* 107: 7501-7506.

114. Tartaj P, del Puerto Morales M, Veintemillas-Verdaguer S, Gonzalez-Carreno T, Serna CJ (2003) The preparation of magnetic nanoparticles for applications in biomedicine. *Journal of Physics D: Applied Physics* 36: R182.
115. Wang Y, Wei X, Zhang C, Zhang F, Liang W (2010) Nanoparticle delivery strategies to target doxorubicin to tumor cells and reduce side effects. *Ther Deliv* 1: 273-287.
116. Shkilnyy A, Munnier E, Hervé K, Soucé M, Benoit R, et al. (2010) Synthesis and evaluation of novel biocompatible super-paramagnetic iron oxide nanoparticles as magnetic anticancer drug carrier and fluorescence active label. *The Journal of Physical Chemistry C* 114: 5850-5858.
117. Galdiero S, Falanga A, Vitiello M, Browne H, Pedone C, et al. (2005) Fusogenic domains in herpes simplex virus type 1 glycoprotein H. *J Biol Chem* 280: 28632-28643.
118. Kreuter J (2014) Drug delivery to the central nervous system by polymeric nanoparticles: What do we know? *Advanced drug delivery reviews* 71: 2-14.
119. Neuwelt E, Abbott N, Abrey L, Banks WA, Blakley B, et al. (2008) Strategies to advance translational research into brain barriers. *Lancet Neurology* 7: 84-96.
120. Guarnieri D, Falanga A, Muscetti O, Tarallo R, Fusco S, et al. (2013) Shuttle-Mediated Nanoparticle Delivery to the Blood-Brain Barrier. *Small* 9: 853-862.
121. Blechinger J, Bauer AT, Torrano AA, Gorzelanny C, Bräuchle C, et al. (2013) Uptake kinetics and nanotoxicity of silica nanoparticles are cell type dependent. *Small* 9: 3970-3980.
122. Galdiero S, Falanga A, Vitiello M, Raiola L, Russo L, et al. (2010) The presence of a single N-terminal histidine residue enhances the fusogenic properties of a membranotropic peptide derived from herpes simplex virus type 1 glycoprotein H. *Journal of Biological Chemistry* 285: 17123-17136.
123. Wang F, Yu L, Monopoli MP, Sandin P, Mahon E, et al. (2013) The biomolecular corona is retained during nanoparticle uptake and protects the cells from the damage induced by cationic nanoparticles until degraded in the lysosomes. *Nanomedicine: Nanotechnology, Biology and Medicine* 9: 1159-1168.
124. Kim JA, Åberg C, de Cárcer G, Malumbres M, Salvati A, et al. (2013) Low Dose of Amino-Modified Nanoparticles Induces Cell Cycle Arrest. *ACS nano* 7: 7483-7494.
125. Gabathuler R (2010) Development of new peptide vectors for the transport of therapeutic across the blood-brain barrier. *Ther Deliv* 1: 571-586.

Acknowledgements

I would like to express my gratitude to my supervisor Dr. Stefania Galdiero, who gave me the opportunity to pursue this PhD degree in nanotechnology; her constant support, stimulating discussions and encouragement helped me in both research work thesis writing.

I would like to thank Dr. Annarita Falanga, who helped me in the lab with suggestions and discussions, that helped me to sort out scientific and technical details of my thesis work.

I wish to thank Dr. Marco Cantisani for numerous discussions that helped me to improve my work and knowledge in the field.

I am grateful to my labmates Ms. Lucia Lombardi, Dr. Daniela Comegna, Dr. Ivan De Paola, with whom I shared many hard and funny moments of my Ph.D. life.

Thanks to my French group, with whom I spent a period of my PhD, Prof. Igor Chourpa, Dr. Katel Herve Aubert, Ms. Ambre Carrouée and Ms. Hoang Truc Phuong Nguyen for all those wonderful moments with them. They helped me to feel 'at home' in Tours, far away from my home.

The list of the people to thank is very long, as all the people I met during the last three years have been helpful and cooperative. Thus, I would like to thank each and everyone of you.

Sincerely,

Emiliana Perillo.

Appendix

Publications

1. Falanga, A., Tarallo, R., Vitiello, G., Vitiello, M., **Perillo, E.**, Cantisani, M., D'Errico, G., Galdiero, M., Galdiero, S. "Biophysical characterization and membrane interaction of the two fusion loops of glycoprotein B from herpes simplex type I virus," PLoS One 7, e32186 (2012).
2. Surfacedecoration with membranotropic peptides as a method to escape endo-lysosomal compartment and reduce nanoparticle toxicity, Daniela Guarnieri, Ornella Muscetti, Annarita Falanga, Sabato Fusco, Valentina Belli, **Emiliana Perillo**, Edmondo Battista, Valeria Panzetta, Stefania Galdiero, Paolo A. Netti, Nanotechnology, submitted.
3. Quantitative and qualitative effect of gH625 on the nanoliposome-mediated delivery of mitoxantrone anticancerdrug to HeLa cells. **Emiliana Perillo**, Emilie Allard-Vannier, Annarita Falanga, Paola Stiuso, Maria Teresa Vitiello, Massimiliano Galdiero, Stefania Galdiero and Igor Chourpa. Int J Pharm, submitted.
4. Liposome armed with Herpes Virus-derived gH625 peptide to overcome resistance in lung adenocarcinoma cell lines. **Emiliana Perillo**, Stefania Porto, Annarita Falanga, Silvia Zappavigna, Paola Stiuso, Massimiliano Galdiero, Stefania Galdiero, Michele Caraglia, Journal of biomedical nanotechnology, submitted.

Poster communications

- Biophysical characterization and membrane interaction of the two fusion loops of glycoprotein B from herpes simplex type I virus. Cantisani M, Falanga A, Tarallo R, **Perillo E**, Vitiello G, Vitiello M, D'Errico G, Galdiero M, Galdiero S. 13th Naples Workshop on Bioactive peptides 2012
- Activity optimization of analogues of Myxinidin, a novel antimicrobial peptide derived from the epidermal mucus of hagfish. Mignogna E., Cantisani M., Kampanaraki A., Incoronato N., Falanga A., **Perillo E.**, Della Pepa M.E., D'Orlando V., Galdiero S., Galdiero M. 13th Naples Workshop on Bioactive peptides 2012
- Viral Peptide Targeted Delivery of Nano-Therapeutics S. Galdiero, A. Falanga, **E. Perillo**, M. Cantisani, M. Galdiero, G. Morelli 1st PepMat 2013
- Shuttle-mediated nanoparticle delivery to the blood brain barrier A. Falanga, M. Cantisani, D. Guarnieri, **E. Perillo**, P. A. Netti, G. Morelli, M. Galdiero, S. Galdiero 1st PepMat 2013
- In vitro investigation on cancer cell uptake and toxicity of liposomes functionalized with the membranotropic peptide gH625 **E. Perillo**, S. Porto, A. Falanga, M. Galdiero, P. Grieco, G. De Rosa, S. Galdiero and M. Caraglia 14th Naples Workshop on Bioactive peptides 2014

- Antiviral activity of a peptide-dendrimer L. Lombardi, A. Falanga, E. Mignogna, N. Incoronato, R. Tarallo, **E. Perillo**, M. Weck, M. Galdiero and S. Galdiero 14th Naples Workshop on Bioactive peptides 2014

Foreign educational experience

- From 12-05-13 to 16-05-13: permanence at Institut Laue-Langevin ,Grenoble, France, head of group Dr. Giovanna Fragneto and Dr. Diego Pontoni
- From 20-10-13 to 20-12-13: permanence at François Rabelais University of Tours, head of the group Prof. Igor Chourpa
- From 25-08-14 to 21-09-14: permanence at François Rabelais University of Tours, head of the group Prof. Igor Chourpa

Labs attended

Department of Pharmacy University of Naples Federico II, supervisor Dr Stefania Galdiero

Microtech S.r.l., supervisor Dr Patrizia Bonelli

Department of Biochemistry, Biophysics and General Pathology, II University of Naples, supervisor Prof. Michele Caraglia

Biophysical Characterization and Membrane Interaction of the Two Fusion Loops of Glycoprotein B from Herpes Simplex Type I Virus

Annarita Falanga^{1,2}, Rossella Tarallo¹, Giuseppe Vitiello³, Mariateresa Vitiello⁴, Emiliana Perillo¹, Marco Cantisani^{1,2}, Gerardino D'Errico³, Massimiliano Galdiero^{2,4*}, Stefania Galdiero^{1,2,5*}

1 Division of Biostructures, Department of Biological Sciences, University of Naples "Federico II", Napoli, Italy, **2** Centro Interuniversitario di Ricerca sui Peptidi Bioattivi, University of Naples "Federico II", Napoli, Italy, **3** Department of Chemistry, University of Naples "Federico II" and Consorzio per lo Studio dei Sistemi a Grande Interfase, CSGI, Monte Sant'Angelo, Napoli, Italy, **4** Department of Experimental Medicine, II University of Naples, Napoli, Italy, **5** Istituto di Biostrutture e Bioimmagini, CNR, Napoli, Italy

Abstract

The molecular mechanism of entry of herpesviruses requires a multicomponent fusion system. Cell invasion by Herpes simplex virus (HSV) requires four virally encoded glycoproteins: namely gD, gB and gH/gL. The role of gB has remained elusive until recently when the crystal structure of HSV-1 gB became available and the fusion potential of gB was clearly demonstrated. Although much information on gB structure/function relationship has been gathered in recent years, the elucidation of the nature of the fine interactions between gB fusion loops and the membrane bilayer may help to understand the precise molecular mechanism behind herpesvirus-host cell membrane fusion. Here, we report the first biophysical study on the two fusion peptides of gB, with a particular focus on the effects determined by both peptides on lipid bilayers of various compositions. The two fusion loops constitute a structural subdomain wherein key hydrophobic amino acids form a ridge that is supported on both sides by charged residues. When used together the two fusion loops have the ability to significantly destabilize the target membrane bilayer, notwithstanding their low bilayer penetration when used separately. These data support the model of gB fusion loops insertion into cholesterol enriched membranes.

Citation: Falanga A, Tarallo R, Vitiello G, Vitiello M, Perillo E, et al. (2012) Biophysical Characterization and Membrane Interaction of the Two Fusion Loops of Glycoprotein B from Herpes Simplex Type I Virus. PLoS ONE 7(2): e32186. doi:10.1371/journal.pone.0032186

Editor: Robert J. Geraghty, University of Minnesota, United States of America

Received: October 24, 2011; **Accepted:** January 23, 2012; **Published:** February 23, 2012

Copyright: © 2012 Falanga et al. This is an open-access article distributed under the terms of the Creative Commons Attribution License, which permits unrestricted use, distribution, and reproduction in any medium, provided the original author and source are credited.

Funding: This work was supported by MIUR (Ministero dell'Istruzione, dell'Università e della Ricerca) (FIRB Prot. RBRN07BMCT). The funders had no role in study design, data collection and analysis, decision to publish, or preparation of the manuscript.

Competing Interests: The authors have declared that no competing interests exist.

* E-mail: massimiliano.galdiero@unina2.it (MG); sgaldier@unina.it (SG)

Introduction

Enveloped viruses infect host cells by fusion of viral and target membranes. The initial apposition step is followed by fusion of the outer leaflets of membranes (the hemifusion step), leading to the formation of a transient fusion intermediate, which evolves into the fusion of inner leaflets and the formation of a pore, with the mixing of the internal compartments of both fusion partners. Thus, the viral genome is transferred to the cytoplasm of the host cell and viral replication ensues [1–3]. This fusion event is triggered by specific glycoproteins in the viral envelope. Fusion glycoproteins belong to either class I, class II or the newly described class III, depending upon their arrangement at the surface of the virion, their structure and the location within the protein of a short stretch of hydrophobic amino acids called the fusion peptide, which is able to induce the initial lipid destabilization that ends in fusion [4].

Although, viral fusion proteins are divided in three classes and the cellular membrane undergoing fusion might vary (plasma membrane vs. endosomal membrane), these proteins have to act on lipid assemblies. Thus, lipids contribute to fusion through their physical, mechanical and/or chemical properties and play a role in determining the preferential partitioning of some amino acid

sequences into membrane microdomains called “rafts”, and/or in modulating the curvature of the membranes involved in the fusion process [3].

Considering lipids and fusion proteins the necessary partners involved in the fusion process, it becomes clear that the overall gist of viral-induced membrane fusion is dictated by several features common to different families of viruses [1]. All fusion machineries need to interact with lipids, so they possess hydrophobic segments (fusion peptides) or are able after rearrangements to make hydrophobic interactions with membranes; moreover, need to adopt specific conformations related to the pre and post-fusion states, since fusion is limited in space and time. Therefore, different viruses infect their host cells by very similar mechanisms at the molecular level and fusion peptides represent a key element of the fusion machinery, being the trigger for controlled membrane destabilization.

Recently, the novel concept of “lipid packing sensor” emerged, indicating protein motifs or domains that recognize the curvature of lipid membranes. The most studied sensor is the amphipathic helical motif present both in cellular membrane proteins and in viral proteins [5,6]; but also other structural motifs, such as loops or unfolded peptides, may be involved in the sensing of the membrane curvature and in the initial steps of membrane fusion.

The discovery of sensor motifs opens new perspectives with respect to viral fusion proteins, which may contain such sensors; and may help our understanding of the subtle and complex interplay between protein-induced fusion and lipid modulation and may represent targets for future antiviral therapies.

Herpes simplex virus type 1 (HSV-1) is a member of the α -herpesvirus subfamily and enters cells through fusion of the viral envelope with a cellular membrane in a cascade of molecular interactions involving multiple viral glycoproteins and cellular receptors. The envelope glycoproteins gH/gL, gB and gD are all essential for the entry process [7] and expression of this quartet of glycoproteins induces the fusion of cellular membranes in the absence of virus infection [8]. gH/gL and gB, also play important roles in primary fusion events that occur during egress of the capsid from the nucleus of infected cells [9]. Recently, it was shown that gB and gH/gL interact with each other concomitantly with fusion and that this interaction is triggered by binding of gD to its cellular receptor [10,11]. Thus, gB may function cooperatively with gH/gL, and each may have some fusogenic potential on its own. Although gB and gH/gL constitute the core fusion machinery of all members of the Herpesviridae, their mechanisms of action are still under investigation.

Peptides derived from the ectodomain of gH block virus entry [12], while others have the ability to bind and disrupt model membranes [13–18]. The recently solved crystal structure of the gH-gL complex [19] showed that gH has no structural homology with any known fusion protein supporting the hypothesis that gH may act as a regulator of fusion through interactions with gB, while the crystal structure of the gH-gL complex of EBV presents considerable differences in the structural arrangements of domains supporting the view that the complex can undergo dynamic rearrangements [7,20].

gB is highly conserved within all the members of the Herpesviridae and is involved in virus attachment, penetration and cell-to-cell spread. gB may undergo large conformational changes to bring about fusion and even though evidence for its refolding has yet to be obtained a model for pre-fusion gB has been proposed and it seems that gB undergoes a refolding transition during fusion. The structures of gB from HSV-1 [21] and EBV [22] demonstrated that gB has structural homology with viral fusion proteins belonging to other virus families: the vesicular stomatitis virus (VSV) G protein [23] and the baculovirus protein gp64 [24] and is probably the key fusion protein; moreover, several synthetic gB peptides induced the fusion of large unilamellar vesicles and inhibited herpes virus infection [25,26]. gB belongs to a newly formed group of fusion proteins, class III, which share similar individual domain structures and contain a central three-stranded coiled-coil reminiscent of the class I proteins. Whereas class I proteins have an N-terminal fusion peptide, class III proteins have internal bipartite fusion loops within domain I which are similar to the single fusion loop of class II fusion proteins. The class II fusion loop is composed entirely of hydrophobic amino acids whereas those of gB have both hydrophobic and charged residues [21–24]. In particular, the fusogenic loops correspond to the domains 173–179 and 258–265 of the protein gB.

Hydrophobic amino acids within the gB loops (W174, F175, G176, Y179, A261) are essential for gB function [27]. Similar studies of VSV G, gp64 and EBV gB support the notion that hydrophobic amino acids of both fusion loops are critical for fusion [28,29] and together constitute a fusion domain. Moreover, also charged amino acids play a fundamental role, in fact, mutations of H263 or R264 also negatively affected gB function [27]. These data support the view that the two fusion loops constitute a

subdomain where key hydrophobic amino acids form a ridge that is flanked on both sides by charged amino acids that enhance the ability to interact with target membranes, in fact, one of the two gB fusion loops (namely HB168–186) was identified by highly interfacial hydrophobicity analysis without the aid of structural data [25].

Although much information has been gathered in recent years, we do not yet know the precise molecular mechanism behind herpesvirus host cell membrane fusion; thus, elucidating the nature of the fine interactions between gB fusion loops and the membrane may help to distillate this interesting matter. In the present study, we report the synthesis and characterization of membrane interactions of the two fusion peptides present in gB. The goals of the experiments reported here were to verify the fusion ability of the two peptides, to assess the dependence of the fusion activity on the composition of the membrane and in particular on the content of cholesterol and to verify the eventual presence of a synergic or cooperative effect when the two isolated peptides are used together.

As far as we know, this is the first biophysical study on the two putative fusion peptides of gB, with a particular focus on the effects determined by both peptides on lipid bilayers of various compositions.

Results

Design of peptides

The proposed post-fusion structure of gB ectodomain is comprised of three protomers, and each protomer coils around the others with a left-handed twist [21]. There are multiple contacts between protomers throughout the molecule contributing to trimer stability. Each protomer of gB can be divided into five distinct domains: I, base; II, middle; III, core; IV crown; and V, arm (Figure 1). Domain I (Ile154 to Val363) is a β sandwich composed of two nearly orthogonal β sheets of four and three strands, with a long loop and short helix covering one opening of the β sandwich. An insertion (Tyr165 to Ile272) between strands β 4 and β 11 creates a subdomain at the base of the trimer, consisting of a four-stranded β sheet (with three long and one short strand), the convex side of which is covered with an α helix, a β hairpin, and a short two-stranded β sheet; the four-stranded β -sheet presents hydrophobic tips that have been proposed to represent the fusion peptides of gB (Figure 1). Fusion peptides are generally considered as being domains with a high interfacial hydrophobicity calculated with the Wimley-White hydrophobicity scale which was systematically used for searching fusion peptides in other viral glycoproteins. HB168–186, comprising the precise fusion loop HB173–179 [21], is located in the insertion between strands β 4 and β 11 and we were able to identify this region on the basis of its hydrophobicity, and analyse its role in peptide/lipid fusion assays [25]. The second loop (HB258–265), identified on the basis of structural data [21] contributes to the formation of the bipartite fusion peptide, but does not correspond to a hydrophobicity peak calculated with the interfacial scale and thus was not considered in our previous study [25].

Both fusion loops have been characterized by point-mutations in the protein sequence and showed to be critical for gB function in cell fusion [30]. In the present study, we report on the structural characterization of the two fusion loops by using peptides corresponding to their sequences. We synthesised a short version, corresponding exactly to the sequences of the loops, and a longer version, embracing the flanking β -sheets, in order to understand the contributions of each region that constitutes the gB fusogenic domain (Table 1). Moreover, we tried to understand the

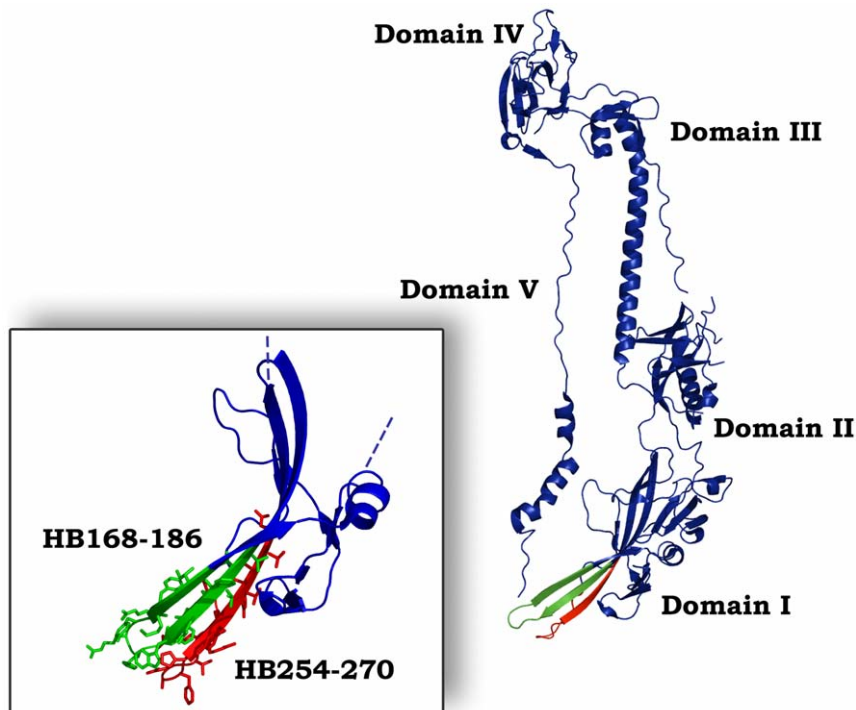


Figure 1. Three dimensional structure of a single gB protomer. The different domains are shown. In the insert are shown molecular details of the two fusion loops: HB168–186 (green) and HB254–270 (red).
doi:10.1371/journal.pone.0032186.g001

contribution of lipids that take part to the interplay between the membrane and fusogenic peptides.

Ability of peptides to induce lipid mixing

To investigate the fusogenicity of gB peptides, NBD and Rho labelled PE were used as the donor and acceptor of fluorescence energy transfer. A population of LUVs labelled with both was mixed with a population of unlabelled LUVs and increasing amounts of peptides were added. Dilution of the fluorescent-labelled vesicles via membrane fusion induced by the peptide results in a reduction of the fluorescence energy transfer efficiency, hence dequenching of the donor fluorescence. The dependence of the extent of lipid mixing on the peptide to lipid molar ratio was analysed. The fusogenic capacity was monitored by measuring their ability to induce lipid mixing of model membranes composed of DOPG, DOPG/Chol (3/2), DOPC, DOPC/Chol (3/2), POPC/Chol (3/2), and POPC/Chol/SM at various ratios (4/1/1, 2/1/1, 1/1/1).

Interestingly, there was a different behaviour of the peptides depending on the lipid composition of LUVs. Figure 2A and B show the results of lipid mixing assays in LUVs of different compositions for peptides HB168–186 and HB254–270. The graphs show that in all tested conditions HB168–186 has higher fusogenic ability. DOPC/Chol, POPC/Chol and DOPG/Chol all proved to be good fusogenic conditions. Furthermore, it is evident from the results obtained that DOPG in presence or absence of cholesterol represents a less fusogenic condition, indicating that the negatively charged phospholipids are not preferred. This is a rather interesting result as both peptides contain arginine residues and thus we could expect a greater interaction with anionic lipids. Several viruses such as HIV, influenza virus and Semliki Forest virus have been shown to involve lipid microdomains, which are enriched in cholesterol during virus budding as well as virus entry. Also herpesvirus has been shown to require cholesterol [31,32], and such a need for cholesterol has also been highlighted in our experiments using model membranes where a significant increase in fusion is always observed in presence of cholesterol. The lipids allowing the highest level of fusion are DOPC and POPC which are both zwitterionic but present a difference in their unsaturation, with POPC having only one unsaturated acyl chain and DOPC having two. DOPC results in a more flexible bilayer, which appears to be an important feature for the fusion activity of the analyzed peptides. We also tested the peptide fusion ability of liposomes containing sphingomyelin, a component commonly found in lipid rafts. The ternary lipid system POPC/Chol/SM is a good model for lipid rafts and from the ternary phase diagram [33] it is possible to determine the boundaries for lipid rafts which are strongly dependent on the percentage of each lipid in the system. We used three different conditions to probe the activity of our peptides in LUVs mimicking rafts: POPC/Chol/SM 4/1/1, 2/1/1 and 1/1/1, characterized by different percentages of the liquid

Table 1. Peptides.

	Sequence
HB168–186	NH ₂ -VTVSQVWFGHRYSQFMGIF-COOH
HB173–179	NH ₂ -VWFGHRY-COOH
HB254–270	NH ₂ -YNPSRVEAFHRYGTTVN-COOH
HB258–265	NH ₂ -RVEAFHRY-COOH
scrambled	NH ₂ -MRWFSVVSQVIGTQFGFH-COOH

doi:10.1371/journal.pone.0032186.t001

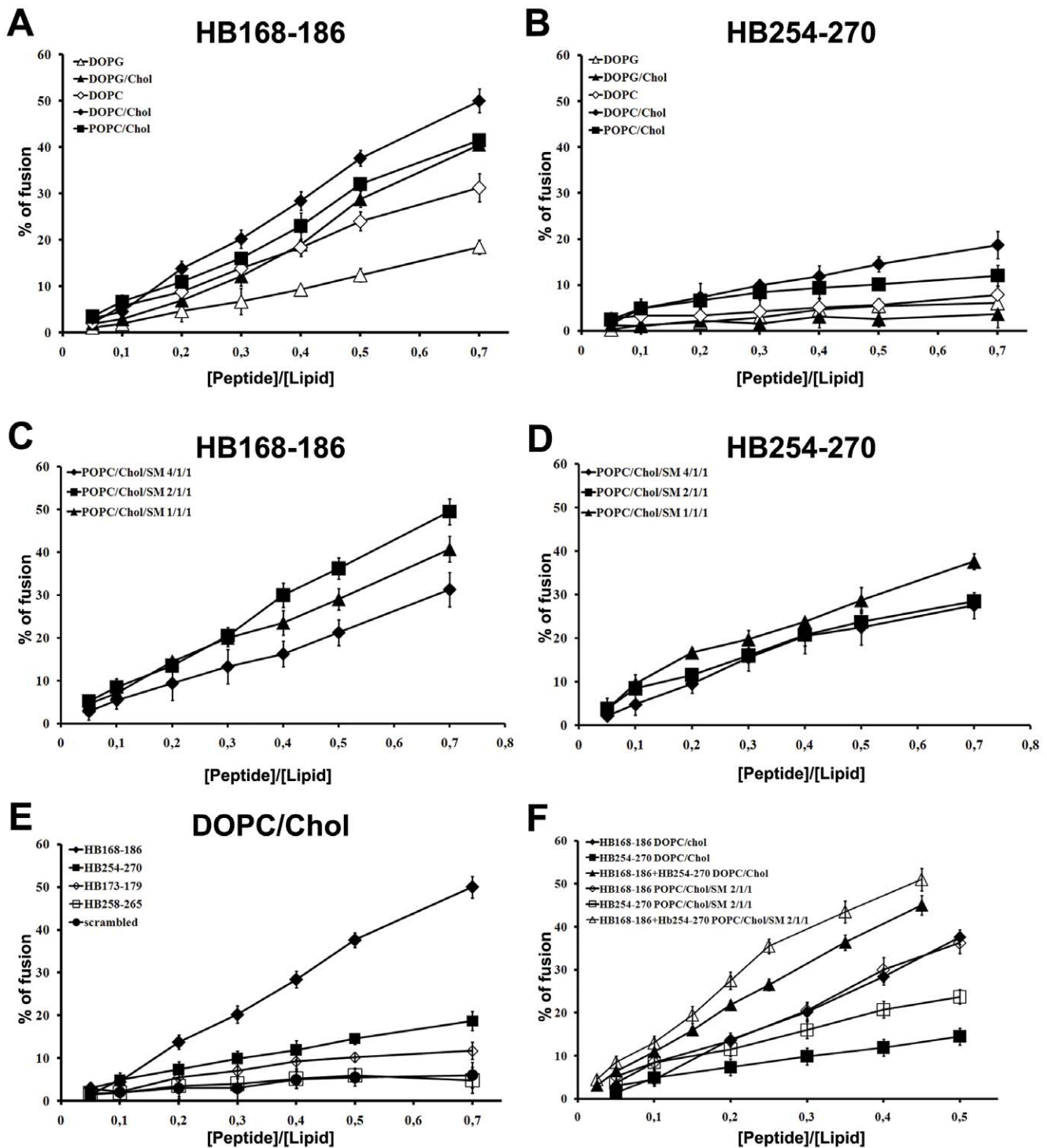


Figure 2. Ability of peptides to induce lipid mixing. Peptide-promoted membrane fusion as determined by lipid mixing; peptide aliquots were added to 0.1 mM LUVs, containing 0.6% NBD and 0.6% Rho. The increase in fluorescence was measured after the addition of peptide aliquots; reduced Triton-X-100 (0.05% v/v) was referred to as 100% of fusion. In figure is reported the dose dependence of lipid mixing at 37°C: panels A and B HB168–186 and HB254–270 in LUVs of different composition; panels C and D HB168–186 and HB254–270 in LUVs mimicking lipid rafts; panel E HB168–186, HB254–270 and shorter versions in DOPC/Chol LUVs; panel F equimolecular mixtures of peptides HB168–186 and HB254–270 in DOPC/Chol (3/2) and POPC/Chol/SM (2/1/1).
doi:10.1371/journal.pone.0032186.g002

ordered and liquid disordered phases. The results obtained (Figure 2 C–D) show that both peptides present a significant percentage of fusion

Figure 2E shows the results obtained in DOPC/Chol for the peptides HB168–186 and HB254–270 as well as their shorter versions corresponding exactly to the loop sequences derived from

the crystallographic structure. The two shorter peptides (HB173–179 and HB258–265) induced lower levels of fusion compared to longer sequences, suggesting that shorter peptides were unable to cross or stably position inside the bilayer. This result further supports the view that fusion loops are structured by the overall organization of the fusion domain of the protein and longer peptides are, therefore, necessary to evidence an appreciable fusion activity.

In the case of the peptide equimolar mixtures (Figure 2F), we can observe that in DOPC/Chol as well as in POPC/Chol/SM (2/1/1) we have a significant fusion activity supporting a cooperative mechanism.

Ability of peptides to induce lipid mixing of inner-monolayer

In the inner monolayer assay, the fluorescence from the vesicles' outer monolayer is eliminated by the addition of an aqueous reducing agent, and this experiment reveals the extent of lipid mixing between the inner monolayers of vesicles in solution. Figure 3A shows a significant fusion of the inner monolayer in DOPC/Chol. This is slightly lower than the fusion level obtained in the lipid mixing experiment, since the latter measures both hemi-fusion and complete fusion. Therefore, this assay clearly indicates that the two peptides are able to induce fusion of both the inner and the outer monolayers.

We also verified the ability of peptide equimolar mixtures to induce lipid mixing of the inner-monolayer. The results obtained indicate that the peptides cooperate in the fusion process.

Ability of peptides to induce membrane leakage

In order to explore the effects of the peptides in the destabilization of membrane vesicles, we studied their effect on the release of encapsulated fluorophores in model membranes made of DOPC/Chol. A content-mixing assay (Figure 3B) was employed to monitor any mixing of internal vesicle components as a result of vesicle exposure to HB168–186 and HB254–270. Release of ANTS and DPX from vesicle is commonly used as a measure of bilayer perturbation and interpreted as “transient pore formation” [34,35]. Content-mixing is manifested by a decrease in fluorescence intensity if vesicles encapsulating fluorescent cargo (e.g., ANTS) merge contents with those containing quenchers (e.g., DPX). The leakage experiment shows that the probe did not leak out significantly to the medium after the interaction with any of the peptides used in this study. Figure 3B shows that no content-mixing occurs over the same P/L range where substantial outer and inner monolayer lipid-mixing occurs, confirming that vesicle fusion may happen within our system without concomitant pore formation. The low leakage value observed for both peptides might be due to the fact that they are located at the membrane interface and do not completely traverse the bilayer. We also verified the eventual ability of equimolar mixtures of HB168–186 and HB254–270 to induce membrane leakage, but no significant difference from results obtained for individual peptides was detected.

Peptide aggregation

The peptide's aggregation state in buffer and DOPC/Chol LUVs was assayed using ThT [36], in order to know the possible effects of the peptide aggregation on the membranes. As observed in Figure 4 A–B, the two peptides present a completely different behaviour. The peptide HB168–186 at a concentration of 4 μ M (Figure 4A) is already aggregated in an aqueous medium, in fact, the fluorescence change increased dramatically after the addition

of the peptide from a stock solution, while in the presence of DOPC/Chol a lower aggregation is reported. The peptide HB254–270 is not aggregated in the aqueous medium nor in the presence of DOPC/Chol at the same concentration. Furthermore, we studied the intrinsic relationship between the concentration of the peptides and the aggregation in buffer and in LUVs and we can interpret the data for HB168–186 reported in Figure 4C as aggregated both in the aqueous medium and in LUVs at high concentrations. Our results are consistent with two hypothesis; the first is an initial aggregation in the aqueous medium, followed by a disaggregation when initially interacting with the membrane and again an aggregation inside the membrane bilayer, indicating that the insertion of the peptide into the membrane could occur in a monomeric form and only afterwards the peptide aggregates again; while the second hypothesis is that the peptide can interact with the membranes already in an oligomerized state.

Tryptophan/tyrosine fluorescence emission analysis

We measured the intrinsic fluorescence of HB168–186 and HB254–270 (due to the presence of a tryptophan residue in the sequence of HB168–186 and two tyrosines for HB254–270) to evaluate the degree of penetration of the peptides into the membrane bilayer. We compared the fluorescence emission spectra in DOPC/Chol vesicles with that in buffer (data not shown). The quantum yield of aromatic residues of a peptide or protein normally changes when the amino acid is located in a more hydrophobic environment such as a phospholipid membrane, normally increasing the intensity of the fluorescence emission and shifting the maximal spectral position toward shorter wavelengths (blue shift). Changes in the spectral properties were observed for both peptides, suggesting that the single tryptophan residue of HB168–186 and the two tyrosines of HB254–270 move to a less polar environment upon interaction with lipids. Emission intensity was enhanced and the maxima shifted to lower wavelength. (Figure S1) Blue shifts of this magnitude are generally observed when amphiphilic aromatic-containing peptides interact with phospholipid bilayers and are consistent with the aromatic moiety becoming partially immersed in the membrane, further suggesting that the analysed peptides are capable of penetrating a lipid bilayer [37].

The increase in fluorescence for tryptophan or tyrosines binding to membrane phospholipids was used for the generation of binding isotherms for HB168–186 and HB254–270, therefore partition coefficients could be calculated. The concentrations of peptides used were low enough to cause minimal aggregation in the aqueous phase and were assumed not to disrupt the bilayer structure. To determine the surface partition coefficient, the fluorescence intensities were converted to moles of bound peptide per moles of lipid and plotted as a function of the free peptide concentration as described in material and methods (Figure 5). As partition coefficients depend on the concentration of lipid accessible to peptide, the curves obtained by plotting X_b^* (the molar ratio of bound peptide per 60% of the total lipid) vs C_f (the equilibrium concentration of free peptide in the solution) are referred to as the conventional binding isotherms. The shape of a binding isotherm of a peptide can provide information on the organization of the peptide within the membrane. A straight line indicates a simple adhesion process. The shape of the binding isotherm of all the peptides tested was not linear indicating that peptide accumulation at the surface is not a simple phenomenon without cooperative association. In particular, this behaviour is the hallmark for peptides that self-associate at membrane surfaces upon partitioning. If aggregation occurred only in the water but not in the bilayer phase, the opposite course of the isotherms

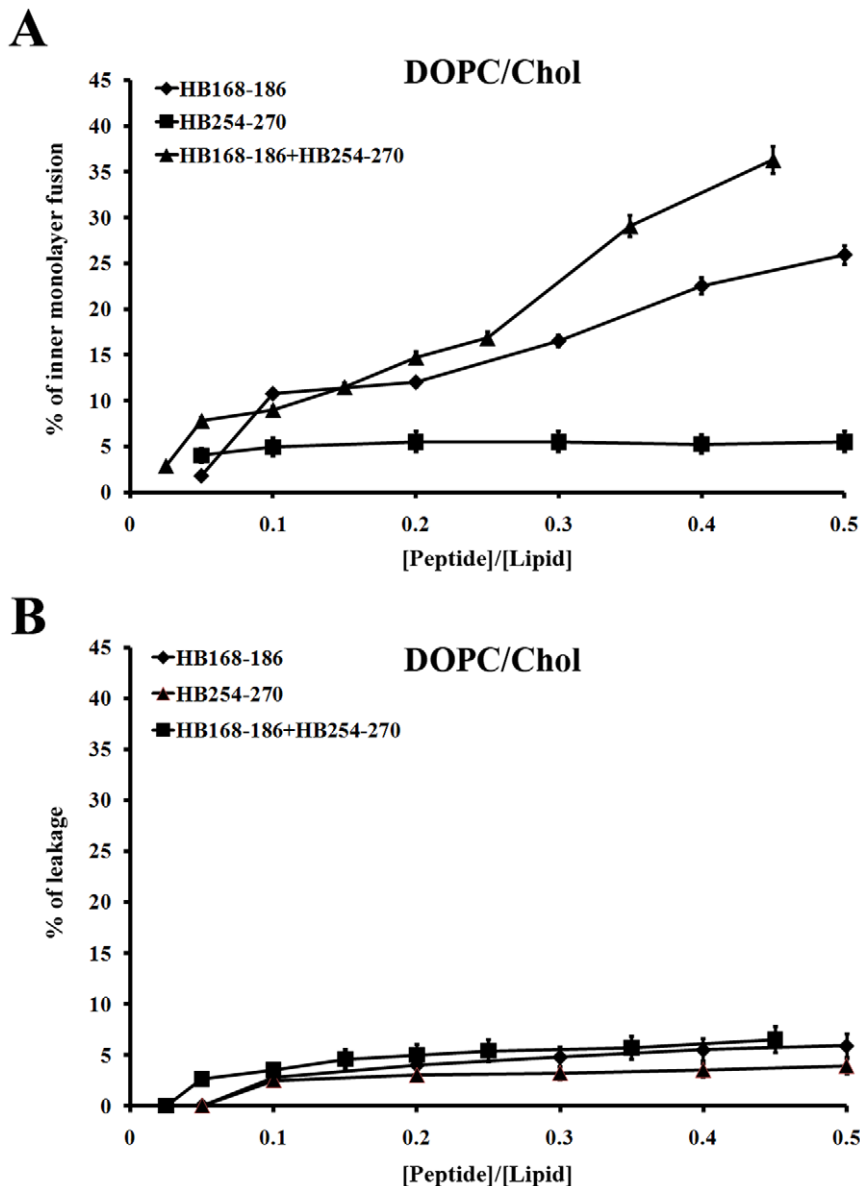


Figure 3. Ability of peptides to induce lipid mixing of inner-monolayer and membrane leakage. Peptide interactions with DOPC/Chol LUVs (A–B), the dose dependence is reported and each trace represents an average of three independent experiments. A) Inner monolayer assay. C) Leakage of ANTS/DPX.

doi:10.1371/journal.pone.0032186.g003

should be expected: a steep rise at the origin, followed by pronounced flattening; thus, the shape of the isotherms obtained could be interpreted as reflecting a process whereby peptides first incorporate into the membrane and then aggregate there within. Moreover, there was no evidence of significant aggregation in water at the concentration used in this experiment (0.1 μM) for HB254–270, although we have an indication of aggregation in water for HB168–186 as shown in Figure 4C. In the isotherms obtained, the total extent of incorporation (X_b^*) slowly increases until a critical concentration is reached, where massive internal aggregation apparently starts to develop.

The surface partition coefficients K_p were estimated by extrapolating the initial slopes of the curves to C_f values of zero. Curves are shown in Figure 5.

The K_p values for the peptides HB168–186 and HB254–270 are shown in Table 2. The K_p value obtained for HB168–186 is

$2.5 \cdot 10^4$, indicating that the tryptophan in HB168–186 is able to interact significantly with the bilayer and that most of the peptide HB168–186 is located inside the liposomes. The K_p value for HB254–270 is $3.2 \cdot 10^4$, indicating that the tyrosine residues present in this peptide are located inside the liposomes and are stably inserted.

Quenching of tryptophan/tyrosines by Acrylamide

The observed changes in the characteristics of the tryptophan/tyrosine emission upon binding of peptides HB168–186 and HB254–270 to lipid vesicles indicate their insertion into the hydrophobic region of the bilayers. We also studied the accessibility of the tryptophan/tyrosine residues of membrane-bound peptides towards acrylamide, a neutral, water-soluble, highly efficient quenching molecule, which is unable to penetrate

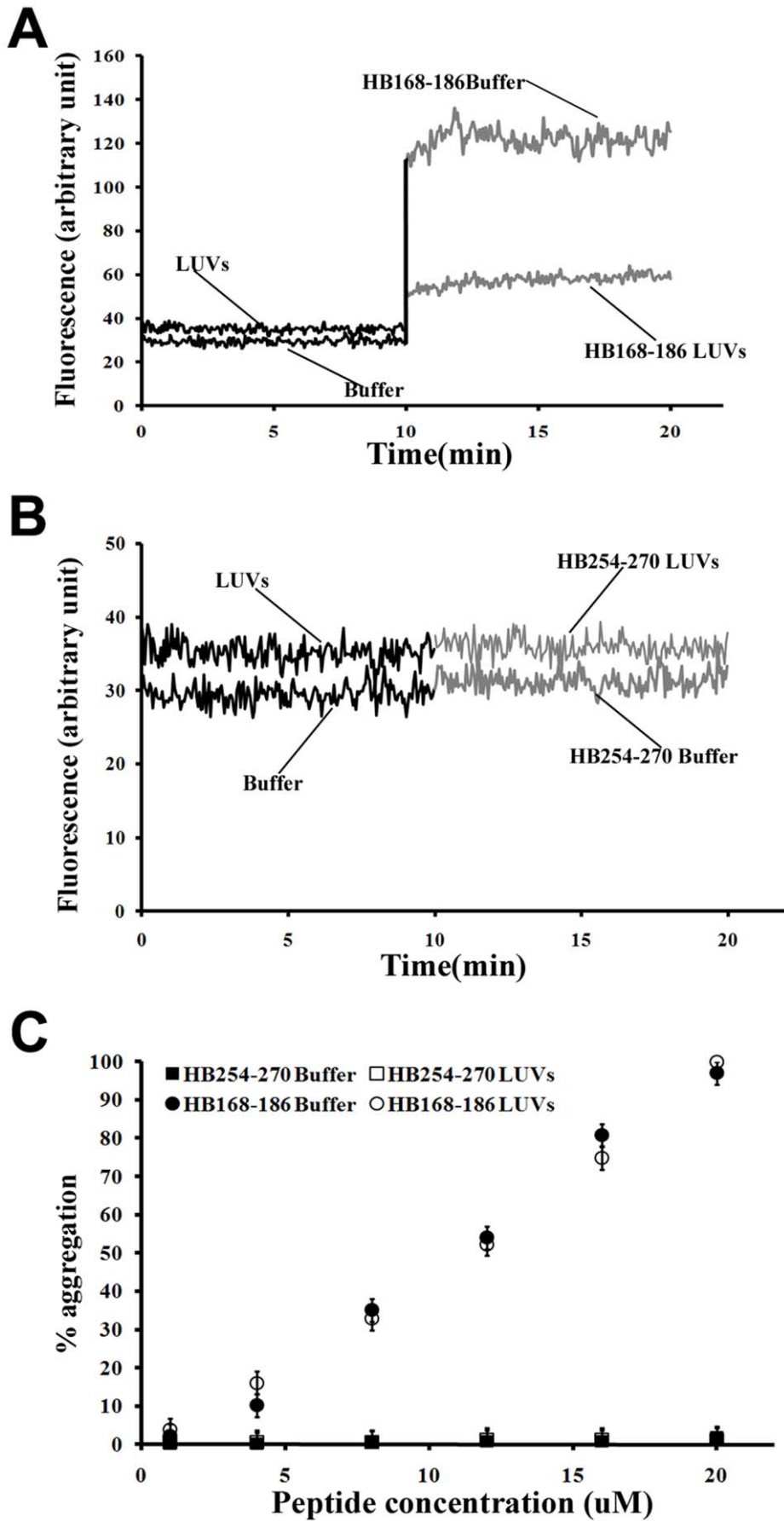


Figure 4. Peptide aggregation. Fluorescence variation of ThT after addition of HB168–186 (A) and HB254–270 (B) peptides to an aqueous solution and in the presence of LUVs of DOPC/Chol at a peptide concentration of 4 μM . (C) Percentage of aggregation as a function of peptide concentration for HB168–186 and HB254–270 in buffer (closed symbols) and in LUVs (open symbols). doi:10.1371/journal.pone.0032186.g004

into the hydrophobic core of the lipid bilayer. The more deeply a tryptophan/tyrosine residue is buried, the less strongly it can be quenched by acrylamide. Stern-Volmer plots for the quenching of tryptophan by acrylamide, recorded in the absence and presence of lipid vesicles, are depicted in Figure 6. Fluorescence of tryptophan/tyrosine decreased in a concentration-dependent manner by the addition of acrylamide to the peptide solution both in the absence and presence of liposomes, without other effects on the spectra. However, we can observe a substantial difference between the two peptides. In the presence of liposomes, a great decrease in fluorescence intensity was evident for HB254–270, thus revealing that tyrosine residues are less accessible to the quencher in the presence of LUVs. In fact, the values for K_{sv} were lower (Table 3) in LUVs, suggesting that tyrosines were more buried in the bilayers, becoming more inaccessible for quenching by acrylamide. From Figure 6, it is evident that we can observe for the peptide HB168–186 a low accessibility to the quencher both in absence and presence of liposomes, indicating that the peptide has a significant tendency to aggregate also in an aqueous solution.

ESR Results

The ESR spectroscopy, by using spin-labelled substances (peptides and/or lipids) has been proved to give substantial information on the interaction of peptide deriving from viral fusion glycoproteins with lipid membranes [38–41]. In the present work, the association of the two peptides, HB168–186 and HB254–270, with lipid bilayers was investigated by analysing changes in ESR spectra of spin-labelled phospholipids. The samples investigated were phosphatidylcholine spin-labelled at different positions, n , in the sn -2 chain (n -PCSL, $n = 5, 7, 10, 14$) incorporated in DOPC/Chol membranes (3/2), in the presence of the peptides. Preliminarily, the spectra in the absence of the peptides were registered. Inspection of Figure 7A (solid lines) shows that all the spectra present a clearly defined axially anisotropic lineshape, an evidence that, due to the high cholesterol content, the DOPC/Chol bilayer is in the liquid-ordered state [42]. In an attempt to quantitatively analyse the spectra, the outer hyperfine splitting, $2A_{max}$, was calculated. The $2A_{max}$ variation, shown in Figure 7B, is an evidence of the flexibility gradient in segmental acyl chain mobility [38,43], indicating that the lipid bilayer presents a rigid surface and relatively fluid interior [44–47].

Association of peptides to the lipid bilayer causes a significant variation in the ESR spectra of spin-labelled phospholipids. In Figure 7A, ESR spectra of 5-PCSL and 14-PCSL in DOPC/Chol bilayers, in the presence of HB168–186, HB254–270 and HB168–186:HB254–270 mixture at a lipid/peptide weight ratio of 1/1, are also reported. The presence of two peptides induces significant changes in the spin-label ESR spectra, which are mainly detectable from the low- and high-field component position and lineshape. In an attempt to quantify this evidence, the $2A_{max}$ values were determined. Figure 7B shows the dependence of these parameters on chain position, n , for the n -PCSL spin-labels in DOPC/Chol membranes, in the absence and in the presence of the peptides. In all cases, the flexibility gradient with the chain position of the lipid bilayer membranes is preserved. However, inspection of the figure reveals a significantly different behaviour of the lipid chain mobility in the co-presence of the two peptides.

In fact, addition of HB168–186 or HB254–270 significantly reduces the $2A_{max}$ value of 5-PCSL. In both cases, no changes in

the spectra of the spin-labels bearing the nitroxide group in the more interior positions were observed. Strikingly, addition of the HB168–186:HB254–270 mixture results in a strongly $2A_{max}$ decrease for all the considered spin-labels. These results show a cooperation of the peptides in perturbing the bilayer microstructure in that only in the presence of both of them the increase of segmental mobility propagates along the whole acyl chains. Thus, the contemporary interaction of both peptides with the lipid membrane surface effectively perturbs the local order and dynamics of the lipid leaflet they come in contact with.

Secondary structure in lipid bilayers

The CD spectra of the peptides in buffer and bound to LUVs made of DOPC/Chol are shown in Figure 8. The binding of the peptides to the membrane bilayer did not affect their structure. The spectra are indicative of random conformation for both peptides.

Discussion

Membrane fusion is of fundamental importance in the biological life of a cell and is of particular interest during enveloped virus infections. A common feature of all fusion events is the involvement of the fusion peptide in these phenomena and the key role played by lipids in the conformational changes leading to the interaction of the fusion peptide with target membranes, and in the membrane deformation following the initial peptide-membrane interactions. Extensive research data on viral membrane fusion proteins have disclosed the existence of several protein domains involved in the viral fusion process. It is, thus, an accepted view the presence of different membrane-active regions in viral fusion glycoproteins, although their biological function is still unclear. It has been hypothesised that these regions may have a different role on either pore formation and stabilization, viral budding or both of them.

In the present work we have investigated the role played by the two fusion loops of HSV-1 gB in the mechanism of membrane fusion. In particular, three important issues were addressed: the ability of peptide analogues of the fusion loops to induce fusion of liposomes, their ability to interact with the membrane bilayer when alone and when used in equimolar concentrations and the role of the target membrane composition. For herpesviruses, cholesterol is thought to play a key role, in fact, lipid raft may act as a platform allowing cell entry and potential coreceptors clustering [32] or cholesterol may modulate the HSV entry process regardless of its ability to promote lipids microdomains [48]. In this work evidences have been obtained indicating the ability of the two fusion peptide to induce fusion of liposomes *in vitro*, their ability to strongly interact with a membrane bilayer containing cholesterol and finally their different mode of interaction with the bilayer indicating that although being both involved in the fusion mechanism they may play a different role.

The two fusion loops constitute a structural subdomain wherein key hydrophobic amino acids form a ridge that is supported on both sides by charged residues. The two charged residues located on both sides of the ridge represent a novel feature of viral fusion peptides and probably enhance the ability of the hydrophobic residues to interact with target membranes and to promote fusion.

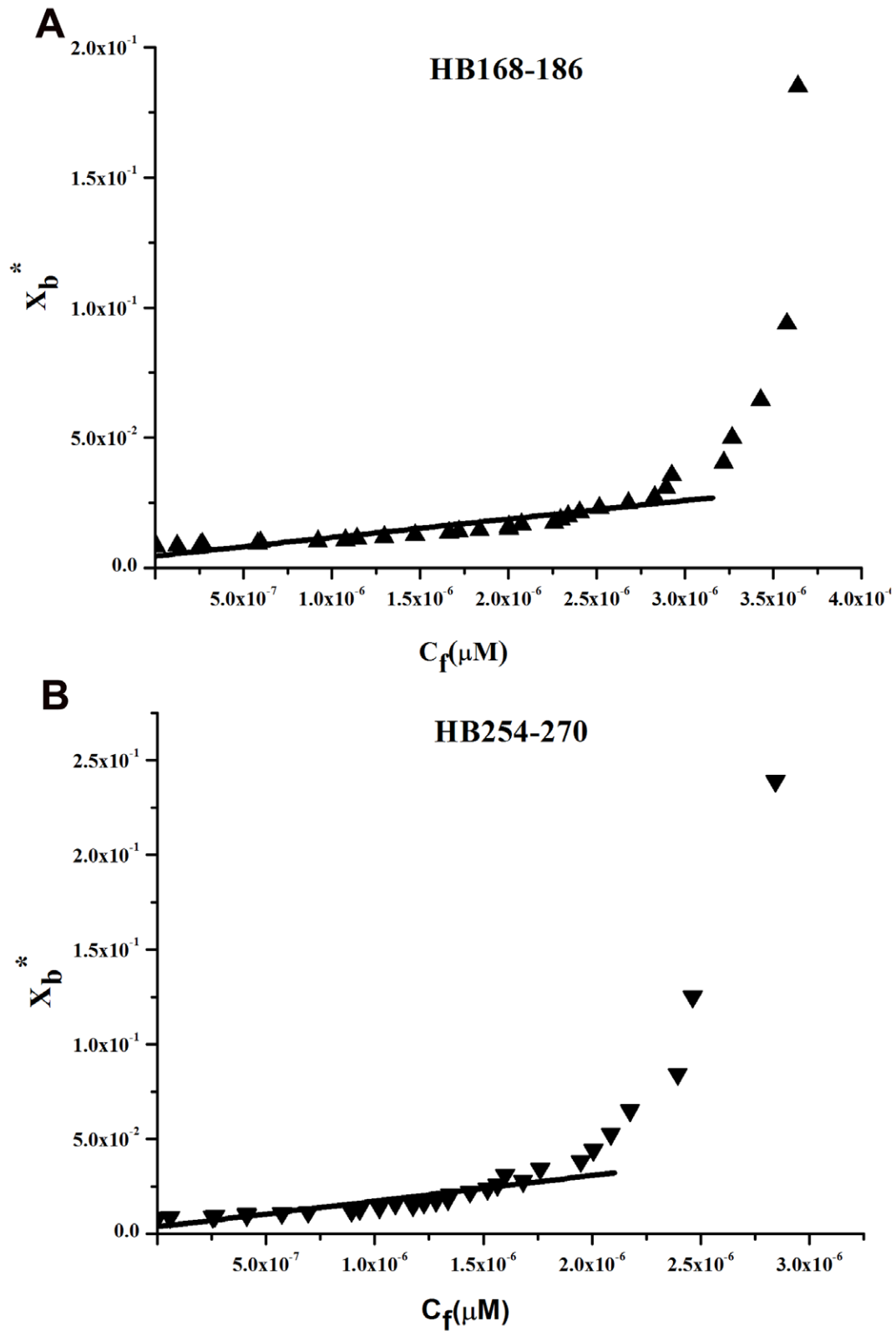


Figure 5. Tryptophan/tyrosine fluorescence emission analyses. Binding isotherms obtained plotting X_b^* versus C_f for HB168–186 and HB254–270.
doi:10.1371/journal.pone.0032186.g005

Table 2. Partition coefficient for the binding of peptides with PC/Chol.

	HB168–186	HB254–270
K_p	$(2.5 \pm 0.3)10^4$	$(3.2 \pm 0.2)10^4$

doi:10.1371/journal.pone.0032186.t002

The analysis of the location of the fusion loops into the three-dimensional structure of gB points out that the hydrophobic residues do not appear to be able to insert deeply into a target membrane. The hydrophilic residues on either side of the hydrophobic ridge may help to stabilize insertion of gB into cholesterol enriched membranes or more generally membranes mimicking lipid rafts, but both fusion loops seem unable to deeply penetrate into the hydrophobic core of the bilayer.

The fusion ability of the two peptides was analysed using LUVs with different compositions. Membrane components, such as anionic lipids (DOPG), unsaturated phospholipids (DOPC, POPC), sphingolipid (SM) and cholesterol (Chol) were used in this study. Lipid raft formation occurs by spontaneous aggregation of certain naturally occurring lipids that aggregate in the plane of the membrane and are characterized by a higher degree of molecular order and by being thicker than the surrounding liquid-disordered lipids in the membrane. To investigate lipid raft characteristics in model membranes, Chol and SM are commonly combined with phospholipids having unsaturated and therefore kinked fatty acyl chains, such as POPC. Our results are consistent with previous studies showing the specific association of gB with cholesterol-rich rafts [32]. We found that gB peptides associate with lower fusion ability with liposomes in the absence of cholesterol. Our data further suggest that the cholesterol dependence of gB is not necessarily dependent on a protein

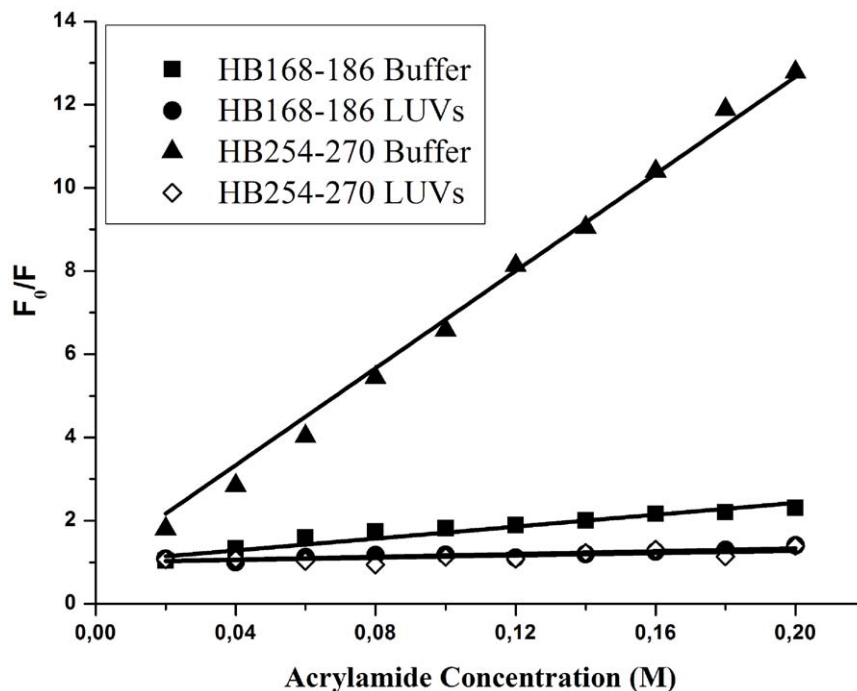
Table 3. Stern-Volmer (K_{sv}) quenching constant calculated from the equation $F_0/F = 1 + K_{sv} [Q]$ for HB168–186 and HB254–270.

	HB168–186	HB254–270
$K_{sv} (M^{-1})$ in buffer	8.3 ± 0.2	71.1 ± 1.1
$K_{sv} (M^{-1})$ in LUVs	6.4 ± 0.4	8.5 ± 0.1

doi:10.1371/journal.pone.0032186.t003

receptor in rafts, but because cholesterol itself enhances insertion of the fusion loops. In Semliki Forest virus fusion protein E1, a class II fusion protein that inserts preferentially into membranes enriched in cholesterol and sphingolipid [49], a point mutation in the loop adjacent to the fusion loop confers increased cholesterol independence [50,51].

Lipid mixing, inner-monolayer and leakage are three independent experiments which describe different processes during the interaction of peptides with liposomes. In particular, the lipid mixing experiment evidences the fusion of both the inner and outer monolayer, the inner monolayer experiment evidences the eventual presence of fusion of the inner monolayer, while the leakage describes the pore formation. Results were consistent among the three experiments for both peptides, supporting the hypothesis that the two peptides induce fusion of inner and outer monolayers but not formation of pores whenever used alone or in equimolar concentrations. The present results can be used as qualitative indicators of bilayer perturbation due to its interaction with the peptides and their superficially positioning. We have not detected any significant pore formation; in fact, vesicle fusion events were not accompanied by leakage of the aqueous contents of the vesicle as also reported for other peptides in a study published by Thoren et al. [52].

**Figure 6. Quenching of tryptophan/tyrosines by Acrylamide.** Stern-Volmer plots of acrylamide quenching of HB168–186 and HB254–270 in buffer (closed symbols) and in LUVs (open symbols).

doi:10.1371/journal.pone.0032186.g006

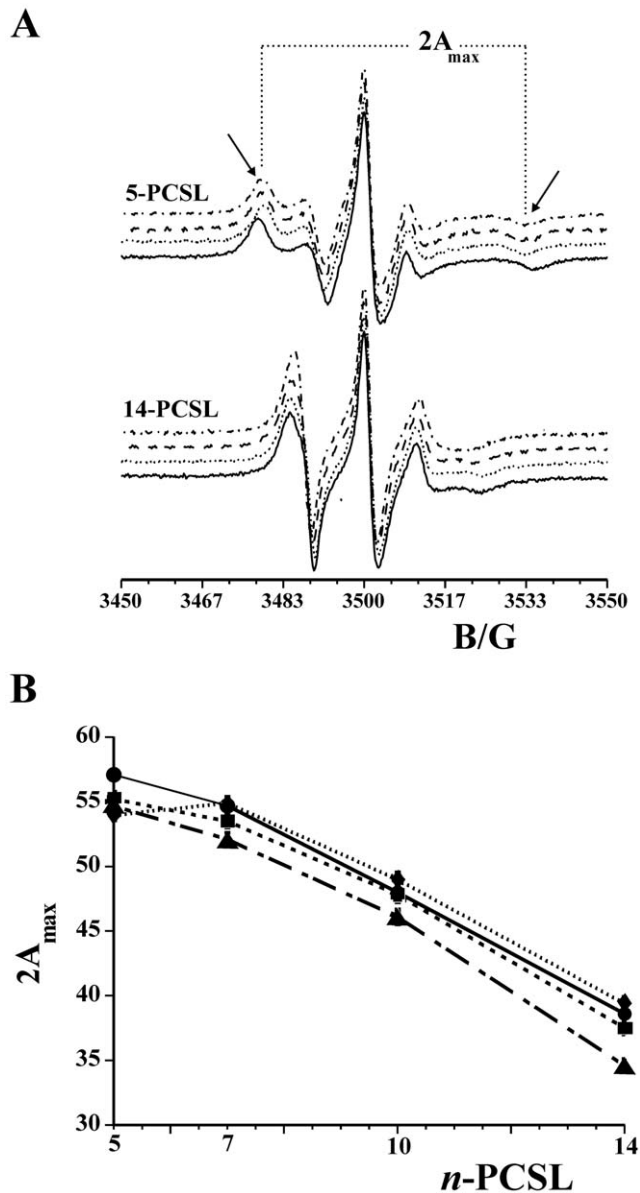


Figure 7. ESR Results. (A) ESR spectra of 5-PCSL and 14-PCSL spin-labels in DOPC/Chol membranes in the absence of peptides (solid line) and in the presence of HB168–186 (dotted line), HB254–270 (dashed line) and HB168–186:HB254–270 mixture (dashed-dotted line). (B) Dependence on spin-label position, n , of the outer hyperfine splittings, $2A_{\max}$, of the n -PCSL in DOPC/Chol bilayers in the absence (\circ) and in the presence of HB168–186 (\blacksquare), HB254–270 (\bullet) or HB168–186:HB254–270 (\blacktriangle) at $T = 25^\circ\text{C}$.
doi:10.1371/journal.pone.0032186.g007

Another novel feature revealed in the present work is the demonstration of oligomerization concomitant to fusion taking place. Although a correlation between penetration and fusion awaits further experimental support, our results suggest that oligomerization is another parameter related to the nature of the interaction of the peptide with the target membrane and plays a key role in governing fusion activity. The peptide HB168–186 presents a high tendency to oligomerize both in aqueous solution and inside the membrane. On the contrary, the peptide HB254–280 is not oligomerized in aqueous solution but it is able to oligomerize when interacting with the membranes.

Tryptophan and tyrosine side chains are often found at the interface between charged phospholipids and hydrophobic fatty acid chains of lipid membranes. The K_p values for the two peptides are reported in Table 2. Since K_p values are all of the same order (10^4), we concluded that the peptides have similar membrane-binding affinities. The values of K_p obtained are within the range of those obtained for membrane-permeating bioactive peptides such as mellitin and its derivatives [53], the Staphylococcus δ -toxin [54], the antibiotic dermaseptin [55], pardaxin analogues [56]. All the results obtained support a shallow insertion of the two peptides that may expand the head-group region of one of the monolayers and generate elastic stresses that are released by bilayer deformation. Our results demonstrate that these two gB peptides bind and interact with membranes and could thus be directly involved in merging of the viral and cellular membranes and might work cooperatively with other membrane active regions present on herpesvirus glycoproteins to boost the fusion process. These results improve the current understanding of the critical features required for viral fusogenic peptides to cross the membrane bilayer and seem promising for the development of new carrier peptides that could exploit viral membranotropic peptides for intracellular delivery [57–59].

HSV-1 might have several domains involved in the fusion process which either directly or indirectly, might interact with biological membranes, contributing to the viral envelope and cell membrane merging. Although the detailed mechanism of herpesvirus entry remains unclear, some important insights into the interplay of the proteins involved in membrane fusion have been gained recently, but there are still many unsolved questions such as if the two fusion loops are the only HSV fusion peptide; what triggers them to be inserted into the target membrane, what is the role of gH in fusion and if fusion domains present in gH are directly involved in fusion.

Materials and Methods

Materials

The Phospholipids: 1-palmitoyl-2-oleoyl-*sn*-glycero-3-phosphocholine (POPC), dioleoyl phosphatidylcholine (DOPC), dioleoyl phosphatidylglycerol (DOPG), N-octadecanoyl-D-*erythro*-sphingosylphosphorylcholine (SM), the fluorescent probes N-(7-nitrobenz-2-oxa-1,3-diazol-4-yl)phosphatidylethanolamine (NBD-PE) and N-(Lissamine-rhodamine-B-sulfonyl) phosphatidylethanolamine (Rho-PE) were purchased from Avanti Polar Lipids (Birmingham, AL, USA), while cholesterol (Chol) and Triton- \times 100 were from Sigma (St. Louis, MO, USA). All other reagents were of analytical grade. Spin-labelled phosphatidylcholines (n -PCSL) with the nitroxide group at different positions, n , in the *sn*-2 acyl chain were synthesized as described by Marsh [60]. The spin-labels were stored at -20°C in ethanol solutions at a concentration of 1 mg/mL.

Peptide synthesis

Peptides were synthesised using standard solid-phase-9-fluorenylmethoxycarbonyl (Fmoc) method as previously reported [25]. All purified peptides (purity higher than 98%) were obtained with good yields (30–40%). Table 1 shows the sequences of all the synthesized peptides. Peptide stock solutions were prepared in buffer with 2% dimethyl sulfoxide (DMSO).

Liposome preparation

Large unilamellar vesicles (LUVs) consisting of DOPG, DOPG/Chol (3/2), DOPC, DOPC/Chol (3/2), POPC/Chol (3/2),

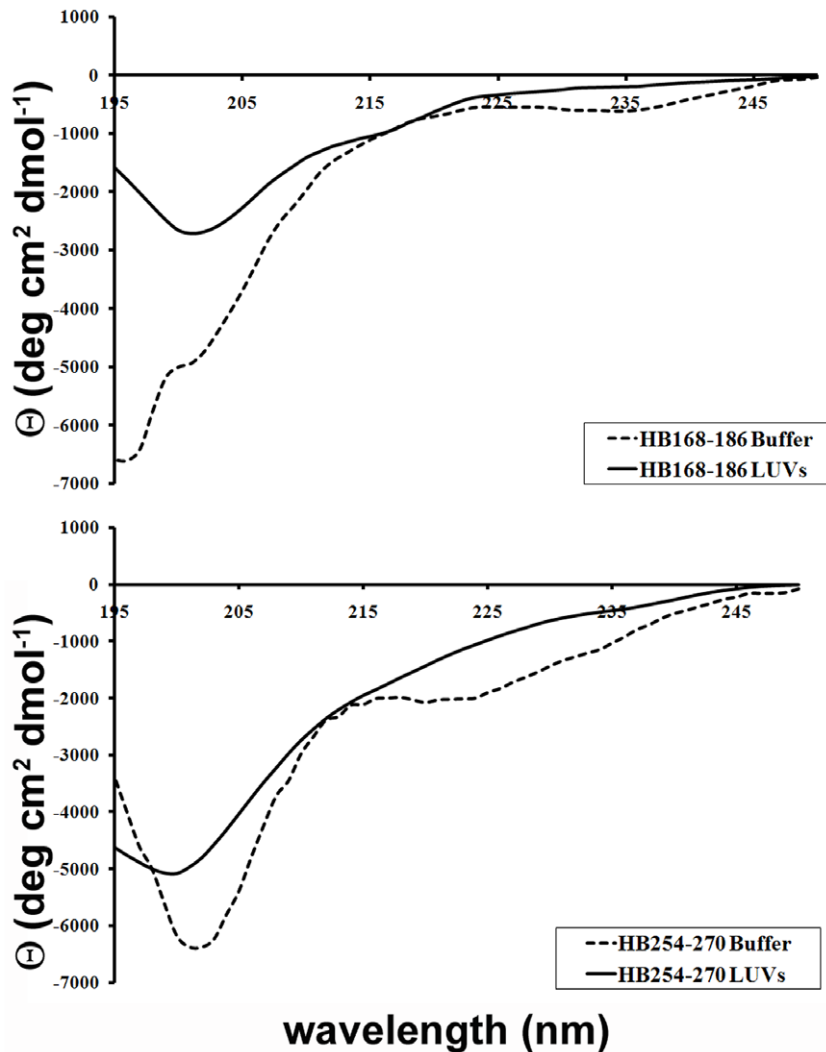


Figure 8. Secondary structure in lipid bilayers. CD spectra of HB168–186 and HB254–270 in buffer and in DOPC/Chol LUVs. doi:10.1371/journal.pone.0032186.g008

POPC/Chol/SM (4/1/1), POPC/Chol/SM (2/1/1) and POPC/Chol/SM (1/1/1), and when necessary containing Rho-PE and NBD-PE, were prepared according to the extrusion method of Hope et al. [61] in 5 mM HEPES, 100 mM NaCl, pH 7.4. Lipids were dried from a chloroform solution with a nitrogen gas stream and lyophilized overnight. For fluorescence and circular dichroism experiments, dry lipid films were suspended in buffer by vortexing for 1 h; then the lipid suspension was freeze-thawed 6 times and extruded 20 times through polycarbonate membranes with 0.1 μm diameter pores to produce LUVs. Lipid concentrations of liposome suspensions were determined by phosphate analysis [62]. For ESR spectroscopy, multi-lamellar vesicles (MLVs) were prepared. In these samples, 1% (wt/wt) of the spin-label, dissolved in ethanol, was added to the lipid mixture in organic solvent before drying. MLVs suspensions were obtained by the same procedure described above, excluding the extrusion step.

Lipid mixing assays

Membrane lipid mixing was monitored using the resonance energy transfer assay (RET) reported by Struck et al. [63]. The assay is based on the dilution of the NBD-PE (donor) and Rho-PE

(acceptor). Dilution due to membrane mixing results in an increase in NBD-PE fluorescence. The change in donor emission was monitored as aliquots of peptides were added to vesicles. Vesicles containing 0.6 mol % of each probe were mixed with unlabelled vesicles at a 1:4 ratio (final lipid concentration 0.1 mM). Small volumes of peptides in dimethylsulfoxide (DMSO) were added; the final concentration of DMSO in the peptide solution was no higher than 2%. The NBD emission at 530 nm was followed with the excitation wavelength set at 465 nm. A cut off filter at 515 nm was used between the sample and the emission monochromator to avoid scattering interferences. The fluorescence scale was calibrated such that the zero level corresponded to the initial residual fluorescence of the labelled vesicles and the 100% value corresponding to complete mixing of all lipids in the system was set by the fluorescence intensity of vesicles upon the addition of Triton X-100 (0.05% v/v) at the same total lipid concentrations of the fusion assay. Lipid mixing experiments were repeated at least three times and results were averaged. Control experiments were performed using a scrambled peptide and DMSO. All the experiments were performed at 37°C.

Inner-monolayer phospholipid-mixing (fusion) measurement

Peptide-induced phospholipid-mixing of the inner monolayer was measured by a modification of the phospholipid-mixing measurement reported elsewhere [64]. The concentration of each of the fluorescent probes within the liposome membrane was 0.6% mol. LUVs were treated with sodium dithionite 100 mM (from a stock solution of 1 M dithionite in 1 M TRIS, pH 10.0) to completely reduce the NBD-labelled phospholipid located at the outer monolayer of the membrane, for approximately 1 h on ice in the dark. Sodium dithionite was then removed by size exclusion chromatography through a Sephadex G-75 50 DNA Grade filtration column (GE Healthcare) eluted with a buffer containing 10 mM TRIS, 100 mM NaCl, and 1 mM EDTA, pH 7.4.

Measurements of ANTS/DPX leakage

The ANTS/DPX assay [34] was used to measure the ability of the peptide to induce leakage of ANTS/DPX pre-encapsulated in liposomes. Details of this assay can be found elsewhere [35]. To initiate a leakage experiment, the peptide, in a stock solution at pH 7.4 containing 5 mM HEPES and 100 mM NaCl, was added to the stirred vesicle suspension (0.1 mM lipid) at 37°C.

Thioflavin T assays for peptide aggregation

Peptide aggregation was assayed using Thioflavin T (ThT). ThT associates rapidly with aggregated peptides giving rise to a new excitation maximum at 450 nm and an enhanced emission at 482 nm [36]. LUVs in 100 mM NaCl, 10 mM Tris-HCl, 25 μ M ThT, pH 7.4 (final phospholipid concentration of 0.1 mM) were titrated with a peptide concentration of 1, 4, 8, 12, 16, 20 μ M. Fluorescence was measured before and after the desired amount of peptide was added into the cuvette using a Varian Cary Eclipse fluorescence spectrometer at 37°C. Samples were excited at 450 nm (slit width, 5 nm) and fluorescence emission was recorded at 482 nm (slit width, 5 nm). Aggregation was quantified according to the equation, $\%A = (F_t - F_0) / (F_{max} - F_0) \times 100$, where F_t is the value of fluorescence after peptide addition, F_0 the initial fluorescence in the absence of peptide and F_{max} is the fluorescence maximum obtained immediately after peptide addition. Kinetic data were obtained at a concentration of 4 μ M.

Tryptophan and Tyrosine fluorescence measurements

Emission spectra of the peptides (1 μ M) containing the tryptophan and tyrosine residue in the absence or presence of target vesicles (DOPC/Chol 1/1) were recorded: between 300 and 400 nm with an excitation wavelength of 295 nm for the peptide HB168–186 and 290 and 350 with an excitation wavelength of 274 nm for the peptide HB254–270. The degree of peptide association with lipid vesicles was measured by adding lipid vesicles to 1 μ M peptides and the fluorescence intensity was measured as a function of the lipid/peptide molar ratio, in three to four separate experiments. The fluorescence values were corrected by taking into account the dilution factor corresponding to the addition of microliter amounts of liposomes and by subtracting the corresponding blank. The lipid/peptide molar ratio was 200:1.

The binding of hydrophobic peptides to membranes can be described as a partition equilibrium: $X_b = K_p C_f$ where K_p is the apparent partition coefficient in units of M^{-1} , X_b is the molar ratio of bound peptide per total lipid and C_f is the equilibrium concentration of the free peptide in solution, as previously suggested by Schwarz et al. [65]. F_∞ was obtained by extrapolation of a double reciprocal plot of the total peptide fluorescence vs the total lipid concentration in the outer leaflet, i.e. $1/F$ vs $1/0.6C_L$.

The fraction of membrane-bound peptide, f_b , was determined by the formula $f_b = (F - F_0) / (F_\infty - F_0)$, where F represents the fluorescence of peptide after the addition of the vesicles and F_0 represents the fluorescence of the unbound peptide. f_b allowed us to calculate the equilibrium concentration of free peptide in the solution, C_f , and the extent of peptide binding X_b . Assuming that the peptides were initially partitioned only over the outer leaflet of the SUV (60% the total lipid) [66], values of X_b were corrected as follows: $X_b^* = X_b / 0.6$.

The curve resulting from plotting X_b^* versus the concentration of the free peptide, C_f , is the binding isotherm.

Tryptophan and Tyrosine quenching by Acrylamide

Aliquots of a 4 M solution of the water-soluble quencher were added to the solution containing the peptide (1 μ M) in the absence or presence of liposomes at a peptide/lipid molar ratio of 1/200. The maximal concentration of acrylamide is 0.2 mmol/ml. Tryptophan fluorescence was measured with an excitation wavelength of 295 nm, to reduce acrylamide absorbance (and the resulting inner filter effect), and emission at a wavelength of 340 nm, to eliminate interference from the Raman band of water [67] and tyrosine fluorescence was measured with an excitation wavelength of 274 nm, and emission at a wavelength of 305. The data were analyzed according to the Stern-Volmer equation [68], $F_0/F = 1 + K_{sv} [Q]$, where F_0 and F represent the fluorescence intensities in the absence and the presence of the quencher (Q), respectively, and K_{sv} is the Stern-Volmer quenching constant, which is a measure of the accessibility of tryptophan to acrylamide. Acrylamide does not significantly partition into the membrane bilayer [67], and the value for K_{sv} is a reliable reflection of the bimolecular rate constant for collisional quenching of the aromatic residues present in the aqueous phase. Accordingly, K_{sv} is determined by the amount of non-vesicle-associated free peptide as well as the fraction of the peptide residing at the surface of the bilayer.

Electron Spin Resonance Spectroscopy

ESR spectra were recorded with a 9 GHz Bruker Elexys E-500 spectrometer (Bruker, Rheinstetten, Germany). The lipid suspensions to be investigated were transferred into 25 μ L glass capillaries and flame sealed. The capillaries were placed in a standard 4 mm quartz sample tube containing light silicone oil for thermal stability. All the measurements were performed at 25°C. Spectra were recorded using the following instrumental settings: sweep width, 100 G; resolution, 1024 points; time constant, 20.48 ms; modulation frequency, 100 kHz; modulation amplitude, 1.0 G; incident power, 6.37 mW. Samples containing the peptides were prepared by hydrating the lipid film directly with the peptide solution in buffer. In all samples, the peptide to lipid ratio was set to 1:1 wt/wt. In samples containing both HB168–186 and HB254–270, the total peptide to lipid ratio was maintained to 1:1 wt/wt, while the HB168–186:HB254–270 ratio was 1:1 wt/wt.

Several scans, typically 16, were accumulated to improve the signal-to-noise ratio. Values of the outer hyperfine splitting, $2A_{max}$, were determined by measuring the difference between the low-field maximum and the high-field minimum, through a home-made, MATLAB-based, software routine. This parameter is a useful empirical measure of the lipid chain dynamics and order in both gel and fluid phases of lipid bilayers [44–46]. The main source of error on the $2A_{max}$ value is the uncertainty in composition of samples prepared by mixing few microliters of mother solutions. For this reason, reproducibility of $2A_{max}$ determinations was estimated by evaluating its value for selected independently

prepared samples with the same nominal composition. It was found to be $\pm 0.2\text{--}0.3$ G.

Circular dichroism spectroscopy

CD spectra were recorded using a Jasco J-715 spectropolarimeter in a 1.0 cm quartz cell at room temperature. The spectra are an average of 3 consecutive scans from 260 to 195 nm, recorded with a band width of 3 nm, a time constant of 16 s, and a scan rate of 10 nm/min. Spectra were recorded and corrected for the blank sample. Mean residue ellipticities (MRE) were calculated using the expression $MRE = Obsd/(lcn)$, where *Obsd* is the ellipticity measured in millidegrees, *l* is the path length of the cell in cm, *c* is the peptide concentration in mol/l, and *n* is the number of amino acid residues in the peptide. Solutions of 4 μM of HB168–186 and 10 μM of HB254–270 with LUVs were prepared as described previously [31]. The measurements were performed at peptide/lipid ratios of 0.5 mol/mol.

References

- Falanga A, Cantisani M, Pedone C, Galdiero S (2009) Membrane fusion and fission: enveloped viruses. *Prot Pept Lett* 16: 751–759.
- Galdiero S (2009) Developments in membrane fusion. *Prot Pept Lett* 16: 711.
- Chernomordik LV, Kozlov MM (2003) Protein-lipid interplay in fusion and fission of biological membranes. *Annu Rev Biochem* 72: 175–207.
- Harrison SC (2008) Viral membrane fusion. *Nature Structural Molecular Biology* 15: 690–698.
- Drin G, Casella JF, Gautier R, Boehmer T, Schwartz TU, et al. (2007) A general amphipathic alpha-helical motif for sensing membrane curvature. *Nat Struct Mol Biol* 14: 138–146.
- Antony B (2011) Mechanisms of membrane curvature sensing. *Annu Rev Biochem* 80: 101–123.
- Connolly SA, Jackson JO, Jardetzky TS, Longnecker R (2011) Fusing structure and function: a structural view of the herpesvirus entry machinery. *Nat Rev Microbiol* 9: 369–381.
- Turner A, Bruun B, Minson T, Browne H (1998) Glycoproteins gB, gD, and gH/gL of herpes simplex virus type 1 are necessary and sufficient to mediate membrane fusion in a Cos cell transfection system. *J Virol* 72: 873–875.
- Farnsworth A, Wisner TW, Webb M, Roller R, Cohen G, et al. (2007) Herpes simplex virus glycoproteins gB and gH function in fusion between the virion envelope and the outer nuclear membrane. *Proc Natl Acad Sci U S A* 104: 10187–10192.
- Atanasiu D, Whitbeck JC, Cairns TM, Reilly B, Cohen GH, et al. (2007) Bimolecular complementation reveals that glycoproteins gB and gH/gL of herpes simplex virus interact with each other during cell fusion. *Proc Natl Acad Sci U S A* 104: 18718–18723.
- Avitabile E, Forghieri C, Campadelli-Fiume G (2007) Complexes between herpes simplex virus glycoproteins gD, gB, and gH detected in cells by complementation of split enhanced green fluorescent protein. *J Virol* 81: 11532–11537.
- Galdiero S, Vitiello M, D'Isanto M, Falanga A, Collins C, et al. (2006) Analysis of synthetic peptides from heptad-repeat domains of herpes simplex virus type 1 glycoproteins H and B. *J Gen Virol* 87: 1085–1097.
- Galdiero S, Falanga A, Vitiello M, Browne H, Pedone C, et al. (2005) Fusogenic domains in herpes simplex virus type 1 glycoprotein H. *J Biol Chem* 280: 28632–28643.
- Galdiero S, Falanga A, Vitiello M, D'Isanto M, Collins C, et al. (2007) Evidence for a role of the membrane-proximal region of herpes simplex virus Type 1 glycoprotein H in membrane fusion and virus inhibition. *Chembiochem* 8: 885–895.
- Galdiero S, Falanga A, Vitiello M, D'Isanto M, Cantisani M, et al. (2008) Peptides containing membrane-interacting motifs inhibit herpes simplex virus type 1 infectivity. *Peptides* 29: 1461–1471.
- Galdiero S, Falanga A, Vitiello M, Raiola L, Fattorusso R, et al. (2008) Analysis of a membrane interacting region of herpes simplex virus type 1 glycoprotein H. *J Biol Chem* 283: 29993–30009.
- Galdiero S, Falanga A, Vitiello M, Pedone C, et al. (2010) Role of membranotropic sequences from herpes simplex virus type I glycoproteins B and H in the fusion process. *Biochim Biophys Acta* 1798: 579–591.
- Galdiero S, Falanga A, Vitiello M, Raiola L, Russo L, et al. (2010) The presence of a single N-terminal histidine residue enhances the fusogenic properties of a Membranotropic peptide derived from herpes simplex virus type 1 glycoprotein H. *J Biol Chem* 285: 17123–17136.
- Chowdary TK, Cairns TM, Atanasiu D, Cohen GH, Eisenberg RJ, et al. (2010) Crystal structure of the conserved herpesvirus fusion regulator complex gH-gL. *Nat Struct Mol Biol* 17: 882–888.
- Matsuura H, Kirschner AN, Longnecker R, Jardetzky TS (2010) Crystal structure of the Epstein-Barr virus (EBV) glycoprotein H/glycoprotein L (gH/gL) complex. *Proc Natl Acad Sci U S A* 107: 22641–22646.
- Heldwein EE, Lou H, Bender FC, Cohen GH, Eisenberg RJ, et al. (2006) Crystal structure of glycoprotein B from herpes simplex virus 1. *Science* 313: 217–220.
- Backovic M, Longnecker R, Jardetzky TS (2009) Structure of a trimeric variant of the Epstein-Barr virus glycoprotein B. *Proc Natl Acad Sci U S A* 106: 2880–2885.
- Roche S, Bressanelli S, Rey FA, Gaudin Y (2006) Crystal structure of the low-pH form of the vesicular stomatitis virus glycoprotein G. *Science* 313: 187–191.
- Kadlec J, Loureiro S, Abrescia NG, Stuart DI, Jones IM (2008) The postfusion structure of baculovirus gp64 supports a unified view of viral fusion machines. *Nat Struct Mol Biol* 15: 1024–1030.
- Galdiero S, Vitiello M, D'Isanto M, Falanga A, Cantisani M, et al. (2008) The identification and characterization of fusogenic domains in herpes virus glycoprotein B molecules. *Chembiochem* 9: 758–767.
- Akkarawongsa R, Pocaro NE, Case G, Kolb AW, Brandt CR (2009) Multiple peptides homologous to herpes simplex virus type 1 glycoprotein B inhibit viral infection. *Antimicrob Agents Chem* 53: 987–996.
- Hannah BP, Heldwein EE, Bender FC, Cohen GH, Eisenberg RJ (2007) Mutational evidence of internal fusion loops in herpes simplex virus glycoprotein B. *J Virol* 81: 4858–4865.
- Roche S, Albertini AA, Lepault J, Bressanelli S, Gaudin Y (2008) Structures of vesicular stomatitis virus glycoprotein: membrane fusion revisited. *Cell Mol Life Sci* 65: 1716–1728.
- Sun X, Belouard S, Whittaker GR (2008) Molecular architecture of the bipartite fusion loops of vesicular stomatitis virus glycoprotein G, a class III viral fusion protein. *J Biol Chem* 283: 6418–6427.
- Hannah BP, Heldwein EE, Bender FC, Cohen GH, Eisenberg RJ (2007) Mutational evidence of internal fusion loops in herpes simplex virus glycoprotein B. *J Virol* 81: 4858–4865.
- Vitiello G, Falanga A, Galdiero M, Marsh D, Galdiero S, et al. (2011) Lipid composition modulates the interaction of peptides deriving from herpes simplex virus type I glycoproteins B and H with biomembranes. *Biochim Biophys Acta* 1808: 2517–2526.
- Bender FC, Whitbeck JC, Ponce de Leon M, Lou H, Eisenberg RJ, et al. (2003) Specific association of glycoprotein B with lipid rafts during herpes simplex virus entry. *J Virol* 77: 9542–9552.
- de Almeida RFM, Fedorov A, Prieto M (2003) Sphingomyelin/Phosphatidylcholine/cholesterol phase diagram: boundaries and composition of lipid rafts. *Biophys J* 85: 2406–2416.
- Ellens H, Bentz J, Szoka JrFC (1984) pH-induced destabilization of phosphatidylethanolamine-containing liposomes: role of bilayer contact. *Biochemistry* 23: 1532–1538.
- Parente RA, Nir S, Szoka JrFC (1990) Mechanism of leakage of phospholipid vesicle contents induced by the peptide GALA. *Biochemistry* 29: 8713–8719.
- Levine III H (1993) Thioflavine T interaction with synthetic Alzheimer's disease β -amyloid peptides: Detection of amyloid aggregation in solution. *Prot Sci* 2: 404–410.
- Yau WM, Wimley WC, Gawrisch K, White SH (1998) The preference of tryptophan for membrane interfaces. *Biochemistry* 37: 14713–14718.
- Gordon LM, Curtain CC, Zhong YC, Kirkpatrick A, Mobley PW, et al. (1992) The amino-terminal peptide of HIV-1 glycoprotein 41 interacts with human erythrocyte membranes: peptide conformation, orientation and aggregation. *Biochim Biophys Acta* 1139: 257–274.

Supporting Information

Figure S1 Fluorescence spectra of tryptophan and tyrosine. Fluorescence spectra of HB168–186 and HB254–270 in buffer and in LUVs. (TIF)

Acknowledgments

The authors thank Mr. Leopoldo Zona for technical assistance.

Author Contributions

Conceived and designed the experiments: MG SG. Performed the experiments: AF RT GV MV EP MC. Analyzed the data: AF GD MG SG. Contributed reagents/materials/analysis tools: MG SG. Wrote the paper: AF GD MG SG.

39. Curtain C, Separovic F, Nielsen K, Craik D, Zhong Y, et al. (1999) The interactions of the N-terminal fusogenic peptide of HIV-1 gp41 with neutral phospholipids. *European Biophysical Journal* 28: 427–436.
40. D'Errico G, D'Ursi AM, Marsh D (2008) Interaction of a peptide derived from glycoprotein gp36 of feline immunodeficiency virus and its lipoylated analogue with phospholipid membranes. *Biochemistry* 47: 5317–5327.
41. Spadaccini R, D'Errico G, D'Alessio V, Notomista E, Bianchi A, et al. (2010) Structural characterization of the transmembrane proximal region of the hepatitis C virus E1 glycoprotein. *Biochim Biophys Acta* 1798: 344–353.
42. Marsh D (2010) Liquid-ordered phases induced by cholesterol: a compendium of binary phase diagrams. *Biochim Biophys Acta* 1798: 688–699.
43. Swamy MJ, Marsh D (1994) Spin-label electron spin resonance studies on the dynamics of the different phases of N-biotinylphosphatidylethanolamines. *Biochemistry* 33: 11656–11663.
44. Moser M, Marsh D, Meier P, Wassmer KH, Kothe G (1989) Chain configuration and flexibility gradient in phospholipid membranes. Comparison between spin-label electron spin resonance and deuterium nuclear magnetic resonance, and identification of new conformations. *Biophys J* 55: 111–123.
45. Rama Krishna YVS, Marsh D (1990) Spin label ESR and ³¹P-NMR studies of the cubic and inverted hexagonal phases of dimyristoylphosphatidylcholine/myristic acid (1:2, mol/mol) mixtures. *Biochim Biophys Acta* 1024: 89–94.
46. Lange A, Marsh D, Wassmer KH, Meier P, Kothe G (1985) Electron spin resonance study of phospholipid membranes employing a comprehensive line-shape model. *Biochemistry* 24: 4383–4392.
47. D'Errico G, Vitiello G, Ortona O, Tedeschi A, Ramunno A, et al. (2008) Interaction between Alzheimer's Abeta(25–35) peptide and phospholipid bilayers: the role of cholesterol. *Biochim Biophys Acta* 1778: 2710–2716.
48. Hammah BP, Cairns TM, Bender FC, Whitbeck JC, Lou H, et al. (2009) Herpes simplex virus glycoprotein B associates with target membranes via its fusion loops. *J Virol* 83: 6825–6836.
49. Ahn A, Gibbons DL, Kielian M (2002) The fusion peptide of Semliki Forest virus associates with sterol-rich membrane domains. *J Virol* 76: 3267–3275.
50. Chatterjee PK, Eng CH, Kielian M (2002) Novel mutations that control the sphingolipid and cholesterol dependence of the Semliki Forest virus fusion protein. *J Virol* 76: 12712–12722.
51. Vashishtha M, Phalen T, Marquardt MT, Ryu JS, Ng AC, et al. (1998) A single point mutation controls the cholesterol dependence of Semliki Forest virus entry and exit. *J Cell Biol* 14: 91–99.
52. Thorén PE, Persson D, Lincoln P, Nordén B (2005) Membrane destabilizing properties of cell-penetrating peptides. *Biophys Chem* 114: 169–179.
53. Stankowski S, Schwarz G (1990) Electrostatics of a peptide at a membrane/water interface. The pH dependence of melittin association with lipid vesicles. *Biochim Biophys Acta* 1025: 164–72.
54. Thiaudière E, Siffert O, Talbot JC, Bolard J, Alouf JE, et al. (1991) The amphiphilic alpha-helix concept. Consequences on the structure of staphylococcal delta-toxin in solution and bound to lipids. *Eur J Biochem* 195: 203–13.
55. Pouny Y, Rapaport D, Mor A, Nicolas P, Shai Y (1992) Interaction of antimicrobial dermaseptin and its fluorescently labeled analogues with phospholipid membranes. *Biochemistry* 31: 12416–23.
56. Rapaport D, Shai Y (1991) Interaction of fluorescently labeled pardaxin and its analogues with lipid bilayers. *J Biol Chem* 266: 23769–23775.
57. Falanga A, Vitiello MT, Cantisani M, Tarallo R, Guarnieri D, et al. (2011) A peptide derived from herpes simplex virus type 1 glycoprotein H: membrane translocation and applications to the delivery of quantum dots. *Nanomedicine* 6: 925–934.
58. Tarallo R, Accardo A, Falanga A, Guarnieri D, Vitiello G, et al. (2011) Clickable Functionalization of Liposomes with the gH625 Peptide from Herpes simplex Virus Type I for Intracellular Drug Delivery. *Chem Eur J* 17: 12659–12668.
59. Marsh D, Vitiello M, Falanga A, Cantisani M, Incoronato N, et al. (2012) Intracellular Delivery: Exploiting Viral Membranotropic Peptides. *Curr Drug Met* 12: 93–104.
60. Marsh D (2008) Electron spin resonance in membrane research: Protein–lipid interactions. *Methods* 46: 83–96.
61. Hope MJ, Bally MB, Webb G, Cullis PR (1985) Vesicles of variable sizes produced by a rapid extrusion procedure. *Biochim Biophys Acta* 812: 55–65.
62. Fiske CH, Subbarow Y (1925) The colorimetric determination of phosphorus. *J Biol Chem* 66: 375–400.
63. Struck DK, Hoekstra D, Pagano RE (1981) Use of resonance energy transfer to monitor membrane fusion. *Biochemistry* 20: 4093–4099.
64. Cummings JE, Vanderlock TK (2007) Aggregation and hemi-fusion of anionic vesicles induced by the antimicrobial peptide cryptidin-4. *Biochim Biophys Acta* 1768: 1796–1804.
65. Schwarz G, Stankowsky S, Rizzo V (1986) Thermodynamic analysis of incorporation and aggregation in a membrane: application to the pore-forming peptide alamethicin. *Biochim Biophys Acta* 861: 141–151.
66. Beschiaschvili G, Seelig J (1990) Melittin binding to mixed phosphatidylglycerol/phosphatidylcholine membranes. *Biochemistry* 29: 52–58.
67. De Kroon AIPM, Soekarjo MW, De Gier J, De Kruijff B (1990) The role of charge and hydrophobicity in peptide-lipid interaction: a comparative study based on tryptophan fluorescence measurements combined with the use of aqueous and hydrophobic quenchers. *Biochemistry* 29: 8229–8240.
68. Eftink MR, Ghiron CA (1976) Fluorescence quenching of indole and model micelle systems. *J Phys Chem* 80: 486–493.

DOI: 10.1002/ ((please add manuscript number))

Article type: Full Paper

Surface decoration with membranotropic peptides as a method to escape endo-lysosomal compartment and reduce nanoparticle toxicity.

Daniela Guarnieri¹, Ornella Muscetti¹, Annarita Falanga², Sabato Fusco¹, Valentina Belli¹, Emiliana Perillo², Edmondo Battista¹, Valeria Panzetta¹, Stefania Galdiero^{2,}, Paolo A. Netti^{1,3,*}*

Dr. D. Guarnieri, Dr. O. Muscetti, Dr. S. Fusco, Dr. V. Belli, Dr. E. Battista, Dr. V. Panzetta, Prof. P.A. Netti

Center for Advanced Biomaterials for health Care (CABHC), Istituto Italiano di Tecnologia, Largo Barsanti, Napoli, Italy

Centro di Ricerca Interdipartimentale sui Biomateriali (CRIB), Università di Napoli Federico II, Piazzale Tecchio 80, Napoli, Italy

*E-mail: nettipa@unina.it

Dr. A. Falanga, E. Perillo, Prof. S. Galdiero

Dipartimento di Farmacia, Università di Napoli Federico II, Via Domenico Montesano 49, Napoli, Italy

*E-mail: sgaldier@unina.it

Keywords: nanoparticles, membranotropic peptides, cell membrane, intracellular fate, lysosomes, nanotoxicity.

gH625 is a membranotropic peptide able to transport different cargos (i.e. liposomes, quantum dots, polymeric nanoparticles) within and across cells in a very efficient manner. However, clear understanding of the detailed uptake mechanism remains elusive. In this work, the journey of gH625-functionalized polystyrene nanoparticles from the interaction with the cell membrane to their intracellular final destination has been investigated in detail in mouse brain endothelial cells in order to elucidate how gH625 affects nanoparticle behavior and their cytotoxic effect on an *in vitro* model of blood brain barrier. Results indicate that the mechanism of translocation of gH625 dictates nanoparticles' fate and this has a relevant impact on the nanotoxicological profile of positively charged nanoparticles.

1. Introduction

Nanotechnology plays a key role in future strategies for drug delivery and also an essential role in brain drug delivery. Nanoparticles are colloidal systems that range in size from 1 to 100 nm. They can be fabricated by a variety of substances such as polymers, lipids, dendrimers, ceramics, and carbon nanotubes; and can be structurally adapted to deliver a wide variety of drugs, enhance delivery efficiency, and reduce side effects by targeted delivery [1, 2]. Nanoparticles are increasingly demonstrating an advantage in effective transportation of various drugs, including temozolomide, loperamide, and doxorubicin, which are not normally able to reach the central nervous system (CNS)[3] in part due to the presence of the blood brain barrier (BBB). The BBB is formed by the endothelial cells of brain capillaries, and restricts the exchange of most endogenous molecules between the blood and the brain; the very tight regulation of brain homeostasis imposed by the BBB prohibits many therapeutic compounds from entering brain tissues[4]. Drugs that are intended to act in the CNS can be administered systemically, if they have the ability to circumvent the BBB or have to be introduced directly in the CNS by invasive methods[5]. The BBB represents the main challenge for the development of new neurotherapeutics, and various strategies are currently under development to enhance the uptake of therapeutic compounds into brain parenchyma. Among the others, the ever expanding use of nanoparticles is giving hope on achieving more efficient drug delivery into the brain but has also determined great concern about their potential risks to human and environmental health[3]. Toxicity of nanoparticles could vary with their physicochemical parameters. The dependence of cytotoxicity on particle size and surface coating has been widely investigated with smaller nanoparticles being more toxic than the larger ones. Moreover, recent works have demonstrated that nanoparticles essentially use the “classical” endocytic mechanism to enter cells. As a result of this route of cellular entrance, nanoparticles tend to accumulate and to remain inside lysosomal compartments. This accumulation leads to two important consequences: i) a low efficiency of BBB crossing

due to lysosomal storage[6] and ii) an increase of nanoparticle toxicological effects due to the lysosomal environment with a low pH and a high degradative potential. [7, 8]

In this framework, NP surface modification may vary their intracellular fate and, therefore, their nanotoxicological profile. Indeed, using appropriate surface modification, nanoparticle carriers have been shown to represent promising strategies for delivery, having good cellular uptake and lower cytotoxicity *in vitro* and *in vivo*. Recently, nanoparticles with multiple surface modifications for delivery to the CNS have been developed such as decoration with poly(ethylene glycol) (PEG)[9], polysorbate-80[10], monoclonal antibody[11], and cationic cell-penetrating peptides[12]. More recently, great attention has been dedicated to the study of hydrophobic peptides that efficiently traverse biological membranes, promoting lipid membrane-reorganizing processes, such as fusion or pore formation, and thus involving temporary membrane destabilization and subsequent reorganization[13], which may be exploited for drug delivery purposes.[14-17] The nineteen-residue peptide gH625 is a membrane-perturbing domain derived from the glycoprotein H (gH) of *Herpes simplex virus 1*[17]; gH625 interacts with model membranes, contributing to their merging[15] and is able to traverse the membrane bilayer and transport a cargo into the cytoplasm and across the BBB.[18-22] In particular, we previously reported the ability of gH625 to transport quantum dots,[18] liposomes,[20] nanoparticles,[21] and dendrimers.[22]

We characterize here a novel theranostic platform that may be broadly applicable for the development of new therapeutics with increased brain penetration using nanoparticles conjugated with gH625. In particular, gH625 was coupled to the surface of fluorescent aminated polystyrene nanoparticles (NPs) via a covalent binding procedure and NP uptake mechanism and permeation across an *in vitro* BBB model were studied. We recently reported that the conjugation with gH625 facilitated the delivery of nanoparticles across the BBB, leading to significant higher cell uptake and crossing, and, most importantly, a reduction of NP intracellular accumulation as large aggregates.[21] These previous observations suggest

that the efficient translocation across cell membranes and cell internalization of gH625-NPs do not involve exclusively “classical” endocytosis mechanisms.

The surface functionalization with gH625 changed NP fate, thus providing a good strategy for the design of promising carriers to deliver drugs across the BBB for the treatment of brain diseases bypassing the endocytosis entrapment.

Further characterization of the brain endothelial cell membrane translocation mechanism of this peptide platform and, hence, of its nanotoxicological impact are presented in this work. In particular, the interaction of gH625-NPs with brain endothelial cell membrane through atomic force microscopy and cholesterol depletion analyses, their intracellular trafficking and distribution as well as their cytotoxic effect compared to non-functionalized NPs, intracellularly delivered by “classical endocytosis” and by gene gun method [7] have been investigated.

2. Results

2.1 Interaction of gH625-NPs with the cell membrane

gH625 enhances nanoparticles’ cellular uptake at early incubation time. In fact, we observed a 2-fold increment of NP internalization within endothelial cells in presence of gH625 compared to blank NPs already after 10 minute incubation.[21] Moreover, accordingly to cellular uptake kinetics, scanning electron microscopy (SEM) analyses indicated a better and more rapid adsorption of gH625-NPs on cell membrane, compared to blank-NPs after 10 min incubation, probably due to the membrane tropism of the peptide and, thus, an enhancement of gH625-NPs internalization.[21]

To better elucidate the interaction of gH625-NPs with the cell membrane, coupling of confocal laser scanning microscopy (CLSM) images with atomic force microscopy (AFM) was carried out. This analysis is very instructive on assessing the status of the NPs at the cell membrane.[23] Indeed, by matching topographical features of cell membrane with

fluorescence signal, we observed that, after 10 minute incubation, there is a partial co-localization between NP fluorescence and cell membrane humps, suggesting that gH625-NPs are both on cell membrane and inside the cytoplasm (Figure 1 B). Moreover, NP deposition on the cell membrane was examined at different time points upon incubation with NPs. As shown by the chart in Figure 1 E, an overall increment of cell membrane roughness is observed upon 10 minute incubation with gH625-NPs compared to control cells (non-treated with NPs) and cells incubated with blank NPs. Conversely, no differences in cell membrane roughness are present among all samples after 24 h incubation, likely due to NP cellular uptake. These observations further confirm the better interaction of gH625-NPs with the cell membrane than blank NPs, in agreement with previously reported results.[21]

gH625 assumes in membrane mimetic environments a helical structure that makes it particularly affine for lipids.[15] Indeed, we previously demonstrated its capability to hemifuse liposomes and its tropism for cholesterol enriched membranes *in vitro*. [15] Therefore, we hypothesized that a similar mechanism could be used by gH625-NPs to bind the cell membrane and, thus, for their translocation within the cell. To address this issue, we treated cells with methyl beta cyclodextrin (M β CD) in order to deplete cholesterol from the cell membrane and investigate the effect of this treatment on nanoparticles' cellular uptake. Results, reported in Figure 2 A-B, show no effects on intracellular distribution of blank NPs after 30 minute treatment with 10 mM M β CD. On the other hand, gH625-NP uptake is inhibited by cholesterol depletion (Figure 2 C and D). In particular, we observed a reduction of about 40% in cellular uptake for gH625-NPs after 30 minute of M β CD treatment compared to non-treated cells (Figure 2 E). Taken altogether these data suggest that the interaction with the cell membrane lipids plays a pivotal role in controlling the mechanism of gH625-NPs uptake.

2.2 gH625-NP intracellular behavior

In order to confirm that the presence of gH625 affects the intracellular behavior of NPs by-passing the endo-lysosomal pathway, we forced cell membrane crossing by shooting NPs with gene gun method.[7]

As previously reported, [7, 21] once internalized by cells, blank NPs show prevalently a pearl-on-a-string behavior, with a little percentage of random walk trajectories (Figure 3 A). On the contrary, if forced to enter cell by using gene gun method, shot blank NPs show almost exclusively random walk trajectories, suggesting very low NP confinement inside endo-lysosomal compartments (Figure 3 B).[7] In the case of gH625-NPs, no significant changes in intracellular trajectories were observed upon delivery of NPs by using gene gun method (Figure 3 B). These data strongly suggest that gH625 allows NPs to by-pass/escape the endo-lysosomal pathway.

Furthermore, by increasing the incubation time, the percentages of random and pearl-on-a-string trajectories remain almost the same for both blank and gH625-NPs (Figure 4 A and B). Interestingly, MPT analyses of later incubation times reveal the presence of a third category of trajectories that we did not consider for the calculation of trajectory percentages since they fit only partially the MSD equation described in the materials and methods section. More precisely, the first part of MSD curves of these trajectories shows a time coefficient $\alpha \leq 1$, typical of random walk behavior, while the second part shows an α coefficient close to zero indicating a confined motion (Figure 4 C). In particular, the percentage of these trajectories is higher and increases with time for blank than gH625-NPs (data not shown). Therefore, we named this kind of trajectories “random caged” and hypothesized to be typical of nanoparticles confined inside the largest perinuclear lysosomes as their final destination. Further investigations are necessary to elucidate this issue.

2.3 gH625-NP intracellular distribution

To further investigate the fate of gH625-NPs, we followed nanoparticles' intracellular distribution by co-localization experiments within endocytic compartments, namely endosomes and lysosomes. After 10 minute incubation, both NPs are able to enter cells and partially co-localize with Rab5 protein, a marker of early endosomes, thus indicating that both NPs use vesicular structures to enter cells (Figure 5). In particular, at earlier incubation time, no significant differences of co-localization percentages are observed between blank and gH625-NPs. By increasing the incubation time, the percentage of co-localization for blank NPs increases up to 30 min and then decreases becoming about 4 % at 2h. Conversely, for gH625-NPs the percentage of co-localization with Rab5 protein remains almost constant with time.

Already after 2h incubation, both blank and gH625-NPs partially co-localize with lysosomes, (Figure 6). However, the percentage of co-localization of blank NPs increases over time, reaching almost 80%. On the other hand, for gH625-NPs, the percentage of co-localization is lower than blank NPs and increases up to 6 h remaining almost constant after 24 h incubation. These observations suggest a partial lysosomal escape of gH625-NPs.

The accumulation of NPs within the lysosomes also affects lysosome size distribution. Indeed, an increment in lysosome size up to $1.5 \mu\text{m}^2$ is observed after 24h incubation with blank NPs (Figure 7 A). Conversely, in presence of gH625-NPs, where a scarce co-localization is observed, lysosome size remains constant over time (Figure 7 B).

2.4 gH625-NP cytotoxicity

The capability to by-pass the lysosomal compartment can offer great advantages in terms of efficacy of nanocarriers to overcome biological barriers [21] and of reduced nanotoxicity. [7] Recent works reported on the cytotoxic effects of positively charged polystyrene NPs as a consequence of their localization in lysosomes and interaction with lysosomal components.[8, 24] Therefore, we tested the effect of gH625 on cytotoxicity of positively charged polystyrene

nanoparticles and compared results to cells treated with blank NPs delivered by “classical” endocytosis and gene gun method, as positive and negative controls, respectively. We chose to work with 100 nm and 50 nm particles with a 35% functionalization degree, in order to evaluate the effect of size on NP cytotoxicity, and a particle concentration of 50 $\mu\text{g/ml}$ NPs, reported in literature as cytotoxic[8] and corresponding in our experimental system to 6×10^4 NPs/cell for 100 nm NPs (Figure S2 A) and 2×10^5 NPs/cell for 50 nm NPs (Figure S2 B).

Data indicate a reduction of viability of cells treated with positively charged NPs, as expected (Figure 8). In particular, a higher cytotoxic effect is observed for 50 nm NPs than 100 nm NPs, likely due to the higher cellular uptake of smaller NPs (Figure S2). On the other hand, after NP shooting, no cytotoxic effect is observed for both 50 and 100 nm NPs, clearly indicating that the cytotoxicity is strongly dependent on NP intracellular localization. More interestingly, after incubation with gH625-NPs, a recovery of cell viability is observed, compared to endocytosed blank NPs. However, the reduction in cytotoxicity of gH625-NPs is less evident than shot blank NPs likely due to their partial co-localization with lysosomes as shown above (Figure 6). Moreover, the effect of gH625 in cytotoxicity reduction is higher for smaller (50 nm) than bigger (100 nm) functionalized NPs, even though the first enter cells more than the second ones. These latter results could be attributed to a different conformation and/or density of peptide molecules on the NP surface. To address this issue, we first verified the secondary structure of the peptide bound to the nanoparticles by circular dichroism (CD) experiments. CD data confirmed that gH625 retains its structure (helical) when bound to both 50 nm and 100 nm [21] -diameter nanoparticle surface (Figure S3). To further characterize the gH625-NPs, we performed dynamic light scattering (DLS) measurements. After functionalization, the hydrodynamic size of nanoparticles with 35% of gH625 in aqueous medium at pH 7 was found to be 102.9 ± 0.6 nm with polydispersity index (PDI) of ca. 0.15 for 100 nm NPs, which is close to those previously obtained for the same preparation, indicating the reproducibility of the synthetic procedures, and 71.0 ± 9.3 nm (PDI 0.24) for 50 nm NPs

(Table S1). To confirm the colloidal stability of functionalized nanoparticles, which is a crucial parameter correlated to their functionalization, measurements of the zeta potential were also carried out. We confirmed previously obtained results. In particular, zeta potential values are around + 25 mV similar for both 100 and 50 nm gH625-NPs (Table S1). On the other hand, the density of peptide molecules on NP surface varies as a function of NP size being 4 peptides/nm² for 100 nm NPs and 11 peptides/nm² for 50 nm NPs. Taken altogether these data indicate that gH625 is able to retain its helical structure both on 100 nm and 50 nm NPs and suggest that its effect on cytotoxicity of polystyrene NPs with different size might depend on the density of peptide bound to the NP surface.

3. Discussion

Endocytosis is the major uptake mechanism of cells;[25] the cargos become entrapped in endosomes and are usually degraded by specific enzymes in the lysosomes; [8, 25-28] thus, a limiting step in achieving an effective biological based therapy is to facilitate endosomal escape and ensure delivery of therapeutics. The discovery that synthetic peptides can be used to deliver biologically active substances inside live cells has provided the basis for developing new effective strategies for drug delivery into the brain[29]. The data presented here further characterize a new drug-delivery platform designed to enhance brain penetration of drugs. In particular, we coupled polystyrene NPs to a membranotropic peptide (gH625) able to cross membrane bilayers. In previous validation studies, gH625 was shown to effectively enter cells and to efficiently transport small cargos by directly penetrating the membrane; although we could not completely exclude the partial involvement of endocytosis.[13, 18, 22] A primary objective of this study was to improve our understanding of the internalization mechanism and of its impact on the nanotoxicological profile of the nanoparticles.

The uptake and subcellular localization of the NPs were investigated by exposing the *in vitro* BBB model to 100 nm polystyrene NPs. It is clear from our results that the majority of blank NPs end up in intracellular organelles, many of them lysosomes, similarly to several other NP

cell systems. [30, 31] As far as we can tell, they accumulate within the lysosomes. A significant number of blank NPs are observed associated with lysosomes and after 24 h the degree of lysosomal accumulation was around 80% indicating a significant fraction of NPs accumulates in lysosomes. Interestingly, gH625-NPs only slightly co-localize with lysosomes and their degree of lysosomal accumulation did not increase with time.

The endothelial brain cells are rich in cholesterol and this may indicate an involvement of lipid rafts.[32] We previously demonstrated that gH625 is able to hemifuse liposomes containing a high percentage of cholesterol.[17] Here we wanted to verify if gH625-NPs were still able to cross the membrane of an *in vitro* model of the BBB depleted of cholesterol. Our hypothesis was confirmed by our results, showing that the depletion of cholesterol did not have any effect on the intracellular distribution of blank NPs but significantly reduced the uptake of gH625-NPs.

gH625-NP interaction with the cell membrane plays a key role in controlling the uptake mechanism, as also demonstrated by the gene gun experiments, which show that blank NP intracellular behavior can be switched from pearl-on-a-string to random, while gH625-NP trajectories are not subject to any change.

Collectively, the evidence of particle movement in the barrier and the information above do suggest that such true barrier crossing events occur for both blank-NPs and gH625-NPs but with different mechanisms that are related to the ability of gH625 to interact with membranes containing a high percentage of cholesterol. In particular, it may be hypothesized that gH625 is able to carry NPs across the BBB with translocation mechanisms or, when endocytosis takes place, it is able to induce endosomal escape (Figure 9).

This last point is extremely important as the cytotoxic effect of NPs is attributed to their localization in lysosomes and interaction with lysosomal components. In order to assess the

effect of the mechanism of uptake on the cytotoxicity, we used 100 nm and 50 nm NPs for their higher cytotoxic potential.[8] We found that when blank NPs are shot, we did not observe any cytotoxic effect; similarly if we decorate the NPs with gH625 we also observe a significant reduction of cytotoxicity compared to blank NPs. We thus, believe that the ability of gH625 to avoid accumulation into lysosomes (both by using uptake mechanisms not involving endocytosis mechanisms, and/or escaping from lysosomes) is responsible of the reduction of cytotoxicity.

Data obtained on the transport mechanism of gH625 clearly indicate that it is able to switch the mechanism of uptake of the cargo and it is able to cross the BBB in a fashion that can be distinguished from other cell-penetrating peptides such as TAT and penetratin.[29] A variety of therapeutic approaches to cross the BBB have been examined previously, but most have been unsuccessful and/or inconvenient.[4] The gH625 platform provides a number of important advantages over these prior approaches. First, it involves only partially the endocytic pathway; second, it is able to facilitate the escape from endocytic vesicles; finally the absence of accumulation in lysosomes determines its lower toxicity.

In conclusion, we have characterized the mechanism of uptake of NPs decorated on their surface with gH625 and their effect on cell viability. The results presented here and in earlier studies[21] suggest that the gH625 platform may have significant utility in overcoming this constraint and could be used as a safe and effective delivery system for the transport of drugs across the BBB. This platform presents high efficacy with extreme flexibility with unlimited targets and these are the first *in vitro* results showing that a membranotropic peptide could be used as a new brain delivery system. Further work is now underway with various therapeutic targets.

4. Conclusion

In summary, this study demonstrated in greater detail the efficacy of gH625 peptide to deliver cargos across the brain endothelial cell membrane and its capability to avoid lysosomal accumulation of nanoparticles. This has got a particular relevance on the impact of nanoparticles in the cytotoxic response. Therefore, NP surface decoration with membranotropic peptides could be a valid strategy to design safe and effective nanocarriers for the treatment of CNS diseases.

5. Experimental Section

Materials: Orange fluorescent amine-modified polystyrene, 100 nm, nanoparticles (100 nm NPs) and blue fluorescent amine-modified polystyrene, 50 nm, nanoparticles (50 nm NPs) were purchased by Sigma-Aldrich.

gH625 synthesis, nanoparticle conjugation and characterization of gH625-NPs: The peptide gH625 (Ac-HGLASTLTRWAHYNALIRAFGGG-COOH) was synthesized using the standard solid-phase-9-fluorenylmethoxycarbonyl (Fmoc) method as previously reported.[17] The peptide was obtained with good yields (30-40%).

The conjugation of gH625 to amine-modified fluorescent polystyrene nanoparticles was performed as described previously[21]. A solution of the peptide, EDC (1-Ethyl-3-(3-dimethylamino-propyl)-carbodiimide, hydrochloride) and NHS (N-Hydroxysuccinimide) in molar ratio of 4:4:1 was prepared in PBS buffer at pH 7.4, at room temperature under stirring for 30 minutes. NPs were conjugated with the preactivated-peptide, in MES 0.1 M buffer at pH 5.5 for 3 hours at room temperature in presence of Tween 20 and the yield of the reaction was higher than 90%. The peptide-NPs were purified from the un-conjugated-NPs by exclusion chromatography on a 1 × 18 cm Sephadex G-50 (Amersham Biosciences) column pre-equilibrated in PBS buffer at pH7.4. The fluorescence spectra of peptide-NPs and un-

conjugated NPs were measured in a Cary Eclipse Varian fluorescence spectrophotometer in the same condition. For both 50 and 100 PS NPs, 35 % of functionalization degree was used.

The gH625-NPs were characterized by circular dichroism and measurements of size and zeta-potential.

CD spectra were recorded using a Jasco J-715 spectropolarimeter in a 1.0 or 0.1 cm quartz cell at room temperature. The spectra are an average of 3 consecutive scans from 260 to 195 nm, recorded with a band width of 3 nm, a time constant of 16 s, and a scan rate of 10 nm/min. Spectra were recorded and corrected for the blank sample. Measurements of zeta potential and size of gH625 NPs and blank-NPs were made with a Zetasizer Nano-ZS (Malvern Instruments, Worcestershire, UK). The measurements were conducted at 25°C using a 3.6×10^{10} NP/ml suspension at pH 7. All measurements were performed in triplicate for each sample.

Cell culture: Immortalized mouse cerebral endothelial cells, bEnd.3 cells (American Type Culture Collection, Manassas, VA) were grown in DMEM with 4.5 g/L glucose, 10% Fetal Bovine Serum (FBS), 3.7 g/L sodium bicarbonate, and 4 mM glutamine, 1% non-essential aminoacids, 100 U/ml penicillin and 0.1 mg/ml streptomycin in 100 mm diameter cell culture dish, in a humidified atmosphere at 37°C and 5% CO₂. Cells used in all experiments were at passage 11–18.

Atomic force microscopy (AFM): For atomic force microscopy, cells were incubated 10 minutes with blank and gH625-NPs, washed twice to remove non internalized NPs and fixed with 4% paraformaldehyde for 20 min. Cells not incubated with NPs were used as a control. AFM (NanoWizard II, JPK, GMBH) analysis was performed in contact mode by using triangular tip with a nominal spring constant of 0.03 N/m (MLCT, Brukerprobes). $30 \times 10 \mu\text{m}^2$ images were taken at different size applying a force of 1.5 nN with a scan rate of 1 Hz and a resolution of 512×171 . At least 10 images were used to calculate the mean roughness (RMS) and processed by JPK analysis software mapping the different regions of the whole cell surface.

Cholesterol depletion: To extract cholesterol from cell membrane, cells were incubated with 10 mM M β CD for 30 minutes at 37°C as previously described.[33, 34] After M β CD treatment, NPs were added to cell culture medium and incubated with cells for 15 minutes at 37°C. Then, cells were rinsed twice with PBS to remove non-internalized NPs and fixed with 4% paraformaldehyde for 20 min. Finally, cell nuclei and membranes were stained with DAPI and red fluorescent wheat germ agglutinin (WGA), respectively. All samples were then observed at confocal microscope (SP5 Leica) with a 63 \times oil immersion objective. Confocal images were analyzed with ImageJ analysis software to quantify NP uptake. At least 20 cells of each three independent experiments were analyzed. Data were shown as mean \pm standard deviation.

Colocalization with endosomes and lysosomes: For co-localization experiments, after 100 nm PS NPs incubation, cells were firstly rinsed twice with PBS to remove non-internalized nanoparticles and fixed.

For endosome staining, cells were fixed with 4% paraformaldehyde for 10 min at room temperature (RT). Then, cells were permeabilized with 0.01% saponin-PBS for 8 min and blocked with FBS-PBS 10% for 20 min at RT. Endosomes were localized with rabbit anti-Rab 5 polyclonal (Abcam) primary antibodies and with AlexaFluor 633 goat anti-rabbit secondary antibodies (Molecular Probes, Invitrogen)

For lysosomes staining, cells were fixed with 4% paraformaldehyde for 20 min at RT. Then, cells were permeabilized with 0.05% saponin-PBS for 20 min and blocked with FBS-PBS 10% for 20 min at RT. Lysosomes were localized with rabbit anti-LAMP 2 polyclonal (Abcam) primary antibodies and with AlexaFluor 633 goat anti-rabbit secondary antibodies (Molecular Probes, Invitrogen). All samples were then observed at confocal microscope (SP5 Leica) with a 63 \times oil immersion objective and dual-channel images were acquired.

The co-localization analyses were performed by LAS AF (Leica) and ImageJ analysis softwares. Data were expressed as co-localization percentage. Moreover, Pearson's

coefficient was also calculated by JACoP plugin[35] to have an estimation of the correlation among the pixels in the dual-channels images (Figure S1).

Intracellular shooting of NPs by gene gun method: To have free NPs in the cytoplasm, a ballistic system (gene gun, BioRad) was used as described elsewhere.[7] Briefly, 50 and 100 nm amine-modified polystyrene NPs were suspended in 30 μ l of distilled water at the final concentration of 2.9×10^{13} and 4.5×10^{12} NPs/ml, respectively, deposited and left to dry on a rupture disk under a sterile hood. After solvent drying, a 900 psi pressure was used to shoot NPs within cells. After shooting, cells were roughly rinsed with PBS to remove non-internalized NPs and, the day after, the cells were recovered and 3×10^4 cells were seeded in each fresh 35 mm culture dish.

Multiple particle tracking (MPT): Images of shot and endo 100 nm NPs in End.3 cells were collected in time-lapse for 100 s with a sampling time of 1 second by using a wide field fluorescence microscope (Olympus Cell-R, 60x oil immersion objective, NA = 1.35). Tracking algorithm has been described in details elsewhere.[36] NP trajectories were built and then the mean square displacement (MSD) was calculated and correlated with the NP diffusion by the equation (1) ,

$$\text{MSD} = 4Dt^\alpha$$

where D is the diffusion coefficient and α represents the time dependence. The MSD curve of each tracked NP was fitted by using equation (1), in order to gain information about the nature of particle motion into the cells. Briefly, we indicate as Brownian or sub-diffusive, NPs exhibiting MSD curve that undergoes a power law with exponent $\alpha = 1$ and $\alpha < 1$, respectively, and super-diffusive, particles presenting MSD, whose dependence on time was described by the power law with $\alpha > 1$. NPs presenting a MSD curves with a time exponent $\alpha \leq 1$ at low Δt and $\alpha \approx 0$ were classified as entrapped (random caged) in confined endo-lysosomal regions and not computed. The percentages of randomly moving NPs ($\alpha \leq 1$) and

transported NPs ($1 < \alpha < 2$) were evaluated and compared for shooting and endocytosis as a function of NP surface functionalization with gH625 peptides. For each experiment, at least, 5 cells were analyzed.

Quantification of internalized nanoparticles: To evaluate the number of endo and shot NPs within cells, 7.3×10^{11} 50 nm NPs/ml and 9.0×10^{10} 100 nm NPs/ml were delivered by “classical” endocytosis and 2.9×10^{13} 50 nm NPs/ml and 4.5×10^{12} 100 nm NPs/ml were delivered by gene gun method. After NP incubation, cells were roughly rinsed with PBS, trypsinized and counted by Neubauer chamber. Afterward, cells were centrifuged and the pellets were lysed with lysis buffer. Cell lysates were analyzed by a spectrofluorometer (Perkin–Elmer, USA) to measure the amount of internalized NPs. Data were reported as NP number normalized to the number of cells. Samples that had the same number of NPs per cell were used and compared each other for cytotoxicity.

In vitro cytotoxicity: bEnd.3 cell viability was quantified by Alamar Blue Assay and compared to non-treated cells, which were used as a control. Briefly, 3×10^4 cells were seeded on a 35 mm cell culture dish and incubated 24 h with NP suspensions to allow endocytosis. Conversely, for NP shooting, cells were shot with NPs by gene gun, washed roughly with PBS and, then, allowed to recover for 24 h at 37°C. After recovery, cells were trypsinized, counted and seeded on fresh 35 mm cell culture dishes. Alamar Blue Assay was performed according to the manufacturer’s procedure at 1 day after NP exposure. Absorbance of Alamar Blue reagent solution was read at 570 nm and 600 nm by a plate reader (Perkinelmer). Data were reported as percentage of viable cells normalized to non-treated cells.

Supporting Information

Supporting Information is available from the Wiley Online Library or from the author.

Acknowledgements

The authors thank Mrs. Roberta Infranca for her precious and careful proofreading.

Received: ((will be filled in by the editorial staff))

Revised: ((will be filled in by the editorial staff))

Published online: ((will be filled in by the editorial staff))

1. Yang, H., *Pharmaceutical Research* **2010**, *27* (9), 1759-1771. DOI 10.1007/s11095-010-0141-7.
2. Paolino, D.; Cosco, D.; Molinaro, R.; Celia, C.; Fresta, M., *Drug discovery today* **2011**, *16* (7), 311-324.
3. Kreuter, J., *Advanced drug delivery reviews* **2014**, *71*, 2-14.
4. Neuwelt, E.; Abbott, N.; Abrey, L.; Banks, W. A.; Blakley, B.; Davis, T.; Engelhardt, B.; Grammas, P.; Nedergaard, M.; Nutt, J.; Pardridge, W.; Rosenberg, G. A.; Smith, Q.; Drewes, L. R., *Lancet Neurology* **2008**, *7* (1), 84-96. DOI 10.1016/s1474-4422(07)70326-5.
5. Abbott, N. J.; Ronnback, L.; Hansson, E., *Nature Reviews Neuroscience* **2006**, *7* (1), 41-53. DOI 10.1038/nrn1824.
6. Bramini, M.; Ye, D.; Hallerbach, A.; Nic Raghnaill, M.; Salvati, A.; Åberg, C.; Dawson, K. A., *ACS nano* **2014**.
7. Guarnieri, D.; Sabella, S.; Muscetti, O.; Belli, V.; Malvindi, M. A.; Fusco, S.; De Luca, E.; Pompa, P. P.; Netti, P. A., *Nanoscale* **2014**, *6* (17), 10264-10273.
8. Wang, F.; Yu, L.; Monopoli, M. P.; Sandin, P.; Mahon, E.; Salvati, A.; Dawson, K. A., *Nanomedicine: Nanotechnology, Biology and Medicine* **2013**, *9* (8), 1159-1168.
9. Hu, K.; Li, J.; Shen, Y.; Lu, W.; Gao, X.; Zhang, Q.; Jiang, X., *Journal of Controlled Release* **2009**, *134* (1), 55-61.
10. Kreuter, J.; Ramge, P.; Petrov, V.; Hamm, S.; Gelperina, S. E.; Engelhardt, B.; Alyautdin, R.; Von Briesen, H.; Begley, D. J., *Pharmaceutical research* **2003**, *20* (3), 409-416.
11. Aktas, Y.; Yemisci, M.; Andrieux, K.; Gürsoy, R. N.; Alonso, M. J.; Fernandez-Megia, E.; Novoa-Carballal, R.; Quiñoá, E.; Riguera, R.; Sargon, M. F., *Bioconjugate chemistry* **2005**, *16* (6), 1503-1511.
12. Rao, K. S.; Reddy, M. K.; Horning, J. L.; Labhasetwar, V., *Biomaterials* **2008**, *29* (33), 4429-4438.
13. Galdiero, S.; Vitiello, M.; Falanga, A.; Cantisani, M.; Incoronato, N.; Galdiero, M., *Current drug metabolism* **2012**, *13* (1), 93-104.
14. Galdiero, S.; Vitiello, M.; D'Isanto, M.; Falanga, A.; Cantisani, M.; Browne, H.; Pedone, C.; Galdiero, M., *Chembiochem* **2008**, *9* (5), 758-767.
15. Galdiero, S.; Falanga, A.; Vitiello, M.; Raiola, L.; Russo, L.; Pedone, C.; Isernia, C.; Galdiero, M., *Journal of Biological Chemistry* **2010**, *285* (22), 17123-17136.
16. Galdiero, S.; Falanga, A.; Vitiello, M.; Raiola, L.; Fattorusso, R.; Browne, H.; Pedone, C.; Isernia, C.; Galdiero, M., *Journal of Biological Chemistry* **2008**, *283* (44), 29993-30009.
17. Galdiero, S.; Falanga, A.; Vitiello, M.; Browne, H.; Pedone, C.; Galdiero, M., *Journal of Biological Chemistry* **2005**, *280* (31), 28632-28643.
18. Falanga, A.; Vitiello, M. T.; Cantisani, M.; Tarallo, R.; Guarnieri, D.; Mignogna, E.; Netti, P.; Pedone, C.; Galdiero, M.; Galdiero, S., *Nanomedicine-Nanotechnology Biology and Medicine* **2011**, *7* (6), 925-934. DOI 10.1016/j.nano.2011.04.009.
19. Smaldone, G.; Falanga, A.; Capasso, D.; Guarnieri, D.; Correale, S.; Galdiero, M.; Netti, P. A.; Zollo, M.; Galdiero, S.; Di Gaetano, S.; Pedone, E., *International Journal of Nanomedicine* **2013**, *8*, 2555-2565. DOI 10.2147/ijn.s44186.
20. Tarallo, R.; Accardo, A.; Falanga, A.; Guarnieri, D.; Vitiello, G.; Netti, P.; D'Errico, G.; Morelli, G.; Galdiero, S., *Chemistry-a European Journal* **2011**, *17* (45), 12659-12668. DOI 10.1002/chem.201101425.

21. Guarnieri, D.; Falanga, A.; Muscetti, O.; Tarallo, R.; Fusco, S.; Galdiero, M.; Galdiero, S.; Netti, P. A., *Small* **2013**, *9* (6), 853-862. DOI 10.1002/smll.201201870.
22. Carberry, T. P.; Tarallo, R.; Falanga, A.; Finamore, E.; Galdiero, M.; Weck, M.; Galdiero, S., *Chemistry-A European Journal* **2012**, *18* (43), 13678-13685.
23. Blechinger, J.; Bauer, A. T.; Torrano, A. A.; Gorzelanny, C.; Bräuchle, C.; Schneider, S. W., *Small* **2013**, *9* (23), 3970-3980.
24. Kim, J. A.; Åberg, C.; de Cárcer, G.; Malumbres, M.; Salvati, A.; Dawson, K. A., *ACS nano* **2013**, *7* (9), 7483-7494.
25. Doherty, G. J.; McMahon, H. T., *Annual review of biochemistry* **2009**, *78*, 857-902.
26. Rappoport, J., *Biochem. J* **2008**, *412*, 415-423.
27. Conner, S. D.; Schmid, S. L., *Nature* **2003**, *422* (6927), 37-44.
28. Fröhlich, E.; Meindl, C.; Roblegg, E.; Ebner, B.; Absenger, M.; Pieber, T. R., *Part Fibre Toxicol* **2012**, *9*, 26.
29. Hervé, F.; Ghinea, N.; Scherrmann, J.-M., *The AAPS journal* **2008**, *10* (3), 455-472.
30. Ragnai, M. N.; Brown, M.; Ye, D.; Bramini, M.; Callanan, S.; Lynch, I.; Dawson, K. A., *European Journal of Pharmaceutics and Biopharmaceutics* **2011**, *77* (3), 360-367. DOI 10.1016/j.ejpb.2010.12.024.
31. Ye, D.; Ragnai, M. N.; Bramini, M.; Mahon, E.; Åberg, C.; Salvati, A.; Dawson, K. A., *Nanoscale* **2013**, *5* (22), 11153-11165.
32. Dodelet-Devillers, A.; Cayrol, R.; van Horssen, J.; Haqqani, A. S.; de Vries, H. E.; Engelhardt, B.; Greenwood, J.; Prat, A., *Journal of molecular medicine* **2009**, *87* (8), 765-774.
33. Rodal, S. K.; Skretting, G.; Garred, O.; Vilhardt, F.; van Deurs, B.; Sandvig, K., *Molecular biology of the cell* **1999**, *10* (4), 961-74.
34. Karnik, R.; Ludlow, M. J.; Abuarab, N.; Smith, A. J.; Hardy, M. E.; Elliott, D. J.; Sivaprasadarao, A., *PloS one* **2013**, *8* (12), e85630.
35. Bolte, S.; Cordelières, F. P., *Journal of microscopy* **2006**, *224* (3), 213-232.
36. Guarnieri, D.; Guaccio, A.; Fusco, S.; Netti, P. A., *Journal of Nanoparticle Research* **2011**, *13* (9), 4295-4309. DOI 10.1007/s11051-011-0375-2.

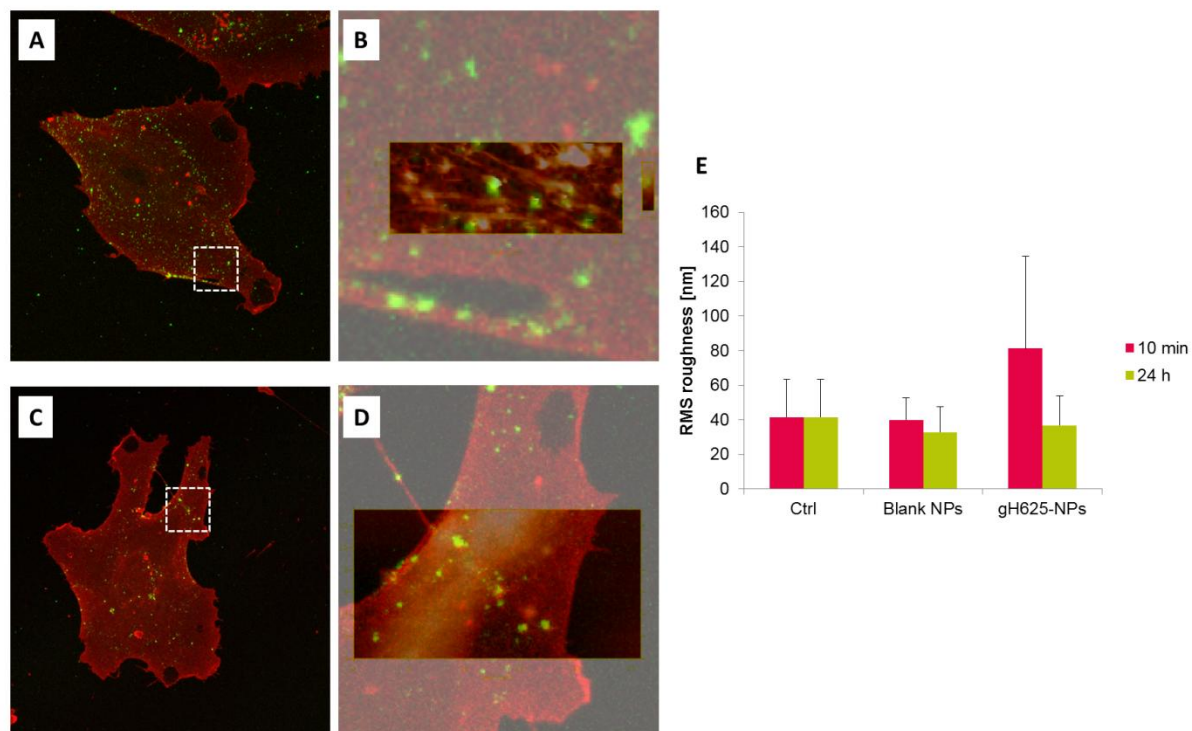


Figure 1. AFM/CLSM coupling analysis. CLSM z-sectioning maximum projection of bEnd.3 cells incubated for 10 min at 37°C with gH625-NPs (a) and blank NPs (c). Red fluorescence: cell membrane staining with WGA; green fluorescence: NPs; the dashed squares indicate the zoomed areas in b (scan area is about $3 \times 8 \mu\text{m}$) and d (scan area is about $14 \times 25 \mu\text{m}$). Transparency image merge of CLSM image and AFM scanning of cell membrane (b and d).

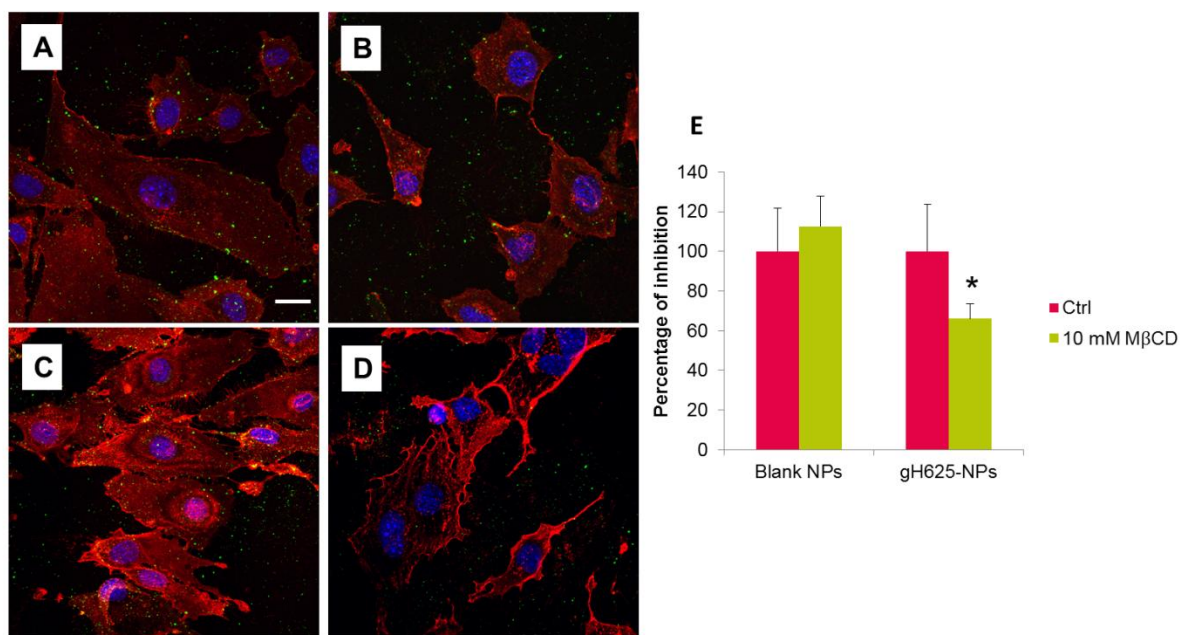


Figure 2. Blank and gH625-NP cellular uptake upon cholesterol depletion treatment. Confocal microscope images of bEnd.3 cells incubated with blank (a and b) and gH625- (c and d) NPs; b and d represent cells treated with 10 mM M β CD. Cell membranes are stained with red fluorescent WGA, cell nuclei are stained with DAPI and green spots are fluorescent NPs. Scale bar 20 μ m. Quantification of NP uptake inhibition (e). Data are reported as mean \pm standard deviation. $p < 0.05$ is considered statistically significant (*).

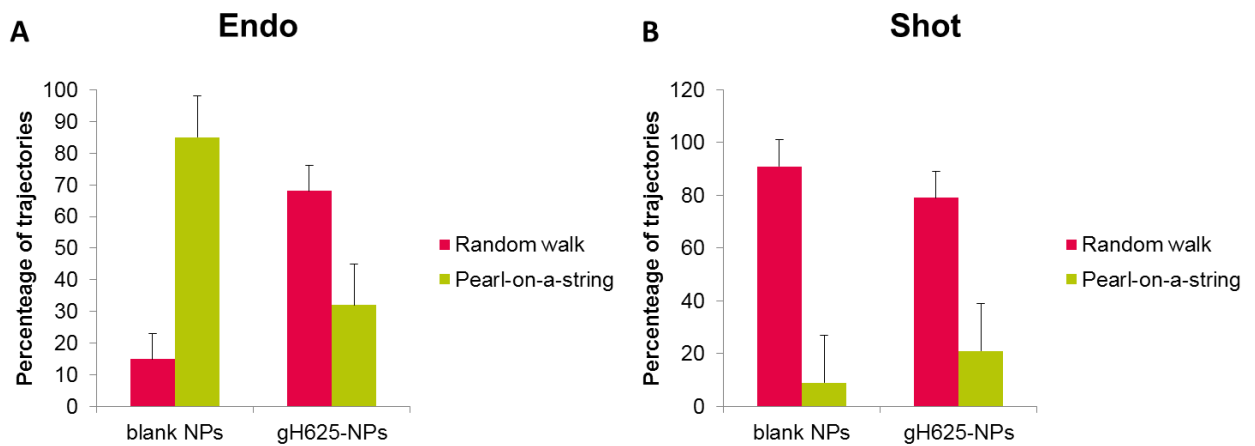


Figure 3. Intracellular trajectories of endocytosed (endo) (a) and shot (b) NPs analysed by MPT technique. The number of analyzed trajectories was 226 for endo blank NPs, 216 for shot blank NPs, 38 for endo gH625-NPs and 101 for shot gH625-NPs.

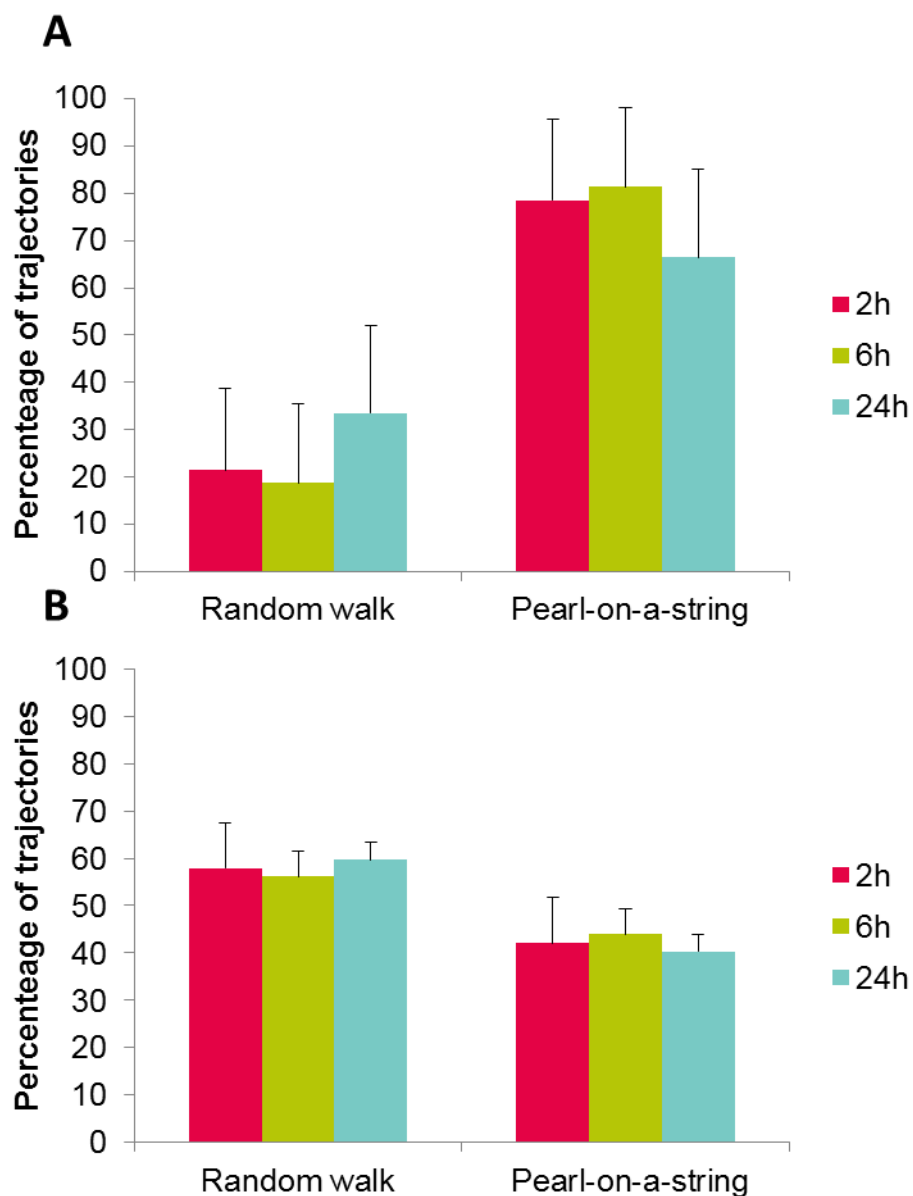


Figure 4. Intracellular trajectories of blank (a) and gH625-NPs (b) over time analysed by MPT technique. The number of analyzed trajectories were 105, 108, 64 for blank NPs at 2, 6 and 24h, respectively, and 34, 113, 87 for gH625-NPs at 2, 6 and 24h, respectively.

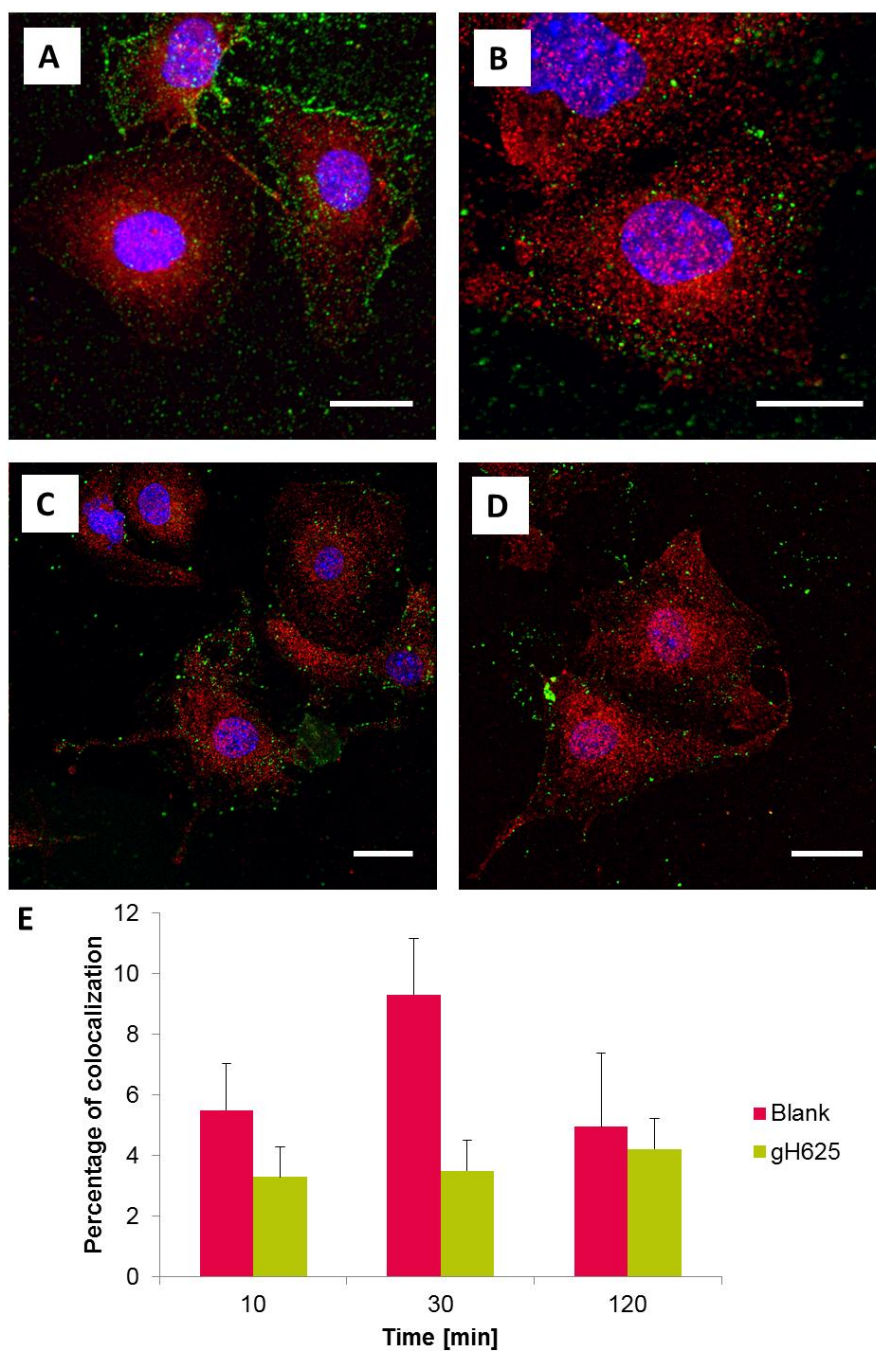


Figure 5. Co-localization of blank and gH625-NPs with endosomes over time. Confocal images of blank (a and c) and gH625-NPs (b and d) upon 10 min (a and c) and 1 h (b and d) of incubation. Scale bar 20 μ m. Quantification of colocalization by ImageJ analysis software (e).

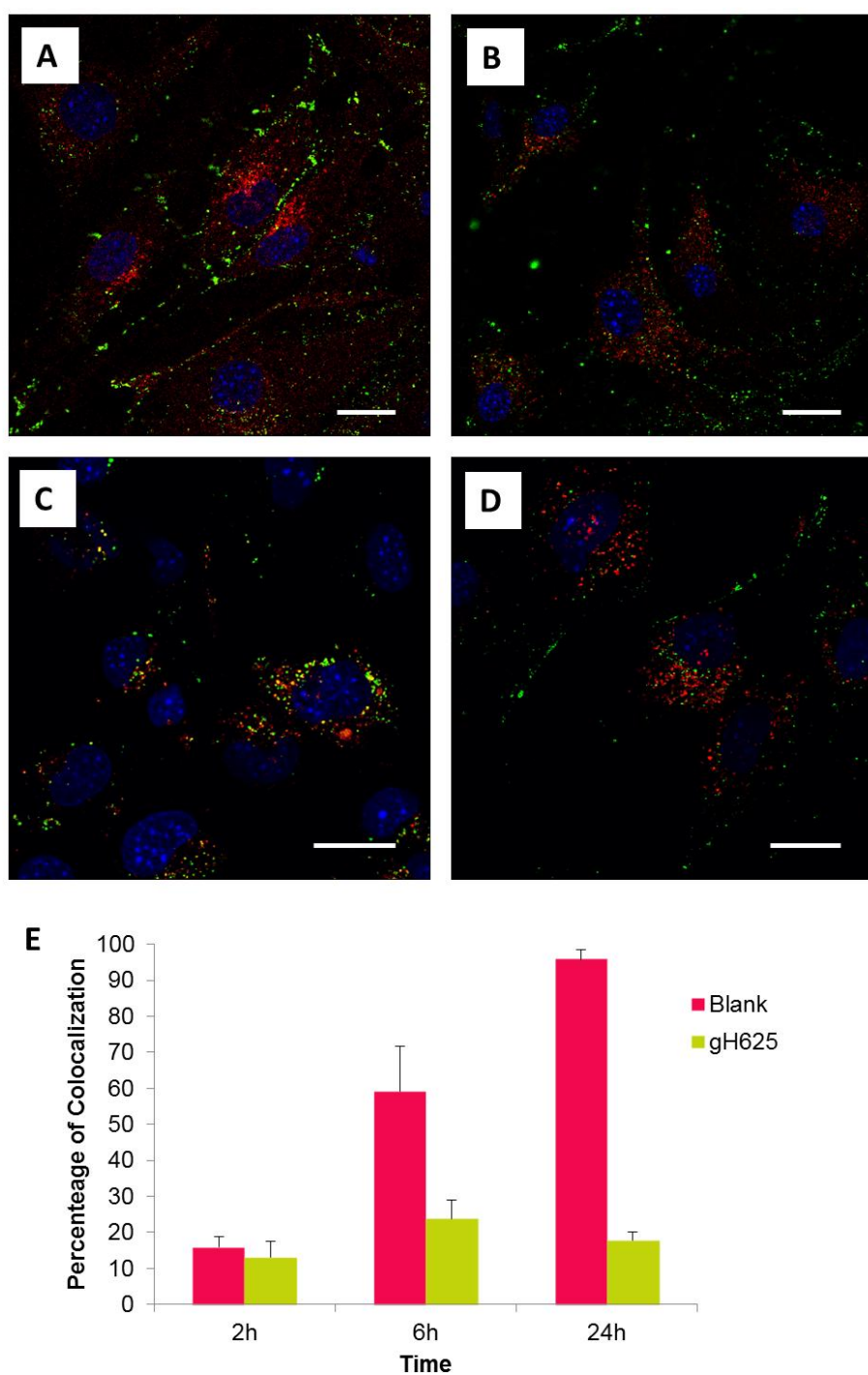


Figure 6. Co-localization of blank and gH625-NPs with lysosomes over time. Confocal images of blank (a and c) and gH625-NPs (b and d) upon 2 h (a and c) and 24 h (b and d) of incubation. Scale bar 20 μ m. Quantification of colocalization by ImageJ analysis software (e).

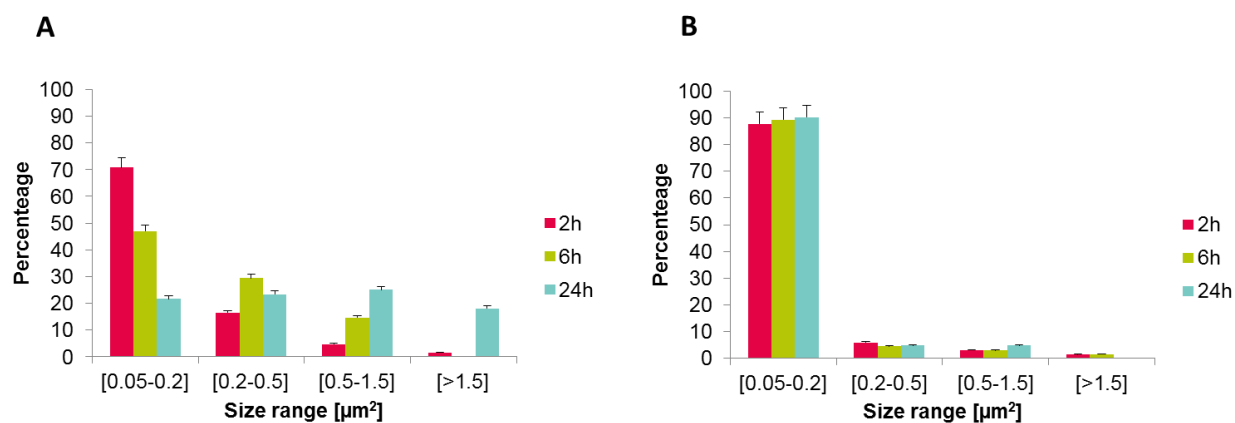


Figure 7. Lysosome size distribution of bEnd.3 cells upon incubation with blank (a) and gH625 (b) NPs over time measured by ImageJ software.

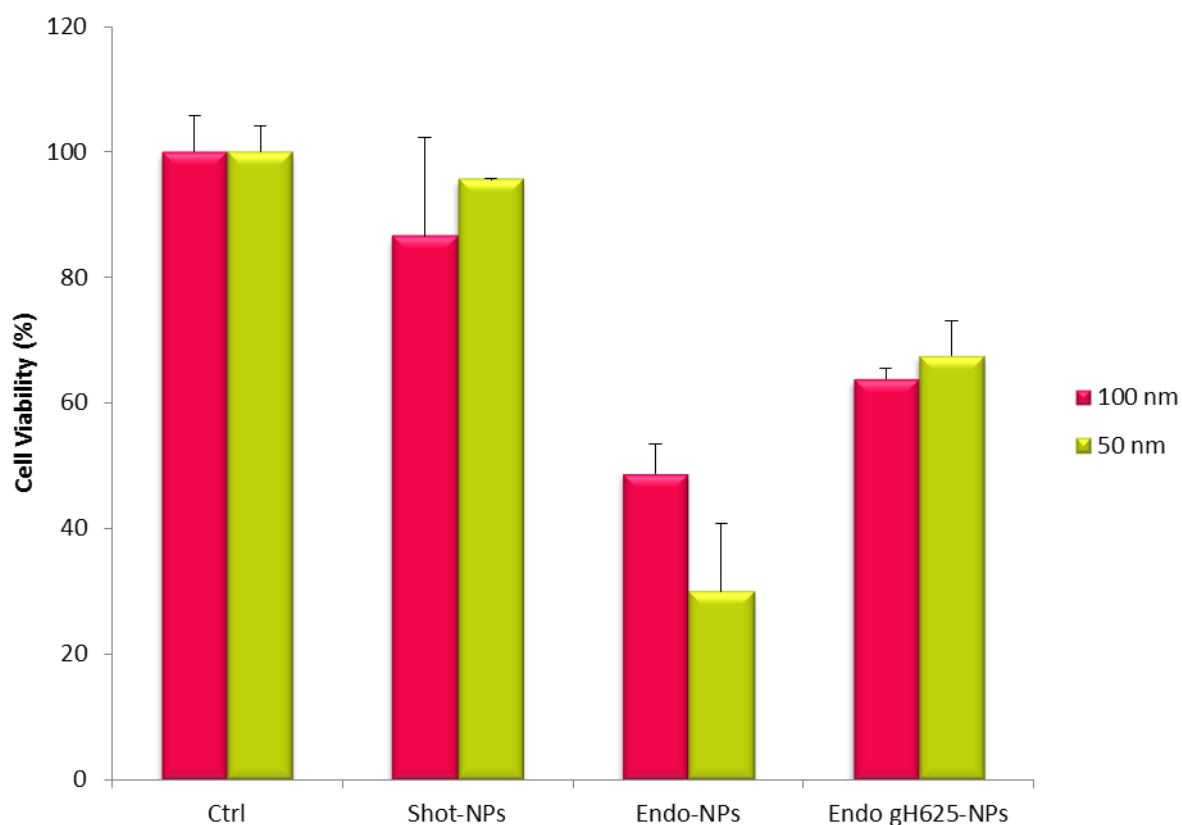


Figure 8. Cytotoxicity of 100 nm and 50 nm gH625-NPs compared to non-treated control cells (ctrl) and cells incubated for 24 h with blank NPs delivered by “classical” endocytosis (endo-NPs) and by gene gun method (shot-NPs). Data are expressed as the average percentage of cell viability normalized to non-treated cells (ctrl) \pm standard deviation. $p < 0.05$ is considered statistically significant (*) (n= 6).

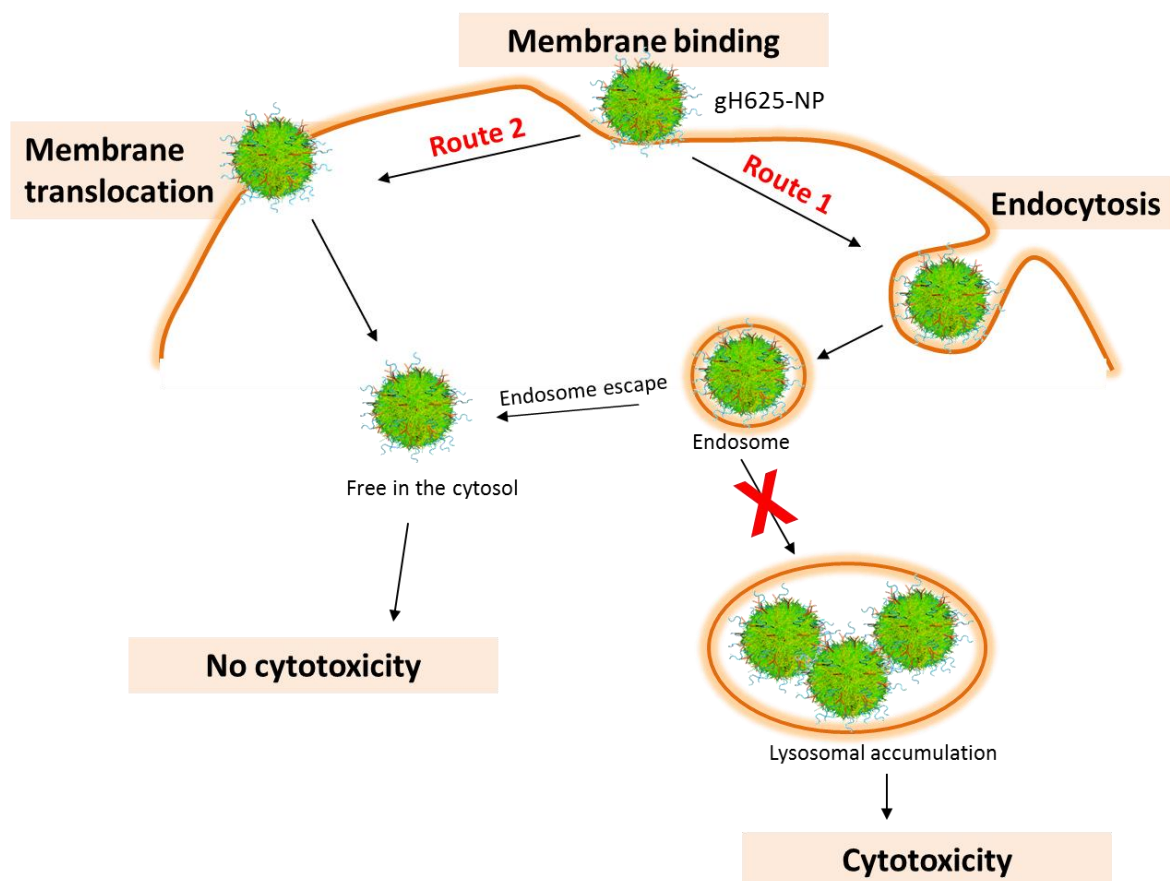
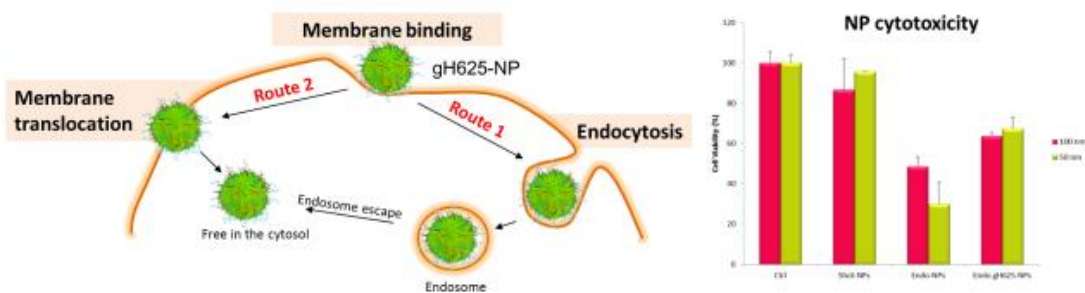


Figure 9. Schematic representation of the hypothesized mechanisms of gH625-NP uptake and intracellular trafficking. gH625 may be able to carry NPs across the cell membrane with translocation mechanisms (route 2) or, when endocytosis takes place, it is able to induce endosomal escape (route 1). The ability of gH625 to avoid accumulation into lysosomes (both by using uptake mechanisms not involving endocytosis mechanisms, and/or escaping from lysosomes) is responsible of the reduction of cytotoxicity.

TOC.

gH625 functionalized nanoparticle (gH625-NP) uptake mechanisms are characterized in brain endothelial cells. No lysosomal accumulation of gH625-NPs compared to blank non-functionalized nanoparticles has relevant consequences in cytotoxicity profile of nanoparticles. As a result, this platform paved the way to design safe and effective nanocarriers for drug delivery to the central nervous system.



Copyright WILEY-VCH Verlag GmbH & Co. KGaA, 69469 Weinheim, Germany, 2013.

Supporting Information

Surface decoration with membranotropic peptides as a method to escape endo-lysosomal compartment and reduce nanoparticle toxicity.

Daniela Guarnieri¹, Ornella Muscetti¹, Annarita Falanga², Sabato Fusco¹, Valentina Belli¹, Emiliana Perillo², Edmondo Battista¹, Valeria Panzetta¹, Stefania Galdiero^{2,}, Paolo A. Netti^{1,3,*}*

Dr. D. Guarnieri, Dr. O. Muscetti, Dr. S. Fusco, Dr. V. Belli, Dr. E. Battista, Dr. V. Panzetta, Prof. P.A. Netti

Center for Advanced Biomaterials for health Care (CABHC), Istituto Italiano di Tecnologia, Largo Barsanti, Napoli, Italy

Centro di Ricerca Interdipartimentale sui Biomateriali (CRIB), Università di Napoli Federico II, Piazzale Tecchio 80, Napoli, Italy

*E-mail: nettipa@unina.it

Dr. A. Falanga, E. Perillo, Prof. S. Galdiero

Dipartimento di Farmacia, Università di Napoli Federico II, Via Domenico Montesano 49, Napoli, Italy

*E-mail: sgaldier@unina.it

Table S1. Size and zeta-potential of 50 and 100 nm NPs with and without gH625 functionalization at pH7.

	Zeta-potential (mV) [a]	Size (d.nm) [a]	PDI
50 nm NP	+ 42.8 ± 6.7	60.0 ± 5.4	0.16
50 nm gH625-NP	+ 23.4 ± 3.0	71.0 ± 9.3	0.24
100 nm NP	+ 56.7 ± 1.1	104.4 ± 0.3	0.11
100 nm gH625-NP	+ 26.9 ± 1.0	102.9 ± 0.6	0.15

[a] (mean value ±SD, n=3)

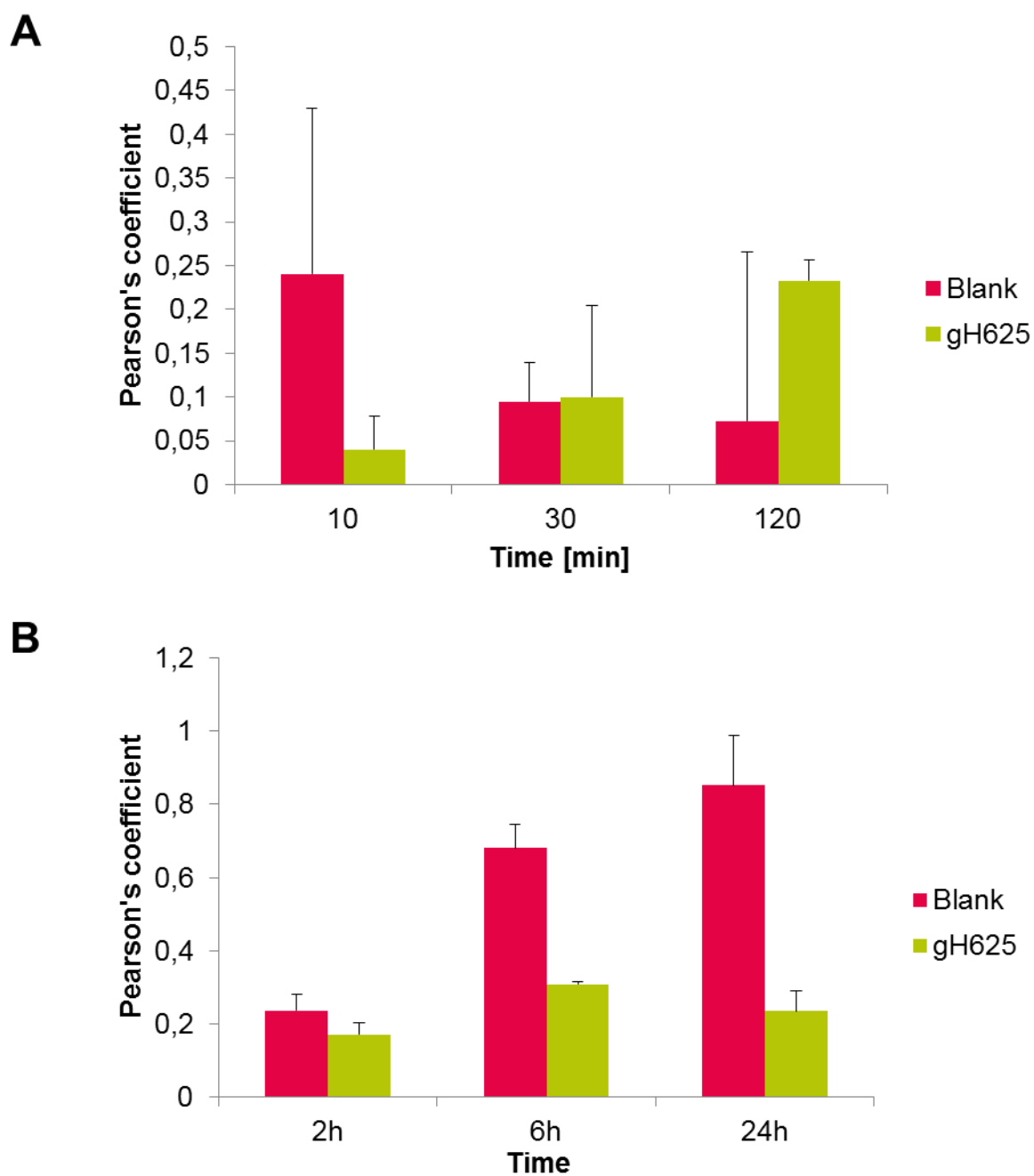


Figure S1. Pearson's coefficients of co-localization experiments of blank and gH625-NPs with Rab5 (A) and LAMP2 (B) calculated by JACoP ImageJ plugin.

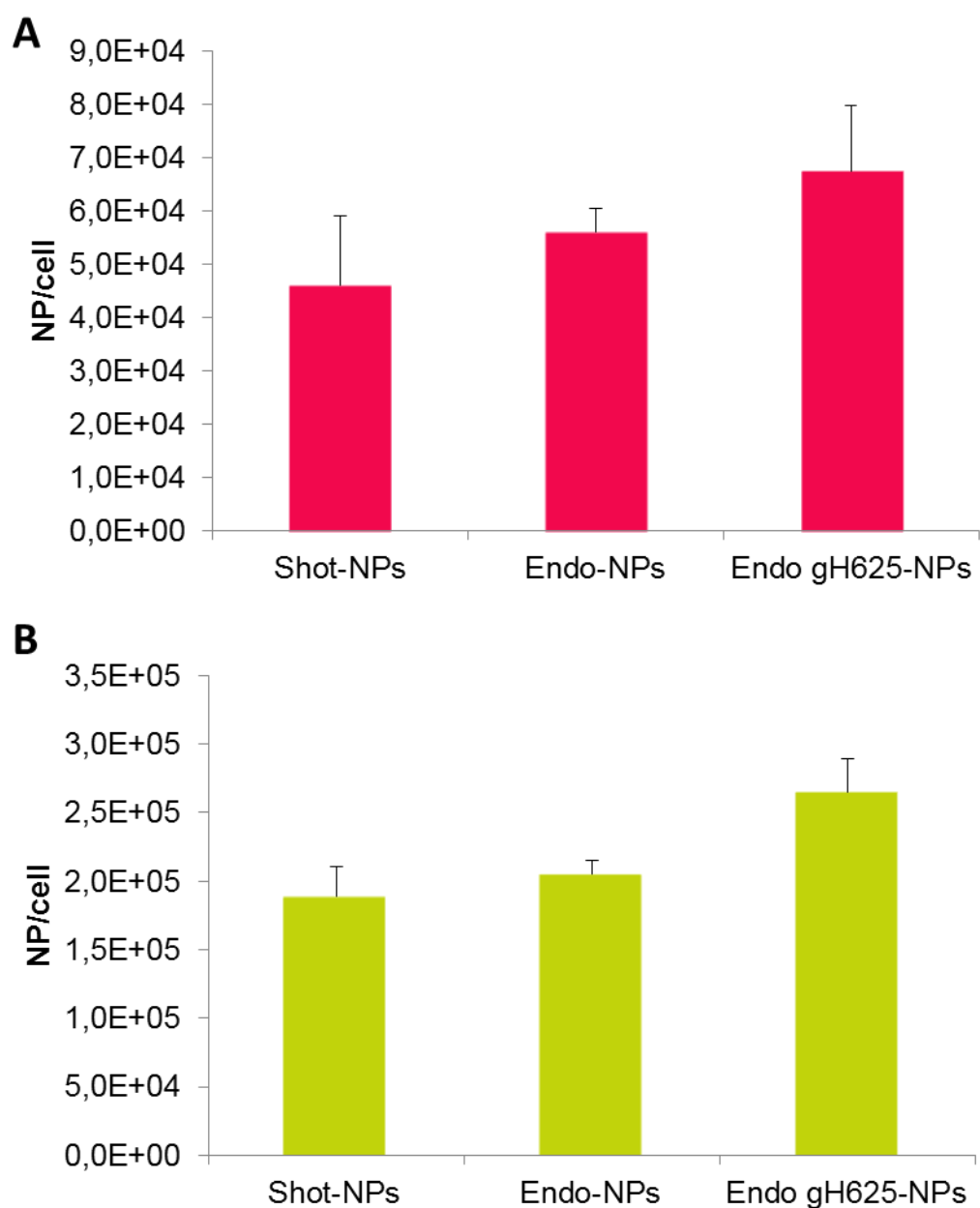
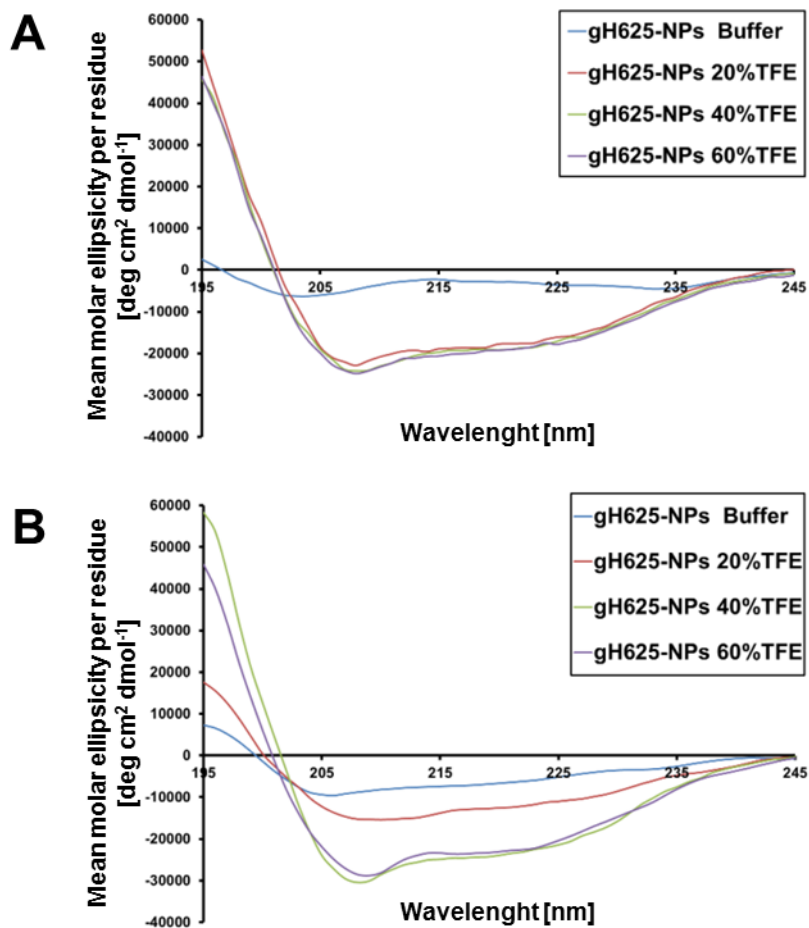


Figure S2. Quantification of 100 nm (A) and 50 nm (B) NP uptake upon endocytosis (endo) and shooting (shot).

Figure S3. Circular dichroism of 50 nm NPs (panel A) and 100 nm NPs (panel B) with 35% of gH625 functionalization.



Quantitative and qualitative effect of gH625 on the nanoliposome-mediated delivery of mitoxantrone anticancer drug to HeLa cells

Emiliana Perillo,¹ Emilie Allard-Vannier,² Annarita Falanga,¹ Paola Stiuso,³ Maria Teresa Vitiello,⁴ Massimiliano Galdiero,⁴ Stefania Galdiero^{1*} and Igor Chourpa^{2*}

¹Department of Pharmacy, DFM Scarl - University of Naples “Federico II”, 80134, Naples, Italy

²Université François-Rabelais, EA 6295 « Nanomédicaments et Nanosondes », Tours, F-37200 France

³Department of Biochemistry, Biophysics and General Pathology, II University of Naples, 80138 Naples, Italy

⁴Department of Experimental Medicine - II University of Naples, 80138, Naples, Italy

Running head:

Cellular delivery of mitoxantrone by gH625-decorated nanoliposomes

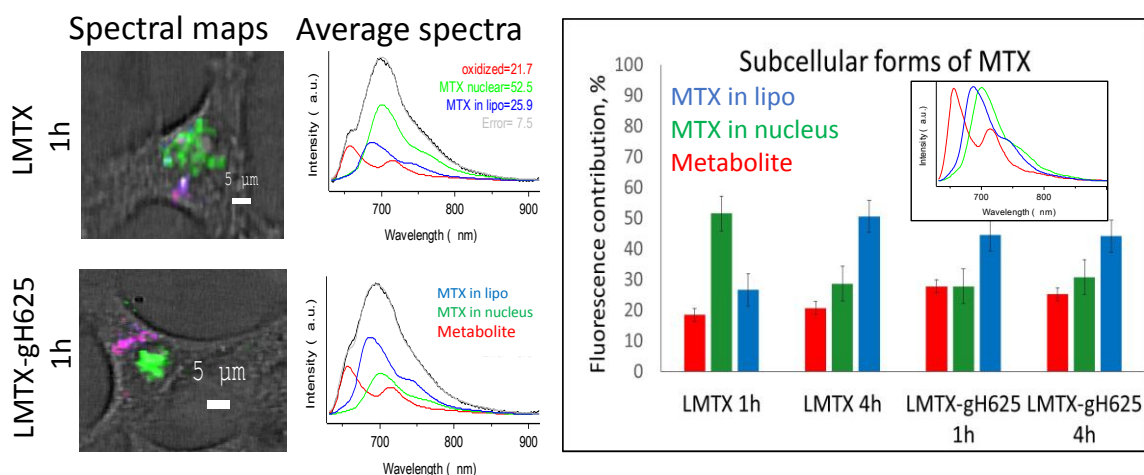
*Address correspondence to:

S. Galdiero and I. Chourpa

SG phone: +39 812536642; e-mail: sgaldier@unina.it

IC phone: +33 247367162; e-mail: igor.chourpa@univ-tours.fr

Graphical abstract:



Abstract

The present work investigates *in vitro* the delivery of the anticancer drug mitoxantrone (MTX) to HeLa cancer cells by means of polyethylene glycol (PEG) liposomes functionalized with the novel cell penetrating peptide gH625. This hydrophobic peptide enhances the delivery of doxorubicin (Doxo) to the cytoplasm of cancer cells, while the mechanism of this enhancement has not yet been understood. Here, in order to get a better insight into the role of gH625 on the mechanism of liposome-mediated drug delivery, we treated HeLa cells with liposomes functionalized with gH625 and loaded with MTX; functionalized and not liposome were characterized in terms of their physico-chemical properties and drug release kinetics. To quantify the MTX uptake and to study the subcellular drug distribution and interaction, we took advantage of the intrinsic fluorescence of MTX and of the fluorescence-based techniques like fluorescence-activated cell sorting (FACS) and confocal spectral imaging (CSI). FACS data confirmed that gH625 increases the total intracellular MTX content. CSI data indicated that when liposomes are decorated with gH625 an enhanced staining of the internalized drug is observed mainly in hydrophobic regions of the cytoplasm, where the increased presence of an oxidative metabolite of the drug is observed. The cytotoxicity on HeLa cell line was higher for functionalized liposomes within 4-6 h of treatment. To summarise, the MTX delivery with gH625-decorated nanoliposomes enhances the quantity of both the intracellular drug and of its oxidative metabolite and contributes to higher anticancer efficacy of the drug at the delay of 4 to 6h.

Highlights

- We report on the delivery of gH625 decorated liposomes
- An enhanced quantity of MTX is delivered
- The formation of an oxidative metabolite of MTX is proposed

Keywords: nanoliposomes, polyethylene glycol (PEG), cell penetrating peptide (CPP), gH625, anticancer drug mitoxantrone (MTX).

1. Introduction

Cancer remains a leading cause of death in the western world. Cancer chemotherapies usually involve the use of cytotoxic molecules which kill highly proliferative cancer cells but also other proliferative cells in bone marrow, the gastrointestinal tract and hair follicles leading to common side effects such as compromised immune system, hair loss etc. [1]. Mitoxantrone (MTX) is a synthetic anthracenedione antineoplastic agent derived from the anthraquinone dye ametantrone [2]. It is structurally similar to the anthracycline agent doxorubicin (Doxo), both drugs having a planar aromatic ring structure which enables them to interact with DNA by intercalation between base pairs. MTX can inhibit the activity of nuclear enzyme DNA topoisomerase (II), interfere with RNA and cause the crosslink of DNA and strand breaks and produce reactive oxygen species. MTX is believed to lack cell cycle phase specificity because it has cytotoxic effects both on proliferating and non-proliferating cells [3]. Similar to Doxo, its main side effect is cardiotoxicity; although also neutropenia, bone marrow suppression and secondary acute myelogenous leukemia have been reported in patients treated with MTX [4]. However, MTX has been shown to produce free radicals to a much lesser degree than Doxo [5].

Actual treatments of cancer disease remains an elusive alternative, offering limited efficacy with extensive secondary effects as a result of severe cytotoxic effects in healthy tissues. The advent of nanotechnology brought the promise to revolutionize many fields including oncology, proposing advanced systems for cancer treatment. Drug delivery systems are among the most successful examples of nanotechnology and allow the reduction of unwanted side effects of systemic delivery, while increasing drug accumulation in tumours and improving the therapeutic efficacy. A delivery tool should transport the drug to the target cells not only with high efficacy, but also with minimal toxicity and immune response avoiding its degradation and entrapment in endosomes. The development of a broad range of nanoparticle platforms with the ability to tune size, composition and functionalities has provided a significant resource for nanomedicine.

Liposomes play a key role as drug carriers and represent a relatively simple form of nanovectors, especially for the delivery of antineoplastic drugs [6,7]; in fact, they modify the pharmacokinetics and biodistribution of the drug, thus resulting in lower toxicity and higher efficacy. Liposomes are able to selectively deliver the drug into malignant areas due to enhanced permeability and retention effects (EPR). As a result, the exposure of healthy tissues to toxic drugs is reduced and therapeutic indexes are improved. Unfortunately, following

intravenous injection, many nanoliposomes are easily recognized by the reticulo endothelial system (RES) resulting in rapid clearance and nonlinear pharmacokinetics. To reduce this effect, polyethylene glycol (PEG) has been introduced on the surface of liposomes. This modification is a milestone breakthrough in the field of drug delivery and is widely known as stealth technology. PEG-coated liposomes display a good pharmacokinetic profile and reduced systemic toxicity; however, their uptake in cells is delayed. In order to facilitate the interaction between liposomes and cells, the liposome surface can be functionalized with cell penetrating peptides (CPPs). CPPs have received much attention because of their ability to enable several kinds of cargoes to cross cell membranes both *in vitro* and *in vivo* [8,9]. CPPs are short and usually basic amino acid rich peptides originating from proteins like the viral TAT protein that are able to cross biological barriers. The CPPs uptake mechanism is highly debated and is thought to involve mainly the endocytic pathway. Trapping the conjugated cargo in endosomes, eventually landing in lysosomes where common enzymatic degradation mechanisms take place, often leads to a limited delivery of therapeutic agents to targets[10].

Hydrophobic peptides, that efficiently traverse biological membranes, promote lipid-membrane reorganizing processes and involve temporary membrane destabilization [9,11,12,13], are able to avoid endosomal entrapment either favouring the escape from the endosome or by translocating directly into the cytosol, thus favouring energy independent processes. This idea has been exploited to design the drug delivery tool called gH625 [12,14], which can be efficiently linked to different potential therapeutic molecules and/or nanovectors and represents an extremely powerful tool to increase their uptake. gH625 is a peptide derived from glycoprotein H of Herpes simplex virus type I, which has been shown to have many applications, from membrane fusion [15], to viral inhibition [16,17] and drug delivery [13]. gH625 has the ability to penetrate deep into the bilayer as a helix without causing significant bilayer perturbations. This ability may help explaining its translocation across the bilayer. It has been recently demonstrated that gH625 is able to transport into the cytosol several compounds, such as QDs [18], liposomes [19], NPs [20], dendrimers [21,22], and proteins [23].

The cellular uptake of liposomes or other nanosystem decorated on their surface with gH625 has been previously determined by flow cytometry (Fluorescence-activated cell sorting - FACS) and confocal fluorescence microscopy [18,19]. It has been shown that the mechanism of nanosystem uptake could be

modified by the presence of the peptide and that the internalization of functionalized nanosystems is mainly not energy-dependent. However, the analysis was limited to the overall detection of the drug used and did not account for the subcellular fluorescence changes, depending on the drug environment/interaction. Confocal spectral imaging (CSI) represents an alternative technique based on measurement, at different points of a cell, of the fluorescence spectra, which provides the opportunity to distinguish different molecular states of the intracellular drug [24]. Thus, CSI is a powerful tool for mapping the MTX molecular interactions within compartments of living cells.

In this work, in order to get a better insight into the role of gH625 on the mechanism of liposome-mediated drug delivery, we have performed a comparative study of HeLa cells treated with MTX-loaded PEGylated liposomes (LMTX) and from LMTX functionalized with gH625 (LMTX-gH625). Prior to cellular experiments, the liposomes were carefully characterized in terms of their physical properties (hydrodynamic size, surface charge), chemical composition (MTX content, gH625 conformation) and drug release kinetics. Both the FACS data on the quantity of total intracellular MTX, the CSI data on the subcellular drug distribution/interaction and the cytotoxicity assay data indicate that the functionalization of liposomes with the peptide gH625 affects the drug delivery qualitatively and quantitatively.

2 Material and methods

2.1 Materials

Fmoc-protected amino acid derivatives, coupling reagents, and Rink amide p-methylbenzhydrylamine (MBHA) resin were purchased from Calbiochem-Novabiochem (Laufelfingen, Switzerland). Fmoc-l-propargylglycine (Fmoc-Pra-OH) was purchased from Polypeptide (Strasbourg, France). Mitoxantrone and other chemicals were purchased from Sigma–Aldrich, Fluka (Buchs, Switzerland), or LabScan (Stillorgan, Ireland) and were used as received, unless otherwise stated. 1,2-Dioleoyl-*sn*-glycero-3-phosphocholine(DOPG) and 1,2-distearoyl-*sn*-glycero-3-phosphoethanolamine-N-[amino(polyethylene glycol)-2000] (ammonium salt) were purchased from Avanti Polar Lipids (Alabaster, AL). HeLa, cervical cancer cell of an African-American woman were purchased from ATCC, Rockville, (MD, USA), Dulbecco's Minimal Essential Medium was obtained from Gibco, Invitrogen Co., (Carlsbad, CA, USA), fetal bovine serum was obtained from Euroclone, Milan, Italy, 100 mg / ml sodium pyruvate, 100 g / ml of nonessential

aminoacids, 100 g / ml penicillin / streptomycin and 100 U / ml glutamine was bought from Invitrogen Life technologies, Italy and Hank's Balanced Salt Solution from Fisher Bioblock Scientific, Illkirch, France. Other reagents were all of analytical grade.

2.2 Solid-phase peptide synthesis

gH625 was synthesized using standard solid-phase 9-fluorenylmethoxycarbonyl (Fmoc) procedures with a Syro I MultiSynThec GmbH (Wullener, Germany) automatic synthesizer, as previously reported[15].

The Rink amide MBHA resin (substitution 0.51 mmol/g) was used as the solid-phase support, and syntheses were performed on a scale of 20 μ mol. The peptide was synthesized by consecutive deprotecting and coupling step. Coupling: Fmoc-protected amino acids (4 equivalents relative to resin loading) HBTU (0.5 M in DMF, 4 equiv), HOBT (0.5 M in DMF, 4 equiv), and DIPEA (2 M in DMF, 8 equiv). Deprotection: 30% piperidine in DMF (v/v).

The gH625-Pra was synthesized to allow binding to preformed-liposomes. Fmoc-Pra-OH was coupled once for 45 min with 2 equivalents of PyBop/HOBT and 4 equivalents of DIPEA. The peptide was fully deprotected and cleaved from the resin with a solution of TFA/water/anisole/thioanisole 93.5/2.5/2.0/2.0, at room temperature for 300 min. Then, it was precipitated with ice-cold ethyl ether, filtered, dissolved in water, and lyophilized. Purification was performed by RP-HPLC on a LC8 Shimadzu HPLC system (Shimadzu Corporation, Kyoto, Japan) equipped with a UV lambda-Max Model 481 detector using a Phenomenex (Torrance, CA) C₁₈ (300 Å, 250 × 21.20 mm, 5 μ) column eluted with H₂O/0.1% TFA (A) and CH₃CN/0.1% TFA (B) from 20–80% over 20 min at a flow rate of 20 mL/min. Purity and identity were assessed by analytical LC-MS analyses using a Finnigan Surveyor MSQ single quadrupole electrospray ionization (Finnigan/Thermo Electron Corporation San Jose, CA), column: C₁₈-Phenomenex eluted with H₂O/0.1% TFA (A) and CH₃CN/0.1% TFA (B) from 20–80% over 10 min at a flow rate of 0.8 mL/min. The final yield of purified peptide ranged between 30 and 40%. Azide-AdOO-Lys(C(O)CH₂CH₂C(O)N-(C₁₈H₃₇)₂)-amide ((C₁₈)₂L-N₃) monomer was synthesized on solid phase under standard conditions using the Fmoc/tBu strategy as previously reported [19].

2.3 Liposomes preparation

Liposomes were prepared by the thin lipid film hydration procedure. Mixed aggregates of DOPG/DSPE-PEG/(C₁₈)₂L-N₃ (85:5:10 molar ratio) were prepared by dissolving the lipids in a small amount of

chloroform, and subsequently evaporating the solvent by slowly rotating the tube containing the solution under a stream of nitrogen and eventually lyophilized overnight. A thin film of amphiphiles was obtained. The dry lipid film was suspended in HEPES-NaCl buffer (5 mM-100mM) at pH 7.4 by vortexing; then the lipid suspension was freeze–thawed ten times and extruded ten times through a polycarbonate membrane with 100 nm pore size using a thermobarrel extruder(Northern Lipids Inc, Canada).

2.4 Functionalization of liposomes with gH-625

The click reaction was carried out on DOPG/DSPE-PEG/(C₁₈)₂L-N₃ liposomes adding CuSO₄•5H₂O (4.4 equiv), ascorbic acid (6.7 equiv), and the peptide derivative (1 equiv) with respect to the azido moiety. In particular, solutions containing CuSO₄•5H₂O (60.5 mM, solution A), ascorbic acid (81.4 mM, solution B), and the alkyn-modified peptide (1 mM, solution C) were freshly prepared in water.

Solution A (11.6 μL), solution B (13.2 μL), and solution C (145.4 μL) were added to a suspension of azido-functionalized preformed liposomes in HEPES-NaCl buffer (400 μL). The concentration of solution C was determined measuring the tryptophan absorbance at 280 nm on a UV/Vis Jasco V-5505 spectrophotometer.

The reaction mixture was stirred at 40°C for 30 min and then left overnight at room temperature. After the conjugation step the liposomes were purified by exclusion chromatography on a 1×18 cm Sephadex G-50 (Amersham Biosciences) column pre-equilibrated with HEPES buffer.

2.5 MTX encapsulation in liposomes

MTX was remote-loaded in DOPG/DSPE-PEG/(C₁₈)₂L-N₃ liposomes through an ammonium sulphate gradient method. Briefly, a liposomal solution was prepared as reported above in an ammonium sulphate solution (250 mM) at pH 5.5. Next, the external buffer was removed by ultracentrifugation at 151332 g, at 4°C for 3h, and the liposomes were resuspended in 400 μL of HEPES-NaCl buffer (5 mM-100mM) at pH 7.4. A MTX solution (18μL at 2mg/mL) in water was added to the liposomal solution, to achieve a final lipid to drug weight ratio of 10:1. This suspension was stirred for 30 min at 60°C. Unloaded MTX was removed with a Sephadex G50 column for determination of entrapment efficiency. The MTX concentration was determined by UV spectroscopy measuring the drug absorbance at λ=655 nm. The Drug Loading Content (DLC, defined as the weight ratio of encapsulated drug vs. the amphiphilic moieties) was quantified by subtracting the amount of MTX removed from the total amount loaded. Finally, the MTX pre-loaded liposomes were modified with gH625 by using the click-chemistry reaction procedure, as reported above.

2.6 Quantification of MTX loaded into the liposomes

The presence of copper in Lipo-MTX-gH625 determines the formation of a complex between copper and MTX which quenches fluorescence and absorbance of the drug. In order to verify that the quantity of MTX in both liposomes conjugated or not with the peptide were equal, both preparations were treated with 0.2% Triton X-100 and then with EDTA (10 mM, 91 μ L) with incubation for 1 h at 37 °C. Finally, the drug absorbance measured at 655 nm was used to determine its concentration according to the previously established calibration curve.

2.7 Particle size and zeta potential analyses

The hydrodynamic diameter (D_H) and the polydispersity index (PDI) of LMTX and LMTX-gH625 were measured using dynamic light scattering (DLS) method (Malvern Nanosizer Nano ZS, Malvern, UK). The zeta potential was determined using Malvern Nanosizer NanoZS (Malvern, Malvern, UK). The instrument uses a He-Ne laser 4mW source operating at 633 nm with the scattering angle fixed at 173°. Each measurement was performed at 25°C, at least in triplicate.

2.8 gH625 conformation monitoring by circular dichroism (CD)

CD spectra in the range from 260 to 195 nm were recorded with a Jasco J-810 spectropolarimeter equipped with a NesLab RTE111 thermal controller unit. For the measurements, liposomes decorated with gH625 were diluted 10 times in a H₂O and placed in a 10 mm quartz cell stabilized at 25°C. Other experimental settings were: scan speed of 10 nm min⁻¹, sensitivity of 50 mdeg, time constant of 16 s, bandwidth of 1 nm. Each spectrum was obtained through averaging three scans, subtracting the contributions from other species present in solution, and converting the signal to mean molar ellipticity.

2.9 *In vitro* drug release

The *in vitro* release kinetics of MTX from liposomes was determined using UV-visible spectrophotometry. LMTX and LMTX-gH625 at equivalent MTX concentration were placed into 2 mL of HEPES-NaCl buffer and into under continuous stirring at 37°C. The release studies were carried out in triplicate. At predetermined time intervals, 200 μ L aliquots were withdrawn and replaced with equal volume of fresh medium. The free drug was collected by a Sephadex G50 column and MTX was quantitated based on the UV-Vis absorbance at 655 nm using a previously established calibration curve. The cumulative amount of MTX released over 24h was quantified, and results were plotted against incubation time.

2.10 *In vitro* cytotoxicity Studies

The estimation of cell viability was performed by staining with Trypan Blue (TB) (Invitrogen). This marker, added to a cell suspension, is able to cross cell membranes that have been changed significantly. The TB penetrates only into damaged cells giving them a blue colour observable under an optical microscope. The viable cells, which are not permeable to the marker, remain colourless. This assay was performed on HeLa, cervical cancer cell of an African-American woman (ATCC, Rockville, MD, USA, CCL-2) grown as monolayers in Dulbecco's Minimal Essential Medium (Gibco BRL, Invitrogen Corporation, Carlsbad, CA, USA), supplemented with 10% fetal bovine serum (FBS - Euroclone, Milan, Italy), 100 mg / ml sodium pyruvate, 100 g / ml of nonessential amino acids, 100 g / ml penicillin / streptomycin and 100 U / ml glutamine (Invitrogen - Life technologies, Italy). These cells were cultured at 37° C, in a humidified incubator in presence of 5% CO₂, using sterile flasks. After reaching the confluence of the flask, the medium was removed and the cells were washed with phosphate buffer saline (PBS). Subsequently, the cells were incubated with a solution of trypsin (0.05% trypsin, 0.0022% EDTA) and PBS at 37 ° C in the presence of 5% CO₂ for 3 minutes. Finally, the cells detached from the flask were transferred into a sterile tube (Falcon) and centrifuged at 325 g for 10 minutes. The cell pellet obtained was resuspended in fresh culture medium and the cells were seeded in 12 well plates (Falcon) in complete medium at a concentration of 350.000 - 400.000 cells / well. The following day, the cells were treated with different concentrations of LMTX and LMTX-gH625; controls were used as untreated cells (negative control) and cells treated with H₂O₂ (positive control). At the end of the treatments of 1, 4, 6, 12, 24, 48 and 72 hours, the cells were washed three times with PBS to remove the liposomes in excess, and then trypsinized. The cells completely detached were transferred in falcon tubes and 25µl of the cell suspension were mixed with 475µl of TB. The cells were counted using the appliance Countess® Cell Counter (Invitrogen). The results were expressed as percentage of control.

2.11 *In vitro* cellular uptake by flow cytometry

The cellular uptake of MTX-loaded liposomes was analysed by flow cytometry. HeLa cells, cultured in Dulbecco's Minimal Essential Medium supplemented with 10% fetal bovine serum, were seeded into six-well at a density of 3×10^5 cells per mL at 37 °C for 48 h. Then, cells were treated with a final concentration of 5 µM of LMTX and LMTX-gH625 in PBS medium for 1 and 4 hours in a volume of 1 mL. Thereafter,

cells were washed three times, trypsinized, harvested and then resuspended in 0.5 mL of PBS. The MTX fluorescence associated to the cells was measured by FACS analysis (BD Accuri), using FL4 channel 675/25 nm. The events collected were ten thousand and BD Accuri C6 software was used to calculate mean fluorescence intensity (MFIs) for each sample. MFIs values were reported as histogram.

2.12 *In vitro* cellular uptake and distribution by confocal spectral imaging (CSI)

HeLa cells were plated at a density of 4×10^4 cells/well in 24-well plates onto cover glasses for 48h in DMEM media supplemented with 10 % serum. HeLa cells were then incubated with either LMTX or LMTX-gH625 at drug concentration of 1 μ M for 1 and 4 h at 37 °C in DMEM media without serum. After the incubation with the liposomes, the medium was removed and the cells were washed three times with fresh HBSS (Hank's Balanced Salt Solution, Fisher Bioblock Scientific, Illkirch, France). Washed cells were placed between slide and slip cover. Fluorescence measurements were carried out using a LabRam confocal microspectrometer (Horiba, Villeneuve d'Ascq, France). The MTX fluorescence was excited with a 632.8 nm line of an internal, air-cooled, helium-neon laser. The power on the samples was $\sim 30 \mu$ W, the acquisition time was 0.02 or 0.05 s/spectrum. After the acquisition, all the spectra were normalized to an intensity corresponding to the same acquisition duration. Treatment of spectral maps was made using LabSpec 4.18 software (Horiba Villeneuve d'Ascq, France).

3. Results

3.1. Physico-chemical properties of liposomes

3.1.a. Synthetic components. The liposome component $(C_{18})_2L-N_3$ and the peptide gH625 bearing a propargylglycine moiety (gH625-Pra) were synthesized by the standard solid phase peptide synthesis (SPPS) protocols with Fmoc/tBu (tBu=tert-butyl) chemistry. The alkyne moiety was introduced at the C-terminus of the peptide as an L-propargylglycine. The compounds identity and the purity were confirmed by mass spectrometry, 1H and ^{13}C NMR spectroscopy (for $(C_{18})_2L-N_3$), and LC-MS[19]. Both gH625-Pra and $(C_{18})_2L-N_3$ were collected in good yields (30–40% and 85%, respectively) after HPLC-RP purification.

3.1.b. Blank liposomes. Liposomes coated with PEG (DOPG/DSPE-PEG/ $(C_{18})_2L-N_3$ liposomes) were generated according to classical procedures [25]. Briefly, the lipid mixture was dissolved into ammonium

sulphate buffer and then the suspension was extruded ten times through a polycarbonate membrane (100 nm).

3.1.c. MTX-loaded liposomes. To obtain the MTX-loaded liposomes (LMTX) we used the well-assessed procedures based on an ammonium sulphate gradient [26]; in particular, a solution containing MTX was incubated with liposomes under stirring for 30 min at 60°C. Subsequently, unloaded MTX was removed using a Sephadex G50 column pre-equilibrated with HEPES-NaCl buffer (5 mM-100mM) at pH 7.4. The drug/lipid weight ratio chosen for the loading experiments was 0.1. The resulting LMTX were used as it or were modified with the gH625-Pra peptide (to become LMTX-gH625) via click-chemistry reaction performed in aqueous medium. The coupling of the Pra moiety of the gH625 to the liposomes surface was obtained due to a copper^(I)-catalyzed Huisgen 1,3-dipolar cycloaddition reaction of azides and alkynes [27]. Cu^I catalyser was generated in situ by reduction of CuSO₄ with ascorbic acid [28]. The LMTX-gH625 were obtained with a yield higher than 90% after 12 h at room temperature. Circular dichroism (CD) spectra showed that gH625 when conjugated to liposomes at a concentration of 1.25x10⁻⁶M adopts an α helical conformation (Figure 1), while the peptide alone in buffer adopts a random coil structure; suggesting that the coupling on the surface of the liposomes was sufficient to induce the secondary structure which is probably playing a key role in translocation across the membrane bilayer.

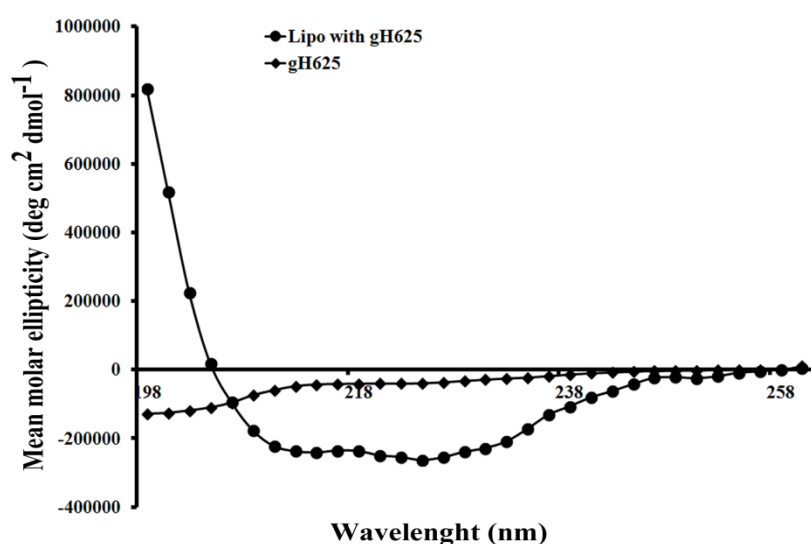


Figure 1. Circular dichroism spectrum of gH625 conjugated to blank liposomes and of gH625 alone.

Dynamic light scattering (DLS) data on LMTX and on LMTX-gH625 dispersed in aqueous medium at pH 7 (Table 1) showed that the liposome functionalization with gH625 only slightly increased their average hydrodynamic diameter, from ca. 112 to 122 nm. The polydispersity index changed from ca. 0.09 to ca. 0.19, indicating that the distribution of the liposome size remained rather narrow and there are no signs of aggregation. These parameters should favour both the effective extravasation of liposomes and their longer retention in tumour tissues.

The surface charge of the liposomes, as determined by measurement of their zeta potential, was also slightly reduced on going from LMTX to LMTX-gH625, from ca. -26 to -21 mV (Table 1). It is widely accepted that at high values of ζ -potential (over 20 mV, positive or negative) the electrostatic repulsions between particles are strong enough to ensure their colloidal stability. At smaller values of ζ -potential, particles can flocculate, except if they have sterical repulsion like in the case of PEG coating. Anyhow, the aqueous suspensions of both LMTX to LMTX-gH625 appear as stable colloids.

Table 1. Colloidal characteristics of LMTX and LMTX-gH625

Liposome type	Hydrodynamic diameter, nm	Polydispersity Index	Zeta potential, mV
LMTX	111.80±1.42	0.09±0.01	-26.30±1.01
LMTX-gH625	122.00±1.05	0.19±0.07	-21.30±1.10

Data obtained for three independently prepared batches of each liposome type, with at least 13 runs per batch.

3.1.d. MTX loading efficiency and release kinetics. The drug loading efficiency calculated from the unloaded MTX absorbance at $\lambda=655$ nm was found at least as high as 97% of the total amount incubated and it was nearly the same in both LMTX-gH625 and LMTX.

In spite of the same concentration inside the liposomes, the MTX fluorescence intensity from LMTX in aqueous suspension was about 5.7 times higher than in LMTX-gH625. The MTX fluorescence in gH625 should be partially quenched by Cu ions used to catalyse the peptide coupling to the liposomes. This hypothesis was confirmed by the experiment described below. Both LMTX and LMTX-gH625 were dissolved by treatment with 0.2% of Triton X-100 and incubation for 1 h with EDTA (10 mM) at 37 °C. This

treatment brought to a full restoration of MTX absorbance intensity of MTX released from LMTX-gH625, while for LMTX, which did not contain copper, the absorbance intensity of the released drug was not affected (Figure 2). Therefore, copper ions are able to penetrate LMTX-gH625 and to quench there the loaded MTX fluorescence and absorbance; however, once the drug escapes from the liposomes, the quenching is no more active.

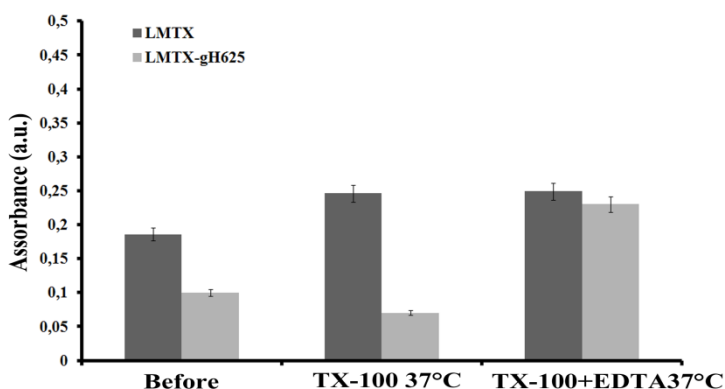


Figure 2. Effect of combination of Triton and EDTA on LMTX and LMTX-gH625. Both liposomes were treated by Triton X-100 (TX-100) and 10 mM of EDTA at 37°C. The presence of EDTA brought full restoration of MTX absorbance intensity in LMTX-gH625, while on LMTX had not effect.

There were no pronounced differences between LMTX and LMTX-gH625 from the point of view of the drug release kinetics *in vitro*, in HEPES-NaCl buffer (Figure 3). Less than 30% of loaded MTX was released within 24 h, indicating the good stability of liposomes.

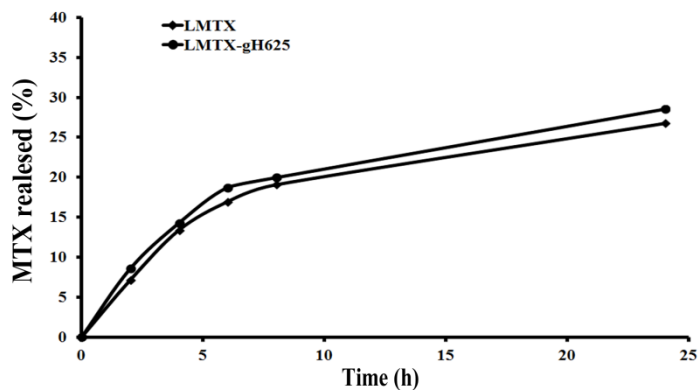


Figure 3. Kinetics of *in vitro* release of MTX from LMTX and LMTX-gH625.

3.2 Biological activity of LMTX and LMTX-gH625 in HeLa cells *in vitro*

The cytotoxicity of liposomes was evaluated staining Tripan Blue on HeLa cells. Within 4 and 6 h treatment duration, cytotoxicity was higher for LMTX-gH625 than LMTX (Figure 4A). At 48 and 72 h we did not notice significant differences between the two types of liposomes; indicating that at high incubation times both are significantly toxic to the cells.

Flow cytometry allowed us to compare quantitatively the MTX uptake by HeLa cells treated with LMTX-gH625 or with LMTX (Figure 4B). We clearly observed an increased uptake of MTX from liposomes decorated with gH625.

For better understanding of the observed cytotoxicity and uptake details, we determined the subcellular distribution and interaction of the delivered MTX in live HeLa cancer cells using confocal spectral imaging (CSI) technique. As described above, the CSI approach consists in recording the complete fluorescence at each scanned point of the cell and therefore exploiting both the spectral shape and intensity.

Full fluorescence spectra (in the 640-920 nm range) were then recorded via point-by-point scanning of the equatorial optical section of the treated cells (see the Experimental section). From these spectra, the parametric maps were generated using either total fluorescence intensity (area of the whole spectrum) or coefficients determined from fitting each experimental spectrum with spectra characteristic of 3 intracellular molecular interactions of the drug: (i) MTX at lipophilic environment, where the spectrum is very close in shape to that of the drug in LMTX in suspension (blue zones and spectra in Figure 5); (ii) MTX in nucleus, where a significant bathochromic shift of the spectrum is observed due to the drug intercalation between DNA base pairs (green zones and spectra); and (iii) an oxidative metabolite of the drug stained in the low polarity environment, with the blue-shifted spectrum (red zones and spectra). These characteristic spectra are consistent with those we previously reported for the MTX incubated as aqueous solution to MDA-MB-231 and MCF-7 cancer cell lines [29].

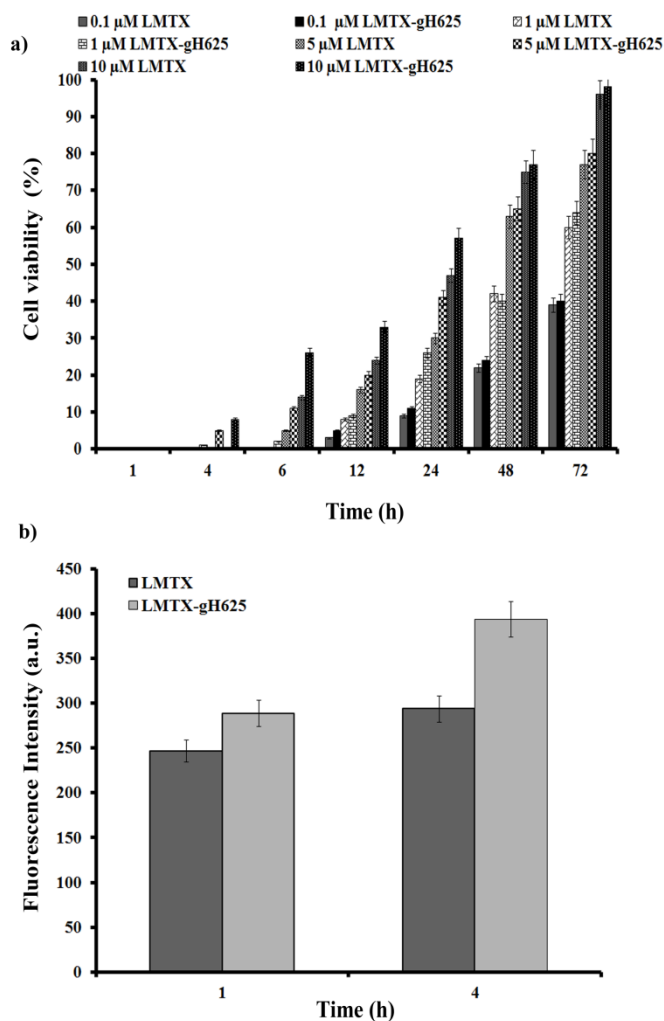


Figure 4 Cytotoxicity of liposomes on HeLa cells at several times of incubation. (**panel a**) Flow cytometry data on the MTX uptake by HeLa cells (**panel b**).

In the present study, the fact that not only the blue spectra but also the shifted ones were observed indicates that the drug was released, at least in part, from the liposomes and was able to reach the nucleus. Interestingly, the blue and red spectra were highly co-localized in some perinuclear regions, indicating that the lipophilic locations favour the drug oxidative metabolism. In our previous study, [29] we found the metabolite to be co-localized with the fluorescent label of endoplasmic reticulum and its presence correlated with higher sensitivity of cancer cells to chemotherapeutic drug MTX. From the point of view of the fluorescence intensity, it is difficult to establish the exact quantum yields (QY) in these three subcellular situations. Nevertheless, it is commonly believed that the lower polarity environment of fluorophore favours

higher QY, while the DNA intercalation leads to a partial quenching of the drug fluorescence. In this consideration, the intensities used in Figure 5 allow only a comparative discussion, but could be calibrated to concentrations once the QY are established (it was not a subject of the present study).

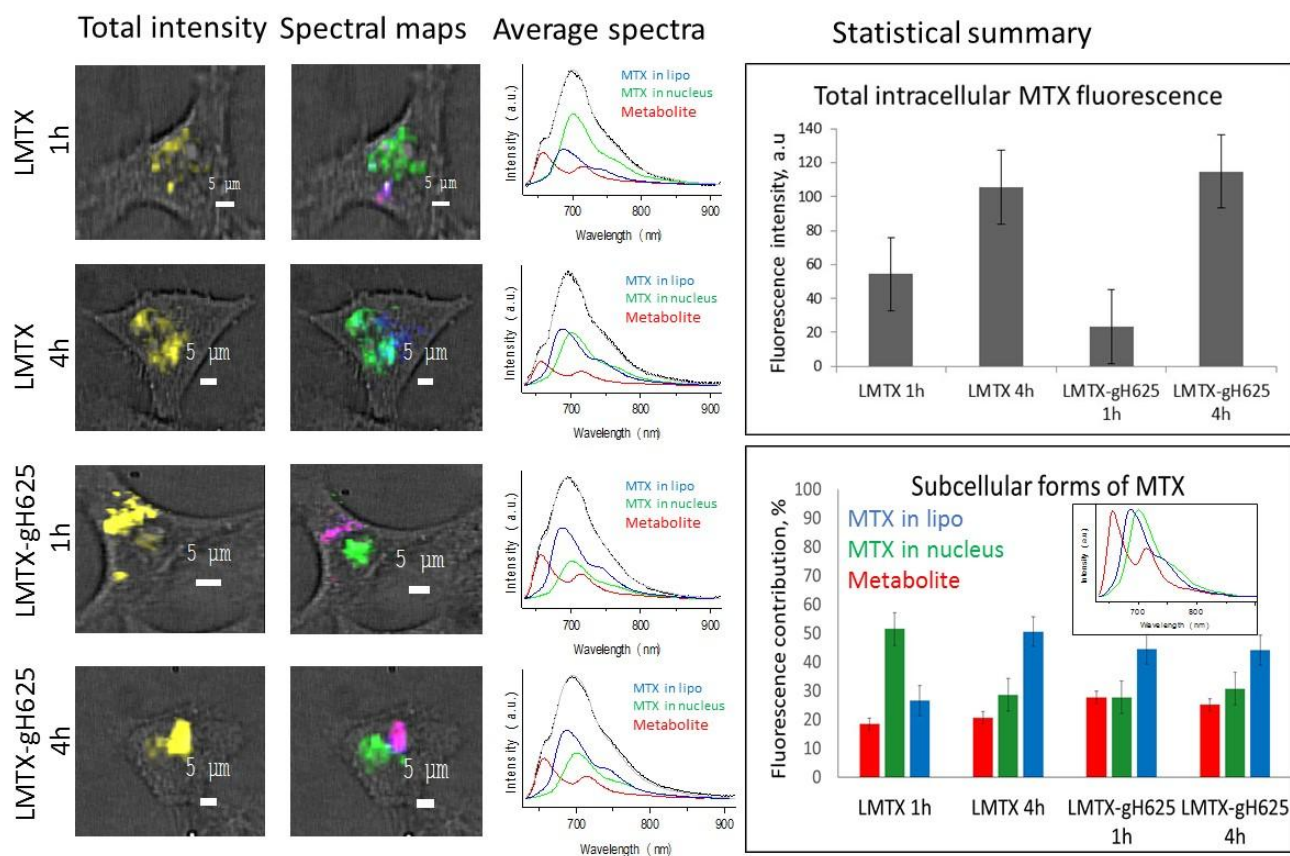


Figure 5. *In vitro* study of subcellular interaction and distribution of MTX delivered from LMTX and LMTX-gH625 to live HeLa cancer cells. Left panel: representative images of individual cells, i.e. merge of the white light images with the fluorescence spectral maps showing either total spectral intensity (yellow zones) or merged spectral maps characteristic of 3 intracellular molecular interactions of the drug: MTX at lipophilic environment (blue zones and spectra), MTX-DNA complex in nucleus (green zones and spectra) and presence of an oxidative metabolite of the drug (red zones and spectra). Average spectra of the respective cells are shown in the middle column. Right panel: statistical summary of the data over a population of at least 6 cells.

The results shown in Figure 5 allow to analyse two effects, that of incubation duration (1h vs 4h) and that of the liposomes functionalization with gH625. The spectral maps show that the increase of the incubation duration from 1h to 4h, determines a significant increase of the total intracellular drug fluorescence (2 to 5 fold, see the statistical summary in Figure 5). Similar total fluorescence intensity was reached with both

types of nanosystems. In contrast, for the LMTX and not for the LMTX-gH625, 4h vs 1h incubation resulted in a subcellular redistribution of the MTX fluorescence: the relative fractions of lipophilic vs nuclear locations were inverted. The analyses of this inversion together with the nearly 2-fold increase of total intensity in LMTX between 1 and 4h, leads one to the supposition that the total drug in the nucleus is probably not decreased while the drug presence in the perinuclear locations is more pronounced. For the LMTX-gH625, the drug fluorescence from the hydrophobic perinuclear regions was dominant even after only 1h of incubation and the subcellular distribution remained nearly constant between 1h and 4h of incubation. The latter means that the 5-fold increase of the intracellular fluorescence intensity for the gH625-modified liposomes is related to the increased uptake of the liposomes and not to the QY changes.

The subcellular distribution of MTX delivered with liposomes was different from that of MTX in solution: while the drug solution was mainly and rapidly stained in nucleus of cancers cells[29], liposomes mainly directed the drug to the perinuclear zones where the metabolite production/staining by the cells was also more significant than with solutions. This could be the effect of the liposomal delivery of MTX.

The above described results lead to the following conclusions about the effect of the liposomes functionalization with gH625: (i) it makes the MTX uptake to the hydrophobic perinuclear staining zones even more efficient; (ii) it favours even more the presence of an oxidative metabolite of the drug in the same perinuclear regions.

4 Discussion

Cell penetrating peptides (CPPs) have recently attracted much interest as very efficient agents to enhance drug delivery into target cells. Among the CPPs, gH625 represents a novel sequence with great possibility of overcoming the known limits of classical CPPs. In previous studies, we have demonstrated that gH625 acts as a potent vector for the cell delivery of molecules and nanosystems [12]. It is widely accepted that drug intracellular distribution changes when they are bound to CPPs [19,30]. The clarification of the mechanism of internalization could be useful to improve the design of anticancer delivery tools that may determine an increase of internalization and may also help in overcoming resistance problems. The purpose of this study was to explore the possibility of using nanoliposomes decorated on their external surface with a novel CPP gH625 to change and enhance the internalization of MTX. We used CSI to distinguish very fine

modifications of MTX intrinsic fluorescence within different intracellular microenvironments.

The obtained results clearly show that the presence of gH625 on the surface of liposomes is favouring their uptake in HeLa cells: in fact, a greater quantity of MTX is internalized (Figure 4B). This correlates well with toxicity data (Figure 4A). Within 4 h, the LMTX-gH625 was more active than LMTX. The gH625 peptide probably induced a greater and more rapid internalization, which could contribute to the earlier cytotoxicity of LMTX-gH625 compared to LMTX. It has also been reported in literature that a fast cytoplasmic delivery of the drug can be related to a better chance to overcome drug resistance [31]. Nevertheless at high incubation times there were no significant differences.

From the CSI spectra, we detected 3 intracellular molecular situation for the drug: MTX at lipophilic environment, MTX in nucleus and an oxidative metabolite of the drug stained in the low polarity environment. The spectra observed indicate that the drug was partially released from the liposomes and was able to reach the nucleus; moreover, the effect of gH625 consists also in an increased presence of an oxidative metabolite of the drug which we previously demonstrated to be correlated with sensitivity of cancer cells to chemotherapy by MTX [29]. We observed that Cu is able to lead to a partial fluorescence quenching for MTX loaded in LMTX-gH625. If we assume that a fraction of subcellular MTX found in lipophilic environment is still encapsulated in liposomes, it means that the real amount of internalized LMTX in presence of gH625 is even higher than what was estimated.

Our results support the view that, in addition to the nuclear one, several mechanisms may be involved in the cytotoxicity of LMTX-gH625 internalization.

5 Conclusions

To summarise, gH625 modifies the internalization of liposomes and therefore the drug transport to the cells. Although the liposome-mediated drug delivery to the nucleus is delayed compared to the drug solution, it could be compensated by complementary mechanisms of cytotoxicity taking place into the cytosol, namely those involving the oxidative metabolism of the drug. These mechanisms are of particular interest for the anticancer activity evaluation of the nanosystems for drug delivery.

Acknowledgements

E.P. thanks Microtech s.r.l. and in particular Dr. Patrizia Bonelli for useful discussions. The authors thank Dr. Katel Hervé-Aubert for help in liposome characterization and Luca De Luca for excellent technical assistance.

References

- [1] C.M. Dawidczyk, L.M. Russell, P.C. Searson, Nanomedicines for cancer therapy: state-of-the-art and limitations to pre-clinical studies that hinder future developments, *Front Chem* 2 (2014) 69.
- [2] C.J. Dunn, K.L. Goa, Mitoxantrone: a review of its pharmacological properties and use in acute nonlymphoblastic leukaemia, *Drugs Aging* 9 (1996) 122-147.
- [3] L.R. Wiseman, C.M. Spencer, Mitoxantrone. A review of its pharmacology and clinical efficacy in the management of hormone-resistant advanced prostate cancer, *Drugs Aging* 10 (1997) 473-485.
- [4] N. Kroger, L. Damon, A.R. Zander, H. Wandt, G. Derigs, P. Ferrante, T. Demirer, G. Rosti, Secondary acute leukemia following mitoxantrone-based high-dose chemotherapy for primary breast cancer patients, *Bone Marrow Transplant* 32 (2003) 1153-1157.
- [5] R.F. Novak, E.D. Kharasch, Mitoxantrone: propensity for free radical formation and lipid peroxidation--implications for cardiotoxicity, *Invest New Drugs* 3 (1985) 95-99.
- [6] J. Cui, C. Li, C. Wang, Y. Li, L. Zhang, H. Yang, Repeated injection of pegylated liposomal antitumour drugs induces the disappearance of the rapid distribution phase, *J Pharm Pharmacol* 60 (2008) 1651-1657.
- [7] A. Madni, M. Sarfraz, M. Rehman, M. Ahmad, N. Akhtar, S. Ahmad, N. Tahir, S. Ijaz, R. Al-Kassas, R. Lobenberg, Liposomal drug delivery: a versatile platform for challenging clinical applications, *J Pharm Pharm Sci* 17 (2014) 401-426.
- [8] F. Heitz, M.C. Morris, G. Divita, Twenty years of cell-penetrating peptides: from molecular mechanisms to therapeutics, *Br J Pharmacol* 157 (2009) 195-206.
- [9] S. Galdiero, A. Falanga, M. Vitiello, P. Grieco, M. Caraglia, G. Morelli, M. Galdiero, Exploitation of viral properties for intracellular delivery, *J Pept Sci* 20 (2014) 468-478.
- [10] Y.S. Choi, A.E. David, Cell penetrating peptides and the mechanisms for intracellular entry, *Curr Pharm Biotechnol* 15 (2014) 192-199.
- [11] A. Falanga, M. Cantisani, C. Pedone, S. Galdiero, Membrane fusion and fission: enveloped viruses, *Protein Pept Lett* 16 (2009) 751-759.
- [12] S. Galdiero, A. Falanga, G. Morelli, M. Galdiero, gH625: A milestone in understanding the many roles of membranotropic peptides, *Biochim Biophys Acta* 1848 (2015) 16-25.
- [13] S. Galdiero, M. Vitiello, A. Falanga, M. Cantisani, N. Incoronato, M. Galdiero, Intracellular delivery: exploiting viral membranotropic peptides, *Curr Drug Metab* 13 (2012) 93-104.
- [14] S. Valiante, A. Falanga, L. Cigliano, G. Iachetta, R.A. Busiello, V. La Marca, M. Galdiero, A. Lombardi, S. Galdiero, The peptide gH625 enters into neuron and astrocyte cell lines and crosses the Blood Brain Barrier in rats, *Int J Nanomedicine* 10.2147/IJN.S77734 (2015).
- [15] S. Galdiero, A. Falanga, M. Vitiello, H. Browne, C. Pedone, M. Galdiero, Fusogenic domains in herpes simplex virus type 1 glycoprotein H, *J Biol Chem* 280 (2005) 28632-28643.
- [16] S. Galdiero, A. Falanga, M. Vitiello, M. D'Isanto, M. Cantisani, A. Kampanaraki, E. Benedetti, H. Browne, M. Galdiero, Peptides containing membrane-interacting motifs inhibit herpes simplex virus type 1 infectivity, *Peptides* 29 (2008) 1461-1471.
- [17] R. Tarallo, T.P. Carberry, A. Falanga, M. Vitiello, S. Galdiero, M. Galdiero, M. Weck, Dendrimers functionalized with membrane-interacting peptides for viral inhibition, *Int J Nanomedicine* 8 (2013) 521-534.
- [18] A. Falanga, M.T. Vitiello, M. Cantisani, R. Tarallo, D. Guarnieri, E. Mignogna, P. Netti, C. Pedone, M. Galdiero, S. Galdiero, A peptide derived from herpes simplex virus type 1 glycoprotein H: membrane translocation and applications to the delivery of quantum dots, *Nanomedicine* 7 (2011) 925-934.
- [19] R. Tarallo, A. Accardo, A. Falanga, D. Guarnieri, G. Vitiello, P. Netti, G. D'Errico, G. Morelli, S. Galdiero, Clickable functionalization of liposomes with the gH625 peptide from Herpes simplex virus type I for intracellular drug delivery, *Chemistry* 17 (2011) 12659-12668.
- [20] D. Guarnieri, A. Falanga, O. Muscetti, R. Tarallo, S. Fusco, M. Galdiero, S. Galdiero, P.A. Netti, Shuttle-mediated nanoparticle delivery to the blood-brain barrier, *Small* 9 (2013) 853-862.

- [21] T.P. Carberry, R. Tarallo, A. Falanga, E. Finamore, M. Galdiero, M. Weck, S. Galdiero, Dendrimer functionalization with a membrane-interacting domain of herpes simplex virus type 1: towards intracellular delivery, *Chemistry* 18 (2012) 13678-13685.
- [22] A. Falanga, R. Tarallo, T. Carberry, M. Galdiero, M. Weck, S. Galdiero, Elucidation of the Interaction Mechanism with Liposomes of gH625-Peptide Functionalized Dendrimers, *PLoS One* 9 (2014) e112128.
- [23] G. Smaldone, A. Falanga, D. Capasso, D. Guarnieri, S. Correale, M. Galdiero, P.A. Netti, M. Zollo, S. Galdiero, S. Di Gaetano, E. Pedone, gH625 is a viral derived peptide for effective delivery of intrinsically disordered proteins, *Int J Nanomedicine* 8 (2013) 2555-2565.
- [24] S. Sharonov, I. Chourpa, H. Morjani, I. Nabiev, M. Manfait, A. Feofanov, Confocal spectral imaging analysis in studies of the spatial distribution of antitumour drugs within living cancer cells, *Analytica Chimica Acta* 290 (1994) 40-47.
- [25] M.J. Hope, M.B. Bally, G. Webb, P.R. Cullis, Production of large unilamellar vesicles by a rapid extrusion procedure: characterization of size distribution, trapped volume and ability to maintain a membrane potential, *Biochim Biophys Acta* 812 (1985) 55-65.
- [26] P.G. Tardi, N.L. Boman, P.R. Cullis, Liposomal doxorubicin, *J Drug Target* 4 (1996) 129-140.
- [27] F. Said Hassane, B. Frisch, F. Schuber, Targeted liposomes: convenient coupling of ligands to preformed vesicles using "click chemistry", *Bioconjug Chem* 17 (2006) 849-854.
- [28] A. Sharma, U.S. Sharma, Liposomes in drug delivery: Progress and limitations, *International Journal of Pharmaceutics* 154 (1997) 123-140.
- [29] S. Vibet, K. Maheo, J. Gore, P. Dubois, P. Bougnoux, I. Chourpa, Differential subcellular distribution of mitoxantrone in relation to chemosensitization in two human breast cancer cell lines, *Drug Metab Dispos* 35 (2007) 822-828.
- [30] S. Aroui, S. Brahim, M. De Waard, J. Breard, A. Kenani, Efficient induction of apoptosis by doxorubicin coupled to cell-penetrating peptides compared to unconjugated doxorubicin in the human breast cancer cell line MDA-MB 231, *Cancer Lett* 285 (2009) 28-38.
- [31] Y. Shen, H. Tang, Y. Zhan, E.A. Van Kirk, W.J. Murdoch, Degradable poly(beta-amino ester) nanoparticles for cancer cytoplasmic drug delivery, *Nanomedicine* 5 (2009) 192-201.

Liposome armed with Herpes Virus-derived gH625 peptide to overcome resistance in lung adenocarcinoma cell lines

Emiliana Perillo,^{1‡} Stefania Porto,^{2‡} Annarita Falanga,¹ Silvia Zappavigna², Paola Stiuso,² Massimiliano Galdiero,³ Stefania Galdiero,^{1*} Michele Caraglia^{2*}

¹Department of Pharmacy, DFM Scarl3 - University of Naples “Federico II”, Via Mezzocannone 16, 80134, Naples, Italy

²Department of Biochemistry, Biophysics and General Pathology, II University of Naples, 80138 Naples, Italy

³Department of Experimental Medicine - II University of Naples, Via De Crecchio 7, 80138, Naples, Italy

***Address correspondence to:**

Stefania Galdiero, Department of Pharmacy, DFM Scarl3 - University of Naples “Federico II”, Via Mezzocannone 16, 80134, Naples, Italy, e-mail: stefania.galdiero@unina.it; Phone: +39 081 2534525 Fax: +39 081 2536642

Michele Caraglia, Department of Biochemistry, Biophysics and General Pathology, Second University of Naples, Italy. Via L. De Crecchio, 7. 80138, Naples, Italy,

e-mail: michele.caraglia@unina2.it or michele.caraglia@alice.it

Phone: +39 081 5665871 Fax: +39 081 5665863

‡ These authors equally contributed to this work

Abstract

The success of pharmacological treatments is often hampered by the onset of the drug resistance. New delivery systems including liposomes have been developed to circumvent drug resistance. To enhance the antitumor efficacy of liposomes encapsulating anti-cancer agents, we have used liposomes externally conjugated to the 20 residue peptide gH625, previously identified as a membrane-perturbing domain in the gH glycoprotein of Herpes simplex virus type I. Physicochemical characterization of the liposome system revealed a size of 140 nm with uniform distribution and high doxorubicin encapsulation efficiency. We have evaluated the growth inhibition on either wild type (A549) or doxorubicin-resistant (A549 Dx) human lung adenocarcinoma cell lines treated with increasing concentrations of liposomes encapsulating Doxo (LipoDoxo), liposomes encapsulating Doxo conjugated to gH625 (LipoDoxo-gH625), empty liposomes (Lipo) or free Doxo for 72 h. We found that the growth inhibition induced by LipoDoxo-gH625 was higher than that caused by LipoDoxo with an IC_{50} of 2.7 and 5 μ M, respectively, in A549 and A549 Dx cells. The data on cell growth inhibition were paralleled by an increased uptake of Doxo induced by LipoDoxo-gH625 compared to LipoDoxo in A549 Dx cells. Cytometric analysis revealed that the antiproliferative effects of each drug treatment were mainly due to the induction of apoptosis. Moreover, the data obtained on oxidative stress suggested a greater internalization of LipoDoxo-gH625 than LipoDoxo in A549 Dx after 72h of treatment. In conclusion, liposomes armed with gH625 are able to overcome resistance in lung adenocarcinoma cell lines.

Keywords: doxorubicin, drug resistance, membranotropic peptide, liposome, lung adenocarcinoma.

Introduction

One of the most important goals in cancer treatment is the achievement of pharmacologically active concentrations of chemotherapeutics in cancer tissues, avoiding drug distribution in healthy tissues. In fact, up-to-date a plethora of pharmacological weapons are available in order to control cancer growth but for none of these selectivity toward cancer cells¹ was demonstrated. An additional challenge is represented by the intracellular targeting of key molecules involved in cancer cell regulation once the efficacious delivery of drugs in cancer cells is achieved. The encapsulation of drugs in nanometric scaled biocompatible materials is a potential strategy for the accumulation of the drugs in the inflamed or tumor tissues through the use of the so-called and well-known enhanced retention and permeation effect (EPR)¹. Once accumulated in tumor tissues nanocarriers can release the drug or can be internalized in cancer cells through endocytosis mechanism, resulting in intracellular trafficking in endosomes. Therefore, cleavage of the drugs out of nanocarriers and escape from the endosomes are further critical steps. A complication of cancer therapy is the potential development of chemoresistance that is due to the selection of cancer cell clones expressing molecules that protect tumour cells from anti-cancer agents^{2,3}. In this light, the overexpression of ATP binding cassette (ABC) transporters - such as P-glycoprotein (Pgp/ABCB1), multidrug resistance related proteins (MRPs/ABCCs) and breast cancer resistance protein (BCRP/ABCG2) - limits the intracellular retention and cytotoxicity of different chemotherapy drugs, conferring to tumor cells a multiple and cross-resistant phenotype known as multidrug resistance (MDR)⁴. Therefore, after the crossing of the fenestrated vessels, that are typical of cancer tissues, nanoparticles have also to overcome

cell membrane barriers, release and retain the drug intracellularly at therapeutic levels for a desired time. Based on these, cancer cell membranes represent another critical barrier that affects both drug internalization and retention in cancer cells.

Among nanosystems used for drug delivery, liposomes have attracted great attention since they are deemed ideal for loading and delivery of different molecules, therefore, offering novel opportunities for cancer treatment⁵⁻⁷. Benefits associated with liposomal drugs can derive from: i) protection of encapsulated drugs from chemical and biological degradation into the blood stream; ii) controlled release and reduced toxicity through decreased exposure of healthy tissues to anti-cancer drugs; iii) increased anti-tumor activity resulting from a relatively long systemic circulation time (especially in the case of PEGylated liposomes)⁸⁻¹⁰; iv) subsequent extended exposure and accumulation in growing tumor sites. To enhance the antitumor efficacy of liposomal drugs and to overcome the obstacle of the membrane barrier of cancer cells, many research groups are actively investigating how to improve liposome cell internalization through the addition of surface ligands. Recently, several cell penetrating peptides (CPPs) such as penetratin and Tat have been successfully used for the intracellular delivery of liposomes^{5,11,12}. CPPs are a group of short, positively charged peptides with a potent ability to penetrate the membrane bilayer, which are well suited as drug delivery vehicles able to cross the biological barriers. The advantages of peptides as delivery enhancers include: i) their relatively small molecular weight, ii) easy synthesis, iii) relatively low cytotoxicity and immunogenicity, and iv) *in vivo* degradation¹³. Cationic cell-penetrating peptide-mediated endocytosis is one of the mechanisms by which drug carriers cross the membrane bilayer¹⁴; subsequently, the cargo is trapped in endosomes, eventually landing in

lysosomes where its intracellular bioavailability is decreased. In order to avoid the endocytic pathway, it is of great importance to discover new molecules exploiting different mechanisms of uptake. Hydrophobic peptides that efficiently cross biological membranes, promoting lipid membrane-reorganizing processes represent a powerful alternative¹⁵⁻¹⁷. Viral-derived peptides, especially those derived from viral entry proteins, can be useful as Trojan horses due to their intrinsic properties of inducing membrane perturbations¹⁶⁻¹⁸. The twenty residue peptide gH625, previously identified as a membrane-perturbing domain in the glycoprotein H (gH) of Herpes simplex virus 1 (HSV-1), is able to cross the membrane bilayer¹⁹ and has been extensively used for vector-mediated strategies *in vitro*, which only partially involves the endocytic pathway²⁰⁻²⁴. We previously showed the drug carrier ability of gH625 functionalized DOPG based liposomes encapsulating Doxo and revealed differences between the uptake mechanisms of free and encapsulated Doxo²². Nuclear accumulation of free Doxo was attributed to drug diffusion, while encapsulated Doxo remained mostly in the cytoplasm with negligible nuclear accumulation²².

Here, we investigated the *in vitro* anti-cancer activity of Doxo-encapsulating liposomes, constituted by soy phospholipids, cholesterol and 1,2-distearoyl-sn-glycero-3-phosphoethanolamine-N-[amino(polyethylene glycol)-2000] (DSPE-PEG), in order to improve biocompatibility and lead to a prolonged presence in the systemic circulation.

The antiproliferative activity of gH625 functionalized or not functionalized with gH625 liposomal formulations was investigated on non small cell lung cancer (NSCLC) A549 cells either sensitive or resistant to Doxo. The differential accumulation and the oxidative stress

caused by the two different formulations in resistant and parental A549 cells were also evaluated.

Material and Methods

Materials

Fmoc-protected amino acid derivatives, coupling reagents, and Rink amide p-methylbenzhydrylamine (MBHA) resin were purchased from Calbiochem-Novabiochem (Laufelfingen, Switzerland). Fmoc-L-propargylglycine (Fmoc-Pra-OH) were purchased from Polypeptide (Strasbourg, France). Doxorubicin hydrochloride, and the other chemicals were purchased from Sigma–Aldrich, Fluka (Buchs, Switzerland), or LabScan (Stillorgan, Ireland) and were used as received, unless otherwise stated. All phospholipids were purchased from Avanti Polar Lipids (Alabaster, AL); in particular the soybean phospholipid mixture is composed of Soy PC (3.8mg) Soy PE (3.0mg) Soy PI (1.8mg) Soy PA (0.7mg) Soy LPC (0.7mg) with 0.1% butylated hydroxytoluene (BHT). Culture medium DMEM, fetal bovine serum and tissue culture plasticware were purchased from Microtech (Naples, Italy). Annexin V-FITC Apoptosis Detection Kit was purchased from eBioscience (San Diego, CA, USA). Dihydroethidium (DHE) was purchased from Sigma-Aldrich (Milan, Italy).

Solid-phase synthesis of gH625 and Azide-AdOO-Lys(C(O)CH₂CH₂C(O)N-(C₁₈H₃₇)₂)-amide

The peptide was synthesized using standard solid-phase 9-fluorenylmethoxycarbonyl (Fmoc) procedures with a Syro I MultiSynThec GmbH (Wullener, Germany) automatic synthesizer

using a Rink amide MBHA resin (substitution: 0.51 mmol/g; synthesis scale: 20 μ mol). The peptide was obtained by repeated cycles of deprotection and coupling. Coupling: 4 equiv of Fmoc-protected amino acids relative to resin loading, HBTU (0.5 M in DMF, 4 equiv), HOBT (0.5 M in DMF, 4 equiv), and DIPEA (2 M in DMF, 8 equiv). Deprotection: 30% piperidine (v/v) in DMF for 10 min (2 times). All couplings were performed twice for 0.5 h. Fmoc-Pra-OH was coupled once for 45 min with 2 equivalents of PyBop/HOBt and 4 equivalents of DIPEA. The peptide was fully deprotected and cleaved from the resin with a solution of TFA/water/anisole/thioanisole 93.5/2.5/2.0/2.0 at room temperature for 300 min, and then precipitated with ice-cold ethyl ether, filtered, dissolved in water, and lyophilized. The crude peptide was purified by RP-HPLC on a LC8 Shimadzu HPLC system (Shimadzu Corporation, Kyoto, Japan) equipped with a UV lambda-Max Model 481 detector using a Phenomenex (Torrance, CA) C₁₈ (300 Å, 250 × 21.20 mm, 5 μ) column eluted with H₂O/0.1% TFA (A) and CH₃CN/0.1% TFA (B) from 20–80% over 20 min at a flow rate of 20 mL min⁻¹. Purity and identity were assessed by analytical LC-MS analyses using Finnigan Surveyor MSQ single quadrupole electrospray ionization (Finnigan/Thermo Electron Corporation San Jose, CA), column: C₁₈-Phenomenex eluted with H₂O/0.1% TFA (A) and CH₃CN/0.1% TFA (B) from 20–80% over 10 min at a flow rate of 0.8 mL min⁻¹. The final yield of purified peptide was ~40%. Azide-AdOO-Lys(C(O)CH₂CH₂C(O)N-(C₁₈H₃₇)₂)-amide ((C₁₈)₂L-N₃) monomer was synthesized on the solid phase under standard conditions using the Fmoc/tBu strategy as previously reported²².

Liposomes preparation

Liposomes were prepared by the thin lipid film hydration procedure. Mixed aggregates of soy phospholipid mixture/cholesterol/DSPE-PEG/(C₁₈)₂L-N₃ (57:28:5:10 molar ratio) were prepared by dissolving the lipids in a small amount of chloroform, and subsequently evaporating the solvent by slowly rotating the tube containing the solution under a stream of nitrogen and lyophilized overnight. In this way a thin film of amphiphiles was obtained. The dry lipid film was suspended in HEPES-NaCl buffer (5 mM-100mM) at pH 7.4 by vortexing for 1 h; then the lipid suspension was freeze-thawed ten times and extruded ten times through a polycarbonate membrane with 100 nm pore size using a thermobarrel extruder (Northern Lipids).

Functionalization of liposomes with gH625

The click reaction was carried out on preformed soy phospholipid mixture/cholesterol/DSPE-PEG/(C₁₈)₂L-N₃ liposomes adding CuSO₄•5H₂O (4.4 equiv), ascorbic acid (6.7 equiv), and the peptide derivative (1 equiv). In particular, solutions containing CuSO₄•5H₂O (60.5 mM, solution A), ascorbic acid (81.4 mM, solution B), and the alkyne-modified peptide (1 mM, solution C) were freshly prepared in water.

Solution A (11.6 μL), solution B (13.2 μL), and solution C (145.4 μL) were added to a suspension of azido-functionalized liposomes in HEPES buffer (400 μL). The concentration of solution C was determined measuring the absorbance with a UV/Vis Jasco V-5505 spectrophotometer.

The reaction mixture was stirred at 40°C for 30 min and left overnight at room temperature.

After the conjugation step the liposomes were purified by exclusion chromatography on a 1 × 18 cm Sephadex G-50 (Amersham Biosciences) column pre-equilibrated with HEPES buffer.

Doxo encapsulation in liposomes

Doxorubicin was remote-loaded in soy phospholipid mixture/cholesterol/DSPE-PEG/(C₁₈)₂L-N₃ liposomes through the ammonium sulphate gradient method and the free Doxo was removed by gel filtration. Briefly, the liposomal film was suspended in an ammonium sulphate solution (250 mM) at pH 5.5. The external buffer was removed by ultracentrifugation at 40000 rpm (Beckman Optima L-70 Ultracentrifuge) at 4°C for 3h, and liposomes were resuspended in HEPES-NaCl buffer (5 mM-100mM) at pH 7.4. A Doxo solution in water was added to the liposomal solution. This suspension was stirred for 30 min at 60°C. The unloaded Doxo was removed using a Sephadex G50 column and the Doxo concentration was determined by UV spectroscopy measuring the absorbance at $\lambda=480$ nm. The drug loading content (DLC, defined as the weight ratio of encapsulated Doxo vs. the amphiphilic moieties) was quantified by subtraction of the amount of Doxo removed from the total amount of Doxo loaded. Finally, Doxo pre-loaded liposomes were modified with gH625 using the click-chemistry reaction procedure, as reported above.

Particle size and zeta potential analyses

The hydrodynamic diameters (D_H) and polydispersity index (PDI) of liposomes (Lipo), Doxo-loaded liposomes (LipoDoxo) and Doxo-loaded liposomes-gH625 (LipoDoxo-gH625) were measured using dynamic light scattering (DLS) (Malvern Zetasizer Nano ZS, Malvern,

UK). The zeta potential of LipoDoxo-gH625 was determined using a Malvern NanoZ (Malvern Zetasizer Nano ZS, Malvern, UK). The analysis were performed with He–Ne laser 4mW operating at 633 nm at scattering angle fixed at 173° and at 25°C. The results were determined three times for each sample and each measurement was performed at least in triplicate.

***In vitro* Doxo release from liposomes**

The *in vitro* release of Doxo from LipoDoxo and LipoDoxo-gH625 was determined using a dialysis method. Briefly, free Doxo and Doxo-loaded liposomes (with free Doxo removed) were placed in a dialysis bag (MW cut off of 1000 Da) and dialyzed against HEPES-NaCl and HEPES-NaCl with 50% fetal bovine serum under continuous stirring at 37°C. At predetermined time intervals, aliquots were withdrawn and replaced with an equal volume of fresh medium. The Doxo concentrations were calculated based on the fluorescence absorbance intensity of Doxo excited at 485 nm using a previously established calibration curve. The cumulative amount of Doxo released over the 72 h was quantified, and results were plotted against time.

Cell culture

Human lung adenocarcinoma cell line wild type (A549) and doxorubicin (Doxo)-resistant (A549 Dx) were kindly provided by Chiara Riganti, MD (Department of Genetics, Biology and Biochemistry, University of Turin, Italy). Both cell lines were grown in DMEM supplemented with 10% heat-inactivated fetal bovine serum, 20 mM HEPES, 100 U/mL penicillin, 100 mg/mL streptomycin, 1% L-glutamine and 1% sodium pyruvate. The resistance to Doxo in A549 Dx cell line was maintained by administering 10 nM of Doxo in

alternating steps. A549 and A549 Dx cells were cultured at a constant temperature of 37°C in a humidified atmosphere of 5% carbon dioxide (CO₂).

Cell proliferation assay

The evaluation of cell proliferation was performed on human lung adenocarcinoma cell line wild type and doxorubicin resistant in the presence of increasing concentrations of LipoDoxo, LipoDoxo-gH625 and Lipo in a range of 5-0.04 µM or free Doxo in a range of 3-0.02 µM. A549 and A549 Dx cells were seeded in 96-well plates in a number of 25 x 10² per well. The growth inhibition was assessed by MTT viability assay after 72 h of treatment as previously described²⁵. Then the concentrations inhibiting 50% of cell growth (IC₅₀) were obtained and these values were used for subsequent experiments. MTT assay was carried out by triplicate determination on at least three separate experiments. All data are expressed as mean ± SD.

Flow cytometric analysis of Doxo accumulation

The accumulation of Doxo was analyzed by FACSARIA™ (BD Biosciences) after treating A549 and A549 Dx cells with a fixed concentration (10 µM) of Lipo, LipoDoxo, LipoDoxo-gH625 and Doxo. Briefly, A549 and A549 Dx cells were seeded in 6-well plates in a number of 2 x 10⁵ cells per well and were treated 24h later with each formulation and free Doxo. After 3, 6, 12 and 24 h of treatment cells were trypsinized, washed twice with PBS 1X and pellets were resuspended in 500 µL of PBS 1X. Doxo fluorescence associated to the cells was measured using FL2 channel and calculated as mean fluorescence intensity (MFIs) for each sample. For each sample, 2 x 10⁴ events were acquired. Analysis was carried out by triplicate determination on at least three separate experiments.

Flow cytometric analysis of oxidative stress

The evaluation of ROS accumulation was detected using dihydroethidium (DHE), a specific marker for the determination of reactive oxygen species, in detail superoxide anion. Once oxidized within the cell, DHE is converted into ethidium (HE) and emits at the wavelength of 605 nm. Briefly, A549 and A549 Dx cells were seeded in 6-well plates in a number of 2×10^5 cells per well and were treated 24 h later with concentration inhibiting 50% of cell growth of each formulation and Doxo. A549 and A549 DX cells were also treated with 500 μM of H_2O_2 , which is able to induce superoxide anion formation, 2000 μM of N-acetylcysteine (NAC) as antioxidant agent, and H_2O_2 in combination with NAC. At the end of treatments, A549 and A549 Dx cells were incubated for 1 h with 20 ng/mL DHE stock solution (2,5 mg/mL). At the time of processing, cells were trypsinized, washed twice with PBS 1X and the pellet was resuspended in 500 μl of PBS 1X. The dye accumulation was analysed by BD FACSAria™ (BD Biosciences). For each sample, 2×10^4 events were acquired. Analysis was carried out by triplicate determination on at least three separate experiments.

Flow cytometric analysis of apoptosis

Apoptotic cell death was analysed by Annexin-V–FITC staining and by propidium iodide (PI) detection systems (eBiosciences, Vienna, Austria). Briefly, A549 and A549 Dx cells were seeded in 6-well plates in a number of 2×10^5 cells per well and were treated 24 h later with concentration inhibiting 50% of cell growth of LipoDoxo, LipoDoxo-gH625, Doxo and 5 μM of Lipo (concentration proved to be not toxic). After 3h-6h-12h-24h of treatment cells were

trypsinized, washed twice with PBS 1X and pellets were resuspended in 200 μ L Binding Buffer 1X. Then, 5 μ L Annexin V-FITC were added to 195 μ L cell suspension, mixed and incubated for 10 min at room temperature. Cells were washed with 200 μ L Binding Buffer 1X, resuspended in 190 μ L Binding buffer 1X and 10 μ L Propidium Iodide (20 μ g/mL) was added. The detection of viable cells, early apoptosis cells, late apoptosis cells and necrotic cells were performed by FACS Aria™ (BD Biosciences). For each sample, 2×10^4 events were acquired. Analysis was carried out by triplicate determination on at least three separate experiments.

Evaluation of intracellular distribution of Doxo by confocal microscopy

After 6 and 24 of incubation of A549 and A549 Dx cells with fluorescent Lipo, cells were fixed for 20 minutes with a 3% (w/v) paraformaldehyde (PFA) solution and permeabilized for 10 minutes with 0.1% (w/v) Triton X-100 in phosphate-buffered saline (PBS) at room temperature. To prevent nonspecific interactions of antibodies, cells were treated for 2 h in 5% bovine albumin serum (BSA) in PBS, then cells were incubated with a specific mouse monoclonal Ab raised against vimentin (1:1,000 in blocking solution, 3% (w/w) BSA in TBS-Tween 0.1%, Sigma) for 2 h at 37 ° C. After several washes, cells were incubated with a secondary IgG goat anti-mouse antibody (Alexa Fluor 488, Life Technologies, Carlsbad, CA) diluted 1:1,000 in blocking solution for 1 h at room temperature. The slides were mounted on microscope slides by Mowiol. The analyses were performed with a Zeiss LSM 510 microscope equipped with a plan-apochromat objective X 63 (NA 1.4) in oil immersion. The fluorescences of the Doxo and Alexa Fluor 488 were collected in multi-track mode using BP550-625 and LP650 as emission filters, respectively.

Statistical analysis.

All data are expressed as mean \pm SD. Statistical analysis was performed by analysis of variance (ANOVA) with Neumann-Keul's multiple comparison test or Kolmogorov-Smirnov where appropriate.

Results and Discussion

Peptide synthesis and conjugation of gH625 to liposomes surface.

The peptide gH625-Pra and the liposome component (C₁₈)₂L-N₃ were synthesized according to standard solid phase peptide synthesis (SPPS) protocols with Fmoc/tBu (tBu=tert-butyl) chemistry. The alkyne moiety of gH625-Pra was introduced in the peptide sequence at the C-terminal position as L-propargylglycine. (C₁₈)₂L-N₃ was synthesized on solid phase following a modified protocol of the classical Fmoc/tBu strategy²². Both gH625-Pra and (C₁₈)₂L-N₃ were collected in good yields (~ 40% and 85%, respectively) after HPLC-RP purification, and analyzed by mass spectrometry, ¹H and ¹³C NMR spectroscopy (for (C₁₈)₂L-N₃), and HPLC to confirm the compound identity and the purity.

The coupling of gH625 on the surface of preformed liposomes was performed by click chemistry (Figure 1). This procedure involves a copper^(I)-catalyzed Huisgen 1,3-dipolar cycloaddition reaction of azides and alkynes yielding 1,4-disubstituted 1,2,3-triazole-linked conjugates²⁶. The click reaction was performed in an aqueous solution and was catalyzed by Cu^I generated, in situ, by reduction of CuSO₄ with ascorbic acid²⁷. An equimolar mixture of

NH₂-gH625-Pra and azido functions on the liposome surface were used and the expected gH625-functionalized liposomes were obtained with a yield higher than 90% after 12 h at room temperature. In the absence of the copper catalyst no reaction was observed.

Drug loading

Doxo was loaded into soy phospholipid mixture/cholesterol/DSPE-PEG/(C₁₈)₂L-N₃ liposomes using the well-assessed procedure based on the ammonium sulphate gradient²⁸; in particular, a solution containing Doxo was incubated under stirring for 30 min at 60°C. Subsequently, unloaded Doxo was removed using a Sephadex G50 column pre-equilibrated with HEPES-NaCl buffer (5 mM-100mM) at pH 7.4. The drug/lipid weight ratio chosen for the loading experiments was 0.1. The drug loading content (DLC) was above 90% of the total.

The drug loaded liposomes were then efficiently modified with the gH625-Pra peptide according to the click-chemistry procedure used in the case of empty liposomes.

Characterization of liposomes.

Dynamic light scattering (DLS) measurements were performed on liposomes alone and on gH625 functionalized liposomes. Table 1 shows that all liposome solutions present a monomodal distribution with a polydispersity index (PDI) < 0.2. indicating a narrow and homogenous size distribution, optimal not only for the more effective extravasation of liposomes, but also for their longer retention in tumor tissues. The analysis of the zeta-potential shows a change between Lipo and LipoDoxo compared to LipoDoxo-gH625, which

indicates a change in the surface of the liposomes upon functionalization with the peptide.

Release of doxorubicin from liposomes

The release of Doxo was carried out in HEPES-NaCl buffer or HEPES-NaCl buffer with 50% FBS and the results are presented in Figure 2. Free Doxo was used as control and its release rate was nearly 100% in 2 h, which means that the release of Doxo from dialysis membrane to buffer solution is not a restricting factor and the release of Doxo from the liposomes is the only rate limiting step. There were no pronounced differences in Doxo release (Figure 2) from LipoDoxo and LipoDoxo-gH625 at each time point, indicating that the decoration of the surface of the liposomes with gH625 did not substantially change the release kinetics of liposomes. The Doxo release from liposomes decorated and not with gH625 is less than 30% within 72 h, indicating their good stability.

Effects of liposomes encapsulating doxorubicin conjugated or not with gH625 viral peptide on A549 and A549 Dx cell proliferation

The effects of Doxo, of empty liposomes and liposomes encapsulating Doxo conjugated or not with gH625 were evaluated on the proliferation of either parental A549 or Doxo-resistant cells (A549 Dx) by MTT assay as reported in “Materials and Methods”. Doxo, LipoDoxo and LipoDoxo-gH625 induced a dose-dependent growth inhibition in both cell lines after 72 h (Figure 3), while treatment with Lipo produced no significant cytotoxic effects in both cell lines (Figure 3). In Table 2, results are reported as concentrations inhibiting 50% of cell growth (IC_{50s}) after 72 h of treatment. The IC_{50} was reached with 0.06 μ M and 0.2 μ M of

Doxo (Figure 3 C, Table 2), with 2.5 μM and 5 μM of LipoDoxo (Figure 3 A and B, Table 2), with 0.5 μM and 2.7 μM of LipoDoxo-gH625 (Figure 3 A and B, Table 2) in A549 and A549 Dx cells, respectively. These data suggested that A549 cells were more sensitive to the treatment with Doxo compared to A549 DX, confirming the drug-resistant phenotype of this cell line. Both cell lines were more responsive to LipoDoxo-gH625 compared to LipoDoxo. These data suggested that the conjugation of liposomes with gH625 probably facilitated the entry and retention of doxorubicin in both sensitive and drug-resistant tumor cell lines allowing an increase of cell growth inhibition.

Doxorubicin accumulation in A549 and A549 Dx cell lines

The accumulation of doxorubicin, free or encapsulated in liposomes conjugated or not with gH625, was investigated by flow cytometry analysis as reported in “Materials and Methods”. A time-dependent accumulation of free and encapsulated Doxo was observed in A549 and A549 Dx cells and the maximal levels were reached after 24 h (Figure 4 and 5). Moreover, LipoDoxo-gH625 induced in both cell lines a greater doxorubicin accumulation than LipoDoxo (Figure 4 and 5). In details, A549 Dx cells showed an early accumulation of doxorubicin after 3 h of treatment with both liposomal formulations and the accumulation was higher if compared to the one observed in parental A549 cells (Figure 4 and 5). This effect was more evident in resistant cells treated with LipoDoxo-gH625 that induced an increase of about 86.9 % of MFI against an increase of about 64.3 % of MFI induced in parental cells (Figure 5 and 4, respectively). Moreover, after 24 h we observed a two-fold increase of percentage of MFI in A549 Dx cells treated with LipoDoxo-gH625 if compared

to those exposed to LipoDoxo (Figure 5). Similar data were also obtained in parental cells but to a lesser extent (Figure 4). Therefore, these data suggested that the conjugation of liposomes with the viral peptide increased the retention of doxorubicin into the cells supporting the data obtained on the growth inhibition.

Evaluation of oxidative stress in A549 and A549 Dx cells

The effects of doxorubicin and liposomes encapsulating doxorubicin conjugated or not with gH625 were also evaluated for analyzing the accumulation of superoxide anions (O_2^-) in either parental or doxorubicin A549 cells, as reported in “Materials and Methods”. In both cell lines free doxorubicin induced a time-dependent accumulation of superoxide anions (Figure 6 and 7) significantly lower compared to that induced by both liposomal formulations. In details, the maximal O_2^- level increase in A549 cell line was detectable after 48 h of treatment with LipoDoxo. LipoDoxo-gH625 induced an accumulation of O_2^- lower than LipoDoxo but this effect was maintained up to the end of treatment (72 h) differently from LipoDoxo (Figures 6). On the other hand, both formulations induced similar effects on A549 Dx cells after 24 h of treatment, but a significant increase of oxidative stress was observed after 72 h of treatment with LipoDoxo-gH625 if compared to the one induced by LipoDoxo (Figure 7). In both cell lines NAC had no effect on the increase of O_2^- levels in contrast to H_2O_2 and acted as a scavenger in combination with H_2O_2 (Figures 6 and 7) decreasing the accumulation of superoxide anions. The data obtained on oxidative stress suggested a greater internalization of LipoDoxo-gH625 than LipoDoxo in A549 Dx after 72h of treatment.

Evaluation of cell death in A549 and A549 Dx cells

A further experiment was performed to evaluate the effects of Lipo, LipoDoxo-gH625, LipoDoxo and Doxo in inducing apoptosis or necrosis as reported in “Materials and Methods”. In agreement with the data obtained from the MTT assay, empty liposomes did not induce any significant toxic effects on both cell lines at any time-point tested (Figure 8 and 9). In contrast, LipoDoxo caused an accumulation of about 27.7% necrotic cells in parental A549 and about 21.1% of late apoptotic cells were recorded after 24h. This effect was more marked when using LipoDoxo-gH625 with about 41.8% of necrotic cells and about 23.3% of apoptotic cells (Figure 8). On the other hand, LipoDoxo induced late apoptosis in about 5.5% of A549 Dx cells while necrosis was recorded in about 36.5% of A549 DX cells after 24h of treatment (Figure 9). This effect was potentiated also in doxorubicin-resistant cells by LipoDoxo-gH625 that caused about 3.8% of late apoptosis and about 50.5 % of necrosis (Figure 9). Free doxorubicin induced more significant effects on A549 cells than on A549 Dx cells but to a lesser extent. In fact, it caused an accumulation of about 25.7% and 16.4% of necrotic cells in A549 and A549 Dx cells, respectively (Figure 8 and 9, respectively).

On the basis of these results, it can be suggested that LipoDoxo-gH625 induced more significant effects on cell death in both cell lines, but with different mechanisms. In fact, we have found that the main mechanism by which LipoDoxo caused cell death in parental A549 was necrosis while it caused apoptosis in doxorubicin-resistant counterpart. These effects were potentiated by LipoDoxo-gH625 in both experimental cell models (Figure 8 and 9).

Intracellular distribution of Doxo in A549 and A549 Dx cells

In order to investigate the intracellular distribution of the different formulations, the Doxo fluorescence associated to the cells was evaluated by confocal laser scanning microscopy (CLSM). A549 and A549 Dx were incubated with IC50s of free Doxo, LipoDoxo and LipoDoxo-gH625 for 6 and 24 h. After 6 h, free Doxo and LipoDoxo-gH625 entered A549 cells and translocated into the nucleus as indicated by the red fluorescence in the center of the cell body (Figure 10 A) while LipoDoxo accumulate in the cytoplasm, without entering into the nucleus (Figure 10 A). In fact, cell nuclei are dark and only few red fluorescent spots, distributed in the cytoplasm, are visible. No fluorescence was observed in A549 treated with empty liposome as expected. On the other hand, in A549 Dx free Doxo was not able to enter into the nucleus accumulating in perinuclear region while CLSM results showed a widespread and intense fluorescence, with intranuclear red spots for cells incubated with LipoDoxo-gH625 (Figure 10 B). Cells treated with LipoDoxo evidenced a significant lower fluorescence intensity, with visible red spots into the cytoplasm (Figure 10 B). We observed a time-dependent uptake of free and encapsulated Doxo and the maximal levels were reached after 24 h in both cell lines (Figure 11 A and B) Therefore, the intracellular uptake of liposomes armed with gH625 could contribute to overcome resistance in lung adenocarcinoma cell lines

Conclusions

A major challenge in cancer therapy is the inability to deliver the chemotherapeutic agents to target tumor cells and tissues selectively, resulting in severe side effects to normal tissues and

organs. Nanotechnology has the potential to promote delivery of drugs improving specificity and enhancing the uptake.²⁹⁻³¹ Moreover, the multidrug resistance (MDR) represents the principal mechanism by which many cancers develop resistance to chemotherapy, and poses the major obstacle to the successful clinical treatments of cancers.^{32,33}

Due to these problems, it is highly important to explore alternative strategies for utilizing currently available drugs against MDR cancer cells. The mechanism of drug action is an important design constraint in defining where the drug must ultimately be delivered. For many platforms designed for intracellular delivery, uptake occurs by an endocytic pathway. Although endocytic pathways can be very efficient in internalization, drug release and endosomal escape are key challenges in achieving high therapeutic efficacy.

Thus, current challenges include developing platforms with improved biodistribution, pharmacokinetic properties, and active targeting. While various active targeting strategies have been explored, there are no FDA-approved platforms^{4,34} highlighting the difficulties in reliably improving accumulation at the tumor site with active targeting.

Doxil is a liposomal formulation of doxorubicin, which was FDA-approved for AIDS-related Kaposi's sarcoma in 1995, for ovarian cancer in 1999, and for multiple myeloma in 2007. In 2013 the use of the generic version Lipodox was approved for treatment of ovarian cancer and Kaposi's sarcoma¹. Doxil is formulated from a combination of fully hydrogenated soy phosphatidylcholine (HSPC), cholesterol, and a lipid with a polyethylene glycol (PEG) head group (DSPE-PEG2k) in a mole ratio of 56.4:38.3:5.3. The DSPE-PEG provides a polymer coating that can inhibit protein adhesion and prolong evasion of mononuclear phagocytic

system (MPS)^{4,12}. Such coatings lead to long circulation half-times (3–4 days in humans) and are essential to achieve significant passive accumulation at a tumor site.

Successful design of nanosystems to treat tumor effectively requires the appropriate surface modification to enhance the uptake; in fact, the activity of cytotoxic drugs that are internalized by cells depends also on their concentration and availability in the cell cytosol and nuclei. Peptide gH625 represents a novel opportunity to overcome the known limits of classical CPPs and proved to be successful for delivery of several molecules, therefore was chosen in our study to increase the cell internalization of liposomes into cells.

The different phospholipids used to prepare the liposomes investigated in the present study are of paramount importance to determine the uptake and mechanism of internalization. We have previously reported preliminary results on the internalization of DOPG liposomes decorated on their surface with gH625 and we proved that gH625 allowed to modify the mechanism of internalization of Doxo, but the eukaryotic membranes are zwitterionic; thus DOPG, being negatively charged, does not well mimics eukaryotic cell membranes. In this study we used liposomes with enhanced biomimetics characteristics (phospholipids derived by soy) and functionalized on their external surface with PEG.

The presence of gH625 on the surface of liposomes is favouring their uptake in both sensitive and drug-resistant tumor cell lines allowing an increase of cell growth inhibition: in fact, a greater quantity of Doxo from functionalized liposomes is accumulated into cells. A higher oxidative stress is obtained after treatment with functionalized liposomes for 72 h indicating that probably also other mechanisms contribute to the activity in presence of gH625. Doxo encapsulated in functionalized liposomes was able to enter in the nuclei of

Doxo-resistant cancer cells indicating that the peptide gH625 was probably inducing a greater and more rapid internalization also in resistant cells, which could contribute to overcome drug resistance ³⁵.

In conclusion, further details have been shed on the mechanism of internalization promoted by gH625 which clearly indicates that this translocating peptide hold promise for the development of a platform for cancer therapy.

Acknowledgements

E.P. thanks Microtech s.r.l. and in particular Dr. Patrizia Bonelli for useful discussions. The authors thank Luca De Luca for excellent technical assistance.

References

1. Caraglia, M.; Marra, M.; Misso, G.; Lamberti, M.; Salzano, G.; De Rosa, G.; Abbruzzese, A. Tumour-specific uptake of anti-cancer drugs: the future is here *Curr Drug Metab* *13*, 4-21 (2012).
2. Kibria, G.; Hatakeyama, H.; Harashima, H. Cancer multidrug resistance: mechanisms involved and strategies for circumvention using a drug delivery system *Arch Pharm Res* *37*, 4-15 (2014).
3. Liang, X. J.; Chen, C.; Zhao, Y.; Wang, P. C. Circumventing tumor resistance to chemotherapy by nanotechnology *Methods Mol Biol* *596*, 467-488 (2010).
4. Gottesman, M. M.; Fojo, T.; Bates, S. E. Multidrug resistance in cancer: role of ATP-dependent transporters *Nat Rev Cancer* *2*, 48-58 (2002).
5. Galdiero, S.; Falanga, A.; Vitiello, M.; Grieco, P.; Caraglia, M.; Morelli, G.; Galdiero, M. Exploitation of viral properties for intracellular delivery *J Pept Sci* *20*, 468-478 (2014).
6. Estanqueiro, M.; Amaral, M. H.; Conceicao, J.; Sousa Lobo, J. M. Nanotechnological carriers for cancer chemotherapy: The state of the art *Colloids Surf B Biointerfaces* (2015).
7. Chaudhury, A.; Das, S. Folate Receptor Targeted Liposomes Encapsulating Anti-Cancer Drugs *Curr Pharm Biotechnol* (2015).
8. Allen, T. M.; Cullis, P. R. Liposomal drug delivery systems: from concept to clinical applications *Adv Drug Deliv Rev* *65*, 36-48 (2013).
9. Allen, C.; Dos Santos, N.; Gallagher, R.; Chiu, G. N.; Shu, Y.; Li, W. M.; Johnstone, S. A.; Janoff, A. S.; Mayer, L. D.; Webb, M. S.; Bally, M. B. Controlling the physical behavior and biological performance of liposome formulations through use of surface grafted poly(ethylene glycol) *Biosci Rep* *22*, 225-250 (2002).
10. Nag, O. K.; Awasthi, V. Surface engineering of liposomes for stealth behavior *Pharmaceutics* *5*, 542-569 (2013).
11. Galdiero, S.; Vitiello, M.; Falanga, A.; Cantisani, M.; Incoronato, N.; Galdiero, M. Intracellular delivery: exploiting viral membranotropic peptides *Curr Drug Metab* *13*, 93-104 (2012).
12. Berry, C. C. Intracellular delivery of nanoparticles via the HIV-1 tat peptide *Nanomedicine (Lond)* *3*, 357-365 (2008).
13. Gabathuler, R. Development of new peptide vectors for the transport of therapeutic across the blood-brain barrier *Ther Deliv* *1*, 571-586 (2010).
14. Jones, A. T. Gateways and tools for drug delivery: endocytic pathways and the cellular dynamics of cell penetrating peptides *Int J Pharm* *354*, 34-38 (2008).
15. Galdiero, S.; Falanga, A.; Vitiello, M.; Browne, H.; Pedone, C.; Galdiero, M. Fusogenic domains in herpes simplex virus type 1 glycoprotein H *J Biol Chem* *280*, 28632-28643 (2005).
16. Galdiero, S.; Falanga, A.; Vitiello, M.; Raiola, L.; Fattorusso, R.; Browne, H.; Pedone, C.; Isernia, C.; Galdiero, M. Analysis of a membrane interacting region of herpes simplex virus type 1 glycoprotein H *J Biol Chem* *283*, 29993-30009 (2008).
17. Galdiero, S.; Falanga, A.; Vitiello, M.; Raiola, L.; Russo, L.; Pedone, C.; Isernia, C.; Galdiero, M. The presence of a single N-terminal histidine residue enhances the fusogenic properties of a Membranotropic peptide derived from herpes simplex virus type 1 glycoprotein H *J Biol Chem* *285*, 17123-17136 (2010).
18. Galdiero, S.; Falanga, A.; Vitiello, M.; D'Isanto, M.; Cantisani, M.; Kampanaraki, A.; Benedetti, E.; Browne, H.; Galdiero, M. Peptides containing membrane-interacting motifs inhibit herpes simplex virus type 1 infectivity *Peptides* *29*, 1461-1471 (2008).
19. Galdiero, S.; Falanga, A.; Morelli, G.; Galdiero, M. GH625: A milestone in understanding the many roles of membranotropic peptides *Biochimica et Biophysica Acta - Biomembranes* *1848*, 16-25 (2015).

20. Carberry, T. P.; Tarallo, R.; Falanga, A.; Finamore, E.; Galdiero, M.; Weck, M.; Galdiero, S. Dendrimer functionalization with a membrane-interacting domain of herpes simplex virus type 1: towards intracellular delivery *Chemistry* *18*, 13678-13685 (2012).
21. Guarnieri, D.; Falanga, A.; Muscetti, O.; Tarallo, R.; Fusco, S.; Galdiero, M.; Galdiero, S.; Netti, P. A. Shuttle-mediated nanoparticle delivery to the blood-brain barrier *Small* *9*, 853-862 (2013).
22. Tarallo, R.; Accardo, A.; Falanga, A.; Guarnieri, D.; Vitiello, G.; Netti, P.; D'Errico, G.; Morelli, G.; Galdiero, S. Clickable functionalization of liposomes with the gH625 peptide from Herpes simplex virus type I for intracellular drug delivery *Chemistry* *17*, 12659-12668 (2011).
23. Smaldone, G.; Falanga, A.; Capasso, D.; Guarnieri, D.; Correale, S.; Galdiero, M.; Netti, P. A.; Zollo, M.; Galdiero, S.; Di Gaetano, S.; Pedone, E. gH625 is a viral derived peptide for effective delivery of intrinsically disordered proteins *Int J Nanomedicine* *8*, 2555-2565 (2013).
24. Falanga, A.; Vitiello, M. T.; Cantisani, M.; Tarallo, R.; Guarnieri, D.; Mignogna, E.; Netti, P.; Pedone, C.; Galdiero, M.; Galdiero, S. A peptide derived from herpes simplex virus type 1 glycoprotein H: membrane translocation and applications to the delivery of quantum dots *Nanomedicine* *7*, 925-934 (2011).
25. Caraglia, M.; Passeggio, A.; Beninati, S.; Leari, A.; Nicolini, L.; Improta, S.; Pinto, A.; Bianco, A. R.; Tagliaferri, P.; Abbruzzese, A. Interferon alpha2 recombinant and epidermal growth factor modulate proliferation and hypusine synthesis in human epidermoid cancer KB cells *Biochem J* *324* (Pt 3), 737-741 (1997).
26. Said Hassane, F.; Frisch, B.; Schuber, F. Targeted liposomes: convenient coupling of ligands to preformed vesicles using "click chemistry" *Bioconjug Chem* *17*, 849-854 (2006).
27. Sharma, A.; Sharma, U. S. Liposomes in drug delivery: Progress and limitations *International Journal of Pharmaceutics* *154*, 123-140 (1997).
28. Tardi, P. G.; Boman, N. L.; Cullis, P. R. Liposomal doxorubicin *J Drug Target* *4*, 129-140 (1996).
29. Peer, D.; Karp, J. M.; Hong, S.; Farokhzad, O. C.; Margalit, R.; Langer, R. Nanocarriers as an emerging platform for cancer therapy *Nat Nanotechnol* *2*, 751-760 (2007).
30. Sun, T.; Zhang, Y. S.; Pang, B.; Hyun, D. C.; Yang, M.; Xia, Y. Engineered nanoparticles for drug delivery in cancer therapy *Angew Chem Int Ed Engl* *53*, 12320-12364 (2014).
31. Zhang, L.; Gu, F. X.; Chan, J. M.; Wang, A. Z.; Langer, R. S.; Farokhzad, O. C. Nanoparticles in medicine: therapeutic applications and developments *Clin Pharmacol Ther* *83*, 761-769 (2008).
32. Kapse-Mistry, S.; Govender, T.; Srivastava, R.; Yegeri, M. Nanodrug delivery in reversing multidrug resistance in cancer cells *Front Pharmacol* *5*, 159 (2014).
33. Wu, Q.; Yang, Z.; Nie, Y.; Shi, Y.; Fan, D. Multi-drug resistance in cancer chemotherapeutics: mechanisms and lab approaches *Cancer Lett* *347*, 159-166 (2014).
34. Paszko, E.; Senge, M. O. Immunoliposomes *Curr Med Chem* *19*, 5239-5277 (2012).
35. Shen, Y.; Tang, H.; Zhan, Y.; Van Kirk, E. A.; Murdoch, W. J. Degradable poly(beta-amino ester) nanoparticles for cancer cytoplasmic drug delivery *Nanomedicine* *5*, 192-201 (2009).

Tables

Table 1. Zeta potential, size, expressed as z-average, as measured by DSL and polydispersity index (PDI). Data are expressed as means±standard deviation (SD) of three separate experiments for each of two batch formulations, with at least 13 measurements for each.

Liposomes	Average Size (nm)	PDI	Zeta potential (mV)
<i>Lipo</i>	104.95±1.63	0.17±0.01	-7.40±1.50
<i>LipoDoxo</i>	129.85±1.82	0.15±0.03	-7.43±1.84
<i>LipoDoxo-gH625</i>	143.90±0.64	0.14±0.02	9.43±1.61

Table 2. IC₅₀ values of the different formulations Concentration inhibiting 50% of cell growth (IC₅₀) reached after 72 h of treatment with Lipo, LipoDoxo, LipoDoxo-gH625, Doxo in A549 and A549 Dx cells. Data are shown as mean ± SD.

Compounds	IC50 ± SD A549	IC50± SD A549 DX
<i>Lipo</i>	$>5 \mu M \pm 0.02$	$>5 \mu M \pm 0.01$
<i>LipoDoxo</i>	$2.5 \mu M \pm 0.01$	$5 \mu M \pm 0.02$
<i>LipoDoxo -gH625</i>	$0.5 \mu M \pm 0.01$	$2.7 \mu M \pm 0.04$
<i>Doxo</i>	$0.06 \mu M \pm 0.03$	$0.2 \mu M \pm 0.01$

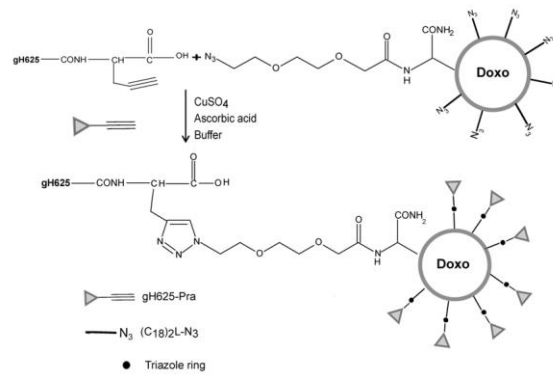


Figure 1. Scheme of the functionalization reaction of gH625 to LipoDoxo

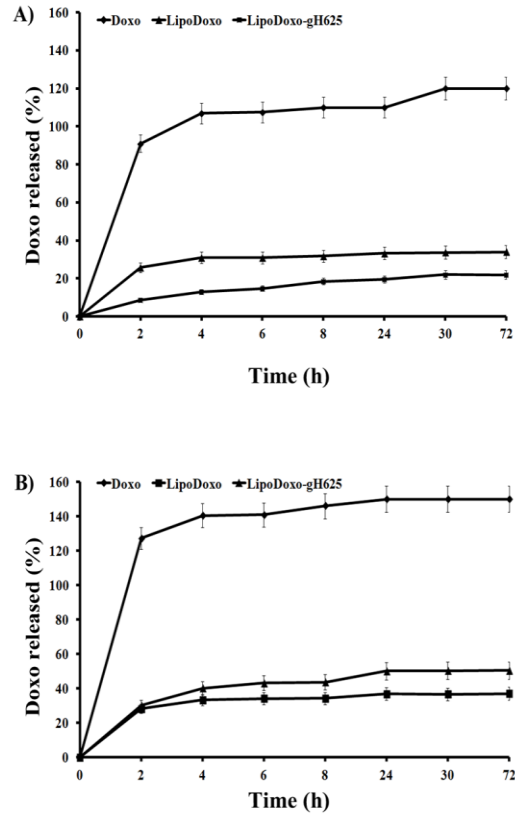


Figure 2. Release profile of doxorubicin from liposomes at 37 °C in HEPES-NaCl buffer (a) and in HEPES-NaCl buffer with 50% FBS (b).

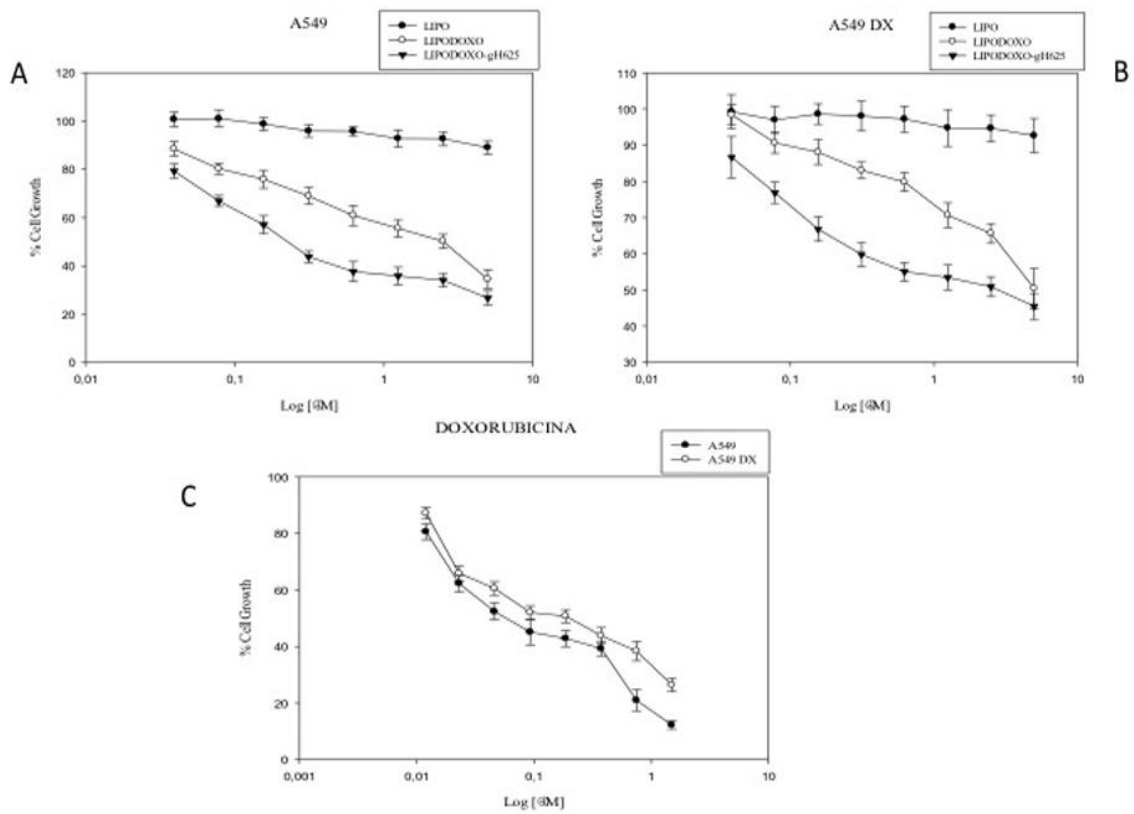


Figure 3. Evaluation of cell growth in lung adenocarcinoma cell line sensitive (A549) and resistant (A549 Dx) to doxorubicin after 72 h of treatment with Lipo, LipoDoxo, LipoDoxo-gH625 (A- B) and doxorubicin (DOXO) (C).

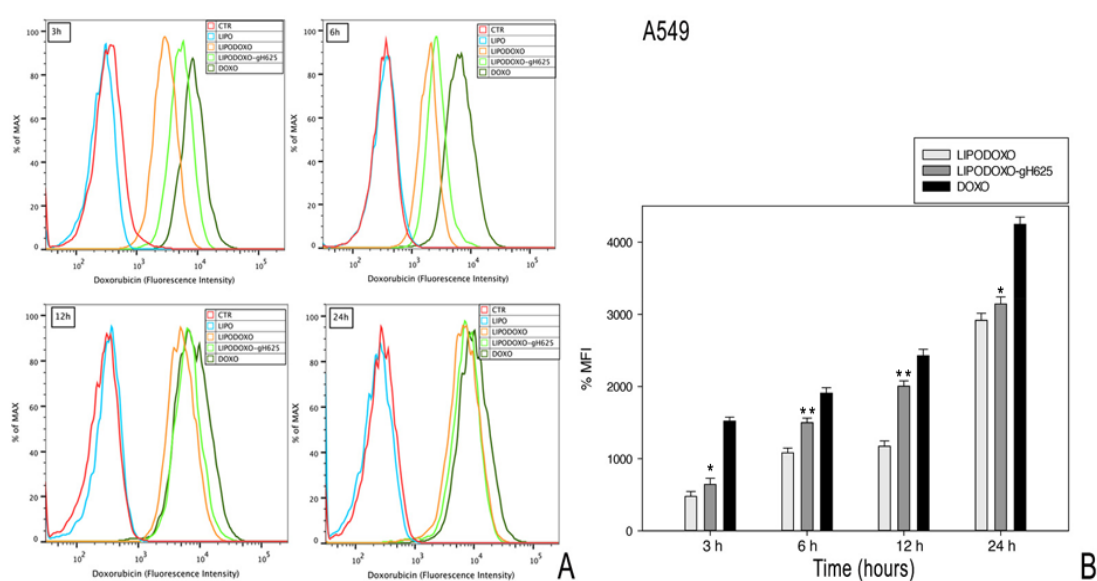


Figure 4. Doxorubicin accumulation in A549 cells after 3, 6, 12 and 24 h of treatment with LipoDoxo, LipoDoxo-gH625 and Doxo. (A) Flow cytometry overlay of Doxo fluorescence intensity. (B) Histogram of Doxo mean fluorescence intensity (% of control). The bars represent means \pm SD of three independent experiments. Asterisks indicate significant difference between LipoDoxo vs LipoDoxo-gH625 (** $P < 0.01$) (* $P < 0.05$)

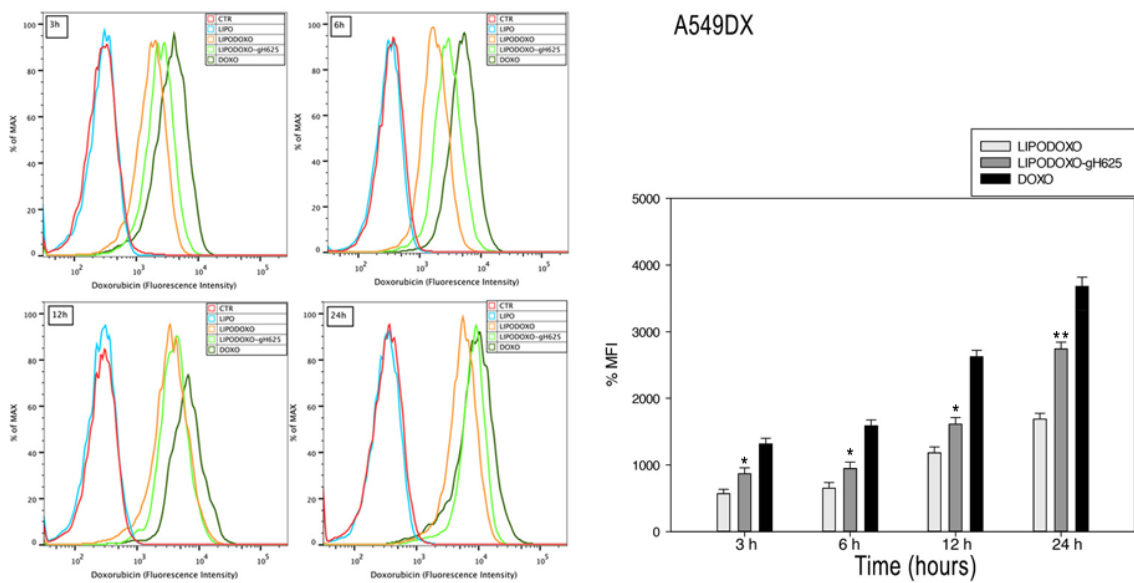


Figure 5. Doxorubicin accumulation in A549 Dx cells after 3, 6, 12 and 24 h of treatment with LipoDoxo, LipoDoxo-gH625 and Doxo. (A) Flow cytometry overlay of Doxo fluorescence intensity. (B) Histogram of Doxo mean fluorescence intensity (% of control). The bars represent means \pm SD of three independent experiments. Asterisks indicate significant difference between LipoDoxo vs LipoDoxo-gH625 (** $P < 0.01$) (* $P < 0.05$).

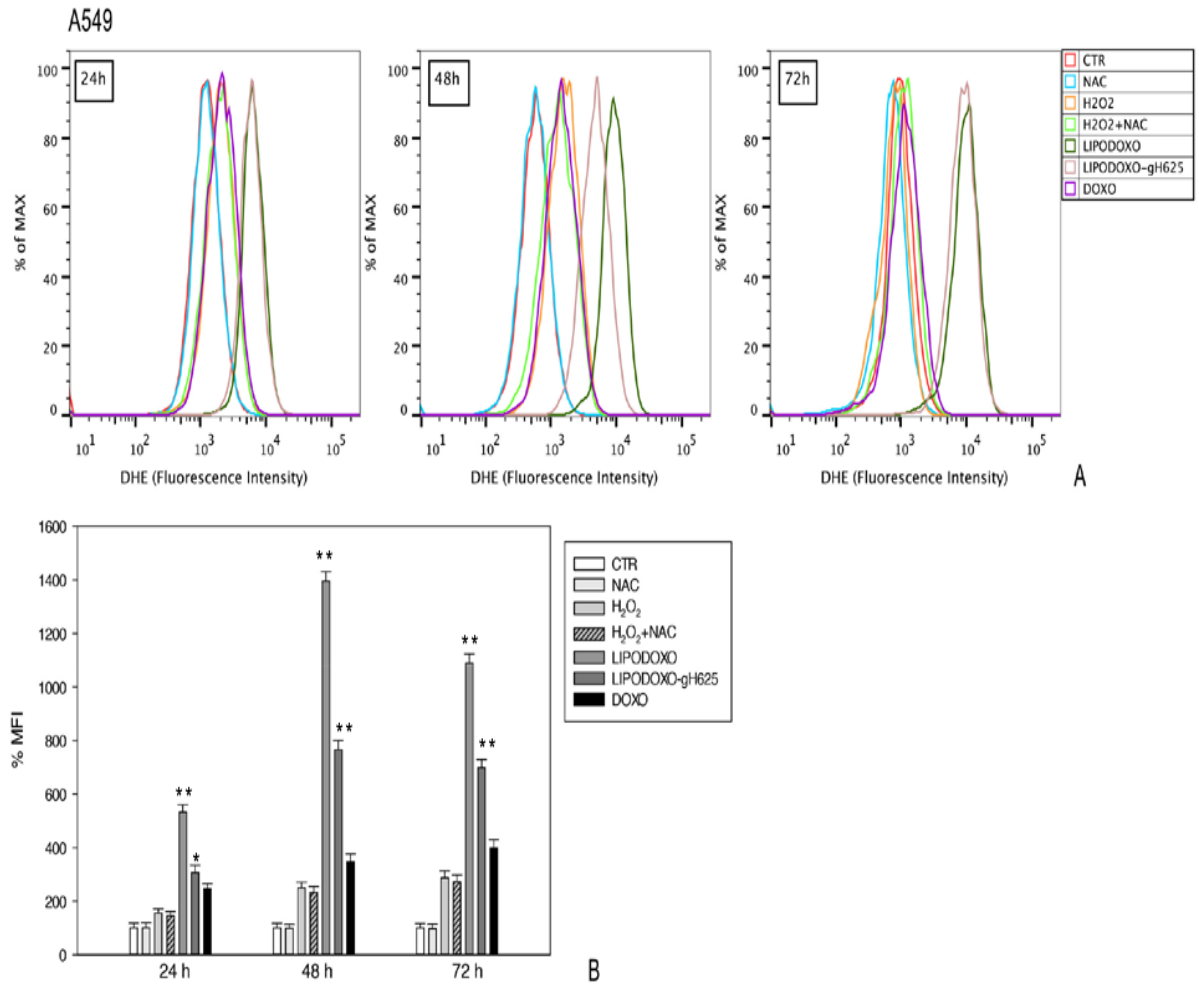


Figure 6. Evaluation of oxidative stress in A549 cells after 24, 48 and 72 h of treatment with LipoDoxo, LipoDoxo-gH625 and Doxo. A) Flow cytometry overlay of dihydroethidium (DHE) fluorescence intensity. (B) Histogram of DHE mean fluorescence intensity (% of control). The bars represent means \pm SD of three independent experiments. Asterisks indicate significant difference between LipoDoxo vs Doxo and LipoDoxo-gH625 vs Doxo (** $P < 0.01$) (* $P < 0.05$).

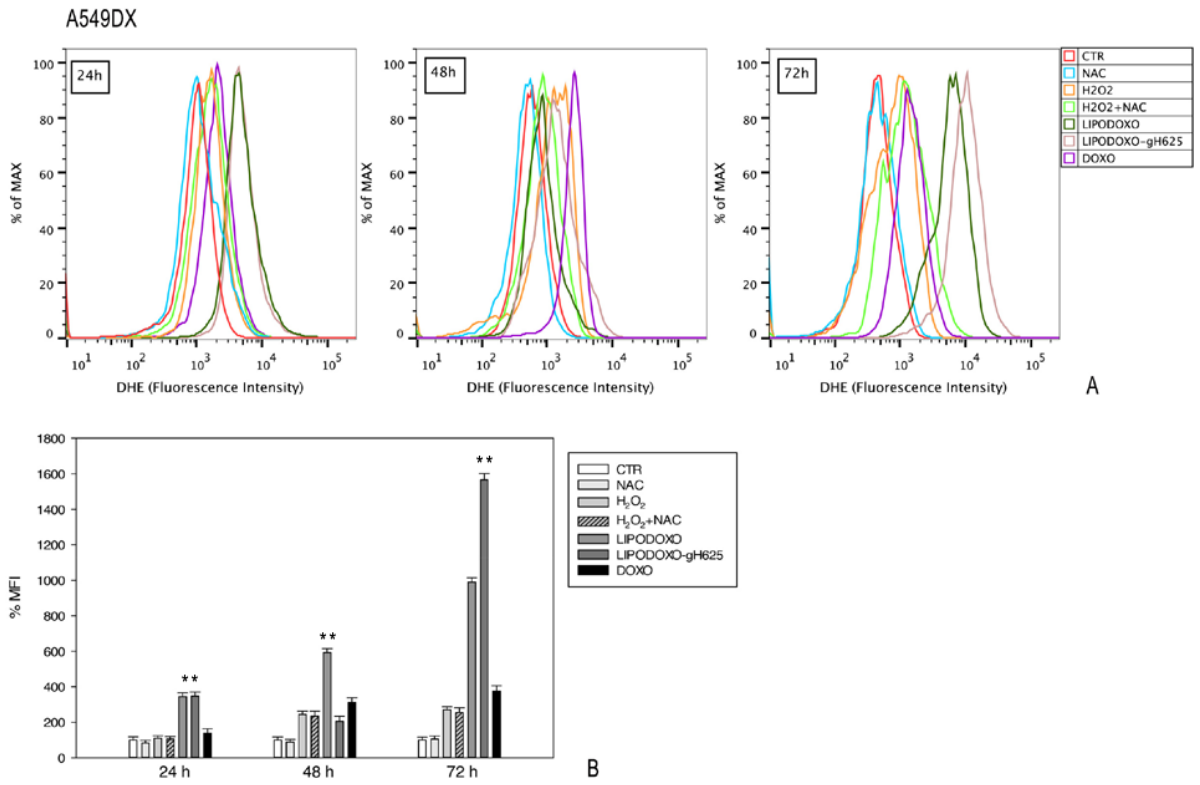


Figure 7. Evaluation of oxidative stress in A549dx cells after 24, 48 and 72 h of treatment with LipoDoxo, LipoDoxo-gH625 and Doxo. (A) Flow cytometry overlay of dihydroethidium (DHE) fluorescence intensity. (B) Histogram of DHE mean fluorescence intensity (% of control). The bars represent means \pm SD of three independent experiments. Asterisks indicate significant difference between LipoDoxo vs Doxo and LipoDoxo-gH625 vs Doxo (**P<0.01).

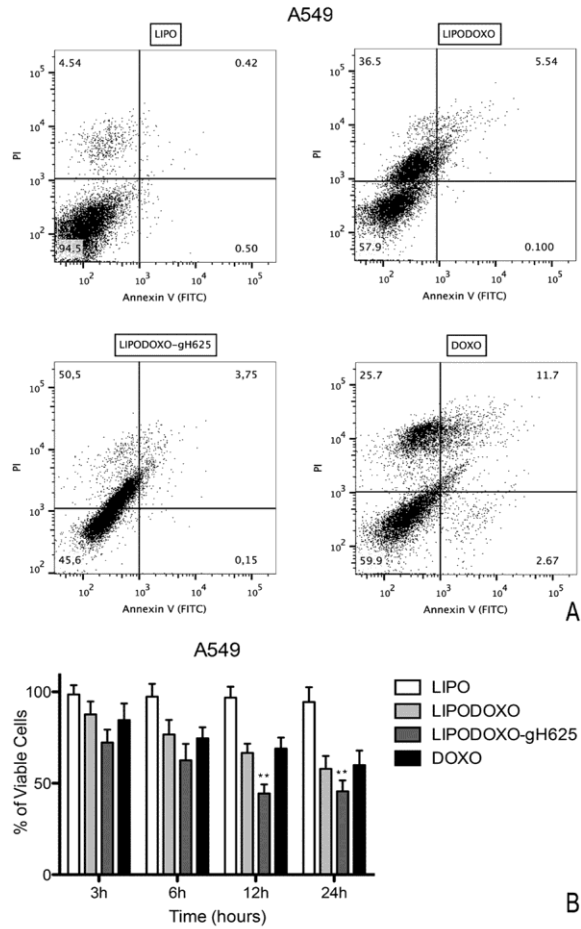


Figure 8. Evaluation of apoptosis in A549 cells by Annexin V/PI assay (flow cytometry) after 48 h of treatment with LipoDoxo, LipoDoxo-gH625 and Doxo. (A) Flow cytometry dot plots. (B) Histogram of data expressed as percentage of viable cells, early/late apoptotic cells and necrotic cells after 3, 6, 12 and 24 h. The bars represent means \pm SD of three independent experiments. Asterisks indicate significant difference between LipoDoxo-gH625 vs Doxo (**P<0.01).

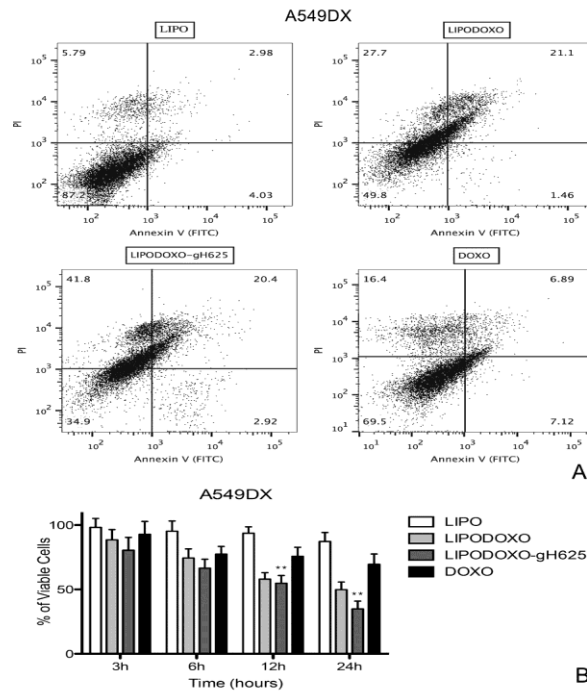


Figure 9. Evaluation of apoptosis in A549dx cells by Annexin V/PI assay (flow cytometry) after 48 h of treatment with LipoDoxo, LipoDoxo-gH625 and Doxo. (A) Flow cytometry dot plots. (B) Histogram of data expressed as percentage of viable cells, early/late apoptotic cells and necrotic cells 3, 6, 12 and 24 h. The bars represent means \pm SD of three independent experiments. Asterisks indicate significant difference between LipoDoxo-gH625 vs Doxo (**P<0.01).

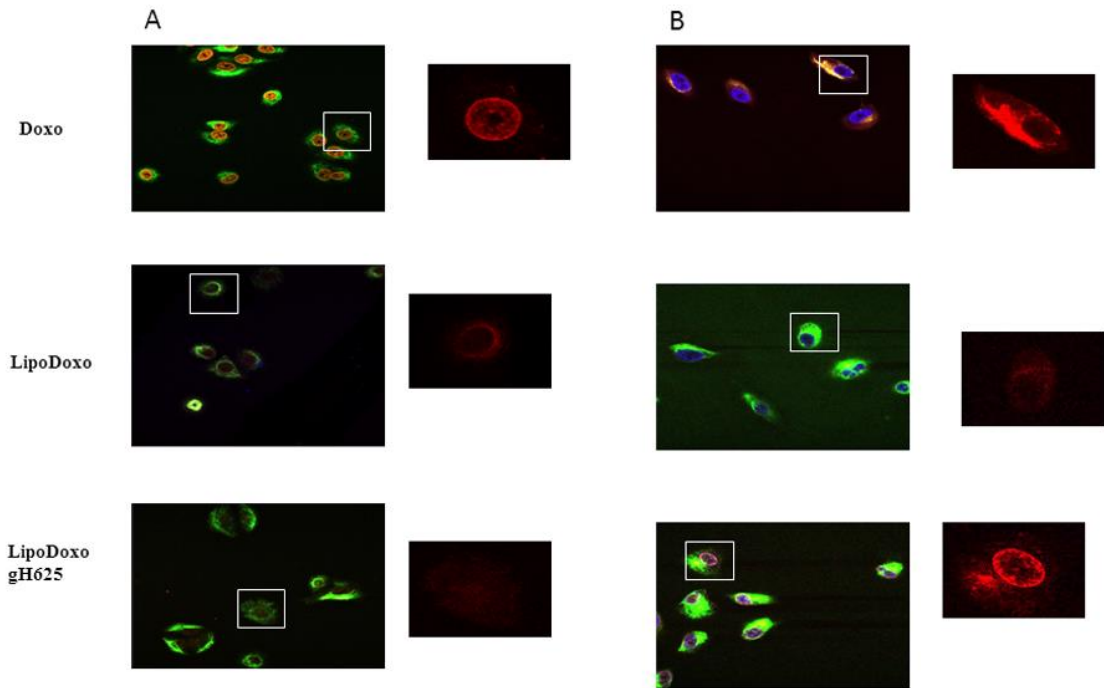


Figure 10. Confocal microscopy images of A549 (A) and A549 Dx (B) cells after 6 h incubation with free Doxo, LipoDoxo, or LipoDoxo-gH625. On the left, merged image (green vimentin; red doxo; blue dapi). On the right, Doxo distribution.

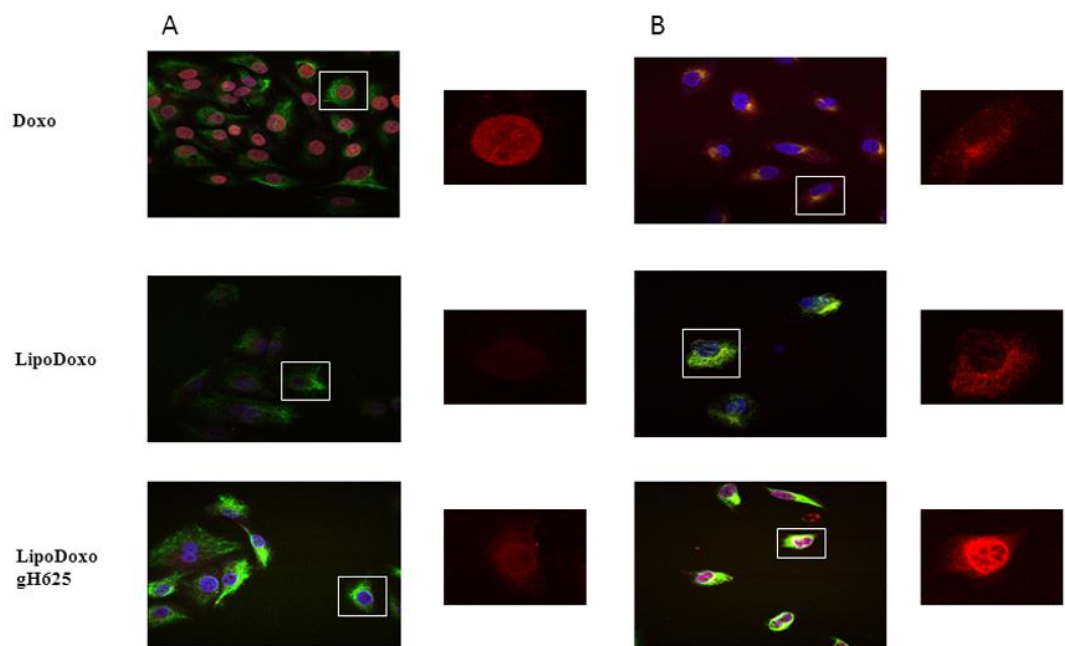


Figure 11. Confocal microscopy images of A549 (A) and A549 Dx (B) cells after 24 h incubation with free Doxo, LipoDoxo, or LipoDoxo-gH625. On the left, merged image (green vimentin; red doxo; blue dapi). On the right, Doxo distribution.